Characterisation of propagating modes and ultrafast dynamics in plasmonic devices

Kellie Pearce

München 2021

Characterisation of propagating modes and ultrafast dynamics in plasmonic devices

Kellie Pearce

Dissertation
an der Fakultät für Physik
der Ludwig–Maximilians–Universität
München

vorgelegt von
Kellie Pearce
aus Orange

München, den 12. Oktober 2021

Erstgutachter: Prof. Dr. Ulf Kleineberg
Zweitgutachter: Prof. Dr. Alexander Högele
Tag der mündlichen Prüfung: 18. January 2022

Contents

List of Figures

List of Tables

Publications by the Author

Journals

K. Pearce, M. Kestler, C. Späth, U. Kleineberg. Femtosecond Dynamics of Extraordinary Optical Transmission Through Hexagonal Gold Nanohole Arrays. *Nanophotonics*, in preparation.

K. Pearce, F. Schuknecht, C. Späth, B. Duschner, F. Richter, U. Kleineberg. Monitoring the surface quality of silver plasmon waveguides with nonlinear photoemission electron microscopy and in-situ ion sputtering. *Ultramicroscopy*, 183:55–60, 2017.

Proceedings

K. Pearce, R. Dehde, A. Spreen, C. Späth, M. Wendl, J. Schmidt, U. Kleineberg. Modulation of extraordinary optical transmission through nanohole arrays using ultrashort laser pulses. *Proc. SPIE 9884, Nanophotonics VI*, 9884:496–502, 2016.

S.H. Chew, K. Pearce, S. Nobis, C. Späth, A. Spreen, S. Radünz, Y. Yang, J. Schmidt, U. Kleineberg. Spatiotemporal characterization and control of lightfield nanolocalization on metallic nanostructures by nonlinear-PEEM. *Proc. SPIE 8457, Plasmonics: Metallic Nanostructures and Their Optical Properties X*, 8457:80–88, 2012.

Book Chapters

S.H. Chew, K. Pearce, C. Späth, A. Guggenmos, J. Schmidt, F. Süßmann, M.F. Kling, U. Kleineberg, E. Mårsell, C.L. Arnold, E. Lorek, P. Rudawski, C. Guo, M. Miranda, F. Ardana, J. Mauritsson, A. L'Huillier and A. Mikkelsen. Imaging Localized Surface Plasmons by Femtosecond to Attosecond Time-Resolved Photoelectron Emission Microscopy —"ATTO-PEEM" in *Attosecond Nanophysics: From Basic Science to Applications*, John Wiley and Sons Inc., 2015.

Zusammenfassung

Oberflächenplasmonen sind kollektive Schwingungen der Leitungsbandelektronen an einer Metall-Dielektrikum Grenzfläche, die typischerweise durch kurze Lichtpulse angeregt werden. Plasmonische Bauelemente besitzen das Potential, hohe spektrale Bandbreiten auf der Nanoskala zu implementieren. Die Herstellung und Charakterisierung von plasmonischen Bauelementen stellen wegen ihrer geringen Größe, ihrer Empfindlichkeit gegenüber ihrer Umgebung und der kurzen Lebensdauer der Plasmonen noch viele Herausforderungen an die Fabrikationstechniken wie auch die Materialeigenschaften. Diese Prozesse erfordern eine Beobachtung der Anregung, Ausbreitung und Wechselwirkung der Plasmonen auf angemessene räumlichen und zeitlichen Skalen (jeweils Nanometer und Femtosekunden). In einigen Fallen wird es auch notwendig, die Oberflächenqualität auszuwerten und zu modifizieren. In dieser Arbeit wurden plasmonische Nanoantennen, Wellenleiter und Arrays von Nanolöchern entwickelt und hergestellt. Die lokalisierten und sich ausbreitenden Oberflächenplasmon-Polaritonen wurden dann mit nichtlinearer 2-Photononen Photoemissionsmikroskopie (2P-PEEM) und Femtosekunden-Pump-Probe-Spektroskopie charakterisiert. Diese Experimente wurden durch Finite-Difference Time-Domain (FDTD) Simulationen ergänzt. Zwei-Photonen PES und Simulationen von Silbernanoantennen (in Form von Doppelellipse- und Schmetterlingsantennen) haben gezeigt, dass Stellen mit hoher Feldverstärkung durch die Veränderung der Polarisationsrichtung der Laserstrahlquelle selektiv angeregt werden können. Plasmonische Streifenwellenleiter mit Spitze aus Silber wurden entwickelt, um einfallendes Licht von der Laserquelle in ausbreitenden Moden zu koppeln und den Einfluss von der Geometrie der Einkopplungsgitter, der Streifenlänge und -breite und der Kegelwinkel zu untersuchen. Die Anregung der sich ausbreitenden Oberflächenplasmon-Polaritonen wurde durch das Vorhandensein von Interferenzstreifen der hohen Photoemissionsintensität entlang der Längsachse der Wellenleiter nachgewiesen. Diese Intensitätsbanden ergeben sich aus der Interferenz zwischen sich ausbreitende Oberflächenplasmonen miteinander und mit dem einfallenden Licht. Diese Wechselwirkung wurde mit Simulationen modelliert. Durch Experimente und Simulationen wurde demonstriert, dass die Regelmäßigkeit der Oberfläche, die Streifenbreite und der Einfallswinkel jeweils die Zahl der Bande beeinflussen können. Es wurde gezeigt, dass eine Oberflächenbehandlung mit niederenergetischen Argon-Ionen-Beschuss die Sichtbarkeit der Interferenzbanden auf dem Wellenleiter erhöhen kann. In einem weiteren Experiment wurde die Übertragung ultrakurzer fs-Laserpulse durch periodische Löcherarrays as Gold mittels Simulationen sowie Pump-Probe-Experimenten untersucht. Der Einfluss der plasmonischen Felder an den Grenzflächen auf die transiente Transmission durch die Locharrays wurde durch Simulationen demonstriert, wobei die Lochgröße, Gitterkonstante, Schichtdicke, und dielektrische Umgebung systematisch verändert wurden. Durch die Einführung eines zweiten Probepulses mit veränderlicher Zeitverzögerung konnte ein Zusammenhang zwischen Plasmonendynamik und Transmissionsdynamik in Simulationen etabliert werden. Die ersten Ergebnisse von Pump-Probe-Experimenten haben die Modulation der Übertragung mittels der vorherigen Anregung der plasmonischen Felder als optischer Schalter nachgewiesen.

Chapter 1

Introduction

Nanostructures — objects defined as having at least one dimension between 1 and 100 nm in size — can possess strongly size-dependent optical, electronic, chemical, and thermal properties which differ greatly from their bulk counterparts. These properties result from several effects which become substantial at the nanoscale. For example, large surface-to-volume ratios increase the influence of surface phenomena, the electron mean free path can be comparable to the size of the structure, and in some cases quantum confinement in one or more dimensions occurs. Given their unique and tailorable properties, there has been enormous interest in potential applications of nanostructures and materials made from them. Over the last several decades, improvements in the ability to fabricate and study nanostructures has given rise to a new field of science and engineering — *nanotechnology*.

Nanophotonics or *nano-optics* falls under the umbrella term of nanotechnology, and refers to the study of the interaction between light and materials on the nanometre scale. In metals, electromagnetic radiation can interact with the conduction electrons on an interface to produce oscillations in the charge density. These oscillations, or *surface plasmons*, lead to enhanced optical near-fields which can be confined to sub-wavelength dimensions, thus overcoming the restriction imposed by the diffraction limit for optical devices. In addition, propagation speeds of these surface plasmons can be on the order of the speed of light [1,2]. The combination of these two capabilities offers the possibility of merging the bandwidth of photonics with the compactness of electronics in nanophotonic circuits and devices — a field of research encompassed by the term *plasmonics*. Devices based on surface plasmon polaritons (SPPs) are expected to serve as both independent, highly integrated sensing and signal-processing elements and as efficient links between current optical communication components and nanoelectronic circuits.

The goal of this thesis was to design plasmonic nanoantennas, waveguides, and nanohole arrays for the excitation of localised and propagating surface plasmon polariton modes, to characterise these modes spatially and temporally on their genuine length and time scales

by photoemission electron microscopy (PEEM) and ultrafast spectroscopy, and support these measurements by numerical modelling with finite-difference time-domain (FDTD) simulations. This thesis is split into 5 chapters, of which Chapter 1 is this introduction. Chapter 2 introduces the history and theory of concepts concerning surface plasmon polaritons which are most relevant to this work. These include classical electromagnetism and solid state theory as applied to metals, formalisms for surface plasmon propagation along planar interfaces, several excitation schemes for surface plasmons, the behaviour of surface plasmons confined in several dimensions, and the dynamics of light transmission through arrays of nanoholes in metal films.

There are several challenges involved in the practical implementation of plasmonic devices. For example, plasmonic waveguides typically have hefty propagation losses which limits their useable length to micron scales [3–5], and there is a trade-off between propagation length and achievable field confinement. Many structures optimised for either efficient waveguiding or field enhancement are difficult to fabricate, or at least difficult to fabricate reliably [6–8]. Finally, integrating the most commonly-used materials for plasmonic structures — gold and silver — with established silicon photonics and electronics is nontrivial [9, 10].

To assist in overcoming these challenges, methods for examining plasmonic devices on the characteristic length- and time-scales of plasmonic processes are needed. Chapter 3 discusses the primary experimental techniques used in this thesis. PEEM imaging is used to investigate plasmon modes in silver nanoantennas and stripe waveguides and the influence of waveguide surface quality on their excitation and propagation. Ultrafast pump-probe spectroscopy is used to examine interactions between plasmon modes in a nanohole array and their subsequent effect on the transmission. The fabrication of plasmonic samples via electron-beam lithography (EBL) and surface treatment with argon ion sputter cleaning are also discussed.

Chapter 4 presents the results of single- and two-photon PEEM (1P- and 2P-PEEM) imaging of fabricated silver nanoantennas and stripe waveguides. Plasmonic nanoantennas can provide strong, direction-dependent coupling between far-field and near-field radiation at optical frequencies, as well as high degrees of subwavelength localisation of electromagnetic fields [11]. Nanoantennas in the form of double bowtie and double ellipses of several different sizes were fabricated to investigate the influence of nanoantenna shape, size, and the polarisation of the excitation source on the plasmonic field enhancement. For these nanoantennas, hot spots from areas of surface and edge roughness are seen to dominate the photoemission signal, which can be selectively excited by rotating the incident polarisation. To support these experiments, FDTD simulations are used to model the effects of nanoantenna shape, size, and surface roughness on the electric field enhancement. Another method to couple optical far-fields to near-fields which spatially separates the two is via tapered waveguides. Plasmons are excited at one location and propagate a certain distance before being focused, which can be achieved by patterned thin metal stripes on dielectric

substrates [12, 13]. Tapered stripe waveguides with different incoupling gratings, widths, lengths, and taper angles were designed and fabricated to try to find the combination of these parameter which would produce the greatest field enhancement at the taper tip under 2P-PEEM excitation conditions. Again, variations in surface morphology and regularity amongst individual waveguides rendered this comparison impractical, but opened up the possibility of studying the effect of surface modification via argon ion sputter cleaning on individual waveguides. Sputter treatment was shown to affect the localised emission from hotspots and intensity of photoemission from propagating modes on the waveguide surfaces.

Two decades ago, it was shown that metal films perforated with arrays of subwavelength holes can transmit visible light with efficiencies which are orders of magnitude higher than the transmission predicted by classical diffraction theory. Since then, progress has been made in understanding this phenomenon of extraordinary optical transmission (EOT), and the crucial role played by both localised and propagating surface plasmons. Due to their selective transmissive properties and the presence of strong surface fields, nanohole arrays can be used as wavelength filters [14, 15], nanopolarisers [16], and as components in novel photonic devices [17, 18]. As with many plasmonic nanostructures, their sensitivity to the local environment and tunability has driven efforts to use nanohole arrays for molecular detection and to enhance Raman and fluorescence spectroscopy [19–21]. There is also the prospect of using the holes as nanochannels to combine biosensing with nanofluidics [22].

One of the major goals of EOT experiments is to exploit the enhanced optical near field for applications in all-optical, electrical, or thermal switching of the transmission [17, 23]. Despite the intense interest in nanohole arrays, comparatively few time-resolved studies have been performed. A full physical description of the process needs to include the dynamics of energy transport through the nanoholes and on the interfaces, which in turn requires time-resolved measurements using an excitation source which is shorter than the damping and coupling time of the SPPs [24]. Short excitation pulses should also allow pump-probe absorption spectroscopy of thin molecular layers, enhanced by the near-fields of the array [17, 25]. Furthermore, having the means for all-optical switching using a combination of nonlinear materials and/or short pulses enables a high degree of control over the spatial and temporal distribution of the electromagnetic fields [26, 27].

Chapter 5 presents results from simulations and experiments of the transmission of single and double ultrashort (10 fs) pulses through gold hole arrays on dielectric substrates. In double-pulse experiments and simulations, the incident pulse is split into two identical pulses separated by a time delay; the idea is that the initial pulse excites plasmonic fields on the array, which will then effect the transmission of the second pulse when it becomes incident on the array at a given time afterwards. The influence of the array geometry (hole size, spacing, and film thickness) on the surface fields and single- and double-pulse transmission is studied using FDTD simulations. By simulating the transmission with time delay and looking at the behaviour of transmission peaks associated with certain

resonances, a description of the interface coupling and transmission dynamics is established. This chapter also details the first experimental results of single- and double-pulse transmission through gold nanohole arrays produced via EBL.

A conclusion summarising the major findings and an outlook complete this work. Further details of the FDTD simulation method and nanohole results are given in the Appendix.

Chapter 2

Theory and Overview of Surface Plasmons

This chapter presents the relevant historical milestones and concepts from electrodynamic and solid state theory, and discusses their application to surface plasmons. It also presents a review of the literature relating to the development and applications of various plasmonic devices investigated in this thesis.

2.1   Historical and Theoretical Background

2.1.1   Discovery of Surface Plasmons

The existence of electromagnetic surface waves on conductors was predicted as early as the turn of the twentieth century, when Sommerfeld [28] and later Zenneck [29] provided mathematical descriptions of such waves in the radio region. Sommerfeld used Maxwell's equations to find a solution to the problem of electromagnetic waves propagating along a long, cylindrical conductor; Zenneck did the same for a planar surface bounding two media of different conductivity and dielectric constants.

During the same period, an experiment by Wood [30] showed that the spectrum of light from a certain metal diffraction grating contained unusual intensity drops. These drops, thereafter known as Wood's anomalies, occurred over narrow ranges of wavelengths and were approximately one order of magnitude. It was not until several decades later that Fano [31] was able to link this experiment with the earlier theories of Sommerfeld and Zenneck, providing an explanation for the anomalies by assuming that the lost energy was converted into surface waves.

The Second World War introduced the large-scale industrial application of thin films for coatings and electronics, spurring scientific and technological interest [32, 33]. In 1948, Ruthemann [34] and Lang [35] independently measured the energy of electrons passing though thin metallic foils and saw losses at given energies for certain metals. Four years later, Pines and Bohm [36] created a collective description of interactions between electrons in a dense electron gas that could account for these losses. They discovered quantised oscillations in the plasma density, similar to those that had been reported over a decade before by Tonks and Langmuir [37] in gases.

In 1956, Ritchie [38] was able to expand the description of Pines and Bohm by considering the influence of the metal film boundary. He realised that the formation of collective surface plasma oscillations, which he called *plasmons*, would lead to lower energy losses in the case of thin films. The first experimental evidence of these excitations was provided two years later by Powell and Swan [39], subsequently termed *surface plasmons* by Stern and Ferrell [40]. In 1968, Ritchie [41] turned his attention to the much earlier studies on anomalous losses in diffraction gratings, and found that in the optical domain, these could be analysed in terms of surface plasmon resonances.

Interestingly, applications of surface plasmon resonance predate the scientific description of the phenomenon by many centuries. Perhaps the most oft-cited of these is the Lycurgus cup, a Roman glass cup dating from the fourth century AD which exhibits dichroism due to colloidal gold and silver nanoparticles embedded in the glass [42]. The integration of metal colloids to create vibrant colours in glass is also seen in the stained-glass windows of certain cathedrals and churches around the world, including the Notre Dame in Paris, constructed during the twelfth and thirteenth centuries [43].

Modern applications of surface plasmons, commonly termed *plasmonics*, began emerging in the 1970s after a couple of significant discoveries were made. The first was a method of exciting surface plasmons on planar metal surfaces using a prism coupler, which can take one of two configurations [44, 45]. These are described below in section 2.5. The second was the increase in the Raman scattering signal from molecules when they were fixed on a silver surface [46]. This effect, now used in surface-enhanced Raman spectroscopy (SERS), has demonstrated enhancement factors up to the order of $10^{14} - 10^{15}$, allowing single-molecule detection [47, 48].

At present, the scope of plasmonics comprises a broad variety of fields, including chemical and biological sensing [49–51], cancer detection and treatment [52–54], microscopy [55, 56], lithography [57, 58], photovoltaics [59–61], computation [3, 62, 63], and data storage [64, 65]. Of these, plasmonic sensors have had the most commercial impact to date, having been in use since the early 1980s [66]. The wealth of current and potential applications is due to the many unique properties of surface plasmons, such as electromagnetic field confinement and enhancement, high group velocities, and sensitivity to local geometry and dielectric environment.

2.1.2 Electromagnetism in Metals

As indicated by their nomenclature, plasmons have particle-like properties and can be considered as quasiparticles, so should in principle be treated in the framework of quantum mechanics. However, most properties of surface plasmons can be sufficiently described by classical electrodynamics. In metallic nanostructures larger than a few nanometres, high free carrier densities lead to spacings in the electron energy levels far smaller than thermal excitations of order $k_B T$ at room temperature [23]. Additionally, objects can be described by a bulk dielectric function if the mean free path of the electrons is shorter than the characteristic dimensions of the object, which is applicable for structures down to approximately $10\,\text{nm}$ in size [67]. Therefore, a classical approach is appropriate for all nano- and microstructures considered in this thesis.

At the core of classical electrodynamics and optics are Maxwell's equations, which describe the relationship between electric and magnetic fields, their propagation in space and time, and their origin from free charges and currents. In the presence of matter, the four macroscopic equations are as follows:

$$\nabla \times \vec{E} = -\frac{\partial \vec{B}}{\partial t} \tag{2.1}$$

$$\nabla \times \vec{H} = \vec{j}_F + \frac{\partial \vec{D}}{\partial t} \tag{2.2}$$

$$\nabla \cdot \vec{D} = \rho_F \tag{2.3}$$

$$\nabla \cdot \vec{B} = 0 \tag{2.4}$$

where $\vec{E}$ and $\vec{H}$ are the electric and magnetic fields, respectively, $\vec{B}$ is the magnetic induction or flux density, $\vec{D}$ is the dielectric displacement, and ρ_F and $\vec{j}_F$ are the free charge and current densities.

In free space, $\vec{E}$ and $\vec{B}$ are sufficient to describe the propagation of electromagnetic fields; in the presence of matter the terms $\vec{D}$ and $\vec{H}$ need to be introduced to account for the material response. In the presence of an electric field, the sum of all individual dipole moments due to the displacement of the free electrons gives rise to a macroscopic polarisation per unit volume, $\vec{P}$. The dielectric displacement is then defined by

$$\vec{D} = \varepsilon_0 \vec{E} + \vec{P} \tag{2.5}$$

Likewise, the magnetic field is defined in terms of the magnetisation $\vec{M}$:

$$\vec{H} = \frac{1}{\mu_0}\vec{B} - \vec{M} \tag{2.6}$$

The constants ε_0 and μ_0 are the permittivity and permeability of free space ($\varepsilon_0 = 8.854 \times 10^{12}$ Fm^{-1} and $\mu_0 = 4\pi \times 10^{-7}$ NA^{-2} in SI units).

By introducing the constitutive relations

$$\vec{D} = \varepsilon_0\varepsilon\vec{E} \tag{2.7}$$

and

$$\vec{B} = \mu_0\mu\vec{H} \tag{2.8}$$

the material response can be condensed into the terms ε and μ, named relative permittivity and relative permeability. Despite both terms being frequency-dependent, ε is commonly referred to as the *dielectric constant*. In general, ε and μ are tensors, but for simplification the medium is often assumed to be linear (field-independent), and homogeneous and isotropic (position and direction-independent).

Lastly, the electric field is related to the current density via

$$\vec{j} = \sigma\vec{E} \tag{2.9}$$

where σ is the conductivity of the medium.

The materials used in this thesis are all non-magnetic, so from this point on only the dielectric response is considered.

2.1.3 Solid State Theory

Although Maxwell's equations had been published in the early 1860s, until the start of the twentieth century very little was known about the structure of matter. Shortly after Thomson's discovery of the electron, Drude proposed a model for electron dynamics in metals based on the kinetic theory of gases which would explain electrical conduction. From the Drude model the equation of motion for an electron of effective mass m_e and collision rate γ is

$$m_e\ddot{\vec{x}} + m_e\gamma\dot{\vec{x}} = -e\vec{E} \tag{2.10}$$

Assuming the external field $\vec{E}$ has a harmonic time dependence $\vec{E}(t) = \vec{E}_0 e^{-i\omega t}$, then solutions for $\vec{x}$ have the form $\vec{x}(t) = \vec{x}_0 e^{-i\omega t}$. The macroscopic polarisation $\vec{P}$ due to electrons with a number density N is $\vec{P} = -Ne\vec{x}$. Inserting this into Equations 2.5 and 2.7 yields an expression for the relative permittivity:

$$\varepsilon_{Drude}(\omega) = 1 - \frac{\omega_p^2}{\omega^2 + i\gamma\omega} \tag{2.11}$$

where

$$\omega_p = \sqrt{\frac{Ne^2}{m_e \varepsilon_0}} \tag{2.12}$$

is the volume plasma frequency. This complex term can be split into real and imaginary parts $\varepsilon_{Drude}(\omega) = Re(\varepsilon) + iIm(\varepsilon)$ with

$$Re(\varepsilon) = 1 - \frac{\omega_p^2}{\omega^2 + \gamma^2} \tag{2.13}$$

and

$$Im(\varepsilon) = \frac{\gamma \omega_p^2}{\omega(\omega^2 + \gamma^2)} \tag{2.14}$$

From the equations above, for very large frequencies $\omega \gg \omega_p$ the dielectric function approaches unity. For the noble metals gold, silver and copper, an adjustment to this free-electron model needs to be made in the region $\omega > \omega_p$ to account for the effect of the filled d-bands [23]. These electrons lie close to the Fermi energy and create a highly polarised background which can be described by a dielectric constant ε_∞, giving

$$\varepsilon(\omega) = \varepsilon_\infty - \frac{\omega_p^2}{\omega^2 + i\gamma\omega} \tag{2.15}$$

The real and imaginary parts of the dielectric function for gold are plotted as solid lines in Figure 2.1, using Equation 2.15 and the values from Table 2.1. Experimental results from Johnson and Christy [69] are plotted as dashed lines. For low energies, the Drude model quite accurately describes the behaviour of the dielectric function. However, as seen from the figure, at visible frequencies the model breaks down due to the presence of interband transitions in this regime, in which photons excite electrons from lower-lying bands into the conduction band. In a classical framework these transitions can be described via the oscillation of bound electrons, whose response is given by a new equation of motion:

$$m_e \ddot{\vec{x}} + m_e \gamma \dot{\vec{x}} + \alpha \vec{x} = -e\vec{E} \tag{2.16}$$

Metal	ω_p $(\cdot 10^{15} s^{-1})$	γ $(\cdot 10^{15} s^{-1})$	ε_∞
Au	13.8	0.11	9.84
Ag	14.0	0.032	3.7
Cu	13.4	0.14	4.5

Table 2.1: Plasma frequency ω_p, damping constant γ, and ε_∞ for the noble metals gold, silver, and copper. The plasma frequency and damping constant are taken from Cai and Shalaev [68]; values for ε_∞ are taken from Johnson and Christy [69].
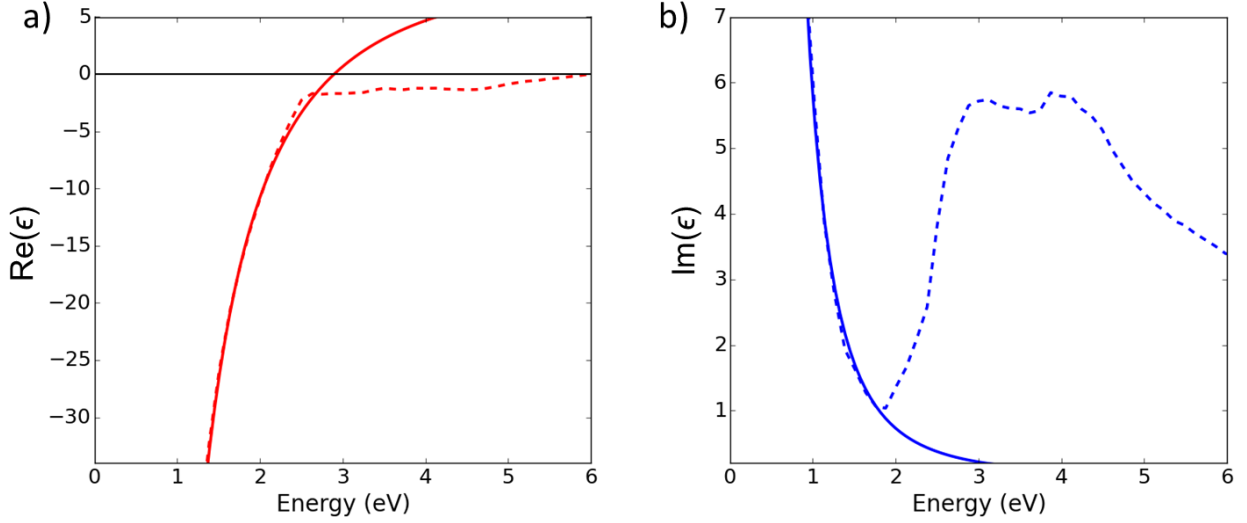
Figure 2.1: a) Real and b) imaginary parts of the dielectric function for gold. The solid lines are the values according to the Drude model; dashed lines are experimental values from Johnson and Christy [69].

where the effective mass m_e is that of a bound electron, the damping constant γ mainly describes radiative damping, and α is the spring constant of the binding potential.

This can be solved to find the contributions of bound electrons to the relative permittivity:

$$\varepsilon_{Drude}(\omega) = 1 + \frac{\tilde{\omega}_p^2}{(\omega_0^2 - \omega^2) + i\gamma\omega} \tag{2.17}$$

where $\omega_0 = \sqrt{\frac{\alpha}{m}}$, and $\tilde{\omega}_p$ a term analogous to the plasma frequency encompasses the density of the bound electrons. The real and imaginary parts of this term display dispersion-like and resonant behaviour, respectively.

2.1.4 Plasmonic Materials

Most of the interest surrounding the applications of surface plasmons has been related to their characteristics of strong field localisation and enhancement at optical frequencies. For these purposes, a large negative value of the relative permittivity is the most important material parameter, which is governed by a large ratio of the plasma frequency to the damping constant as seen in Equation 2.15. The plasma frequency 2.12 is proportional to the square root of the carrier density; noble metals with their very large carrier densities therefore have high plasma frequencies. Semiconductors, graphene, and nonstoichiometric compounds such as metal oxides and nitrides can be doped to increase their carrier densities by several orders of magnitude [70]. The ratio ω_p/γ of some common plasmonic materials is given in Table 2.2.

Material	ω_p ($\cdot 10^{15} s^{-1}$)	γ ($\cdot 10^{15} s^{-1}$)	ω_p/γ
Au	13.8	0.11	125
Ag	14.0	0.032	438
Cu	13.4	0.14	96
Al	18.2	0.19	96
Pt	7.8	0.1	75
AZO (2%)	2.63	0.07	38
ITO (10%)	2.69	0.23	12
TiN (deposited at $800 \deg C$)	12	0.28	43
InGaAs (doping $2 \times 10^{19} cm^{-3}$)	1.2	0.02	60

Table 2.2: Plasma frequency ω_p, damping constant γ, and ratio ω_p/γ for some common plasmonic materials. Values are taken from Cai and Shalaev [68] and Naik, Shalaev, and Boltasseva [71].

From the table it is clear that using this metric, silver is the 'best' plasmonic material. However, when considering a given application, the best material will depend on a range of material properties such as resonance wavelength, tunability, compatibility with the substrate, loss mechanisms, environmental stability, and cost. For example, doped semiconductors have smaller electron densities than metals, giving them lower plasma frequencies (in the infrared), and lower Fermi levels meaning fewer states into which electrons can scatter. Compatibility with existing silicon and III–V technologies can also be an important consideration.

2.2 Surface Plasmons on Planar Interfaces

2.2.1 Formalism

Surface plasmon polaritons (SPPs) are defined as electromagnetic excitations that travel along the interface of a conductor and a dielectric, arising from the coupling of an electromagnetic field with the free electrons in the conductor. They propagate as longitudinal waves of field intensity and surface charge density, and are highly confined in the plane of the interface. Propagation speeds along the interface can be on the order of the speed of

light [1, 2].

Mathematically, SPPs can be described by beginning with Maxwell's equations, and finding solutions which are eigenmodes of the system localised at the interface. Equations 2.1 and 2.2, in the absence of external charges and currents, can be combined to produce

$$\nabla \times \nabla \times \vec{E} = -\mu \frac{\partial^2 \vec{D}}{\partial t^2} \tag{2.18}$$

Using the identities for the curl and divergence $\nabla \times \nabla \times \vec{E} = \nabla(\nabla \cdot \vec{E}) - \nabla^2 \vec{E}$ and assuming for now that the dielectric function is constant over the spatial profile ($\nabla \varepsilon = 0$) gives

$$\nabla^2 \vec{E} - \frac{\varepsilon}{c^2} \frac{\partial^2 \vec{E}}{\partial t^2} = 0 \tag{2.19}$$

with the speed of light $c = \frac{1}{\sqrt{\mu_0 \varepsilon_0}}$. Assuming a harmonic time-dependence $\vec{E}(t) = \vec{E}_0 e^{-i\omega t}$ yields

$$\nabla^2 \vec{E} + k_0^2 \varepsilon \frac{\partial^2 \vec{E}}{\partial t^2} = 0 \tag{2.20}$$

where $k_0 = \frac{\omega}{c}$ is called the *wave vector*.

Let the interface be defined as the plane $z = 0$. Two frequency-dependent dielectric functions ε_1 and ε_2 exist for the regions $z < 0$ and $z > 0$. Figure 2.2 shows the geometry of the system. An illustration of a surface plasmon with accompanying fields is shown in Figure 2.3. Continuity conditions at the interface exclude the existence of transverse
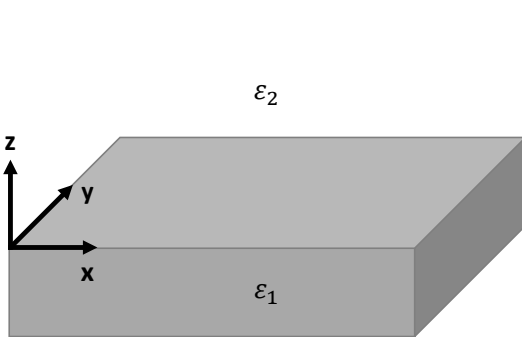
Figure 2.2: Geometry of the interface
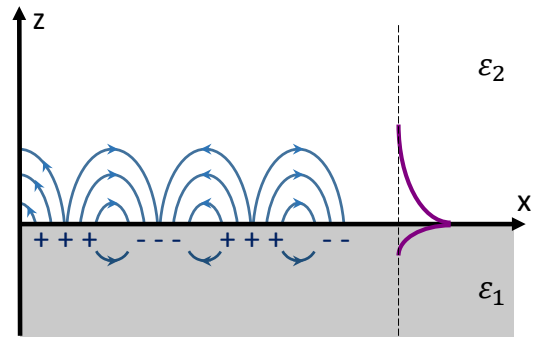
Figure 2.3: Illustration of SPP charges (blue, left) and fields (purple, right) at an interface.

electric (TE) surface modes [23], so only transverse magnetic (TM) polarisation needs to be considered. Given the requirement for confinement to the interface, solutions are sought in which the fields decay evanescently in the z-direction. Such solutions for the halfspaces

$j = 1$ and $j = 2$ can be written as follows:

$$\vec{E}_i = \begin{pmatrix} \vec{E}_{j,x} \\ 0 \\ \vec{E}_{j,z} \end{pmatrix} e^{ik_x x - i\omega t} e^{ik_{j,z} z} \qquad j = 1, 2 \tag{2.21}$$

It can be shown that continuity and the requirement to fulfill the wave equation leads to the following relations for the wave vector components [23] [72]:

$$\frac{k_{2,z}}{k_{1,z}} = \frac{\varepsilon_2}{\varepsilon_1} \tag{2.22}$$

and

$$k_x^2 + k_{j,z}^2 = \varepsilon_j k^2 \qquad j = 1, 2 \tag{2.23}$$

where $k = \frac{2\pi}{\lambda}$; λ is the vacuum wavelength. Together, these two equations give the dispersion relation

$$k_x^2 = \frac{\varepsilon_1 \varepsilon_2}{\varepsilon_1 + \varepsilon_2} k^2 = \frac{\varepsilon_1 \varepsilon_2}{\varepsilon_1 + \varepsilon_2} \frac{\omega^2}{c^2} \tag{2.24}$$

which describes the relation between the wave vector k_x along the direction of propagation and the angular frequency ω. For the component of the wave vector normal to the interface:

$$k_{j,z}^2 = \frac{\varepsilon_j^2}{\varepsilon_1 + \varepsilon_2} k^2 \qquad j = 1, 2 \tag{2.25}$$

Assuming that the metal is a perfect electrical conductor (PEC) with $Im(\varepsilon_1) = 0$, to obtain solutions which propagate along x and are bound in z necessitates that k_x be real and $k_{j,z}$ imaginary, which places constraints on the denominator in Equation 2.25 and therefore the numerator in Equation 2.24 so that

$$\varepsilon_1(\omega) + \varepsilon_2(\omega) < 0 \tag{2.26}$$

$$\varepsilon_1(\omega) \cdot \varepsilon_2(\omega) < 0 \tag{2.27}$$

The dispersion relation for a Drude metal in air ($\varepsilon_2 = 1$) is plotted in Figure 2.4. The light line is indicated by a dashed straight line. At small wave vectors, the SPP dispersion lies close to the light line. This region corresponds to frequencies in the mid-infrared and lower, where SPPs are also known as Sommerfeld-Zenneck waves [23]. As the wave vector becomes larger, the SPP frequency approaches the asymptotic characteristic value

$$\omega_{spp} = \frac{\omega_p}{\sqrt{1 + \varepsilon_2}} \tag{2.28}$$

At small wave vectors and high frequencies, there exists an upper branch called a *Brewster mode*. This mode is not a true surface mode, since Equation 2.25 in this case is not purely
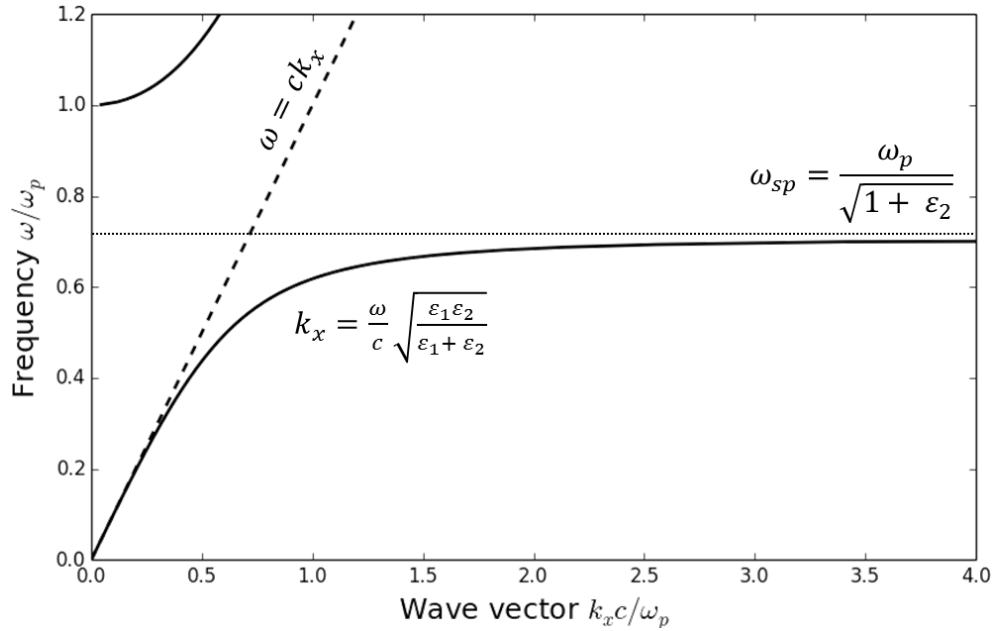
Figure 2.4: Dispersion curve of an SPP for a Drude metal in air (solid black lines). The light line is shown as a dashed straight line, which approaches the SPP curve asymptotically at small wave vectors. The characteristic plasmon frequency is indicated by a dotted line.

imaginary and energy is radiated away from the surface. In real metals, there are several processes aside from radiative damping which contribute to the damping of electron oscillations, giving a complex dielectric function and propagation constant. Interband transitions of bound electrons become significant at small wave vectors, and electron-electron, electron-phonon, and electron-ion interactions are important at larger wave vectors. As the SPP curve approaches the horizontal line given by Equation 2.28, the losses severely increase. The dispersion curve does not extend to infinity, but bends back at a finite wave vector and joins the upper branch. There is therefore a limit on the maximum wave vector, mode confinement, and minimum surface plasmon wavelength that can be realised experimentally.

2.2.2 Excitation

From Figure 2.4 it is clear that the SPP wave vector is always larger than that of light in free space, so direct excitation of SPPs on an idealised flat surface by a such light beam is not possible. One method to increase this light vector is to use a medium with a refractive index greater than 1, such as a glass prism, which tilts the light line, since $\omega = \frac{ck}{n}$. The relevant dispersion curves are displayed in Figure 2.5. The beam reflected at an angle θ at the boundary of the glass prism has an in-plane momentum $k_x = k\sqrt{\varepsilon}\sin\theta$ which is sufficient to excite SPPs if the evanescent wave can tunnel through to the metal/air

interface. This excitation scheme is known as attenuated total internal reflection or prism coupling. There are two configurations for prism coupling — the Otto configuration, which uses a small gap between the prism and metal surface, and the Kretschmann configuration, which uses a thin layer of metal placed directly on top of the prism. Both configurations are shown in Figure 2.6. The Kretschmann configuration is more commonly used, as it is difficult to precisely tune the width of the air gap in the Otto configuration [72]. The thickness of the metal layer in the Kretschmann configuration must also be finely chosen to ensure the wave is neither absorbed in the metal nor strongly damped in the glass.
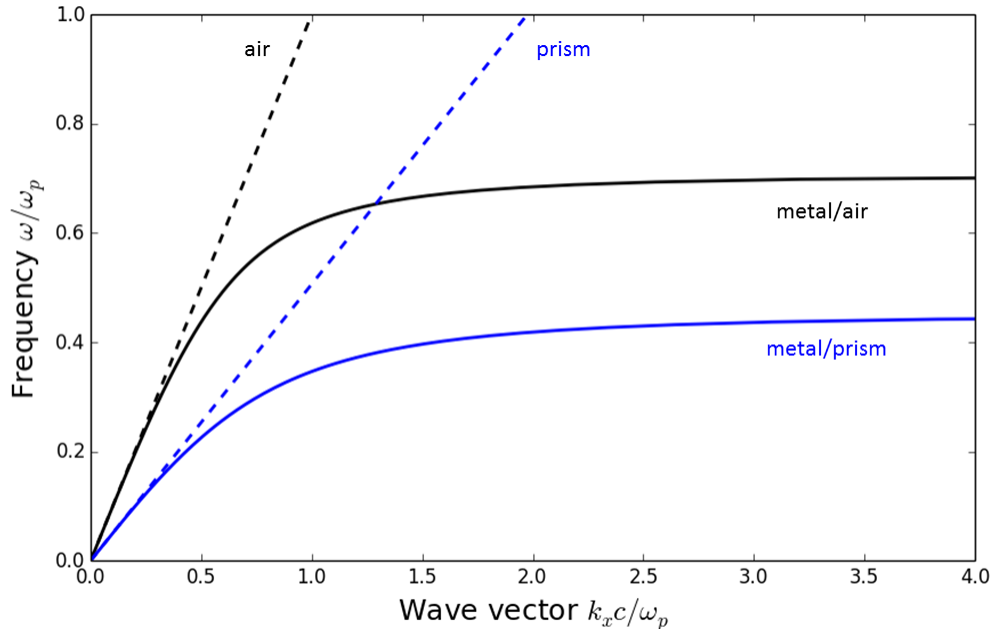
Figure 2.5: Dispersion curves for SPPs (solid lines) and light lines (dashed lines) at a metal/air (black) and metal/glass interface (blue). The introduction of a glass prism allows the light line to intersect one of the SPP curves.

Another alternative is to pattern the metal surface with grooves, protrusions, or holes to create a grating coupler. Light incident at an angle θ can undergo Bragg scattering from the grating, increasing or decreasing the in-plane wave vector k_x by integer multiples of the grating wave vector $\frac{2\pi}{a}$. For a one-dimensional grating of periodicity a, phase matching therefore occurs when the condition

$$k_x = k \sin \theta \pm \frac{2\pi n}{a} \tag{2.29}$$

is fulfilled, where n is an integer. The geometry of this coupling to a square grating is depicted in Figure 2.7; the corresponding dispersion relation and a possible coupling point are shown in Figure 2.8. It has been shown that one groove (slit) or protrusion is sufficient to excite SPPs on a surface [73], although gratings with more periods increase the coupling
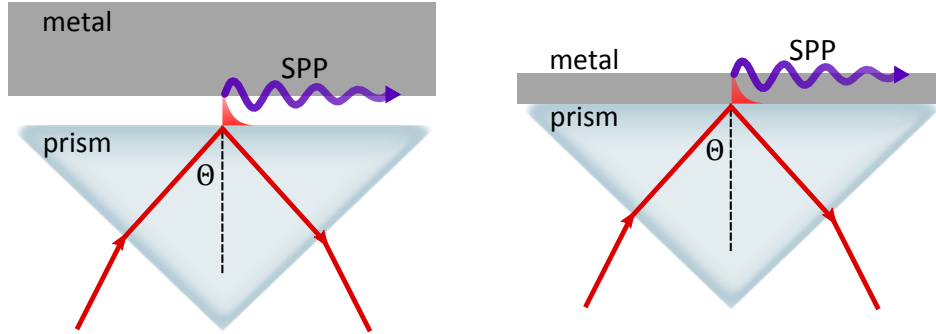
Figure 2.6: Otto (left) and Kretschmann (right) configurations for coupling of light to surface plasmons using a glass prism. The width of the gap (Otto) or metal (Kretschmann) must be small enough to allow the evanescent fields to reach the other side.
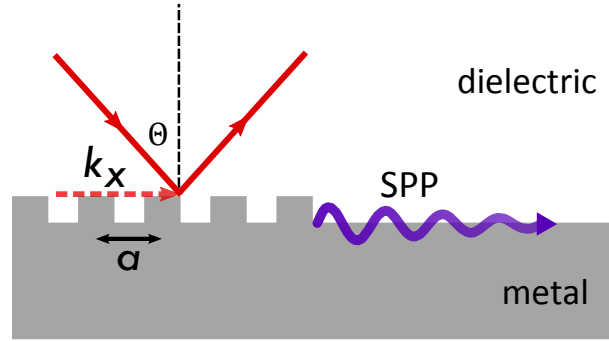
Figure 2.7: Coupling of light with wave vector k at an incident angle θ to surface plasmons using a grating with protrusions. The in-plane wave vector k_x is increased or decreased by integer multiples of the grating wave vector $\frac{2\pi}{a}$ through Bragg scattering.

efficiency [74]. The efficiency of SPP generation from single slits displays a sinusoidal dependence on slit width, which can be explained by diffraction theory [75].

For 1D gratings, the grating profile $\varsigma(x)$ can be approximated by decomposition into a Fourier series:

$$\varsigma(x) = c_0 + \sum_{n=1}^{\infty} c_n \sin\left(\frac{2\pi n x}{a} + \phi_n\right) \tag{2.30}$$

where ϕ_n represents the symmetry (blaze) of the grating around the x-axis. For a perfect sinusoidal profile, the Fourier series only has a first-order term, which corresponds to grating vectors for which $n = \pm 1$. Other grating profiles which include higher-order terms can couple light into SPPs with higher wave vectors. The coupling efficiency of any given order to incident light has a complex dependence on the relative amplitudes of the Fourier coefficients [76–78]. For finite square gratings with the same pitch and depth, maximum coupling has been demonstrated theoretically and experimentally for a groove width:pitch
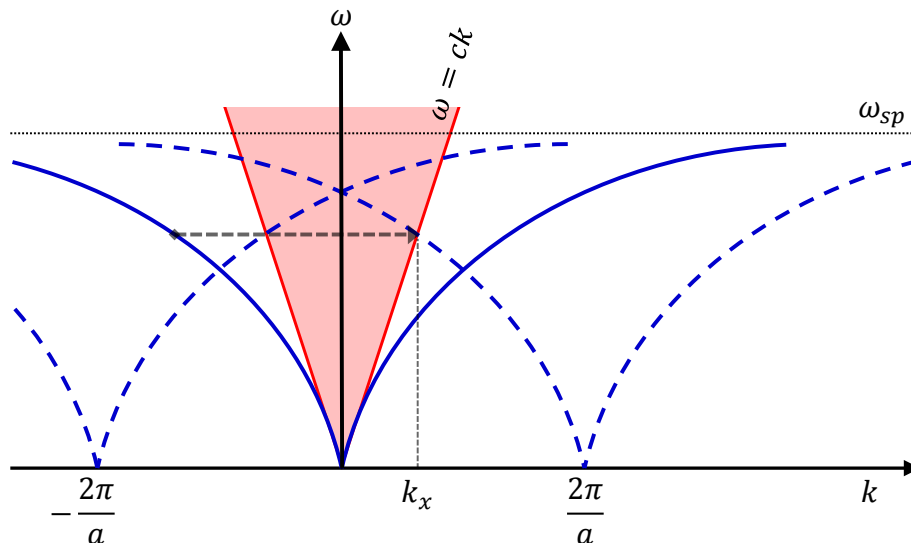
Figure 2.8: The dispersion curve for grating-coupled SPPs. The addition of the grating wave vector shifts the the dispersion curve (blue) along the momentum axis, allowing the new curve (blue, dashed) to intersect the light line (red).

ratio of 1:2 [74, 77].

For small groove depths (or protrusion heights), the grating is treated as a perturbation to the flat surface; this is no longer applicable for larger depths and the grating introduces pronounced changes to the dispersion relation [23, 74]. Band gaps appear for modulation depths of 20 nm and greater. Localised modes inside the grooves can appear for large depths, causing distortions of the first higher-order band folded back at the Brillouin zone boundary and a lowering of the frequency of the dispersion curve [23, 74, 79]. Gratings can also be regarded as one- or two-dimensional photonic crystals (for single- and bi-gratings, respectively), and photonic band gaps appear when the grating period is equal to the SPP wavelength or half this value [76, 80]. This geometry leads to two standing wave solutions whose nodes correspond to either peaks or troughs in the grating (for $a = \lambda_{SPP}$), or peaks/troughs on groove edges (for $a = \frac{\lambda_{SPP}}{2}$). The solutions have different frequencies because of the different distributions of field and surface charges.

Surface plasmons can also be excited by areas of random surface roughness, which can be considered as superpositions of gratings with various periodicities, but this provides an additional mechanism for scattering losses over a wide range of angles. Sufficiently sharp edges of plasmonic surfaces may also provide the necessary momentum to launch SPPs [81].

Several other excitation methods exist. Microscope objectives with high numerical apertures can be used to strongly focus the light, providing either a normal-incidence alternative to the Kretschmann configuration [82], or a means of exciting waveguide modes in sub-wavelength SPP waveguides [83]. Local excitation of SPPs in regions much smaller than

the incident wavelength can be achieved with near-field optical microscopy techniques [84]. Fast electrons can be used to excite surface plasmons, as predicted by Ritchie [38] and seen in early experiments by Powell and Swan in 1959 [39]. More recently, electron beams have been shown to be capable of providing localised sources of SPPs [85, 86].

If plasmonic components and devices are to be integrated into conventional photonic circuits, perhaps the most suitable excitation scheme is via coupling with dielectric optical waveguides. End-fire coupling matches the spatial profile of a photonic waveguide mode with that of a plasmonic waveguide, rather than employing phase-matching. The coupling efficiency depends on the overlap of the fibre and plasmon waveguide modes, but can be on the order of 90% [87]. This technique also has the advantage of exciting bound, long-ranging SPP modes. In situations where the excitation wavelength is larger than the dimensions of the SPP waveguide, the mismatch between the light spot from the tapered fibre end and the SPP waveguide prohibits efficient spatial mode matching. However, phase-matched evanescent coupling can still take place if the fibre end and waveguide are sufficiently close [88, 89].

2.3   Localised Surface Plasmons

There exists a subset of surface plasmon excitations which do not propagate, instead being confined to subwavelength particles or regions. These are known as localised surface plasmons (LSPs), and possess properties which differ somewhat from those of SPPs. For particles with a radius $r \ll \lambda$, the external electric field displaces the cloud of conduction electrons in the particle in-phase, producing a restoring force due to Coulomb attraction between the electron cloud and the now positively charged region. This is depicted in Figure 2.9. This restoring force enables a resonance of the induced dipole with the external field, which occurs at a frequency that depends on the density of electrons in the metal, their effective mass, and the shape and size of the charge distribution [90]. With respect to the driving field, the electron response displays a phase lag of $\frac{\pi}{2}$. This resonant oscillation creates a dipole field outside the particle, causing enhanced absorption and scattering cross-sections and an enhanced near-field which can be can be 100-10000 times stronger than that of the incident field [91, 92].

The field outside a spherical, homogeneous particle with $d \ll \lambda$ can be calculated by solving Maxwell's equations in the quasi-static approximation [90, 93], which gives

$$\hat{E_{out}} = E_0 \hat{z} - \left[\frac{\varepsilon_{in} - \varepsilon_{out}}{\varepsilon_{in} + 2\varepsilon_{out}} \right] r^3 E_0 \left[\frac{\hat{z}}{R^3} - \frac{3z}{R^5}(x\hat{x} + y\hat{y} + z\hat{z}) \right] \tag{2.31}$$

where E_0 is the incident field, ε_{in} and ε_{out} are the dielectric constants of the metal nanoparticle and the external environment respectively, and R is the radial distance from the centre
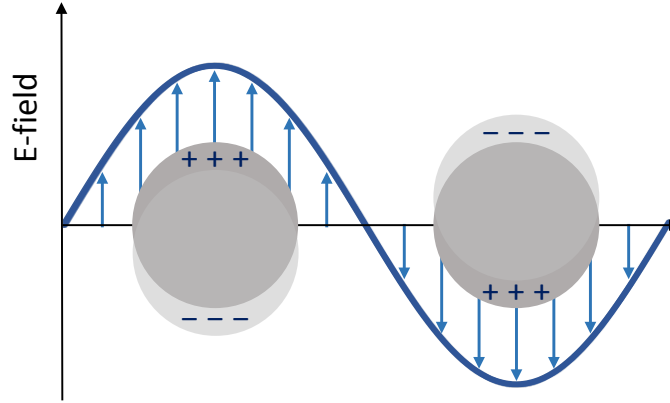
Figure 2.9: Excitation of a localised surface plasmon. The incident electric field displaces the electron cloud, producing an oscillating dipole.

of the particle. The second term describes the scattered field, and is equal to the electro-static field of a dipole with dipole moment $\hat{p}$ located at the centre of the particle. The dipole moment $\hat{p}$ is related to the polarisability α of the particle via $\hat{p} = \varepsilon_0\varepsilon_{out}\alpha\hat{E}_0$. Using Equation 2.31, it can be shown that the polarisability can therefore be written as

$$\alpha(\omega) = 4\pi r^3 \frac{\varepsilon_{in}(\omega) - \varepsilon_{out}}{\varepsilon_{in}(\omega) + 2\varepsilon_{out}} \tag{2.32}$$

A resonant maximum of the polarisability occurs when the term $\varepsilon_{in}(\omega) + 2\varepsilon_{out}$ is at a minimum. If the imaginary part $Im[\varepsilon_{in}(\omega)]$ is small, or varies slowly with ω, the resonance condition can be simplified to

$$Re[\varepsilon_{in}(\omega)] = -2\varepsilon_{out} \tag{2.33}$$

This relationship is known as the Fröhlich condition, and determines the frequency of the dipole plasmon resonance of a metal nanoparticle. Scattering and absorption of incident light by the particle are also enhanced as a result of the resonant polarisability.

For larger particles in which the phase of the driving field changes significantly over the particle volume, the quasi-static approximation is no longer valid. In 1908, Mie was the first to solve the problem of scattering and absorption of electromagnetic radiation by a sphere by solving Maxwell's equations with a rigorous electrodynamic approach [94]. In *Mie theory*, the spherical symmetry of the particle permits the internal and external fields to be expanded into a set of normal modes described by vector harmonics. The quasi-static approach described above can then be recovered by taking just the first term of this expansion.

The amplitude of the plasmon oscillation is limited by radiative and non-radiative damping, which is ignored in 2.33 since in reality $Im[\varepsilon_{in}(\omega)] \neq 0$. Radiative damping (i.e. direct

decay of the electron oscillations by emission of photons) is the main decay route for larger particles. Non-radiative decay occurs via intraband transitions within the conduction band or interband transitions from d-bands into the conduction band, creating electron-hole pairs. These decay mechanisms govern the lifetime and bandwidth of the plasmon resonance.

The inverse of the nanoparticle structure — where a dielectric inclusion of subwavelength dimensions is embedded in a metal environment — is called a nanovoid and also supports LSPs. Nanovoid resonances often occur near nanoparticle resonances, such as in nanoshell structures and in gaps between particles. More complex structures such as these can be considered as hybridised systems of elementary plasmon modes whose degree of interaction is determined by the spatial separation.

When two particles are brought close together, the dipole of one can induce a dipole in the other, resulting in four possible dimer modes depending on the orientation and phases of the individual dipole moments. The strength of the interaction depends on the separation d between dipoles. For small gaps $d \ll \lambda$ the scaling term d^{-3} dominates this interaction; for larger gaps the interaction is dominated by far-field dipolar coupling with a dependence d^{-1}. Scattering into the far-field is suppressed by near-field nanoparticle coupling, resulting in strong field localisation and enhancement in small gaps. An energy diagram for the hybridised modes of a nanoparticle dimer is illustrated in Figure 2.10. Bonding and antibonding modes have resonance energies which are red- and blueshifted, respectively, from those of the elementary particles. In-phase modes readily couple to linearly polarised light and are also termed bright modes, whilst out-of-phase modes whose fields cancel in the centre of the gap are termed dark modes. Since dark modes do not readily couple to free-space radiation, their radiative decay is suppressed and they exhibit longer lifetimes [95].

2.3.1   Nanoantennas

Some of the most promising plasmonic devices are nanoscale optical antennas, or *nanoantennas*, whose design is based on well-established radio and microwave frequency (RF) antenna patterns. The responses of antennas in these frequency regimes differ significantly for a couple of reasons. For optical frequencies, metals can no longer be assumed to behave as perfect electrical conductors (PEC), meaning electric fields penetrate into the metal and result in much higher Ohmic losses. RF antennas typically have dimensions on the order of several centimetres; optical antennas have dimensions on the order of a few hundred nanometres. Just as for nanoparticle dimers, strong field confinement due to near-field coupling occurs at subwavelength gaps in nanoantennas, making these gaps useful as feeding or receiving points for the system [96]. The strongest enhancement occurs for small gap sizes on the order of tens of nanometres [97, 98]. Nanoantennas based on variations
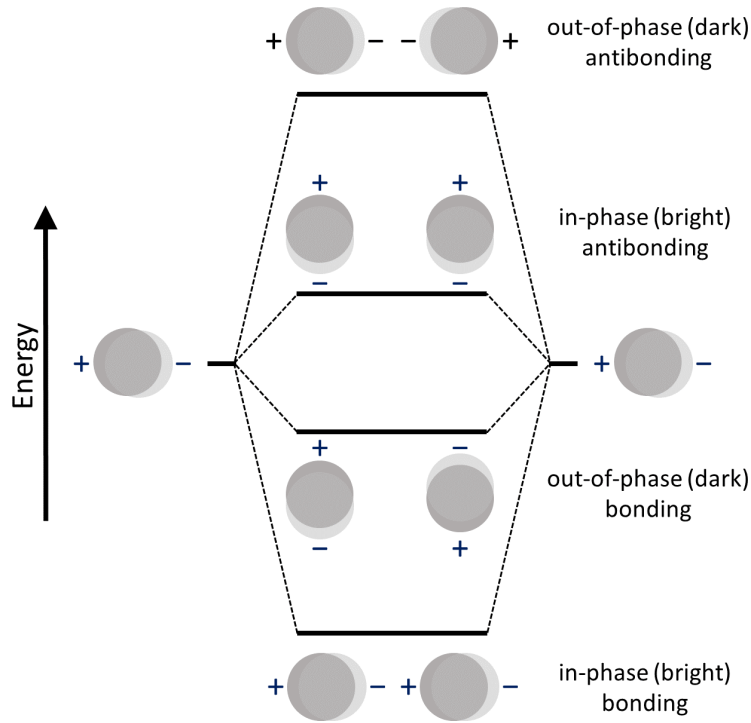
Figure 2.10: Energy diagram of the plasmon modes of a nanoparticle dimer. The proximity of individual particle modes can produce bonding and antibonding hybrid modes.

of metallic bowtie antennas have been investigated in this thesis. The basic structure of a bowtie antenna is shown in Figure 2.11.
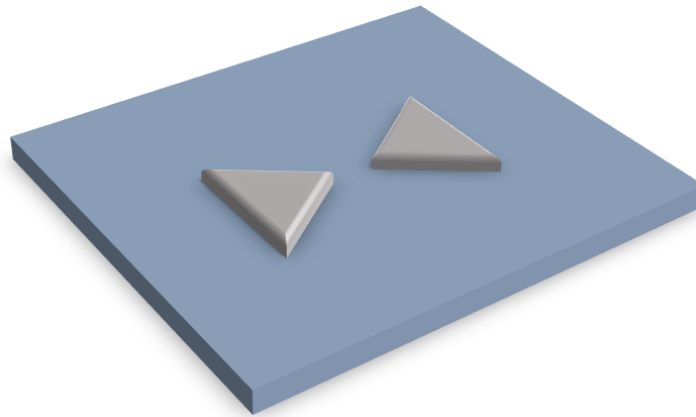
Figure 2.11: Illustration of one possible nanoantenna geometry — the bowtie nanoantenna on a substrate. The gap between the two sides of the antenna is typically tens to hundreds of nanometres.

The strong field enhancement and confinement in nanoantennas can be combined with

nonlinear optical materials to enhance nonlinear processes which depend superlinearly on the local field [99]. These processes include second harmonic generation [100–102] and soliton excitation [103]. Nanoantennas can also be used to modify the rates of photodynamic processes such as photoluminescence and spontaneous emission [104, 105].

2.4 Surface Plasmons in Stripe Waveguides

2.4.1 Stripe Waveguide Modes

The system described in Chapter 2 consisted of a planar interface between semi-infinite metal and dielectric regions. The addition of another dielectric interface to the other side of the metal creates a metal slab. For large slab thicknesses, SPP modes on the individual surfaces are degenerate, but as the thickness of the metal layer is reduced coupling occurs. In the case of symmetric metal slab, where the surrounding dielectric is the same on both sides (i.e. $\varepsilon_2 = \varepsilon_3$), these coupled modes form so-called *supermodes* [106]. These two modes are TM polarised and are termed either asymmetric or symmetric (designated a_b and s_b, respectively) based on how the z-component of the electric field varies across the slab. This is illustrated in Figure 2.12.
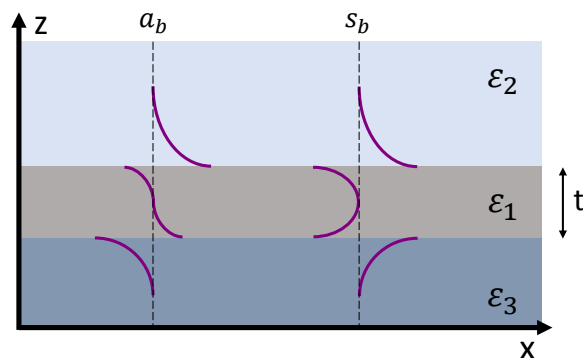
Figure 2.12: Geometry of the metal slab. The metal slab (ε_1) of thickness t is surrounded by two semi-infinite dielectrics (ε_2 and ε_3). The purple lines indicate the distribution — asymmetric (a_b, left) or symmetric (s_b, right) — of the transverse electric field component of the SPP modes for a symmetric environment ($\varepsilon_2 = \varepsilon_3$), which propagate perpendicular to the page.

Each of these modes has a distinct dispersion curve and response to changing slab parameters. Applying appropriate boundary conditions in the symmetric case for the normal and tangential electric field components, the dispersion relation can be separated into two

equations:

$$\tanh\left(k_z^1 t/2\right) = -\frac{k_z^2 \varepsilon_1}{k_z^1 \varepsilon_2} \tag{2.34}$$

for the symmetric mode, and

$$\tanh\left(k_z^1 t/2\right) = -\frac{k_z^1 \varepsilon_2}{k_z^2 \varepsilon_1} \tag{2.35}$$

for the antisymmetric mode, where

$$k_z^{1,2} = \sqrt{k_{s_b,a_b}^2 - \varepsilon_{1,2} k_0^2}. \tag{2.36}$$

As slab thickness t decreases, the approximation $\tanh x \approx x$ can be used, and the expressions for the mode wave vectors simplify to

$$k_{s_b} \approx k_0 \sqrt{\varepsilon_2 + (t k_0 \varepsilon_2/2)^2 \cdot (1 - (\varepsilon_2/\varepsilon_1))} \tag{2.37}$$

and

$$k_{a_b} \approx k_0 \sqrt{\varepsilon_d + (2\varepsilon_2/(t k_0 \varepsilon_1 1))^2}. \tag{2.38}$$

where k_0 is the free space wave vector.

So, as $t \to 0$, the s_b mode extends farther into the dielectric and the attenuation of the mode decreases. The lower the refractive index of the dielectric, the larger the field penetration depth into it and therefore the lower the propagation loss, since less mode power is residing inside the lossy metal. In the case of a lossless surrounding dielectric, as $t \to 0$, the attenuation decreases smoothly and the mode evolves into the background vertically-polarised transverse electromagnetic (TEM) wave [107, 108]. The s_b mode in the symmetric slab is also known as the long-range SPP mode. Conversely, with decreasing t the a_b mode becomes increasingly confined to the metal and is more greatly attenuated by the higher losses therein, making it a short-range mode.

For an asymmetric slab, where $\varepsilon_2 \neq \varepsilon_3$, the s_b mode has a cutoff thickness below which it does not propagate, which increases with the difference between the permittivities of the dielectrics of the top and bottom layers. A large difference increases the propagation loss, so the long-range SPP mode is absent in this case. With increasing slab thickness the s_b mode evolves into the metal/lower-index dielectric mode; the a_b mode evolves into the metal/higher-index dielectric mode.

If the width (x-direction) of the metal slab is finite, it becomes a metal stripe. These can also support long-range SPP modes when embedded in a homogenous dielectric environment, but for most applications the material above and below the stripe are different for practical reasons. Moreover, whilst the long-range SPP mode has been shown to reach propagation lengths up several hundred microns, or even centimetres for infrared wavelengths [109, 110], the significant branching of this mode into the outer dielectric renders it

unsuitable for integration into subwavelength photonic components [108]. Therefore, only the asymmetric environment is considered from this point. In this environment no true field symmetries about the x-axis exist; instead, symmetric- and asymmetric-like modes occur at the interfaces. A cross-section of a stripe waveguide is shown in Figure 2.13, where w is the stripe width.
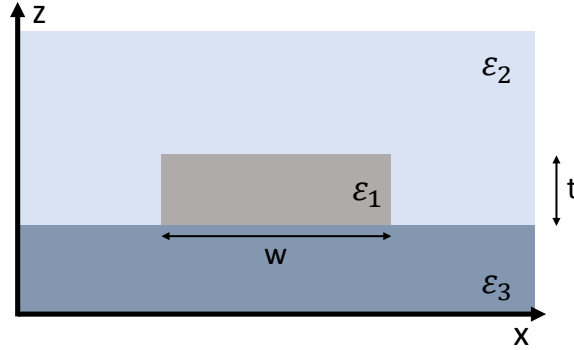
Figure 2.13: Cross-section of a metal stripe waveguide in an asymmetric dielectric environment.

The added confinement increases the number of modes and prevents the derivation of analytical solutions. Modal solutions to Maxwell's equations in metal stripes must be found numerically. The four fundamental modes that are supported are designated aa_b^0, as_b^0, sa_b^0, and ss_b^0 [111]. In this nomenclature, the first letter refers to the horizontal dimension (x-direction), the second refers to the vertical dimension (z-direction), the subscript signifies that the modes are bound (i.e. non-radiative), and the superscript indicates the number of extrema in E_z along the x-axis, excluding maxima at the corners of the stripe. As for the case of the metal slab, for a stripe waveguide in an asymmetric environment the symmetric-like modes are localised along the metal/lower-index dielectric interface, while the asymmetric-like modes are localised along the metal/higher-index dielectric.

In addition to these fundamental modes, higher order modes that display one or more extrema along the x-axis are supported. The number of extrema occurring along these two interfaces may be different. Unlike slab modes, stripe plasmon modes are not purely TM in character since the E_y components are always non-zero, but E_z is the dominant field component for wide stripes where $w \gg t$.

Waveguide modes can be characterised by the effective mode index n_{eff}, propagation length L_{SPP} (defined as the length at which the intensity has decreased to $1/e$), and mode profile (distribution and number of extrema) [112]. For a mode with propagation constant β, the first two quantities are given by

$$n_{eff} = \text{Re}\left\{\frac{\beta}{k_0}\right\} \tag{2.39}$$

and

$$L_{SPP} = \frac{1}{2\text{Im}\{\beta\}} \tag{2.40}$$

Since all modes are coupled modes, their evolution with stripe parameters is complex. Theoretical and experimental investigations into these dependencies that have been conducted to-date are described in the following paragraphs. These experiments have mapped near-fields in stripe waveguides using several techniques.

There have been several studies which have examined the effect of stripe width. In 2001, Lamprecht et al. gathered data on L_{SPP} values for 70 nm-thick gold and silver stripes with widths varying from 1 - 54 μm and an excitation wavelength of 633 nm [12]. They found that the propagation length decreased from that of an extended film ($L_{SPP} \approx 60$ μm) with decreasing stripe width, and that the decrease became dramatic for $w \leq 20$ μm. Waveguides with $w = 3$ μm had propagation lengths of 25 μm; those with $w = 1$ μm had propagation lengths of just a few microns. Comparable results for 60 nm-thick silver films and 50 nm-thick gold films were found in other experiments [13, 113]. Lamprecht et al. attributed this decrease to the modification of the dispersion relations and increased contribution of scattering from the edges. A theoretical study by Zia et al. on 55 nm-thick films found that even without considering scattering losses, there is a change in the modal propagation constant due to the finite width of the stripe which decreases the propagation length, but this decrease only becomes significant for stripes with $w \leq 5$ μm.

Changing the width of stripe waveguides also affects which modes are allowed. As for the case of waveguide thickness, there exists a cutoff width below which propagating modes are not supported [114], which is smaller for bound modes and higher for so-called "leaky" modes that re-radiate into the higher-index substrate. Increasing w above the cutoff permits higher-order modes with higher numbers of peaks along the width of the stripe [114, 115], and also increases mode confinement within the metal stripe. This gives higher losses for bound modes, for which Ohmic heating is the sole loss mechanism, and lower losses for leaky modes, for which radiation losses are dominant.

Zia et al. derived an expression for the approximate number of supported modes along a stripe by considering the lower limit for the propagating component of momentum [114]. For SPPs to be guided, they should not couple into the radiation modes of the dielectric (i.e. $|k_y| > (\omega/c)\sqrt{\varepsilon_d}$), which can be used to derive a maximum value for the lateral wave vector:

$$|k_x| < \frac{\omega}{c}\sqrt{\frac{\varepsilon_d\varepsilon_m}{\varepsilon_d + \varepsilon_m} - \varepsilon_d}. \tag{2.41}$$

The lateral wave vector of the highest supported mode with N extrema along the x-axis would be

$$|k_{x,max}| = \frac{N\pi}{w} \tag{2.42}$$

which, combined with Equation 2.41, gives the maximum number of supported modes:

$$N < \frac{2w}{\lambda} \sqrt{\frac{-\varepsilon_d^2}{\varepsilon_d + \varepsilon_m}} \tag{2.43}$$

Early analysis by Weeber et al. suggested that the origin of these stripe modes must be fundamentally different to those in dielectric waveguides — that is, not arising from interfering reflections from the waveguide edges — since the high number of reflections needed to produce the observed modes would lead to dramatic damping along the stripe axis and propagation lengths much lower than those of plasmons on an extended film [115]. This was later resolved by noting that only the central intensity peaks are true mode peaks, and that the fields at the edges are not true edge modes [116].

A closer look at the effect of the waveguide edges using dual-plane leakage microscopy and near-field microscopy demonstrated that the edges act as an additional radiative decay channel [113]. There is a large n_{eff} mismatch between the plasmon waveguide mode and the bound edge mode, so the existence of a hybridised mode formed from these two modes is unlikely since the coupling would be very inefficient. By measuring the variation in SPP linewidth and intensity of the lines in Fourier space with respect to the waveguide width, Berthelot et al. found that for stripes narrower than a few microns, edge diffraction is the prominent cause of SPP attenuation.

Interference fringes perpendicular to the propagation direction, arising from SPP reflections at the waveguide ends, have also been mapped in near-field experiments and simulations [13, 113, 117].

As for the metal slab described above, decreasing film thickness decreases the vertical mode confinement and increases coupling between interfaces. Thicker metal stripes also show weaker confinement across the width of the stripe [112, 115]. However, at least one experimental result shows that stripes which are otherwise geometrically identical but vary in thickness retain similar mode profiles, suggesting that the observed modes are not created by coupling between interfaces, and that the fields are mostly localised at the air/metal interface [115]. This conflicts with numerical results which suggest that ss_b^n modes should be efficiently excited and the mode distribution should be sensitive to the film thickness [111, 115].

Planar metallic stripe waveguides are currently the most popular plasmonic waveguide design for potential industrial applications, since they are relatively easy to fabricate via electron-beam or photolithography [12, 13, 113, 115, 117, 118], widely tuneable, and can be integrated into existing photonic components [59].

2.4.2 Nanofocusing

Concentration of optical energy from a propagating plasmon mode with a given polarisation and symmetry into a subwavelength region can be achieved using tapered waveguide structures; this process is termed nanofocusing [6]. As the plasmon travels along the narrowing taper, its field is localised and the field amplitude enhanced, and typically both the phase and group velocity of the mode are reduced. Fields can be localised to areas as small as a few nanometres, so field enhancement in these areas is strongly affected by the geometry and environment at the tip [119]. Nanofocusing was first theoretically proposed by Nerkararyan in 1997 [120], and has since been verified both theoretically and experimentally in a number of different geometries including tapered metal rods [4, 121, 122], metal wedges [5, 123], one- and two-dimensional tapered gaps [124–126], and tapered metal strips [127].

Nanofocusing can occur in one of two regimes. In the adiabatic regime, the focusing occurs gradually in weakly tapered structures so that there are no significant reflections or scattering of the propagating mode from the taper. In the wider part of the taper, the SPP mode resembles that in a uniform metal film, forming four coupled corner modes as the mode propagates towards the tip [127]. The adiabatic regime is valid when the change in the SPP wavelength over a length scale equal to one SPP wavelength is small. This can be expressed in terms of the adiabatic parameter $\delta(x)$ as [125]

$$\delta(x) = \left| \mathrm{d}(q_{1,x})^{-1}/\mathrm{d}x \right| \ll 1 \tag{2.44}$$

where $q_{1,x}$ is the real part of the SPP wavenumber along the propagation direction x and dissipation is assumed to be small i.e. $q_1 \gg q_2$. In most cases this condition can be relaxed to $\delta(x) \leq 1$ [4, 124]. Since the plasmon wavenumber only begins to vary significantly with reducing waveguide size when the waveguide width becomes smaller than the plasmon wavelength, if the taper is linear and the adiabatic approximation is valid near the tip, then it is valid everywhere along the taper.

Simple expressions for the critical angle can be found for tapered gaps and wedges. In a uniform dielectric constant with permittivity ε_d, the critical angle is [125]

$$\gamma_c \approx \frac{-2\varepsilon_d}{\mathrm{Re}(\varepsilon_m)} \tag{2.45}$$

When a wedge is placed on a dielectric substrate, the critical angle becomes [5]

$$\gamma_c \approx \frac{\varepsilon_{d,1} + \varepsilon_{d,2}}{\mathrm{Re}(\varepsilon_m)} \tag{2.46}$$

For all linear tapers increasing the taper angle increases reflections from the taper, but it also reduces the distance the SPP mode has to propagate. Thus, for small taper angles field enhancement at the tip tends to increase with increasing angle; as the taper angle

is increased considerably above γ_c strong reflections reverse this trend. There exists an optimum taper angle to maximise tip enhancement, which is generally close to γ_c [4, 128], as well an optimum distance from the tip that an SPP should be excited or incoupled. This is the distance over which the increase in SPP amplitude due to localisation exceeds the decrease due to Ohmic losses and is strongly material- and wavelength-dependent, varying between $\approx$ 1 - 20 μm [4, 5].

For tapers on metal stripe waveguides there may be considerable scattering from the stripe edges and non-uniformities on the surface, so care must be taken when using Equation 2.44. The degree of nanofocusing that can be achieved in such structures depends on whether the bound mode at the metal/higher-index interface or the leaky mode at the metal/lower index is being focused. The findings of Zia et al. suggest that SPP modes could not be focused along a tapered waveguide below the cutoff width [114], yet later experiments and simulations showed no evidence for a cutoff width for asymmetric bound modes [112, 127]. Towards the tip of the taper, the fields of these modes are primarily confined to the corners of the waveguide and also extend to the lower-index side of the film. Although the propagation length decreases for small stripe widths, nanofocusing potential may increase due to increased confinement.

Leaky modes are not suitable for true nanoscale focusing [114, 127], but given their relative ease of excitation may still be convenient for concentrating plasmon modes on the micron scale [13, 113]. Results of near-field studies suggest that taper angles of 90° offer the best compromise between SPP localisation and losses due to dissipation and scattering from the edges [13, 113].

2.4.3   Other SPP Waveguides

Many other types of nanostructures have been proposed for plasmonic waveguiding and focusing including planar diffractive elements [73], chains of metal nanoparticles [129–131], nanowires [132–135], tapered nanorods [4, 121, 122], metal-insulator-metal (MIM) nanogaps [124, 126, 136], V-groove channels [137, 138], wedges [139–141], and hybrid dielectric-metal waveguides [142, 143]. Given the scope of this topic, only the most relevant factors will be discussed. For all types of waveguides, there is a compromise that must be made between mode confinement and propagation loss. There are currently two main avenues being pursued in the development of SPP waveguides — waveguides that support extremely confined SPP modes, and waveguides that display relatively low losses and can be electrically controlled [108].

In contrast to the large propagation lengths but weak confinement of SPPs in metallic slabs, nanowires or nanoparticle waveguides exhibit transverse mode confinement below the diffraction limit but have large attenuation losses, limiting their propagation lengths to the order of a micron [23]. Propagation occurs via near-field coupling between nanoparticles

in close proximity. If the separation between particle centres is a with $a \ll \lambda$, dipole interactions between adjacent particles are dominated by a near-field term which scales as a^{-3}. In nanoparticle chains, this coupling gives rise to one longitudinal and two transverse propagating modes [144], with group velocities of up to $0.06c$ for linear chains of Au spherical nanoparticles, and potentially higher for other shapes [130, 145].

Nanowires are analogous to stripe waveguides with both width and thickness having sub-wavelength dimensions. They have been shown to support leaky and bound propagating modes, depending on the excitation scheme [133, 146]. The leaky modes observed in lithographically-fabricated nanowires display significantly shorter propagation lengths than those of stripe waveguides with widths of several microns [132,133]. Using chemically-grown nanowires and a high-NA microscope objective as a local optical excitation source, Ditlbacher et al. demonstrated propagation lengths of $\approx 10 \, \mu m$ for bound modes [146]. Through reflection of the SPPs from the end-facet, nanowires can also display transverse confinement and act as Fabry-Perot resonators [118, 146].

2.5 Surface Plasmons in Nanohole Arrays

2.5.1 Diffraction Through Subwavelength Holes

The problem of the diffraction of light through a small hole in a metal screen was considered by Bethe in 1944 [147]. He modelled a subwavelength hole in an infinitely thin, perfectly conducting metal (shown in Figure 2.14), and obtained the following expression for the transmission through the hole as a function of wave vector k and hole radius r:

$$T = \frac{64}{27\pi^2}(kr)^4 \propto (\frac{r}{\lambda})^4 \tag{2.47}$$

Bouwkamp later found that this transmission coefficient could be written as a series in kr, with the above expression as the first term [148]. The scaling factor is in agreement with Rayleigh's theory of scattering by small objects.

Extending this theory to films of finite thickness prohibits exact analytical solutions; numerical simulations must be used to solve the problem. Assuming a finite thickness further reduces the expected transmission, since for wavelengths larger than a cutoff wavelength λ_C, given by $\lambda_C = 3.4r$, propagating modes inside the hole cannot exist and the fields become evanescent [149]. Bethe and Bouwkamp's expressions are only applicable in such cases, diverging for smaller wavelengths and overestimating the transmittance for all wavelengths [150]. Subwavelength holes in metal films should therefore be very poor transmitters of light, and this is indeed the case for single holes in otherwise smooth films.
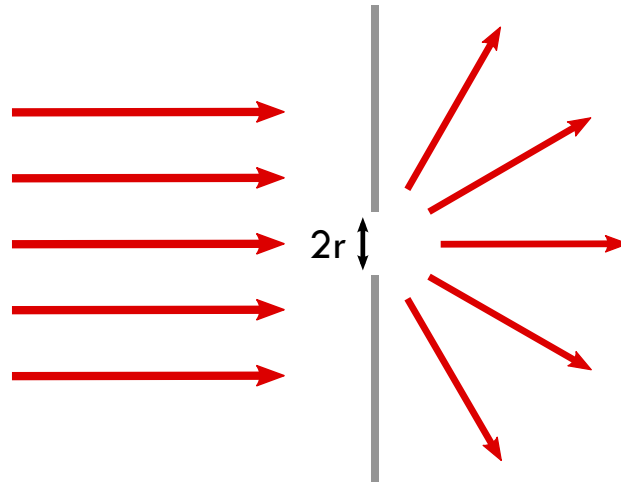
Figure 2.14: Diffraction of light through a circular aperture of diameter $2r$ in an infinitely thin screen.

2.5.2 Extraordinary Optical Transmission

On the contrary, arrays of subwavelength holes in certain metals have demonstrated transmission properties utterly unpredicted by the above models. An example of a hole array is illustrated schematically in Figure 2.15. Their remarkable properties were first seen by Ebbesen et al. in 1998, when they performed transmission experiments on optically thick metal films perforated with square arrays of submicron cylindrical cavities [151]. They found that for films made from Au, Ag, and Cr, the transmittance was many orders of magnitude higher than expected, even surpassing unity at certain wavelengths when normalised to the area of the holes. Furthermore, the transmission was highly directional. They termed this phenomenon *extraordinary optical transmission* (EOT). The film thickness was typically 200 nm, with the hole diameter and spacing varying between 150 nm and 1 µm, and 0.6 and 1.8 µm, respectively. The transmission spectra displayed a series of maxima and minima, including peaks at wavelengths larger than the periodicity of the array which cannot be explained by diffraction. In this first experiment and a subsequent experiment performed soon after, they described the dependence of the transmission spectra on the hole size, lattice spacing, film thickness, incident angle, type of metal, surrounding dielectric, array size, and hole shape [152]. The angular dependence of the spectra and the absence of enhanced transmission in Ge films lead them to the conclusion that surface plasmons play a major role in EOT.

These initial findings incited significant interest in the origins, properties, and applications of the enhanced transmission. Numerous studies have explored the influence of film and array parameters on EOT. The spectral positions of the maxima and minima depend primarily on distance between the holes, with both increasing monotonically and almost
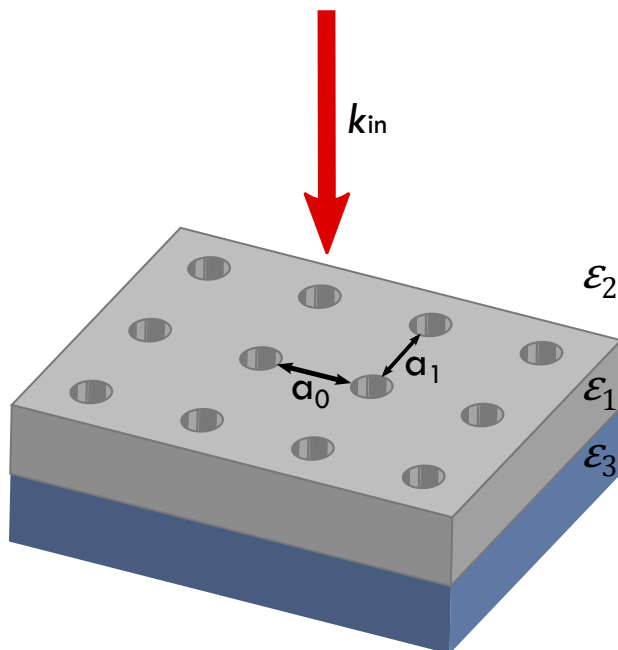
Figure 2.15: A schematic representation of a possible hole array. In this geometry, the holes through the metal film with dielectric constant ε_1 are arranged in a rectangular lattice with spacings a_0 and a_1. Light is incident at the air side (ε_2), and the metal film sits on a dielectric substrate (ε_3).

linearly with increasing lattice period [151, 153]. Both maxima and minima exhibit dispersion, as seen in experiments investigating the response of the transmission to changing the angle of incident light [152, 154]. Widening the holes increases the height of the transmission peaks [151] and their linewidth [155], and causes a slight redshift [156], although the increase in transmittivity begins to saturate at a given hole size [157]. The spectral lineshape dependence supports a model in which SPPs undergo Rayleigh scattering by the holes [158]. Depending on the depth and shape, wider holes can also accommodate propagating waveguide modes. The cutoff criterion described in the section above is based on the assumption of a perfect conductor; in a real metal, damped propagating modes can exist for longer wavelengths [159]. For these propagating modes, impedance mismatch causes reflection from the end of the holes, giving rise to Faby-Perot resonances and increased transmittance if the multiple reflections interfere constructively [160, 161].

There has been some debate about the physical mechanism behind EOT. In the experiments described above, there is wide range of geometric and material variables which characterise the arrays. This may advocate the existence of several transmission regimes with different coexisting transmission mechanisms. Small transmission enhancements have also been found in perforated structures in the microwave region [162, 163] and PECs [164], which has led some authors to question the role of surface plasmons [165, 166]. However, such materials are still able to support surface electromagnetic modes, including so-called *spoof*

plasmons [167, 168]. In more recent years the central role of SPPs in EOT has been reaffirmed [17,159,169–171], with the additional finding that quasi-cylindrical waves — the fields diffracted from subwavelength surface indentations — have a greater contribution as excitation wavelengths and metal conductivities increase [17, 172].

In the SPP description, the periodic hole array acts as a grating coupler for the incident light, exciting SPPs on the top surface of the film. As for the case of the one-dimensional grating Equation 2.29, the plasmon wave vector $\vec{k}_{SPP}$ is then equal to the in-plane component of the incident wave vector $\vec{k}_{in} = \frac{2\pi}{\lambda}\sin\theta$ plus or minus integer multiples of the reciprocal lattice vectors $\vec{G}_x$ and $\vec{G}_y$:

$$\vec{k}_{SPP} = \vec{k}_{in} \pm p\vec{G}_x \pm q\vec{G}_y \tag{2.48}$$

Using the SPP dispersion relation 2.24, for a square lattice with lattice spacing a_0 and hence lattice vectors $\left|\vec{G}_x\right| = \left|\vec{G}_y\right| = \frac{2\pi}{a_0}$, at normal incidence ($\theta = 0$) Equation 2.48 reduces to

$$\lambda = \frac{a_0}{\sqrt{(p^2 + q^2)}}\sqrt{\frac{\varepsilon_1\varepsilon_2}{\varepsilon_1 + \varepsilon_2}} \tag{2.49}$$

This simplified description gives approximate positions of the transmission peaks for various values of p, q [152]. Scattering losses from the holes are not considered, so experimentally observed peaks occur at slightly longer wavelengths [14].

For a hexagonal lattice, $\left|\vec{G}_x\right| = \left|\vec{G}_y\right| = \frac{4\pi}{\sqrt{3}a_0}$ [14, 173], giving transmission peaks at

$$\lambda = \frac{a_0}{\sqrt{\frac{4}{3}(p^2 + pq + q^2)}}\sqrt{\frac{\varepsilon_1\varepsilon_2}{\varepsilon_1 + \varepsilon_2}} \tag{2.50}$$

According to this model, enhanced transmission should therefore also occur for a single aperture surrounded by an incoupling device consisting of regular periodic corrugations, which has indeed been verified for 1D slits and circular *bull's eye* structures [174, 175]. Cloning these corrugations on the outcoupling interface can greatly reduce the divergence of the emitted beam [175,176]. Light from arrays with a small number of holes also displays very little divergence [17].

The coupling between holes on each surface is complex, and derives from an interplay of radiative, diffraction, and SPP modes that varies as a function of film parameters [17,177]. The relative contribution from diffraction modes dominates at small lattice spacings ($\ll \lambda$) where diffracted fields do not cancel; coupling through SPPs becomes more prominent as the spacing extends to several wavelengths [178, 179].

Multiple studies have used near-field optical microscopy to image SPPs on the film and identify the peak in the transmission spectra owing to these surface modes [158, 180–184].

Standing-wave patterns from interfering SPPs can be seen in arrays with lattice spacings larger than the excitation wavelength [182]. High field amplitudes between the holes on a given interface are associated with maxima in the transmission intensity.

The original work of Ebbesen et al. and many subsequent experiments have examined the role of film material. High absorption impairs the resonant process, giving low transmission peaks with larger linewidths for metals such as Ni and Cr when compared to Au, Ag, or Cu [153, 185]. The skin depth of the material determines the effective hole size [164, 185]. As anticipated, given the properties of surface plasmons, the transmission peak intensity and position is also influenced by the surrounding dielectric environment [186].

The film thickness affects the strength of the coupling between the two interfaces. In order to observe any EOT effects, the thickness should be at least the skin depth of the metal [187]. Beyond several skin depths the transmittance begins to decrease and there is a slight blueshift of the peaks, until the hole depth prohibits propagating modes and the interfaces become weakly coupled. For the case of a silver film, increasing the thickness beyond approximately $300\,\mathrm{nm}$ causes the peak intensity to fall off exponentially, ascribed to the exponential decay of the hole waveguide mode [188]. As with the stripe waveguides described in Chapter 5, the surfaces are maximally coupled when the film is in a dielectrically symmetric environment [186]. Asymmetric geometries give rise to two sets of transmission peaks [14].

The polarisation of the incident light with respect to the lattice vectors determines which surface modes and transmission resonances are excited, and the polarisation state of the transmitted light [17]. Birefringence is therefore observed in arrays with different lattice vectors along orthogonal axes, or when a square array is placed at non-normal incidence.

Changing the hole shape has dramatic effects on the transmittance. Arrays with rectangular holes display large redshifts and increased transmission when compared to arrays of circular holes, even if the individual hole area is smaller [189, 190]. Rectangular and elliptical holes also exhibit polarisation anisotropy which — like peak wavelength and transmission — increases with higher aspect ratios. It has been shown that for high aspect ratios, localised surface plasmons around individual holes have a higher contribution to the transmittance than for circular or square holes, although the contribution from SPPs remains the primary mechanism in EOT [191, 192]. In these cases the holes approximate one-dimensional slits, which allow propagating modes.

2.5.3   Dynamics

The first investigations into the dynamics of the EOT process were made a few years after its discovery. Dogariu et al. developed a technique to determine the transit time through a nanohole array by measuring the correlation function between the transmitted beam and

a reference pulse [193]. For a 300 nm thick film they found a transit time of 7 fs, which gives a group velocity of $\frac{c}{7}$. Later, a relationship was found between this transit time and the lifetime of the resonant modes, which is limited by plasmon scattering with the array itself and has a direct effect on the linewidths of the resonance peaks [158].

The time structure of the transmission process contains two distinct features: the almost immediate and unperturbed transmission of the incident pulse, followed by a longer-lived tail from resonant reemission [194–196]. This structure is characteristic of a Fano-type process, in which a narrow resonance interferes with a broad continuum, producing asymmetric lineshapes [197]. This has been corroborated by investigations of the point-spread function [198]. The total transmitted field $\vec{E}_{tot}(t)$ can be written as a sum of these non-resonant $\vec{E}_{nr}(t)$ and plasmonic $\vec{E}_{SPP}(t)$ components:

$$\vec{E}_{tot}(t) = \vec{E}_{nr}(t) + \vec{E}_{SPP}(t) = \vec{E}_{nr}(t) + \sum_j \vec{E}_j e^{-i\omega_j \cdot t - \Gamma_j \cdot t} \tag{2.51}$$

The far field transmission spectra $T(\omega) = |t(\omega)|^2$ can then be found via the transmission coefficient $t(\omega)$, obtained by Fourier transformation of 2.51:

$$t(\omega) = a_{nr} + \sum_j \frac{b_j \Gamma_{r,j} e^{i\phi_j}}{\omega - \omega_j + i(\gamma_j + \Gamma_{r,j})} \tag{2.52}$$

with coefficients a_{nr} and b_j. The resonance linewidth $\Gamma_j = \gamma_j + \Gamma_{r,j}$ consists of nonradiative and radiative damping terms γ_j and $\Gamma_{r,j}$ due to absorption and reradiation of SPP modes, respectively.

If the incident light is only weakly coupled to the SPP resonances, the initial direct transmission is strong compared to the longer-lived tail. If the coupling is optimised (for example, through tuning the incident angle), this latter component becomes strongly enhanced and persists much longer. Ropers et al. monitored the sensitivity of the transmission time structure to the incident angle and found that coherent coupling between SPP modes could increase the SPP lifetime from 30 fs to more than 200 fs. By combining these findings with near-field microscopy, they related this lifetime to the symmetry of the plasmon mode. If the maxima of the fields spatially overlap with the nanoholes or -slits (the *symmetric mode*), the radiative damping is increased and the SPP lifetime is short. If the maxima of the fields lie between the apertures (the *antisymmetric mode*), the radiative damping is greatly suppressed and the SPP lifetime is long.

Three-dimensional finite-difference time-domain (FDTD) simulations with 10 fs pulses have revealed that coupling between the interfaces produces temporal oscillations in the transmission [24, 199]. The period of these oscillations is on the order of femtoseconds and is governed by the hole size, increasing for larger hole diameters. The closer the SPP excitations at both interfaces are to being in resonance, the longer the oscillations persist. These simulations also mapped the spatial near-field profiles, showing the interference of SPP

waves between different holes and interfaces. From this the authors presented a physical picture of the transmission process:

1. Light impinging on the array is scattered at the nanohole grating, exciting SPPs at the interface

2. Counterpropagating SPPs from different holes interfere, creating standing waves and field distributions over the incident surface

3. SPPs funnel into nanohole channels, are guided or tunnel through the channels, and are reflected or scattered from the opposing ends

4. Scattered radiation beams into the far-field or excites SPPs at the exit of the nanoholes which propagate along the second interface

5. Steps 2-4 are repeated in the other direction, giving rise to a periodic energy transfer between the two interfaces

There are two processes which contribute to the plasmon damping — absorption (or Ohmic loss) and scattering. For hole diameters $\ll 300\,\text{nm}$, absorption is the dominant process and the oscillation period scales with inverse hole area. For holes beyond this diameter, scattering becomes the dominant process, and SPP excitation at the second interface is low. Large hole diameters therefore result in short radiative SPP lifetimes.

Müller et al. also examined the effect of the surrounding dielectric on the transmission dynamics. Strong coupling between the interfaces when the dielectric constants of the sub- and superstrates match is associated with high transmission and pronounced oscillations in the transmission. The spatial near-field profiles do not markedly vary after the initial impulsive excitation. When the sub- and superstrates differ but the excitation source remains resonant with SPP excitations at both interfaces, long-lived oscillations are seen. No oscillations are apparent when the resonant peaks at each interface are significantly detuned (by more than $50\,\text{nm}$ in this case). A simplified coupled mode picture can be used to relate the period of the oscillations T to the coupling strength V via

$$T = \frac{\pi}{|V|} \tag{2.53}$$

This description cannot reproduce the asymmetric lineshapes of the transmission spectra, as it fails to include the interference between resonant SPP radiation and the nonresonant transmission from photon tunnelling [194, 199].

2.6   Fabrication Challenges

Successful development of plasmonic devices hinges on having optimally designed structures, reliable fabrication methods, and efficient detection techniques [108]. The nanoscale sizes of such structures and their sensitivity to their surrounding environment poses challenges for fabrication and characterisation. Techniques used in this work will be discussed in detail in Chapter 3.

Surface quality is also a key factor in the applicability of plasmonic devices, as parameters such as grain size and surface roughness affect the plasmonic properties [6–8]. Currently, strategies for improving the surface quality include optimising the seed layer [200], thermal annealing [201], and using chemical bottom-up fabrication methods to grow single-crystalline films [62]. However, whilst a suitable seed layer can improve the smoothness of the surface, the resulting smaller grain sizes lead to increased electron scattering and higher losses [202]. Thermal annealing produces an inverse effect, decreasing scattering from grain boundaries by increasing grain size, but may increase surface roughness if parameters are not carefully controlled [201]. Finally, bottom-up methods can be challenging to implement and are currently not available for all materials.

Chapter 3

Experimental Techniques

This chapter presents and discusses experimental techniques which have been used extensively throughout the course of this thesis. These include methods for fabricating planar plasmonic structures, spatially mapping plasmonic modes, and observing plasmon interactions and dynamics. Where alternative techniques for fabrication or analysis exist, some discussion of these alternatives and justification for a particular method are provided.

3.1   Background: Observing SPPs

To adequately observe surface plasmons, techniques capable of imaging electromagnetic fields on nanometre scales are needed [203]. Conventional far-field imaging techniques alone are of limited use, given that the sizes of plasmonic structures and features are often below the diffraction limit.

Several developments in the 1980s made observations of plasmonic near-fields possible by using physical probes placed near the sample. The first detection of plasmonic near-fields was performed by scanning tunnelling microscopy [204], later superseded in popularity by near-field scanning optical microscopy (NSOM, also called SNOM). NSOM offers typical spatial resolutions of 50-100 nm [205], which can be reduced to 10 nm using apertureless, or point-like probes [206]. However, one major drawback of this method is that the introduction of a tip in close proximity to the metal surface results in a perturbation of the electromagnetic field due to the interaction between the tip and the sample, which complicates the interpretation of results.

An alternative imaging method which does not perturb the plasmon field is photoemission electron microscopy (PEEM). The first PEEM was built in 1933 by Brüche, who demonstrated 10-fold magnification of a zinc plate [207]. Brüche's principle design is still used

in modern instruments — ultraviolet light from a mercury lamp is focused onto the sample, which also acts as the cathode for the electron optics. Photoemitted electrons are accelerated by a potential difference of 30kV and focused onto a phosphor screen. Since the inelastic mean free path of the electrons in solids is on the order of a few nanometres, PEEM is sensitive to only a thin layer. The PEEM therefore provides an image of the sample surface based on the spatial variations in electron emission intensity. Unlike NSOM, PEEM is not a scanning technique; all points on the image are obtained simultaneously. Additionally, the distance between the sample and the extractor is on the order of a few millimetres, so the collection electron optics do not influence the plasmon field.

For single-photon emission processes, image contrast originates from differences in the work function of materials on the surface, the electronic density of states, the topographical relief, and the presence of magnetic domains (in the case of circularly-polarised x-ray sources), with the dominant mechanism depending on the material and the illumination source. As for the scanning techniques mentioned above, the use of PEEM as an effective tool for surface science became possible in the 1980s after technological advancements. Spatial resolution in PEEM is determined by the electron optics, rather than the illumination source, so imaging below the diffraction limit is possible. Resolutions of several tens of nanometres in the spatial domain are routinely achievable; aberration-corrected instruments can reduce this to under 10 nm, approaching the fundamental resolution limit of electron emission microscopy — the inelastic mean-free path of the emitted electrons [205, 208]. With the addition of an energy filter, PEEM can also provide energy-selective imaging with resolutions of around 50 meV [209].

The use of PEEM to study plasmonics is more recent, dating from 2002 when Schmidt et al. imaged areas of high electron emission (hot spots) on silver islands using femtosecond laser pulses [210]. Mapping of the near-fields uses a multiphoton emission process, typically two-photon photoemission (2PPE), due to the difference between work functions and plasmonic excitation energies [203]. The currently accepted three-step model [211] for the generalised 2PPE process is shown in Figure 3.1. A photon with an energy below the work function is absorbed by an electron in the metal, shifting the electron into an intermediate excited state above the Fermi level. If a second photon is absorbed by the electron within the lifetime of the excited state, the electron is further elevated into the vacuum.

This description needs to be carefully considered with regards to the nature of the intermediate state for plasmon excitation, since there is no unoccupied state above the Fermi level [212]. Studies comparing the photoemission yield and spectra on continuous and nanostructured films using short pulses (on the order of several picoseconds and below) have distinguished different dominant photoemission regimes. For particles smaller than several tens of nanometres, where the mean free path of the electrons is greater than the particle size, decoupling of the electrons and phonons leads to thermally-assisted processes dominating [213, 214]. For larger particles and continuous films, the strong inhomogeneity of the electromagnetic field at the surface due to the resonant excitation of SPPs
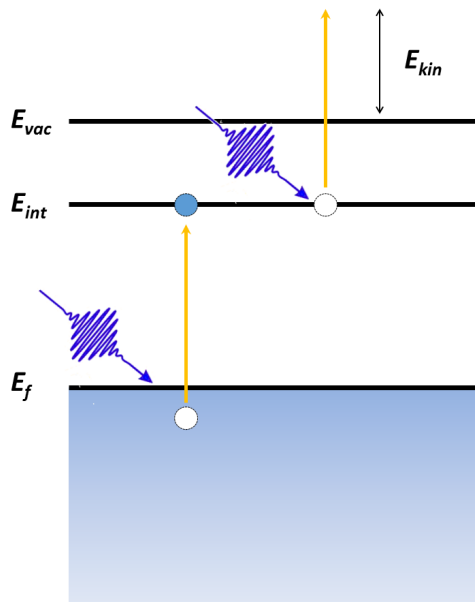
Figure 3.1: An illustration of the generalised 2PPE process. The first photon elevates an electron from the Fermi level to a short-lived intermediate state; the second liberates the electron into the vacuum.

supplies free electrons with quiver energy which can be converted to electron kinetic energy [215,216]. In this depiction of multiphoton emission, the intermediate state is a virtual state created by plasmon decay (Landau damping) [212], and the mechanism is more accurately described as plasmon-assisted multiphoton emission [203]. An illustration of this model is given in Figure 3.2.

The yield of emitted photoelectrons Y_{2PPE} is proportional to the time-integrated fourth power of the local electric field:

$$Y_{2PPE} \propto \int E^4(r,t)dt \tag{3.1}$$

This, combined with the fact that the typical electron escape depth for 2PPE processes is on the order of a few nanometres [217], makes the measured PEEM signal very sensitive to electromagnetic surface fields, and in particular to plasmonic near-fields. Since the work functions of the most commonly-studied plasmonic materials (gold, silver, aluminium) are around 4 - 5 eV, 2PPE typically uses pulsed laser sources in the blue-violet region of the visible spectrum.

In 2005, two independent groups demonstrated the potential of two-photon PEEM (2P-PEEM) to map plasmonic near-fields. Cinchetti et al. [218] imaged silver crescent-shaped nanoparticles on a silicon substrate using a mercury UV lamp and a Ti:sapphire femtosecond laser ($\lambda = 400\,\text{nm}$, pulse width $< 200\,\text{fs}$). Under UV illumination, the particles
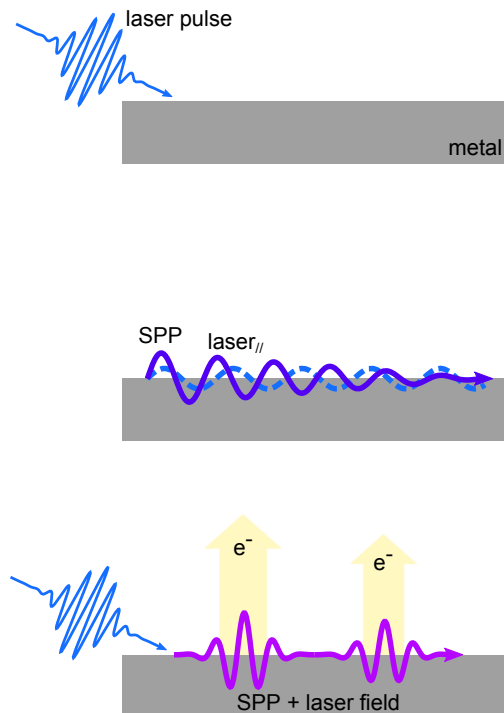
Figure 3.2: The plasmon-assisted multiphoton emission process. The intermediate state is a virtual state created by the excited plasmon.

appeared uniformly bright; under laser illumination the observed photoemission was localised in the gap of the silver crescents, where strong local fields were present. Kubo et al. [219] performed a similar experiment on a silver grating with nanometre-scale surface roughness. They used 10 fs laser pulses in an interferometric pump-probe setup to monitor the evolution of the plasmonic near-fields over time. This extended the idea introduced by Schmidt et al. three years earlier — time-resolved PEEM — to even finer temporal resolutions. Before this, NSOM had achieved sub-wavelength spatial resolution, and integrating 2PPE techniques had realised femtosecond time resolution, but simultaneous measurements of both these parameters had not been carried out.

Over the last decade, PEEM has proven a valuable tool for inspecting surface plasmons. It has been able to map plasmonic near-fields in nanoantenna structures [220]. It has been used to demonstrate selective excitation of hot spots in various structures by choosing wavelength and polarisation [221] or shaping the laser pulse [222]. It has probed the dynamics and coupling of localised surface plasmons in nanoparticles [223, 224]. It has monitored the growth of metal nanowires *in situ* [225]. It has characterised SPP creation, propagation, and focusing on surfaces [226, 227]. The advantage of PEEM in these studies, and others, is the capacity to image near-fields with high resolution, and the potential to

perform time-resolved experiments with a suitable choice of light source.

3.2   Photoemission Electron Microscopy

A schematic of a PEEM is shown in Figure 3.3, depicting the electron optics, detectors, and one possible electron path. The microscope used for experiments in this thesis was purchased from Focus GmbH. In general, PEEM electron lenses can be either magnetic or electrostatic. Magnetic lenses have lower chromatic and spherical aberrations, but may lead to residual magnetic fields at the sample, making them unsuitable for imaging magnetic materials. Focus GmbH microscopes use electrostatic lenses.

As previously mentioned, the sample acts as the cathode and is part of electron optics. The extractor, focus, and column form the objective lens. The extractor creates a field that accelerates photoemitted electrons, while the focus forms a strong convex lens. The degree of magnification is largely determined by the ratio of the extractor voltage to the column voltage. The Focus PEEM has a maximum extractor field strength of 16 kV/mm. The microscope can operate in one-, two-, or three-lens mode — determined by choice of projective lens voltages — with three-lens mode giving the greatest magnification. Imaging in k-space mode is also possible by selecting the transfer lens voltage that projects the back focal plane onto the screen.

There are several inherent effects leading to image degradation, which can be minimised with the electron optics. Tilted or misaligned samples introduce astigmatism, which can be corrected (up to a certain limit) by stigmators. The deflector adjusts the alignment of the optical axis. Large photoemission angles lead to spherical aberrations, which can be reduced by using a contrast aperture to limit the acceptance angle. This improves contrast at the expense of brightness, although very small apertures can introduce diffraction aberrations. Chromatic aberrations are caused by large electron energy spreads. These can be minimised by choice of contrast aperture, and by limiting the energy range.

The standard detector consists of a microchannel plate (MCP) to amplify the electron signal, followed by a fluorescent screen. A CCD camera is then used to acquire the resulting photon image. Alternatively, a delay line detector (DLD) can be used for greater sensitivity and energy filtering. Combined with a pulsed light source that provides a trigger signal and a drift tube that separates the electrons in energy, the DLD can record the time-of-flight of single electrons. Previous experiments have demonstrated that the PEEM used in this thesis has a spatial resolution of 25 nm and an energy resolution of 46 meV [228].

The piezoelectrically-controlled sample stage is mounted approximately 1.8 mm from the objective lens and is mechanically coupled to the microscope to minimise vibration problems [209]. A μ-metal casing around the sample stage and end of the microscope ensures
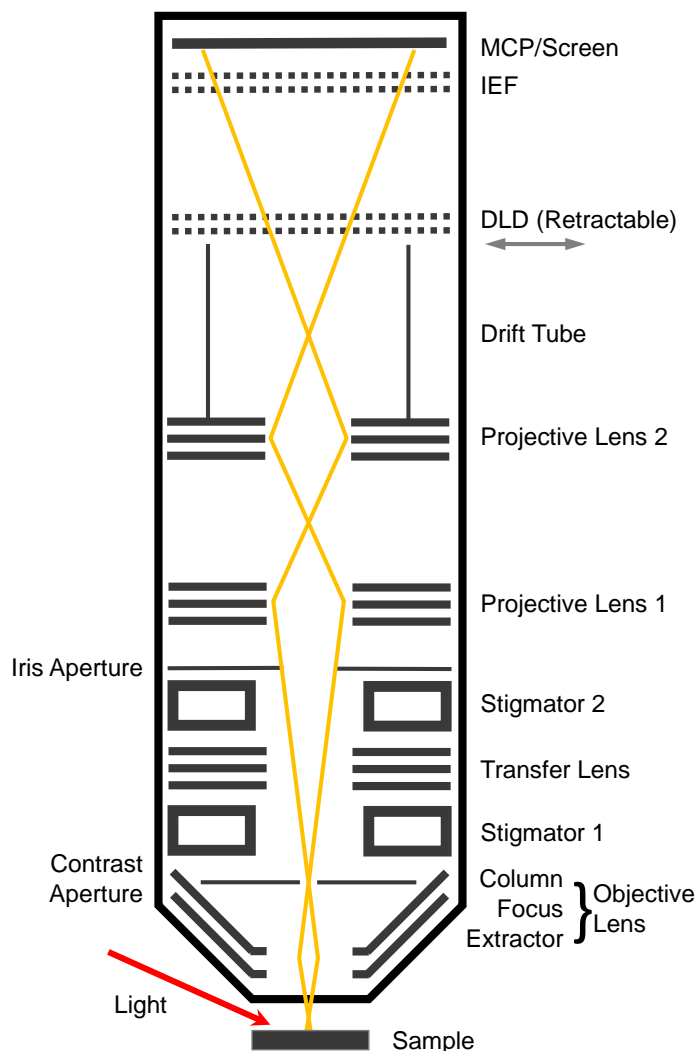
Figure 3.3: A schematic of the PEEM, showing the electron optics, detectors, and a possible electron path (yellow).

good magnetic shielding. On account of the expected large number of sample holders needed, for the PEEM and other setups, it was decided to fabricate holders in-house.

The two sides of the sample holder are shown in Figure 3.4. The holder is made from molybdenum and is therefore suitable for heating. The front window is 10×10 mm, and can accommodate samples a millimetre within these dimensions. A groove etched into the sample recess allows a spring made from molybdenum wire to be fitted in the back, which fixes the sample flat within the holder. The protrusion at the top allows the sample holder to be easily gripped by the wobblestick for transfer into and out of the sample stage.

Imaging of samples was first performed under illumination with a Hg lamp (Focus GmbH).
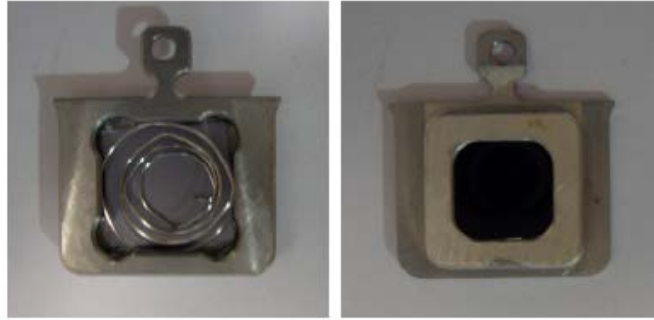
Figure 3.4: Photographs of the sample holder used in the PEEM, showing the recess and fixing spring (left) and the front sample surface (right).

The lamp can be fitted to one of the ports of the PEEM vacuum chamber, which is positioned so that the light strikes the sample at an incident angle of 65°. The mercury emission lines are pressure-broadened, so the lamp serves as a continuum source extending into the low-energy UV range with a peak photon energy of 4.9 eV. This makes the Hg lamp suitable for single-photon (1P-PEEM) images to characterise the topography of the sample. The MCP detector was used during 1P-PEEM imaging.

For 2P-PEEM images, a pulsed diode laser (LDH-D-C-405, PicoQuant) was used in combination with the DLD. This laser provided pulses at 405 nm ($\pm$ 10 nm) or 3.06 eV, with pulse lengths around 50 ps, repetition rates of 40 MHz, and average powers that could be adjusted by the intensity setting of the driver of between 1.0 mW 3.0 mW.

3.3   Two-Pulse Transmission Spectrometry

This section describes the tools used to carry out ultrafast pump-probe transmission spectroscopy on nanohole arrays. Since the typical time scales for EOT processes are in the tens of femtoseconds, pulses with durations below this range are required to reveal the full complex SPP time dynamics [199]. These were generated by a femtosecond laser oscillator in combination with a series of chirped mirrors. The pulses were then fed into a setup designed to measure pulse length via intensity autocorrelation. By exchanging just one component, this setup could also be used for performing the pump-probe transmission experiment.

3.3.1 Laser Pulses

The laser source was a commercial Ti:sapphire oscillator (Femtosource Rainbow, Femtolasers GmbH), pumped by a solid-state diode laser at $532\,\text{nm}$ (Verdi V-5, Coherent Inc.). The oscillator produced pulses centred around $790\,\text{nm}$ with a spectral width of $300\,\text{nm}$ via Kerr-lens mode-locking in the crystal. The pulse energy was approximately $3\,\text{nJ}$ at a repetition rate of $78\,\text{MHz}$. The oscillator spectrum is shown on the left in Figure 3.5.

The product of the pulse duration and spectral bandwidth satisfies the inequality $\Delta t \Delta \omega \geq C$, where Δt and $\Delta \omega$ are the widths (typically the full width at half maximum, or FWHM) of the pulse in the time and frequency domains, respectively, and C is a constant that depends on the pulse shape. For example, $C \approx 0.44$ for Gaussian-shaped pulses , whereas $C \approx 0.315$ for $sech^2$-shaped pulses. For a given spectral bandwidth, pulses which have the minimum possible time duration are described as being *bandwidth-* or *transform-limited.*

The phase and group velocity of light in transparent media are frequency-dependent — a phenomenon termed *(chromatic) dispersion.* The frequency response of light can be represented via a Taylor expansion around the centre frequency ω_0 as

$$k(\omega) = k_0 + \frac{\delta k}{\delta \omega}(\omega - \omega_0) + \frac{1}{2}\frac{\delta^2 k}{\delta \omega^2}(\omega - \omega_0)^2 + \frac{1}{6}\frac{\delta^3 k}{\delta \omega^3}(\omega - \omega_0)^3 + \dots \tag{3.2}$$

The zeroth order term contains the inverse of the phase velocity

$$v_{ph} = \frac{\omega_0}{k_0} \tag{3.3}$$

and describes a collective phase shift. The first order term contains the inverse group velocity

$$v_g = \frac{\delta \omega}{\delta k} \tag{3.4}$$

and describes the propagation speed of the pulse envelope. The quadratic term contains the group velocity dispersion (GVD)

$$\frac{\delta^2 k}{\delta \omega^2} = \frac{\delta}{\delta \omega}\left(\frac{1}{v_g(\omega)}\right) \tag{3.5}$$

Higher-order terms are referred to simply as third-order dispersion (TOD) and so forth.

The GVD is a quantity which is often used to parametrise dispersive media. It can be used to estimate the change in the time dependence of the instantaneous frequency (the *chirp*) of a pulse as it passes through a medium of a given length. In normal dispersive media, the GVD is positive and introduces a positive chirp, meaning higher frequency components travel slower. The inverse is true for anomalous dispersion.

Due to their large spectral widths, the temporal structure of ultrashort pulses is very sensitive to even modest amounts of dispersion introduced by optical components such

as lenses and windows. The oscillator contained several sources of material dispersion, namely the wedged plate of the output coupler and the compensating plate which adjusted the angular dispersion introduced by this wedge. This is ordinarily compensated by 4-6 reflections an extra-cavity chirped mirror pair which inverts the GVD the pulses acquire in the oscillator and brings their temporal width close to the transform limit. During the course of this thesis, this extra-cavity mirror pair was not available, so pulses were compressed using another chirped mirror stage and thin (1 mm) silica window.

3.3.2 Autocorrelation

To measure the duration of pulses from the oscillator and perform the pump-probe experiment, modifications were made to an available NOPA-Pal autocorrelator [229]. The intensity autocorrelator was designed for simple, dispersion-free measurement of pulse lengths from $\approx$ 100 - sub-10 fs in the 420 - 1460 nm range.

The setup is shown in Figure 3.5. The oscillator pulses pass through the compression stage and enter the autocorrelator through an iris. Two identical pulse replicas are created by reflection from a split-mirror pair, one half of which is mounted on a piezoelectric linear translation stage (PX 38, later PX 50 from Piezosystem Jena GmbH) connected to a piezo amplifier (5V10 OEM, Piezosystem Jena) that is used to set the relative delay τ between the replicas. The most relevant specifications of the two stages are given in Table 3.1. The first

Name	Range (μm)	Range (fs)	Control Modes	Measured resolution (fs)
PX 38	39	260	open loop	0.52
PX 50	50	334	open or closed loop	0.2

Table 3.1: Specifications of the two translation stages used to set the delay between incident pulses in time-resolved transmission experiments.

piezostage used did not have an encoder, and a calibration measurement showed that over a relatively large range of displacement corresponding to approximately 70 fs of delay the stage displayed additional vibrations. Details of this calibration can be found in Reference [230]. It was hypothesised that the interference was caused by a nearby turbopump whose resonance frequency was very close to the 760 Hz of the stage. Additionally, the stage did not move linearly near the end of its range. For these reasons, the piezostage was later swapped for one with an encoder and demonstrated linear displacement.

The other half of the mirror was fixed on a manual translation stage that was used for course alignment. The two replicas were focused by an off-axis parabolic mirror into a

25 µm-thick beta barium borate (BBO) crystal under a small angle. A thin crystal is required to ensure phase matching over the large spectral bandwidth of the pulse.
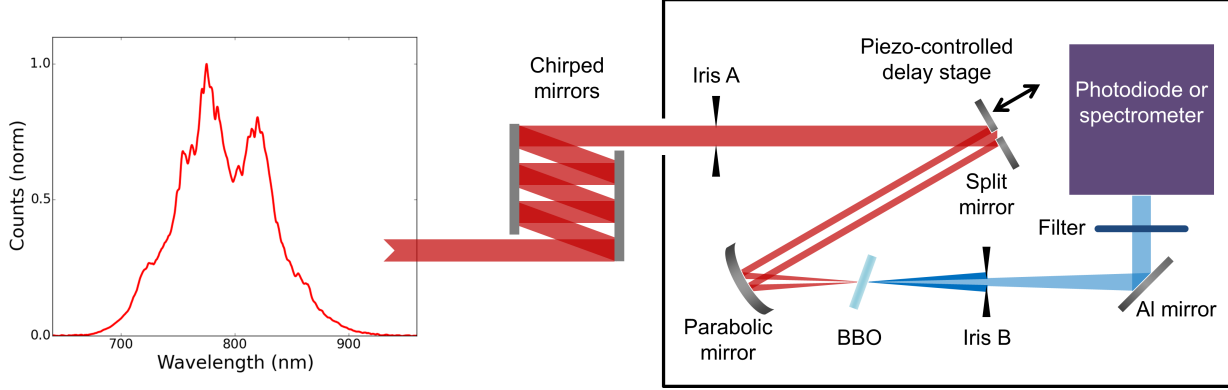
Figure 3.5: Setup of the autocorrelator for pulse length measurement. The oscillator produces pulses with the spectral distribution shown on the left, which have been temporally broadened by dispersive optical elements in the cavity. The acquired GVD is compensated by a compression stage consisting of six chirped mirrors. Upon entering the autocorrelator the pulses are divided into two pulse replicas whose temporal offset can be controlled via a split-mirror that is mounted on a piezo translation stage. The pulse replicas are then overlapped in a BBO crystal, where the width in time of the resulting SHG signal is used to determine the pulse length.

The resulting second harmonic generation (SHG) signal has three components: the frequency doubling of each pulse replica $E(t)$ and $E(t - \tau)$ with itself, and a cross-term which appears when there is temporal and spatial overlap between the two replicas in the crystal. Due to conservation of momentum, this cross-term bisects the angle between the SHG signals from individual beams, so can be isolated from these and the co-propagating fundamental beams using an iris. A planar UV-enhanced aluminium mirror steers the cross-term through a colour filter (BG-18, Newport) to remove the remaining fundamental light, and then onto a detector.

Ordinarily, the autocorrelator detector is an integrating photodiode module with a UV-sensitive silicon photodiode (PDI-400-1-P-UV, Becker & Hickel GmbH). The energy of the signal (S) measured by the detector is a function of the relative time delay τ

$$S(\tau) \propto \int |E_{SHG}(t, \tau)|^2 dt \propto \int I(t)I(t - \tau)dt \tag{3.6}$$

The recorded signal is highest when the pulses perfectly coincide and zero when there is no overlap. The pulse duration can be determined from this autocorrelation function if a general pulse shape is assumed. If $I(t)$ has a Gaussian pulse shape, then $S(\tau)$ is also a Gaussian and the pulse width $\tau_{I,FWHM}$ is related to the autocorrelation width $\tau_{S,FWHM}$ via

$$\tau_{I,FWHM} = \frac{\tau_{S,FWHM}}{\sqrt{2}} \tag{3.7}$$

Due to technical complications with the photodiode, it was swapped for a spectrometer (HR4000, Ocean Optics). Recording the SHG spectra with delay in a spectrogram enables the method of frequency-resolved optical gating (FROG) to be applied. This method can be used to characterise the spectral phase of the pulse in addition to the duration but requires a complex two-dimensional phase-retrieval algorithm to do so. Since only the pulse duration was needed, the collected spectra at each delay were integrated over the wavelength to give the intensity. The spectrogram and autocorrelation traces are shown in Figure 3.6.
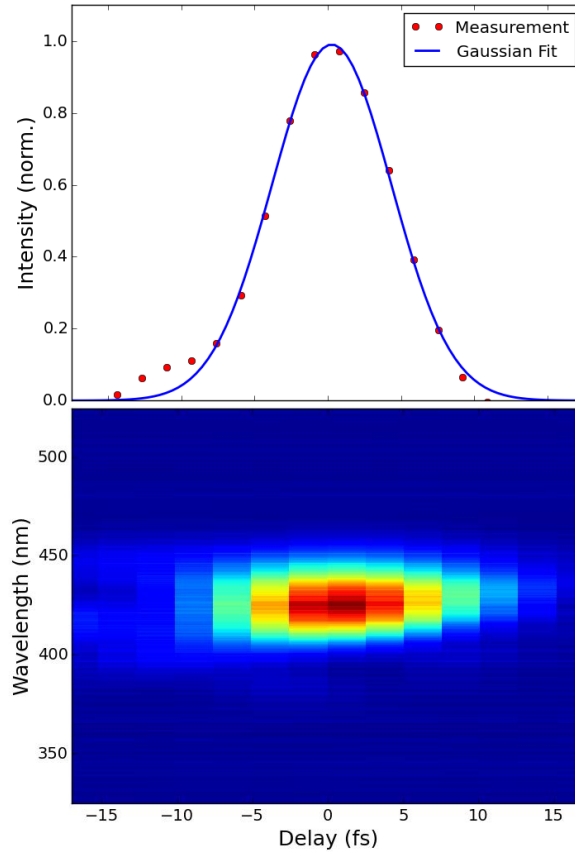
Figure 3.6: Spectrogram (bottom) of the SHG signal from the oscillator pulses recorded for 16 delays in steps of 1.3 fs and the autocorrelation trace (top) found by integrating over the wavelength range for each delay step and fitting a Gaussian curve to the points.

The FWHM of the fitted Gaussian curve is

$$\tau_{S,FWHM} = 14.4 fs \tag{3.8}$$

giving a pulse length of

$$\tau_{I,FWHM} = 10.2 fs \tag{3.9}$$

Later measurements using smaller time steps gave the same result for pulse length to within 3% [230].

3.3.3   Transmission Setup

The same setup could be used for autocorrelation and EOT measurements by simply removing the filter and exchanging the BBO crystal for a nanohole array sample. The transmission setup is shown in Figure 3.7. The samples were mounted on an XYZ translation stage (M-MT-XYZ, Newport) for alignment. Iris B could be placed so that either only light from one transmitted beam, or only scattered light between the beams was sampled.

In the initial set of measurements, the transmitted beam was collected with a lens to couple the beam to a multimode optical fibre (0.22 NA) send it to a spectrometer (HR4000, Ocean Optics). Spectrograms collected from these measurements showed a dominant autocorrelation signal which masked any effects of plasmon interaction (details in Chapter 5). It was hypothesised that dispersion in the collection optics (lens, fibre and spectrometer) contributed to this effect, so measurements were also performed using a photodiode without a lens (PDA100A, Thorlabs). Measurements were performed in the dark to reduce background effects of ambient light.
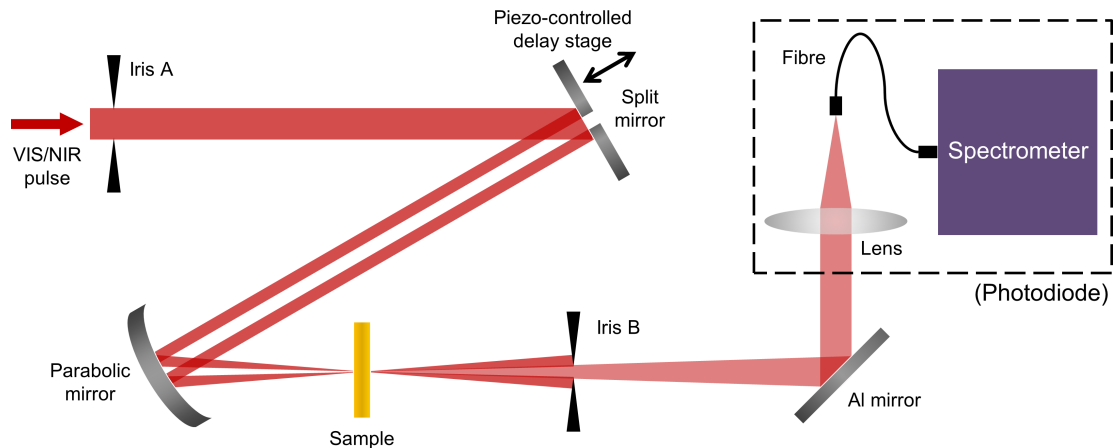
Figure 3.7: Schematic of the setup for dynamic transmission measurements. The nanohole sample takes the place of the BBO crystal in the autocorrelator. Transmission spectra are collected either with a lens focused onto the end of a fibre-coupled spectrometer, or with a photodiode.

3.4   Sample Fabrication

3.4.1   Lithographic Samples

Unlike the so-called *bottom-up* fabrication through chemical synthesis that can be used to produce nanoparticles and nanowires, *top-down* fabrication via lithography enables precise placement of nanostructures on the substrate, with a trade-off in the minimum possible feature size and crystallinity [7, 231].

Waveguide and nanoantenna samples studied in this thesis were fabricated by members of the Kleineberg group using electron-beam lithography (EBL) with a two-layer photoresist method, depicted in Figure 3.8. The substrate — typically silicon, or glass covered by an indium-tin-oxide (ITO) layer — is first ultrasonically cleaned and spin coated with photoresist in a bilayer configuration. An 80 nm layer of low molecular weight poly(methyl methacrylate) (PMMA) is placed directly onto the substrate, followed by a 145 nm layer of high molecular weight PMMA. An electron beam at 30 kV then selectively etches these layers, producing an undercut in the photoresist from backscattered electrons impinging on the lower layer. After chemical development of the etched nano- and/or microstructures, a chromium or titanium adhesion layer 2 - 3 nm thick may be thermally evaporated onto the sample, followed by the metal (silver or gold) of chosen thickness. Finally, lift-off in acetone removes the photoresist, leaving the exposed metal structures. The undercut in the photoresist reduces the likelihood that parts of the metal layer are removed during this final step.

Several fabrication methods were tried for nanohole arrays, including electroplating with resist masks and focused ion beam (FIB) lithography on evaporated films, but ultimately EBL with a negative photoresist was used. This allowed for multiple copies of each array to be fabricated on the same film. Various dose factors were tested across arrays on the same sample to try to optimise the EBL process for the negative resist and large layer thicknesses. The results of these trials are briefly presented in Chapter 5, and in detail in Reference [232].

3.4.2   Argon Ion Sputter Cleaning

Samples examined in the PEEM were primarily silver, which oxidises readily in air and over time in even high-vacuum environments. The lithography process can also leave residual resist on the sample, which can cause high extractor currents, thus limiting the attainable extractor voltage and therefore the resolution. In addition, it was found that fabricated waveguides and antennas suffer from high amounts of surface roughness which produces undesirable hot spots and large scattering losses.
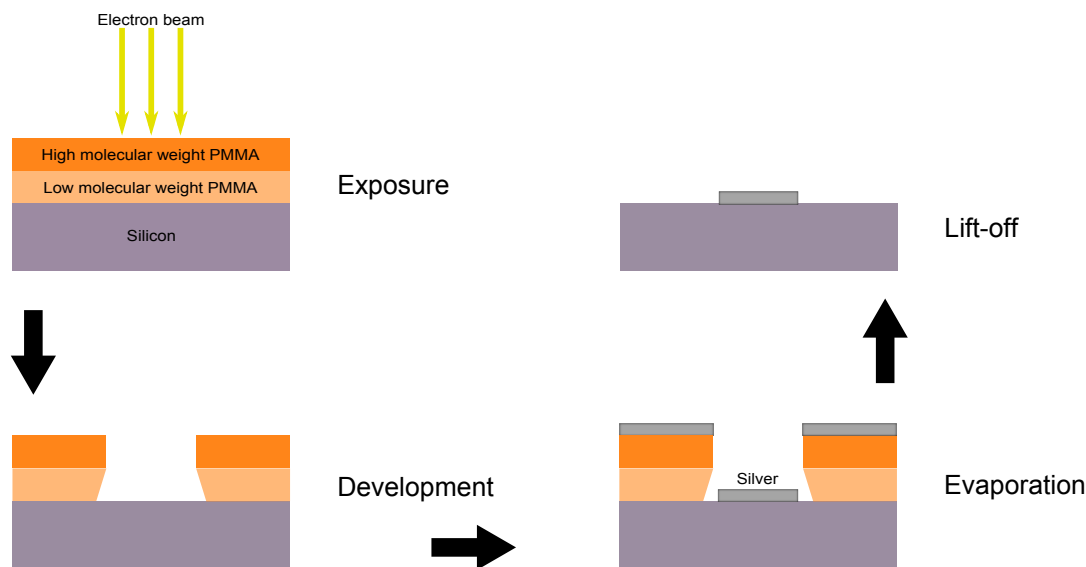
Figure 3.8: A depiction of the 2-layer e-beam nanolithography process. Coating the substrate with a layer of low molecular weight PMMA followed by high molecular weight PMMA creates an undercut when the resist is exposed to the electron beam. This decreases the chance that the evaporated metal layer is moved during the lift-off process.

An ion source based on microwave plasma discharge (tectra IonEtch GenII, tectra GmbH) was attached to the sample transfer arm of the PEEM chamber for in-situ sputter cleaning and surface modification. Argon gas was fed into the chamber through a gas inlet. Ionisation of argon in the chamber is achieved via resonance heating with microwaves at 2.45 GHz and enhanced by a magnetic quadrupole around the discharge chamber which increases the plasma density. Ions are accelerated using an extractor grid and their energy (25 eV - 5 keV) is adjusted by an additional anode grid farther along the chamber. A blanking grid can be placed before the sample to reduce the cross-section of the ion beam. The power supply for the ion source has independent controls for magnetron current, ion energy, and extractor voltage. These parameters as well as the argon pressure and working distance could be varied to change the ion current, current density, and energy at the sample, although there is a complex interdependency between these parameters.

The effects of ion bombardment on a surface are complex and depend on the species involved, ion energies, ion doses, gas pressures, surface temperature, and incidence angle [233, 234]. Possible effects include removal of adsorbed gases, ion implantation, variable degrees of sputtering, and alteration of the surface morphology [235, 236]. Argon ion energies of a few hundred eV are typically used for cleaning of surfaces via removal of oxides and polymers; higher energies on the order of keV for sputtering of the target. Aside from the parameters listed above, sputtering rates are also dependent on the presence of convex or concave features on the surface [237, 238]. Due to geometry, convex and concave structures are eroded respectively faster and slower than corresponding flat structures at

Ion Energy (eV)	300	700	1000
Penetration depth (nm)	1	1.5	1.8
Sputter yield (atoms/ion)	1.7	3.2	3.8

Table 3.2: The average penetration depth and sputtering yield of Ar^+ in Ag for three different ion energies.

Setting	Value
Ion energy	300 - 1000 eV
Magnetron current	$25\,\text{mA}$
Extractor voltage	$600\,\text{V}$
Working distance	$120\,\text{mm}$
Chamber pressure	$\approx 6 \times 10^{-4}\,\text{mbar}$
Current density	$0.5\,\mu\text{A}\,\text{cm}^{-2}$

Table 3.3: Argon ion sputtering settings used for the cleaning and modification of silver surfaces.

normal incidence, which can lead to an increased deviation in the height of surface features.

Monte Carlo simulations (The Stopping and Range of Ions in Matter [239]) were used to estimate the average penetration depth and sputtering yield of Ar ions in Ag for various ion energies. These are listed in Table 3.2 for the three ion energies used in this thesis. Further details of the Monte Carlo method and results can be found in Reference [240].

Experiments described in Chapter 4 showed that the lowest ion energy setting used (≈ 300 eV) was effective in removing surface oxidation and resist residue without visibly damaging the sample, whilst the highest energy (≈ 1000 eV) resulted in significant removal of parts of the 40 nm-thick silver layers. The other parameters were kept constant, and are given in Table 3.3.

Chapter 4

Photoemission Electron Microscopy on Plasmonic Structures

This chapter describes the design and PEEM imaging of plasmonic silver nanoantennas and stripe waveguides. Structures of various sizes and shapes were designed with the intent of investigating the effect of geometry on the plasmonic field enhancement, as probed by 2P-PEEM. Scanning electron microscopy (SEM) and 1P-PEEM were used to inspect the samples after lift-off, compare the geometry of the resulting structures with their original design, and gauge the surface quality.

Where appropriate, experiments were supported by three-dimensional finite-difference time-domain (FDTD) simulations which model the interaction of the 2P-PEEM excitation source with the plasmonic structures. Frequency-domain planar field monitors were used to record the resulting steady-state electric field intensities at the vacuum/silver interface. Simulations allow the effects of overall nanoantenna and waveguide shape and size to be separated from the effects of surface irregularity.

After imaging various silver structures and observing the effects of surface oxidation and roughness, the PEEM chamber was fitted with an ion source and argon inlet for in-situ argon ion sputtering. Two waveguide samples were exposed to sputtering at several ion energies and doses, which modified the surfaces in different ways.

4.1   Nanoantennas

4.1.1   Fabrication and PEEM Imaging

Various silver nanoantennas were fabricated using the two-layer photoresist EBL method described in Chapter 3 to examine the effects of shape, size, and laser polarisation on the plasmonic field enhancement at the edges of structures and coupling across small gaps. In order to achieve the highest field localisation and enhancement at the desired locations on the nanoantennas, the antenna geometry, gap size, and surface quality must be carefully controlled.

Single and double bowtie and double ellipse nanoantennas of 20 nm thickness and varying sizes were produced on the same silicon substrate with a 2 nm chromium adhesion layer. Three sizes of each shape were designed, defined by the long axis of individual antenna components (triangles or ellipses) — 750 nm, 500 nm, and 250 nm. From this point, these sizes will referred to as large, medium, and small. The ratios of the short to long axes of the triangles and ellipses remained at 0.9 and 0.6, respectively, so the tip angles remained constant for all three sizes. Gap sizes between tips of large, medium, and small bowties were 550 nm, 300 nm, and 100 nm, respectively. Gap sizes between large, medium, and small ellipses were 500 nm, 250 nm, and 60 nm.

SEM images of large double bowtie and medium double ellipse nanoantennas after lift-off are shown in Figure 4.1. The gap sizes in all shapes were within 10% of their designed size.
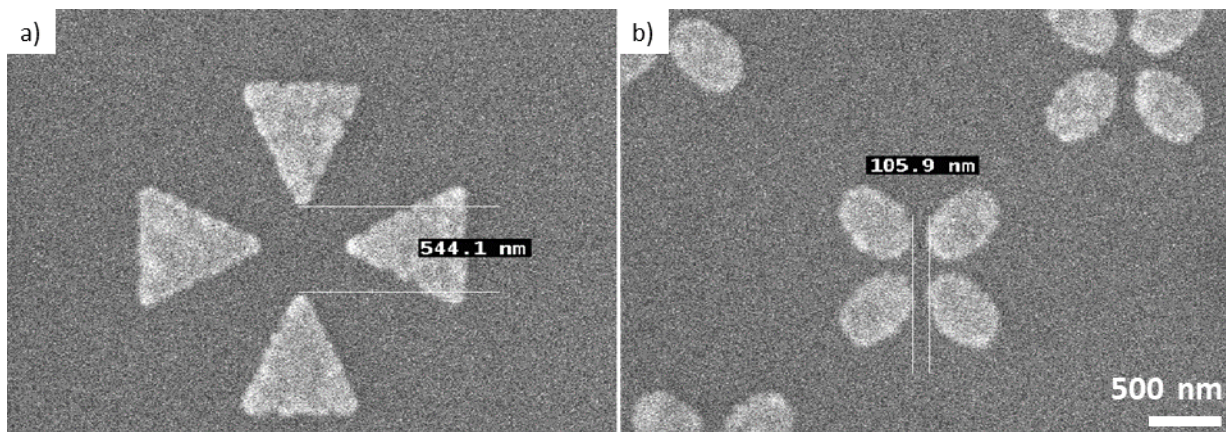
Figure 4.1: SEM images of some of the silver nanoantenna structures produced by EBL. Images in the top row show a) large double- and b) medium single-bowtie nanoantennas with gaps of approximately 550 nm and 250 nm. Images in the bottom row show c) medium and d) small double ellipses with 250 nm and 60 nm gaps between the vertices.

After fabrication, nanoantennas were imaged by 1P- and 2P-PEEM. For 2P-PEEM images, a half-wave plate was used to rotate the linearly polarised laser field. Figures 4.2 to 4.6 show 1P-PEEM and pseudocolour 2P-PEEM images from large and medium double bowtie and ellipse nanoantennas. White circles in the 1P-PEEM images indicate which nanoantennas have been imaged in the corresponding 2P-PEEM images. A colour lookup table has been applied to the greyscale 2P-PEEM images to produce pseudocolour images which illustrate photoemission intensity; colour scales are shown to the right of the 2P-PEEM images. The direction of incident illumination is always from the left of the image, as indicated by the pink arrow in the top-left corner of each figure, and at 65° to the surface normal. For the 2P-PEEM images the orientation of the in-plane component of the incident electric field is indicated with yellow arrows to the top right of each image. For simplicity, this direction will be described in the text as 0° when the in-plane component is oriented vertically to the image (TE polarisation), and as 90° when it is oriented horizontally (TM polarisation).
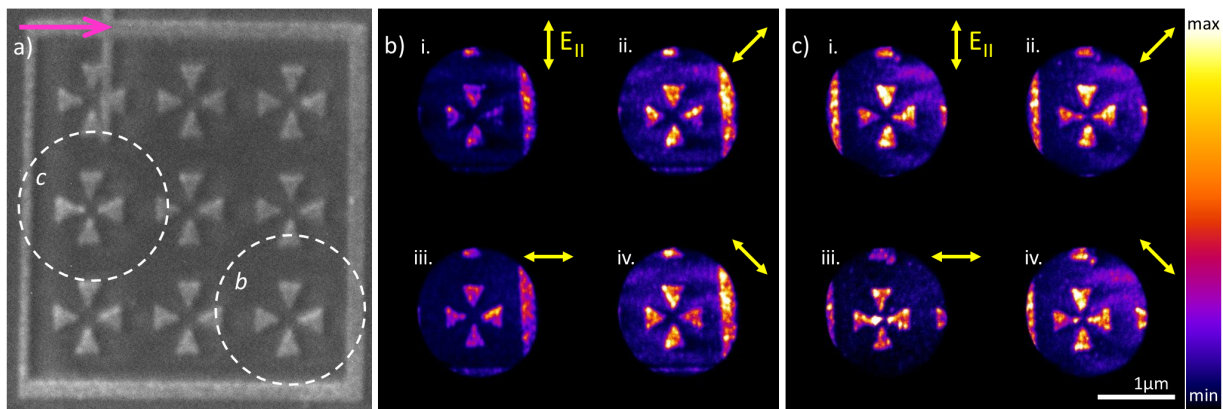
Figure 4.2: a) 1P-PEEM image of large double bowtie nanoantennas. Pseudocolour 2P-PEEM images of individual nanoantennas indicated by white circles are shown in b) and c) with the in-plane component of the electric field at i. 0°, ii. 45°, iii. 90°, and iv. 135°.

Slight variations amongst individual nanoantenna structures can be seen in 1P-PEEM images, even at this modest resolution. For example, in Figure 4.2a), the double bowtie in the leftmost circle (labelled 'c') appears to have brighter and sharper tips at the gap than the nanoantenna in the rightmost circle (labelled 'b'), whilst the nanoantenna in this circle has a bright upper edge on the rightmost triangle. These differences become more apparent under 2P-PEEM imaging, as rotating the polarisation selectively excites different regions on the antennas. The sharp tips at the gap of the nanoantenna in Figure 4.2c) show strong photoemission when the electric field is at 90°, and almost none when it is at 0°. Likewise, the top edge of the rightmost triangle in Figure 4.2b) appears brightest when the electric field is oriented roughly parallel to this edge, and dimmest when it is oriented perpendicularly. For clarity, enlarged side-by-side 1P-PEEM and 2P-PEEM images of nanoantenna 'b' are shown in Figure 4.3.
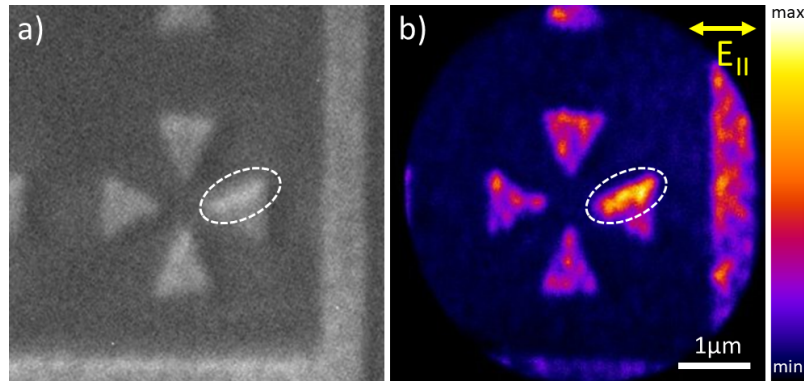
Figure 4.3: Enlarged a) 1P-PEEM and b) 2P-PEEM images of the large double bowtie nanoantenna 'b' in Figure 4.2. The 1P-PEEM image shows a bright edge on the rightmost triangle, suggestive of a sharper edge or rougher surface. Under illumination by TM-polarised light plasmon hot spots are excited along this edge, seen in the 2P-PEEM image.
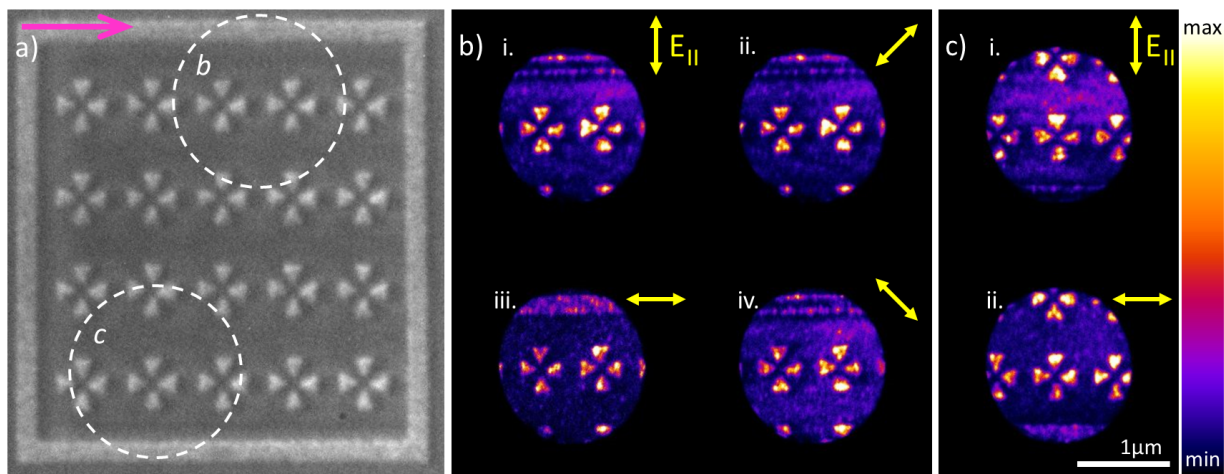
Figure 4.4: a) 1P-PEEM image of medium double bowtie nanoantennas. Pseudocolour 2P-PEEM images of the regions in white circles are shown to the right with the in-plane component of the electric field at i. 0°, ii. 45°, iii. 90°, and iv. 135° for the nanoantennas in b), and i. 0°, and ii. 90° for the nanoantennas in c).

Figures 4.2 to 4.5 each show 2P-PEEM images from multiple nanoantennas with the same nominal geometry. All sizes and shapes of nanoantenna show strong photoemission from hot spots with dimensions on the order of tens of nanometres, with the relative intensity of these hot spots varying with the laser polarisation. Multiple adjacent medium double bowties are shown in Figure 4.4. In these images, it is apparent that the distribution of hot spots in these nanoantennas varies from structure to structure, as does their dependence on polarisation. For the double ellipses shown in Figures 4.5 and 4.6, the rightmost ellipses appear dark when the incident in-plane electric field is at 0°, slightly brighter for 45° and 135°, and bright for 90°. The other ellipses appear more or less equally bright for
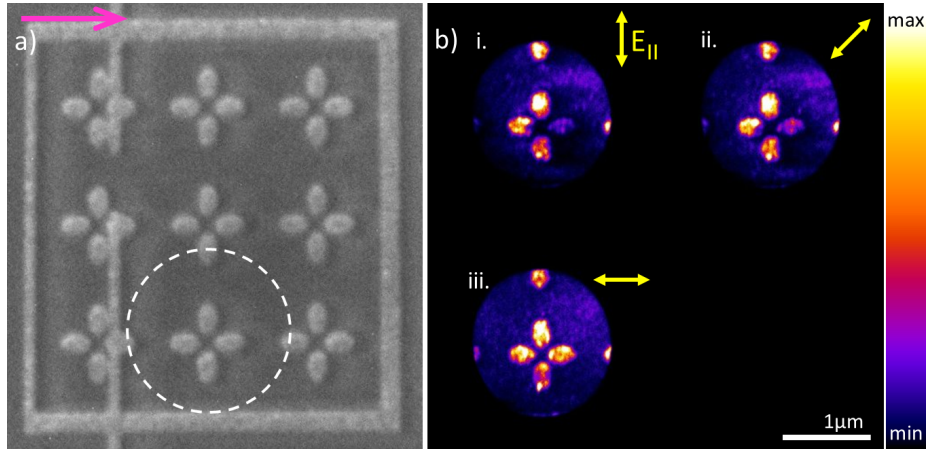
Figure 4.5: a) 1P-PEEM image of large double ellipse nanoantennas. b) Pseudocolour 2P-PEEM images of an individual nanoantenna with the in-plane component of the electric field at i. 0°, ii. 45°, and iii. 90°.
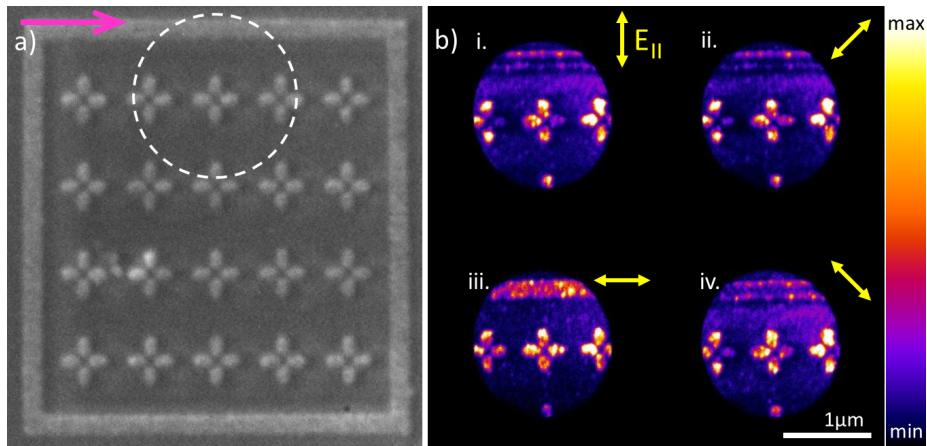
Figure 4.6: a) 1P-PEEM image of medium double ellipse nanoantennas. b) Pseudocolour 2P-PEEM images of individual nanoantennas with the in-plane component of the electric field at i. 0°, ii. 45°, iii. 90°, and iv. 135°.

all orientations. Further discussion about the polarisation-dependent excitation of these regions is presented in the next section.

4.1.2   Simulation

The influence of structural variations between nanoantennas — both intentional (shape, size) and unintentional (surface roughness, tip curvature) — on the field localisation and enhancement was modelled using simulations. Simulations were performed using a commercial-grade FDTD simulator [241]. Details of this method can be found in the

Appendix.

The simulation setup is shown in Figure 4.7. The laser excitation was replicated by a source with wavelength 405 nm injected at an incident angle of 65°. The direction of propagation is indicated by a pink arrow; the polarisation axis is shown with a blue arrow. The source was a total-field scattered-field (TFSF) source, which is used to separate the simulation area into two regions — a volume containing the total field (the sum of the incident and scattered fields), which is shown bounded by a white box, and the volume outside this box which contains only the scattered field. Ultimately only the near fields in the total field region were investigated, so a plane wave source could also have been used.
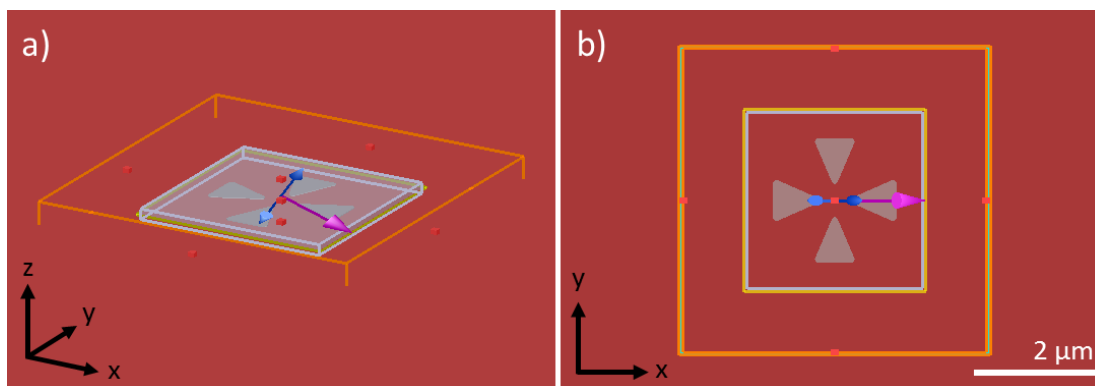
Figure 4.7: The FDTD simulation setup for calculating the field enhancement of nanoantennas, shown in a) perspective view and b) the x-y plane. The propagation direction and polarisation axis of the source are indicated by pink and blue arrows respectively. A white box shows the region where the total field (i.e. the sum of the incident and scattered fields) is calculated. The boundaries of the FDTD region are shown in orange — PML boundaries in the z-direction, Bloch boundaries in the x- and y-directions.

The simulation region in each case was centred on a single silver nanoantenna on a silicon substrate (with a chromium adhesion layer) enclosed by perfectly matched layer (PML) boundaries in the z-direction and Bloch boundaries in the x- and y-directions (shown in orange), which are necessary for sources propagating at an angle to the z-axis. The predefined *steep angle* profile was used for the PML layers to reduce reflections. The total simulation region volume was $5 \times 5 \times 1\,\mu m$. At this distance, any reflections from the boundaries were negligible.

The substrate and adhesion layers extended through the boundaries in the x- and y- directions, with the semi-infinite substrate also extending though the z-boundary. Materials were modelled with complex dielectric constants ε at $\lambda = 405$ nm of silver ($\varepsilon = -4.02 + 0.69i$), chromium ($\varepsilon = -11.06 + 11.13i$), and silicon ($\varepsilon = 29.45 + 3.72i$). A 2D frequency-domain field and power monitor at the silver/vacuum interface recorded the electric field intensity $|E(\omega)|^2$ at each point in the plane of the nanoantennas, normalised to

the source field intensity. The sizes of the mesh steps around structures were set to $1.5\,$nm for small, $3\,$nm for medium, and $4\,$nm for large nanoantennas.

Figures 4.8 and 4.9 show simulated electric field intensities of the double bowtie and ellipse nanoantennas fabricated in the previous section, illuminated under the same conditions as the 2P-PEEM images. Colour scales to the right of each image indicate the values of the normalised field intensities. For each nanoantenna shape and size, three field profiles for source polarisations of 0°, 45°, and 90° were collected.
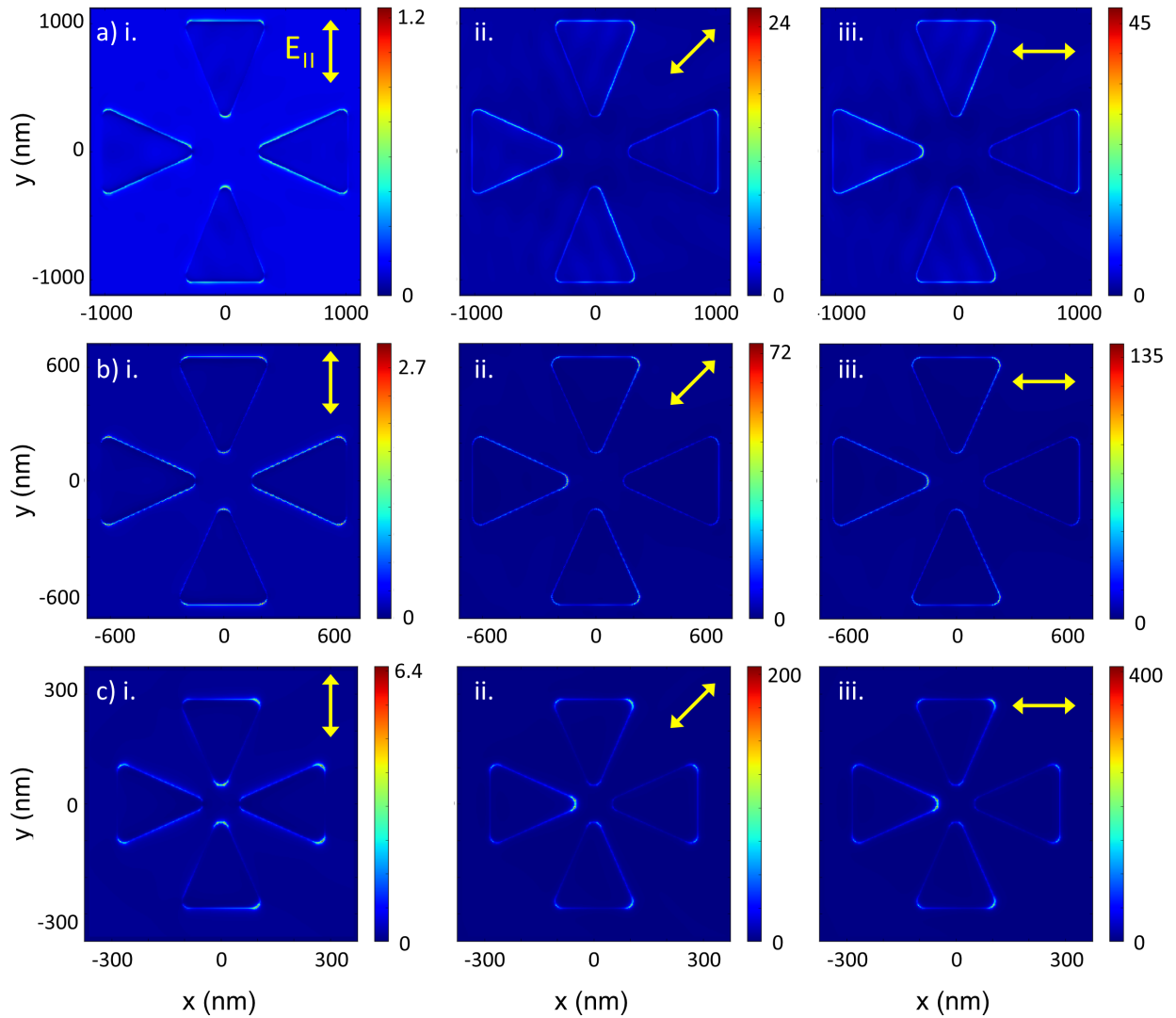
Figure 4.8: Electric field intensity profiles of a) large, b) medium, and c) small double bowtie nanoantennas excited by a source with the polarisation oriented at i. 0°, ii. 45°, and iii. 90°. The direction of the incident source is the same as in the PEEM experiments in the previous section — from the left at an angle of 65° from normal.
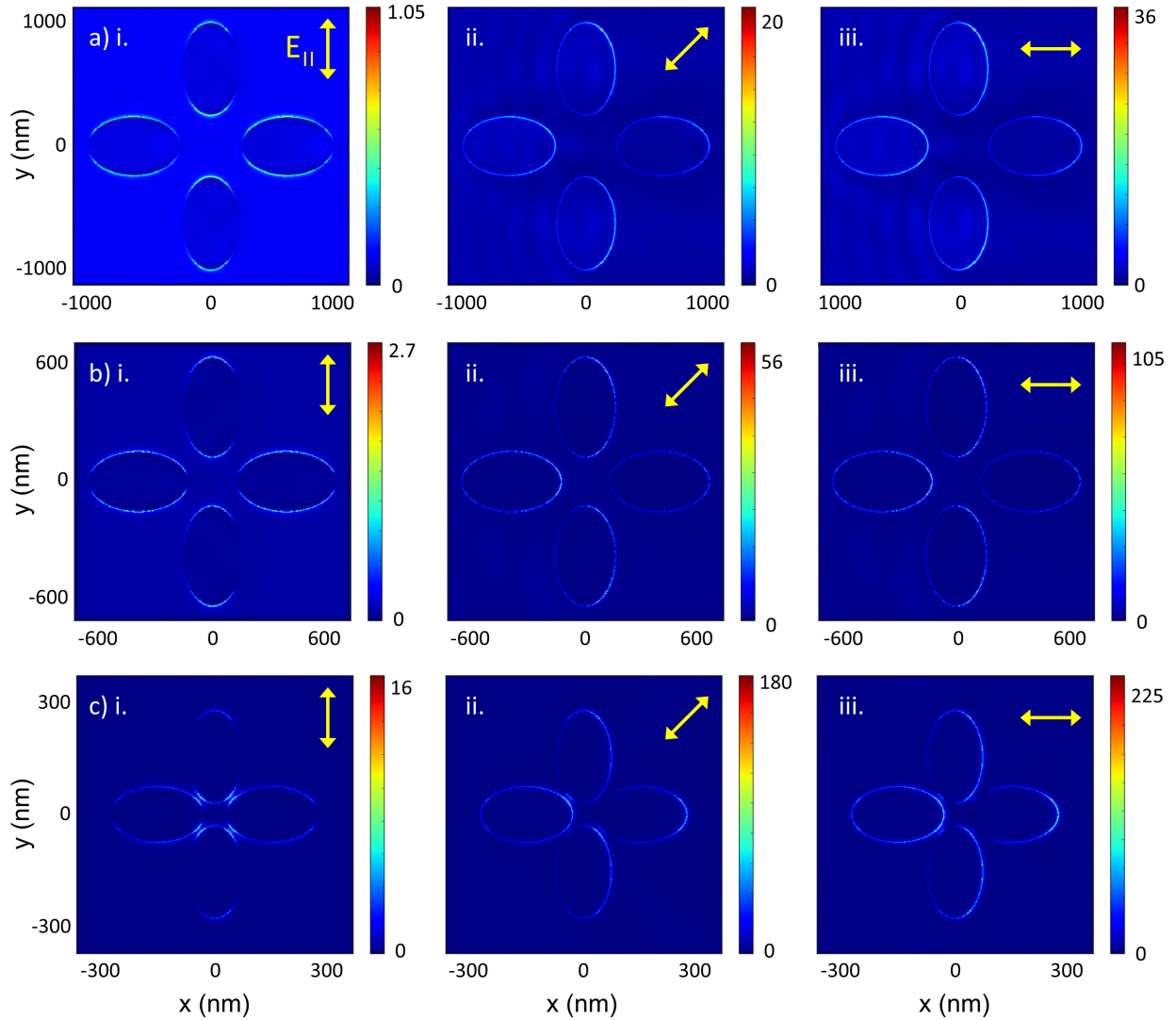
Figure 4.9: Electric field intensity profiles of a) large, b) medium, and c) small double ellipse nanoantennas excited by a source with the polarisation oriented at i. 0°, ii. 45°, and iii. 90°.

For large and medium double bowties, at 0° polarisation there is only a slight enhancement of the incident field found on the nanoantenna edges that are fully or partially perpendicular to the polarisation axis, with no particular left-right bias. For small bowties, these areas become localised to the vertices which have some orientation along the polarisation axis, particularly those to the right side of the structure. As the polarisation of the source is rotated from 0° to 90°, the maximum field intensity for all nanoantenna sizes increases $\approx 40 - 60$ fold, and becomes localised at the right tip of the leftmost triangle i.e. the tip that is oriented parallel to both the polarisation and incident light direction. The maximum field intensity on the small bowtie is $\approx 9\times$ greater than that on the large bowtie.

Similar trends occur for the double ellipse nanoantennas. At 0° polarisation, the top

and bottom edges of each ellipse in large and medium nanoantennas show slight field enhancement; this enhancement increases and shifts to the right-hand edges of the ellipses as the polarisation is rotated to 90°. For the small nanoantenna at 0°, there are relatively strong fields localised in the small gaps between adjacent ellipses, which intensify as the polarisation is rotated. At 45° and 90°, the right edges of the small ellipses also show strong enhancement.

Since the incidence angle of the light source is relatively large, for 90° (TM) polarisation there is a sizeable component of the electric field vector which is oriented normal to the sample plane. This evidentially has a large effect on the location and amplitude of the electric field enhancement, since the double nanoantennas themselves are symmetric along the x- and y-axes. The explanation for this is that incident light strikes the nanoantennas from the left, launching propagating surface plasmons from the left edges of each nanostructure which become focused at the right vertices.

For each shape, strongest field enhancements are found for the smallest structures and gap sizes; the increase in maximum intensity from large to small nanoantennas is about 6-9 fold. Comparable levels of enhancement are seen in similarly-sized double bowties and ellipses. In all cases, fields are strongest at the edges of the structures and very little can be seen on the metal surface, although the largest structures show faint fringes at 45° and 90° polarisation. This is due to the interference between incident light which propagates from the left of the image and back-reflected fields from the edges of the structures.

To more easily compare the 2P-PEEM images with results from simulations — which show a large difference between 0° and 90° polarisation — images were created by taking the 0° polarisation as a background, and subtracting this from the 90° polarisation. Figures 4.10 to 4.13 show comparisons between 1P-PEEM, background-subtracted 2P-PEEM, and simulated results. For large double bowtie nanoantennas, both experiment and simulation show field enhancement around the edges of the triangles and at the vertices, especially at the inner tip of the left triangle. For medium double bowties the field enhancement in background-subtracted 2P-PEEM images is seen around the edges, but the enhancement at the vertices is more randomly distributed. The background-subtracted 2P-PEEM images for both large and medium double bowtie nanoantennas display field enhancement around the edges of all ellipses and on the surface of the right ellipse.

From these images it is evident that some, but not all, of the experimentally-observed photoemissison hot spots are found at locations predicted by simulations. The inconsistencies in hot spot locations, combined with the fact that the simulations predict a much greater difference between enhancement between 0° and 90° polarisation, indicate that many of the hot spots are due to surface roughness and are thus independent of the nanoantenna size and shape.

To study the effects of small variations in nanoantenna geometry on the field enhancement,
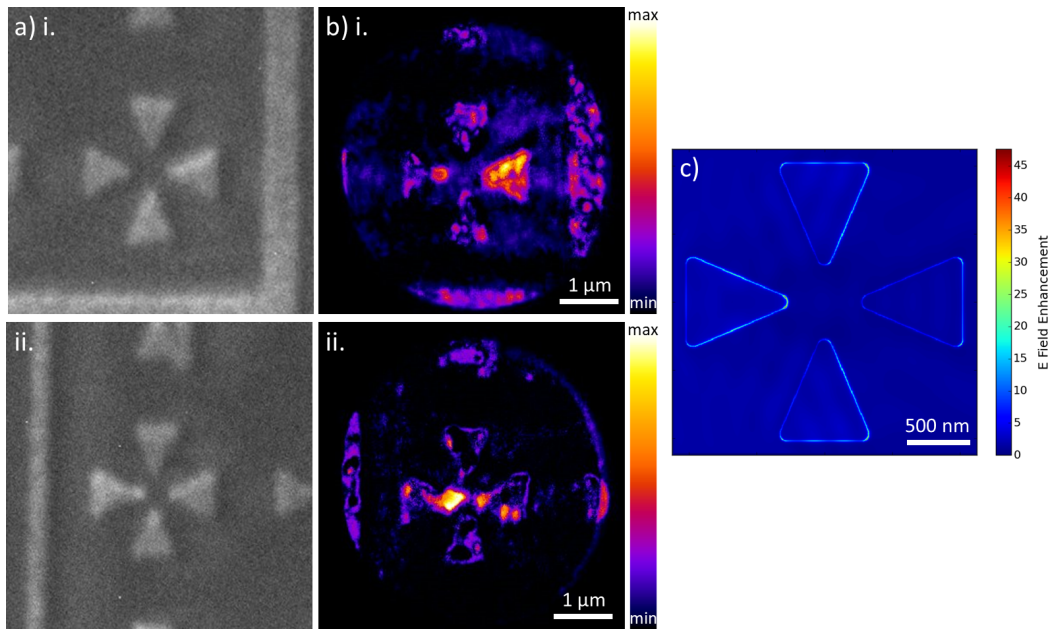
Figure 4.10: a) 1P-PEEM and b) background-subtracted 2P-PEEM images of the large double bowties circled in Figure 4.2, set side-by-side with c) the simulated electric field intensity profile. Both experiment and simulation exhibit field enhancement at the edges and the vertices to the right of each triangle, particularly the inner tip of the left triangle.
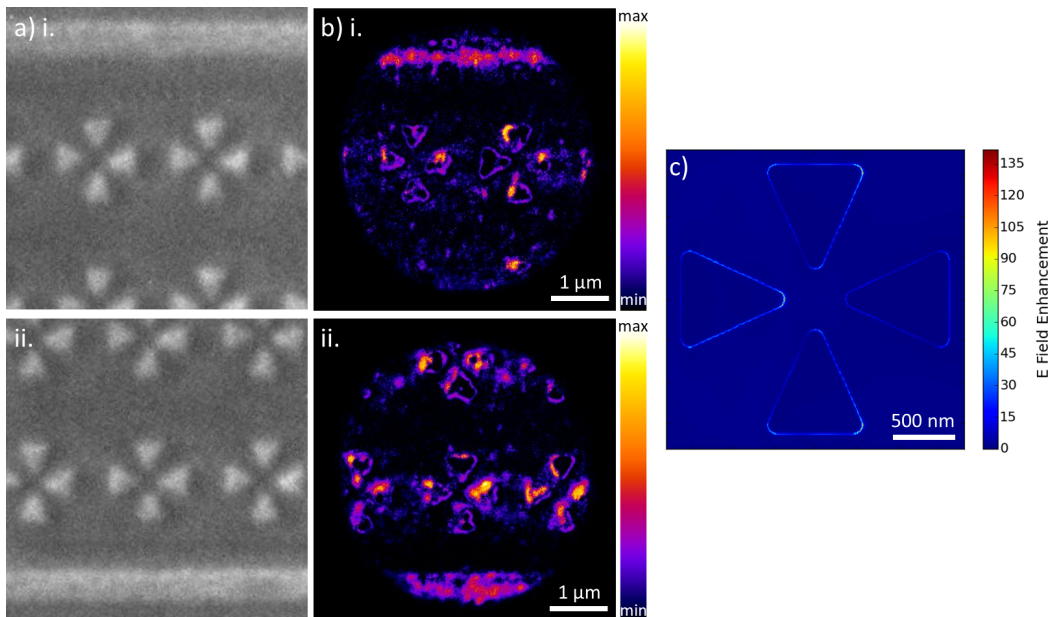
Figure 4.11: a) 1P-PEEM and b) background-subtracted 2P-PEEM images of the medium double bowties circled in Figure 4.4, set side-by-side with c) the simulated electric field intensity profile. Field enhancement in experiment and simulation can be seen around the edges of the triangles; enhancement at the vertices is less consistent.
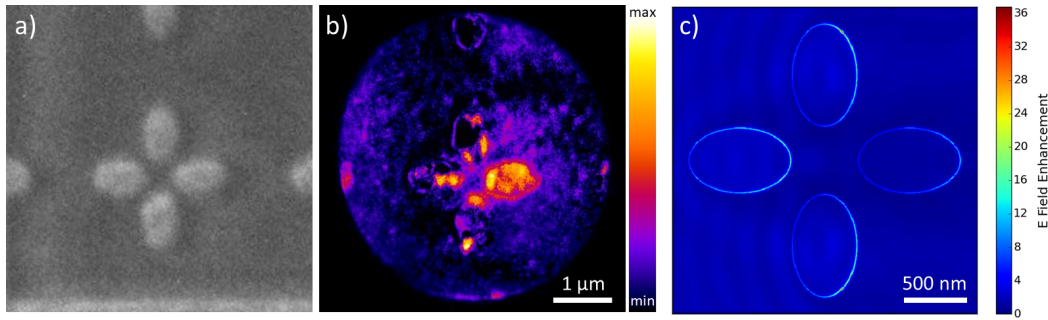
Figure 4.12: a) 1P-PEEM and b) background-subtracted 2P-PEEM images of the large double ellipse circled in Figure 4.5, set side-by-side with c) the simulated electric field intensity profile. Both experiment and simulated nanoantennas show field enhancement at the right edges of the ellipses; the whole surface of the right ellipse in the background-subtracted 2P-PEEM image is bright.
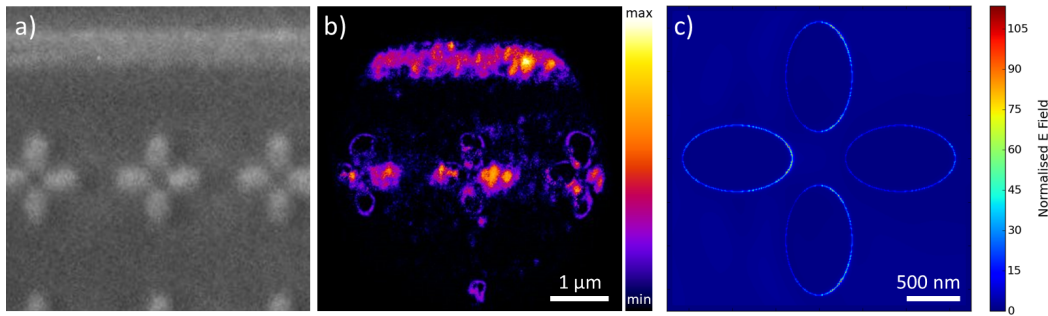
Figure 4.13: a) 1P-PEEM and b) background-subtracted 2P-PEEM images of the medium double ellipses circled in Figure 4.6, set side-by-side with c) the simulated electric field intensity profile. As for the large double ellipses, both experiment and simulated nanoantennas show field enhancement at the right edges and the 2P-PEEM image shows field enhancement over the whole surface of the right ellipse.

a single small bowtie nanoantenna with a gap size of 100 nm (with the long axis parallel to the incident light direction) was chosen as a model. The source polarisation was kept at 90°.

Field profiles were taken as the gap between the tips was varied from 20 nm to 180 nm in steps of 20 nm. Figure 4.14 shows field profiles for gaps of 20 nm, 100 nm, and 180 nm. To better visualise the dependence of relative field intensity at the tips on gap size, slices of the field intensity along the x-axis (integrated over the range $-20\,\text{nm} \leq y \leq 20\,\text{nm}$) are plotted in Figure 4.15. Intensities have been normalised to the maximum field intensity for the 100 nm gap. These plots show that the field intensity on the left tip shows a slight increase as the gap is widened from 20 to 80 nm, which then slowly declines for larger gaps. The field intensity on the right tip increases dramatically from 20 to 60 nm, increases steadily between 60 and 100 nm, and plateaus for gaps wider than 100 nm. The experimental excitation source was monochromatic, so any shifts in the resonance wavelength with gap
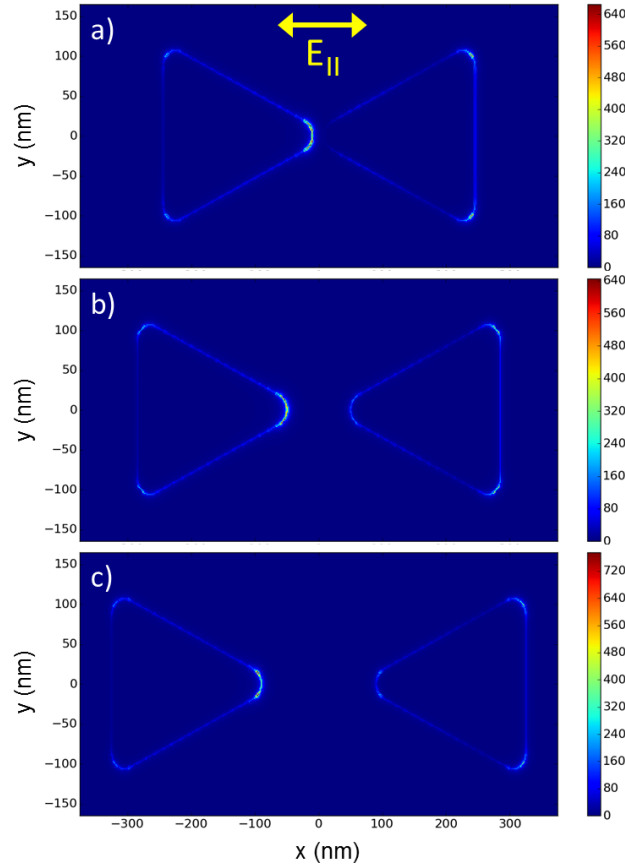
Figure 4.14: Field intensity profiles of small single bowtie nanoantennas with gap sizes a) 20 nm, b) 100 nm, and c) 180 nm. The polarisation of the excitation source is along the long axis of the nanoantenna.

size were not considered.

So far, all triangular nanoantennas have been simulated with a degree of corner roundness matching that observed in fabricated structures, corresponding to a radius of curvature (ROC) of 20 nm. Nanoantennas with tips with ROC = 0 to 20 nm in steps of 5 nm were simulated to test the hypothesis that pointier tips would increase the maximum field intensity and localisation. Figure 4.16 shows field profiles for an ROC of 15 nm, 10 nm, 5 nm, and 0 nm.

To compare the results, a few figures of merit (FOM) which can quantify the field enhancement have to be defined. The *summed intensity* is the total field intensity summed over the mesh cells in the region $-65 \, \text{nm} \leq x \leq -45 \, \text{nm}$ and $-25 \, \text{nm} \leq y \leq -25 \, \text{nm}$ around the left tip. The *localisation* is the fraction of this region over which 50% of the *summed intensity* is distributed, subtracted from 1. So the higher this value, the smaller the area containing most of the field enhancement. Finally, the field intensity E^2 is calculated for a point just to the right of the tip $(x, y = -45 \, \text{nm}, 0 \, \text{nm})$, which is the most pertinent quantity
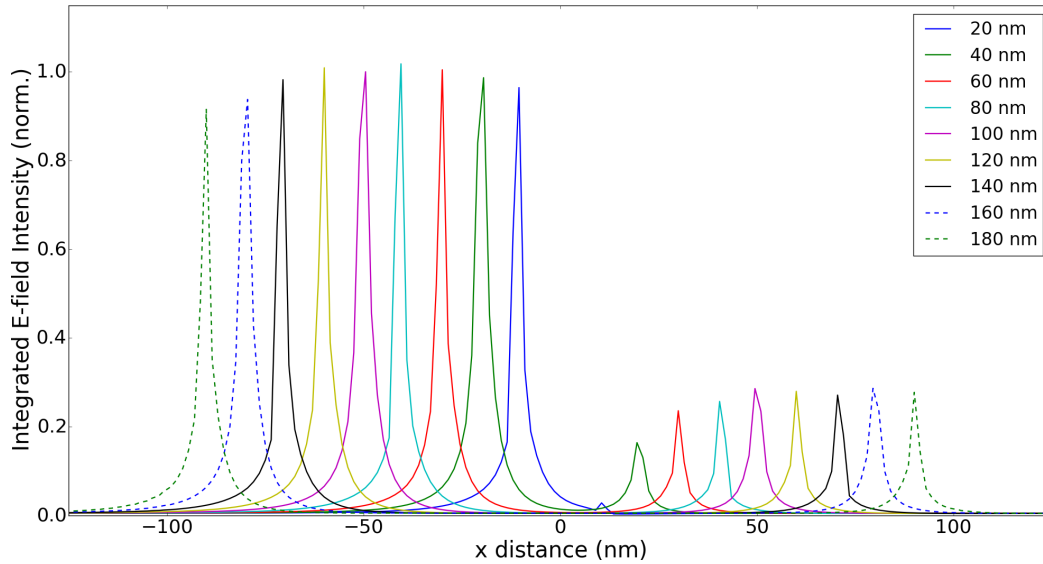
Figure 4.15: Plots of the field intensity (integrated over the range $-20\,\text{nm} \leq y \leq 20\,\text{nm}$) across the nanoantenna gap for gap sizes in the range 20 to 180 nm.
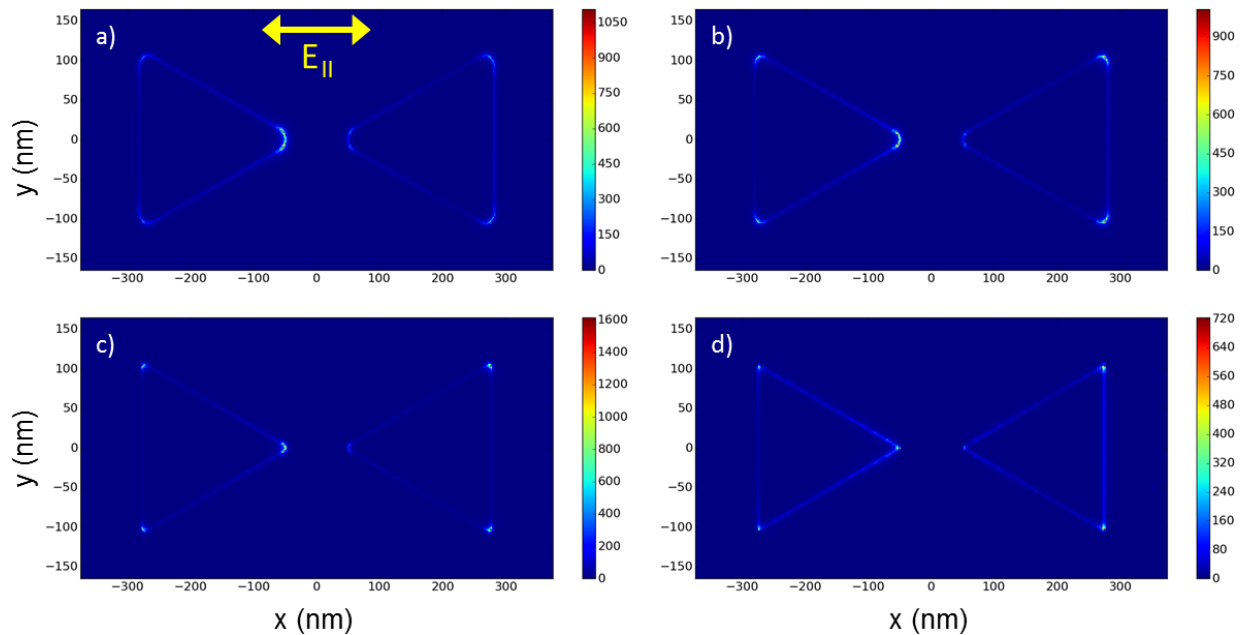
Figure 4.16: Field intensity profiles of small single bowtie nanoantennas with radii of curvature of a) 15 nm, b) 10 nm, c) 5 nm, and d) 0 nm

for applications involving materials placed in the gap (e.g. enhancement of Raman signals from molecules). Figure 4.17 plots each of these FOM with ROC. The *summed intensity* and $E^2(45, 0)$ have been normalised to the maximum value.

The total field intensity at the tip peaks at a ROC of 15 nm but then decreases monotoni-
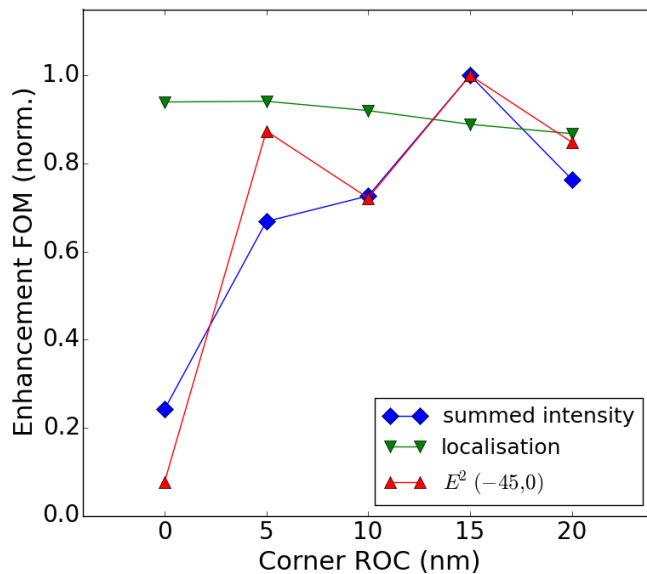
Figure 4.17: Normalised enhancement figures of merit (FOM) for small single bowtie nanoantennas with varying radii of curvature on the corners, normalised to the maximum value for each FOM. Blue diamonds show the total field intensity summed over an area around the tip, green triangles show the fraction of this region over which 50% of the intensity is distributed (subtracted from one), and red triangles show the field intensity at a point just in front of the tip.

cally for smaller curvatures. As expected, the localisation increases as the ROC decreases from 20 nm to 5 nm and the tip becomes more pointed. However, completely removing the roundness by decreasing the ROC from 5 nm to 0 nm actually produces a slightly lower degree of localisation. This can be seen in Figure 4.16, where for the most pointed tip there is a significant amount of field intensity along the edges of the triangles near the vertices. The third parameter — the field intensity at a point just in front of the tip — is to an extent a consequence of the first two. This value is highest when there is both a large summed intensity over the tip and a high degree of localisation, so there are two peaks at ROC = 15 and 5 nm.

It is apparent from the experimental results that the nanoantenna response can be dominated by hot spots which vary between structures due to the surface roughness. In the simulations, roughness can be applied to a surface by a model which generates a matrix of uniform random numbers in k-space. The model then takes a user-defined correlation length L_c to filter the high frequency components, then transforms the resulting values back to real space where the amplitude is modified by a specified sigma RMS value σ. The relationship between these quantities is described by a Gaussian surface correlation function:

$$\left\langle H(\vec{r})H(\vec{r}+\vec{\delta})\right\rangle = \sigma^2 e^{-\frac{\delta^2}{L_c^2}} \tag{4.1}$$

Small and large nanoantennas were simulated with $\sigma = 1$ to $5\,\text{nm}$ in steps of $0.5\,\text{nm}$. The correlation length was kept constant at $L_c = 20\,\text{nm}$, as was the seed for the random number matrix. Field profiles of small and large nanoantennas with $\sigma = 1\,\text{nm}$ and $\sigma = 5\,\text{nm}$ are shown in Figure 4.18. In all cases, hot spots are seen along the edges, which become more isolated for larger values of σ. For the large nanoantenna, field enhancement can also be seen on the surface of the triangles, particularly for the rougher surface. At an RMS roughness of $\sigma = 1\,\text{nm}$ the highest field intensity is still found at the left tip for both sizes; this is not the case $\sigma = 5\,\text{nm}$. Comparison of field profiles shows that as the roughness increases, the location of maximum intensity moves away from the left tip when $\sigma = 3\,\text{nm}$ for both small and large nanoantennas. This crossover point between $\sigma = 2.5$ and $3\,\text{nm}$ may vary with the seed used to generate the surface profile; this effect was not investigated. Nonetheless, it provides an estimate of the surface quality needed for the response of a nanoantenna under these illumination conditions to be dictated by its shape, rather than its roughness.
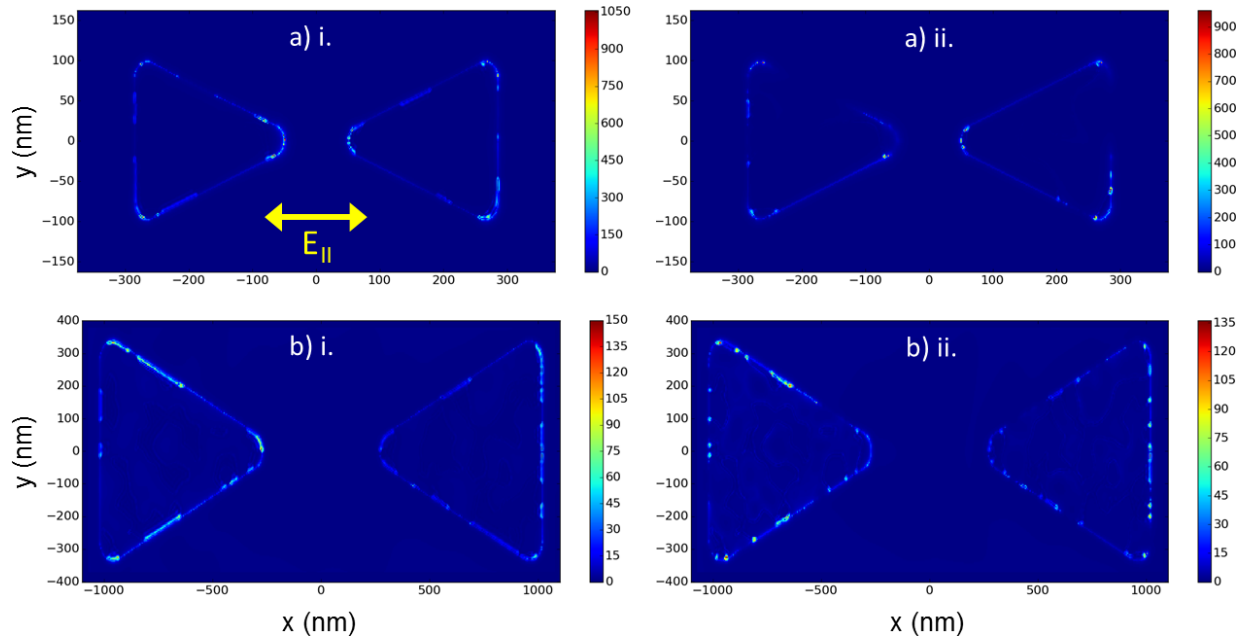
Figure 4.18: Field intensity profiles of a) small and b) large single bowtie nanoantennas with RMS surface roughness values of i. $\sigma = 1\,\text{nm}$ and ii. $\sigma = 5\,\text{nm}$. The correlation length in all cases is kept at $20\,\text{nm}$.

4.2 Stripe Waveguides

4.2.1 Fabrication

Stripe tapered waveguides were designed with the aim of creating a device that would couple light into SPPs at one end, propagate these SPPs a short distance, and then focus them into a small area to create strong fields at the tip and in the dielectric substrate through field enhancement. It was hoped that by choosing an appropriate waveguide design, such localised fields could be strong enough to cause optical-field-induced currents in the dielectric [242].

Waveguides were designed to have a grating coupler at one end and a triangular tapered tip at the other. Given the complexity of creating a device with optimal light coupling, propagation length, and focusing properties, several parameters for grating geometry, stripe width and taper angle were chosen. These parameters are indicated in Figure 4.19.
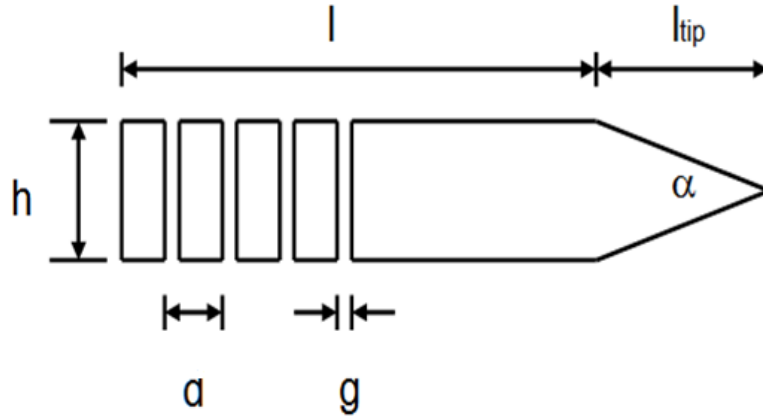
Figure 4.19: A tapered silver stripe waveguide with variable geometrical parameters. Grating periodicity a and lengths l are a constant 1.7 μm and 15 μm, respectively; widths h are 2 or 3 μm; the 2 - 4 grooves have widths g and 200, 400 or 600 nm; and the taper angles α are 30, 60, or 90°, giving tip lengths l_{tip} which vary from 1 to 5.6 μm according to h.

The periodicity of the gratings a was selected using silver as the waveguide material and according to the available wavelength and incident angle of the excitation source (LDH-D-C-405, PicoQuant). From Equation 2.29 and Equation 2.24 with $\lambda = 405$ nm, $\theta = 65°$, $\varepsilon_1 = 1$ and $\varepsilon_2 = $ -4.02 (silver at 405 nm [243]), the required grating periodicity was found to be $a = 1.69$ μm ≈ 1.7 μm.

Stripe widths h were either 2 or 3 μm, allowing moderate mode confinement without compromising the propagation length too greatly. Waveguide lengths l from the base until the

start of the taper were set at a constant 15 µm, so the number of grooves in the grating and the taper length l_{tip} determined the length the SPP must propagate to reach the tip, which varied from $\approx$ 9 - 17 µm. This is within the range of propagation lengths observed for stripe waveguides and nanofocusing structures with widths of a few microns, as outlined in Section 2.4.1. Taper angles of α of 30, 60, and 90° were chosen to investigate the effect on tip enhancement of longer propagation lengths but lower reflections from the taper edges for shallower taper angles and vice versa. The grating couplers consisted of 2 - 4 grooves with groove widths g of 200, 400, and 600 nm, which should produce different SPP generation efficiencies due to the sinusoidal form of the coupling efficiency with groove width. The permutation of three groove widths, three grating lengths, two stripe widths, and three taper angles gave 54 different waveguide geometries, which are shown in Figure 4.20.
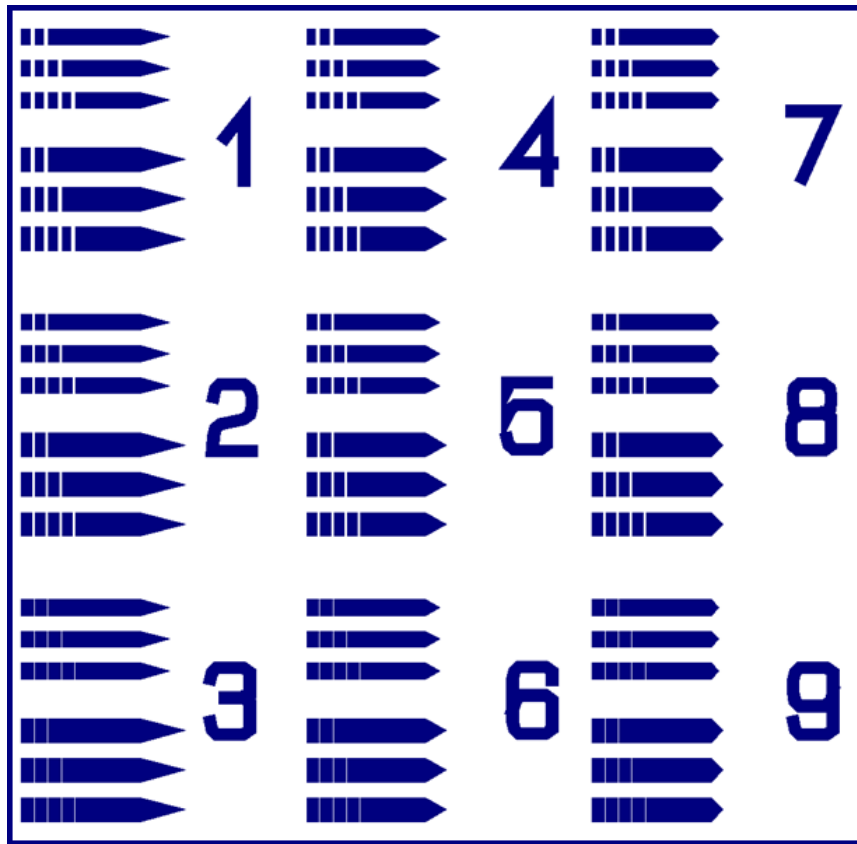
Figure 4.20: Waveguide design created with the lithography software (Raith 150). All waveguides are 15 µm from the base until the start of the taper, with various widths, grating geometries, and taper angles, giving a total of 54 different waveguides in each writefield.

Waveguides were arranged into groups of six, each designated by a numerical marker to locate and reference the group easily. All waveguides in a numbered group had the same taper angle and groove width. The top three waveguides in each group had a width of

2 μm; the bottom three had a width of 3 μm. Each subgroup of three waveguides defined by width had an increasing number of grooves in the positive direction along the *v-axis*. Between groups, groove width increased moving up each column; taper angle decreased moving left-right across each row.

All samples were fabricated using the electron-beam lithography method with a double photoresist layer presented in Chapter 3. During the course of this thesis, three stripe waveguide samples were produced and studied with PEEM. In each case, the design remained the same and the thickness of the silver layer was kept at 40 nm. The first two samples were on a silicon substrate with no adhesion layer; the third (fabricated $\approx$ 16 months later) was on an ITO/glass substrate with a 2 nm chromium adhesion layer. For each sample, many copies of the fields were written on the substrate to test the reliability of the fabrication process. Having multiple copies of the same waveguides would also allow the generation of statistics about the optimal geometry for field enhancement.

SEM images of some of the waveguides from from groups 2, 6, 7 and 8 of one field on one of the silicon samples after lift-off are shown in Figure 4.21. Fabricated waveguide widths were roughly 5% wider than the specified 2 and 3 μm; grating periods were exactly 1.7 μm. The measured groove widths in group 7 were most similar to their design goals — within 1% of the intended 600 nm. Groove widths from group 8 were approximately 5% smaller than designed, and those from group 6 were more than 30% smaller. All the measured taper angles were within a few degrees of their designed values.

4.2.2   PEEM Imaging

After lift-off the samples were imaged with 1P- and 2P-PEEM. The pulsed diode laser had an elliptical beamshape and gave an uneven illumination across the field of view, which was partially compensated in the final images by flatfield correction.

Figure 4.22 compares low-magnification SEM and 1P-PEEM images of the waveguide field imaged in Figure 4.21. Comparisons at higher magnification between selected individual waveguide groups are shown in Figures 4.23 to 4.25. The apparent brightness of the waveguides in the 1P-PEEM image varied considerably, with some waveguides or parts thereof appearing very dark (such as those in group 3) whilst others were very bright (such as the central 3 μm-wide waveguide in group 4). The 1P-PEEM image was taken some weeks after the SEM image, and whilst the sample was mostly kept under vacuum it was transported to the PEEM in air, giving an opportunity for a silver oxide layer to form. The work function of polycrystalline silver is 4.26 eV, which gradually increases with the inclusion of silver oxide [244]. Given that the peak photon energy for the Hg source is quite close to this (4.9 eV), and that the PEEM is sensitive to the first few nanometres of a surface, small differences in the degree of surface oxidation will result in large differences in the electron emission. These differences were seen across isolated parts of individual
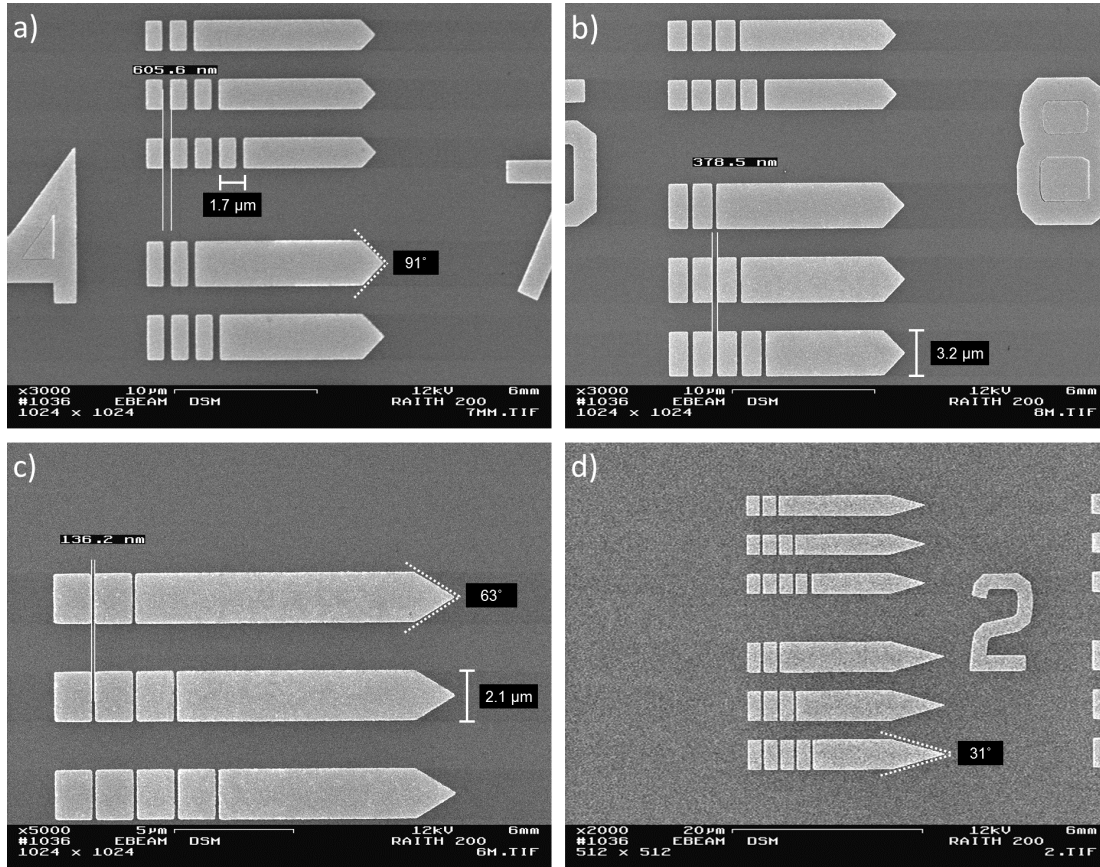
Figure 4.21: SEM images of all waveguides from groups a) 7, b) 8, c) 6 and d) 2 after lift-off. The dimensions of the two waveguide widths are approximately 5% larger than the designated 2 and 3 µm. The measured grating period 1.7 µm matches the designed value. The designed groove widths g were 600, 400, 200, and 400 nm and taper angles α 90, 90, 60, and 30° for groups shown in a)-d).

waveguides from group 4 in Figure 4.24. A couple of the waveguides in groups 3 exhibited only photoemission from blurred regions around the edges of the waveguide, appearing as distorted outlines (see Figure 4.25). Blurry streaks were also seen in waveguides in group 7. These may have been introduced by contaminants after the SEM images were taken. There also appeared to be some surface defects or contaminants which are visible in the SEM images but more prominent in the 1P-PEEM images, such as a dark spot on the uppermost 3 µm-wide waveguide in groups 3 and 9 in Figures 4.25 and 4.23.

For two-photon excitation, orientation of the laser field with respect to the waveguide axis affected the intensity of photoemission along the stripe. Figure 4.26 shows a 1P-PEEM image of the 3 µm-wide waveguides from group 6 in a different field (of which SEM images were not taken), along with two 2P-PEEM images taken with the in-plane polarisation of the laser perpendicular and parallel to the long axes of the waveguides. Only when the laser
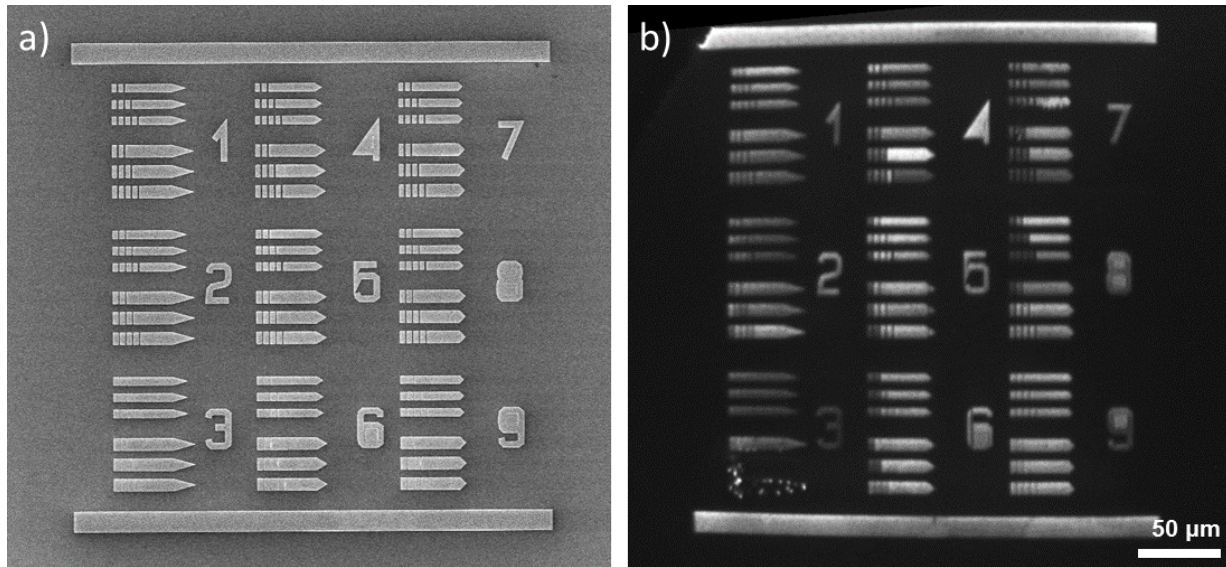
Figure 4.22: a) SEM and b) 1P-PEEM images of one of the waveguide fields. The larger degree of contrast in the 1P-PEEM image stems from the sensitivity to the work function and therefore level of oxidation of the silver surfaces. Note that there is a small amount of barrel distortion in the PEEM image at this magnification.

polarisation is oriented parallel to the grating vector (TM polarisation) can incident light couple to the grating and excite propagating plasmons on the surface of the waveguide. Given the grazing incidence angle, for TM polarisation there is also a significant portion of the incident field oriented along the z-direction. The excitation of localised surface plasmons on roughened regions can occur for any polarisation, as seen for the nanoantennas in Section 4.1. In Figure 4.26b) (TE polarisation), the photoemission intensity from the surface of the waveguide is very low, appearing roughly as bright as the silicon substrate. A faint outline of the waveguides that extends onto the substrate can be seen, likely due to the interference between the incident light and light diffracted from the waveguide edges. In Figure 4.26c) (TM polarisation), the intensity of photoemission from the waveguide surface compared to the substrate is 15-20 fold. The edges of the waveguide and grating appear very bright, and on the surface of the waveguide parallel to the waveguide axis are bands of brighter and darker intensity.

In the near-field studies discussed Section 2.4.1, these bands were indicative of higher-order SPP modes being excited on the waveguide, resulting from interfering reflections of propagating SPPs from the waveguide edges. In 2P-PEEM images, interference can also occur between propagating surface plasmons and the excitation source, which can create complex beating patterns that depend on the orientation of the source and the geometry of the metal boundaries [81, 225, 245, 246]. For SPPs on a planar surface, the interaction between the incident light with in-plane component $\lambda_\parallel$ and SPP waves with wavelength
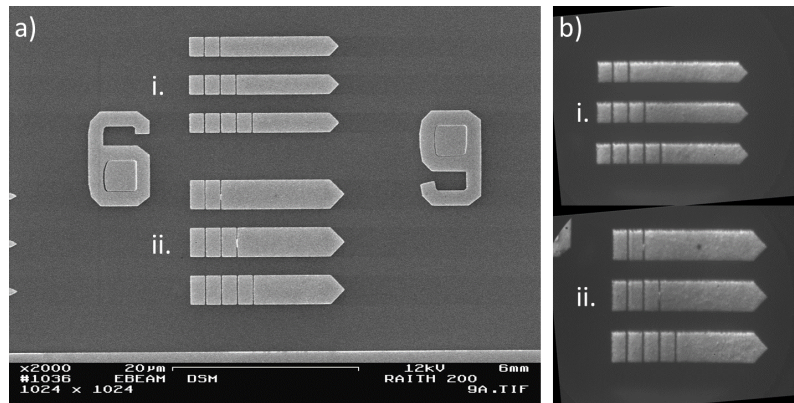
Figure 4.23: a) SEM and b) 1P-PEEM images of the waveguides from group 9. The uppermost and central 3 µm-wide waveguides each have one grating groove which remains partly metallised from incomplete lift-off. The uppermost waveguide also has darkened spots on its surface which is more conspicuous in the 1P-PEEM image.
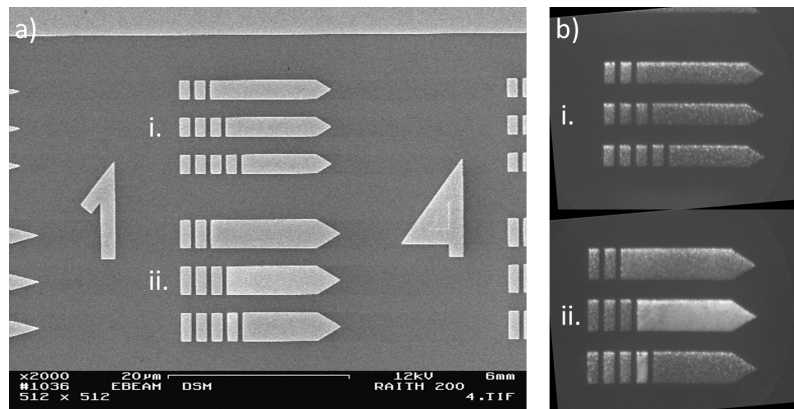
Figure 4.24: a) SEM and b) 1P-PEEM images of the waveguides from group 4. Segments of the 3 µm-wide waveguides show varying photoemission intensities and uniformity, most likely due to differing degrees of surface oxidation.
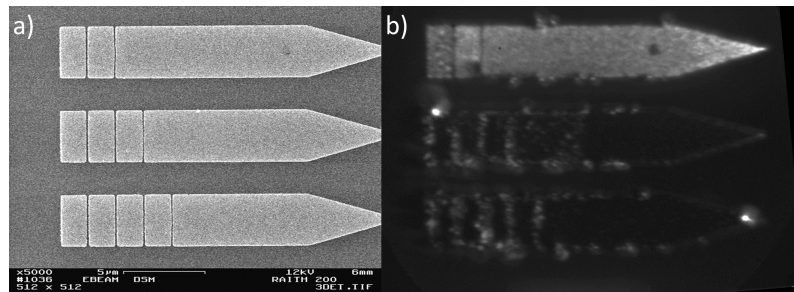
Figure 4.25: a) SEM and b) 1P-PEEM images of the 3 µm-wide waveguides from group 3. The darkened surfaces and blurred photoemission around the edges of the waveguides in the 1P-PEEM image suggests some surface contaminant has been introduced to the sample.
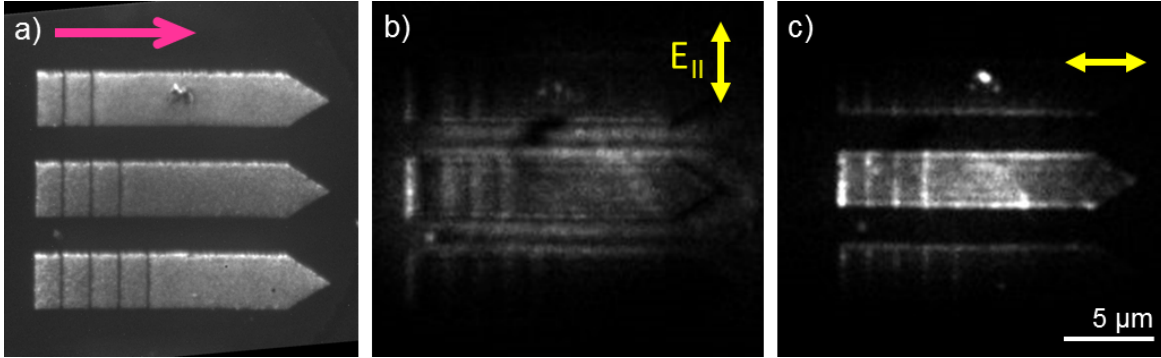
Figure 4.26: a) 1P-PEEM image of the 3 µm-wide waveguides from group 6. b) 2P-PEEM image taken with the in-plane component of the incident electric field (indicated in yellow) perpendicular to the grating vector and the long axes of the waveguides. Photoemission from the silver regions is very low, appearing equally as bright or less than the silicon substrate. The magnification of this image is identical to a) and b), but the waveguide appears larger due to photoemission from the silicon substrate, likely due to interference between the incident light and light diffracted from the waveguide edges. In c), the in-plane electric field of the laser is parallel to the grating vector and SPP modes in the waveguide are excited, indicated by bands of varying intensity parallel to the waveguide axis. The intensity of emission from the silver region is 15-20 fold that from the silicon substrate. Note: the relative brightness of b) has been increased compared to c) for clarity. The direction of the incident illumination is indicated by a pink arrow, and is the same in all three images.

λ_{SPP} creates a beating pattern with a wavelength given by:

$$\lambda_{beat} = \frac{\lambda_{\|}\lambda_{SPP}}{\sqrt{\lambda_{\|}^2 + \lambda_{SPP}^2 - 2\lambda_{\|}\lambda_{SPP}\cos\phi}} \tag{4.2}$$

where ϕ is the angle between the SPP propagation direction and the in-plane light vector. When $\phi = 0°$, the beating wavelength is the same as the spacing for a resonant grating $\lambda_{beat} = 1.69\,\mu$m. If $\phi = 5°$, the beating wavelength reduces to $\lambda_{beat} = 0.33\,\mu$m. Reflections of SPPs from the waveguide edges would contribute non-zero, unknown values for ϕ, making the expected beating wavelength impossible to calculate accurately from Equation 4.2 alone. There are indeed observable variations in the intensity along the long axis of the waveguides in Figures 4.26 and 4.31, but these are difficult to distinguish from hot spots, making measurement of their periodicity impractical.

The orientation of the waveguide can be described by a vector that points from the grating towards the tip. Using this description, the wave vector of incident light in the plane of the waveguide can be oriented parallel or anti-parallel to it. If the sample is rotated 180° around its normal axis so that the incident light is anti-parallel, the efficiency of the grating for exciting SPPs along the waveguide dramatically decreases. For a symmetric grating with light at normal incidence, the coupling efficiency to the two propagation directions is equal; for non-normal incidence, excitation will be favoured in the direction of the light

wave vector. At an oblique incidence angle of 65°, practically all excitation is in this direction. Figure 4.27 shows a 2P-PEEM image of the same waveguide illuminated with the laser oriented parallel and anti-parallel to it. Excitation of SPPs can be seen for the parallel case and are absent in the anti-parallel case.
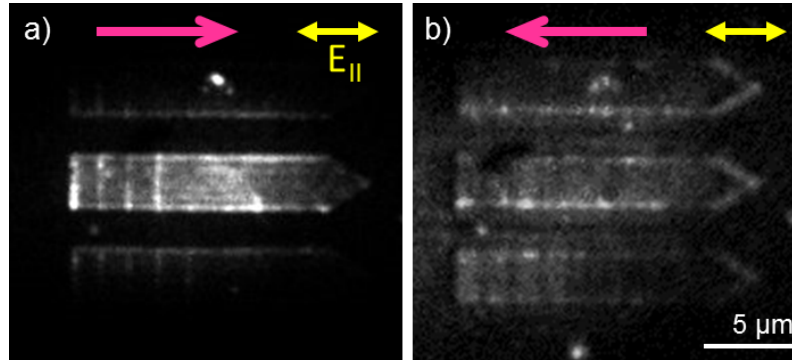
Figure 4.27: 2P-PEEM images of waveguides from group 6 with the laser incident from opposite ends of the waveguide. The direction of the incident laser and its in-plane polarisation are indicated by pink and yellow arrows, respectively. When the wave vector of the incident light is parallel to the waveguide (a), efficient excitation of propagating SPP modes occurs. When the wave vector is oriented anti-parallel to the waveguide (b), no propagating modes can be observed on the surface. Note: the relative brightness of b) has been increased compared to a) for clarity.

To model the interactions between the incident light and SPPs propagating along the waveguide and reflected from the edges, 3D FDTD simulations were used. Since the waveguide structures have dimensions an order of magnitude or so larger than the excitation wavelength, modelling the entire structure with an appropriate mesh size would take a significant amount of computation time. To reduce this, the simulation region contained only the grating (with groove width $200\,\mathrm{nm}$) and part of the waveguide body on a semi-infinite substrate defined by a refractive index $n = 5.45$. A plane wave source was used, with wavelength $405\,\mathrm{nm}$ ($\pm\ 10\,\mathrm{nm}$) injected at an incident angle of 65°. The simulation region was bounded by PML boundaries in the z-directions and Bloch boundaries in the x- and y-directions, with a simulation volume of $18 \times 10 \times 3\,\mathrm{\mu m}$. A 2D frequency-domain field and power monitor at the top surface of the waveguide recorded the electric field intensity $|E(\omega)|^2$ at each point, normalised to the source field intensity. The size of the mesh steps around the grating and waveguide structures was $\approx 12\,\mathrm{nm}$.

Figure 4.28 shows the calculated electric field intensities on at the vacuum/silver interface for 2- and $3\,\mathrm{\mu m}$-wide waveguides when the polarisation of the excited source is perpendicular and parallel to the grating vector. For both widths the fields for TM polarisation are much more intense than for TE polarisation, and the number of bands across the waveguides matches what is seen in the 2P-PEEM images.

These bands are more clearly depicted in Figure 4.29, which shows pseudocolour 2P-PEEM
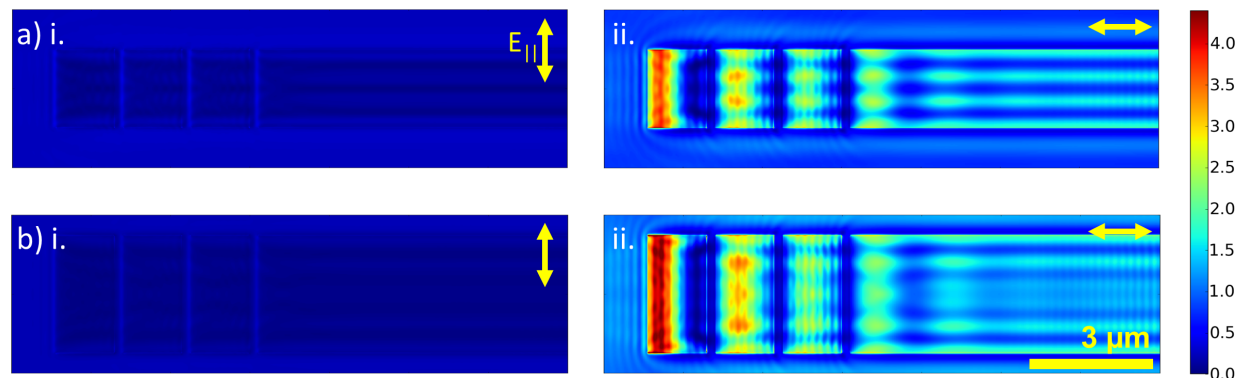
Figure 4.28: Simulated electric field intensities on the grating and part of the surfaces of the a) 2 µm-wide and b) 3 µm-wide waveguide at the vacuum/silver interface when the excitation source is i. TE and ii. TM polarised.

and simulated images of 2- and 3 µm-wide waveguides under TM polarisation, together with intensity profiles taken across the widths of the four waveguides. The intensity is averaged over the length of the waveguides between the end of the grating and the start of the tip.

In the simulated results the most intense fields are found at the left edges of the grating, which is also observed in many of the 2P-PEEM images. A faint beating pattern with a period ≈ 2 µm can be seen along the x-axis on the body of the waveguide, as well as fringes with a period ≈ 200 nm from the interference of forward-propagating waves and those back-reflected from the right-hand edges of the grating or waveguide structure. These latter fringes are too small to be seen or resolved in 2P-PEEM images.

To investigate the beating pattern further, two more simulations were performed with the incidence angle θ at 60 and 70°. Field profiles for these are shown in Figure 4.30. When $\theta = 60°$, the period of the faint beating pattern is ≈ 1.5 µm, lengthening to ≈ 2 µm for $\theta = 65°$ and ≈ 2.3 µm for $\theta = 70°$. The period of the shorter fringes on the gratings does not change significantly.

Figure 4.31 shows some more 2P-PEEM images of various waveguides taken with the excitation source parallel to the grating vector. All waveguides appear bright and exhibit strong edge emission and hot spots, the emission from which is often the strongest photoemission signal in the image. For example, the uppermost waveguide in Figure 4.26c) shows intense emission from the defect in its centre, even though this region is not well illuminated in the image. Areas of the waveguides which — from 1P-PEEM images — appear to have an even coverage of unoxidised silver at the surface display central intensity bands. Examples of such waveguides are shown in Figure 4.31b), c), e), and f). The 2 µm-wide stripes all show two central intensity bands, whilst the 3 µm-wide stripes show three, consistent with simulations. In Figure 4.31e, strong emission can be seen along the edges in the centre of the waveguide, where the edge appears particularly rough. Waveguides with less even surfaces in 1P-PEEM images such as those in Figure 4.31a) and d) not clearly show such
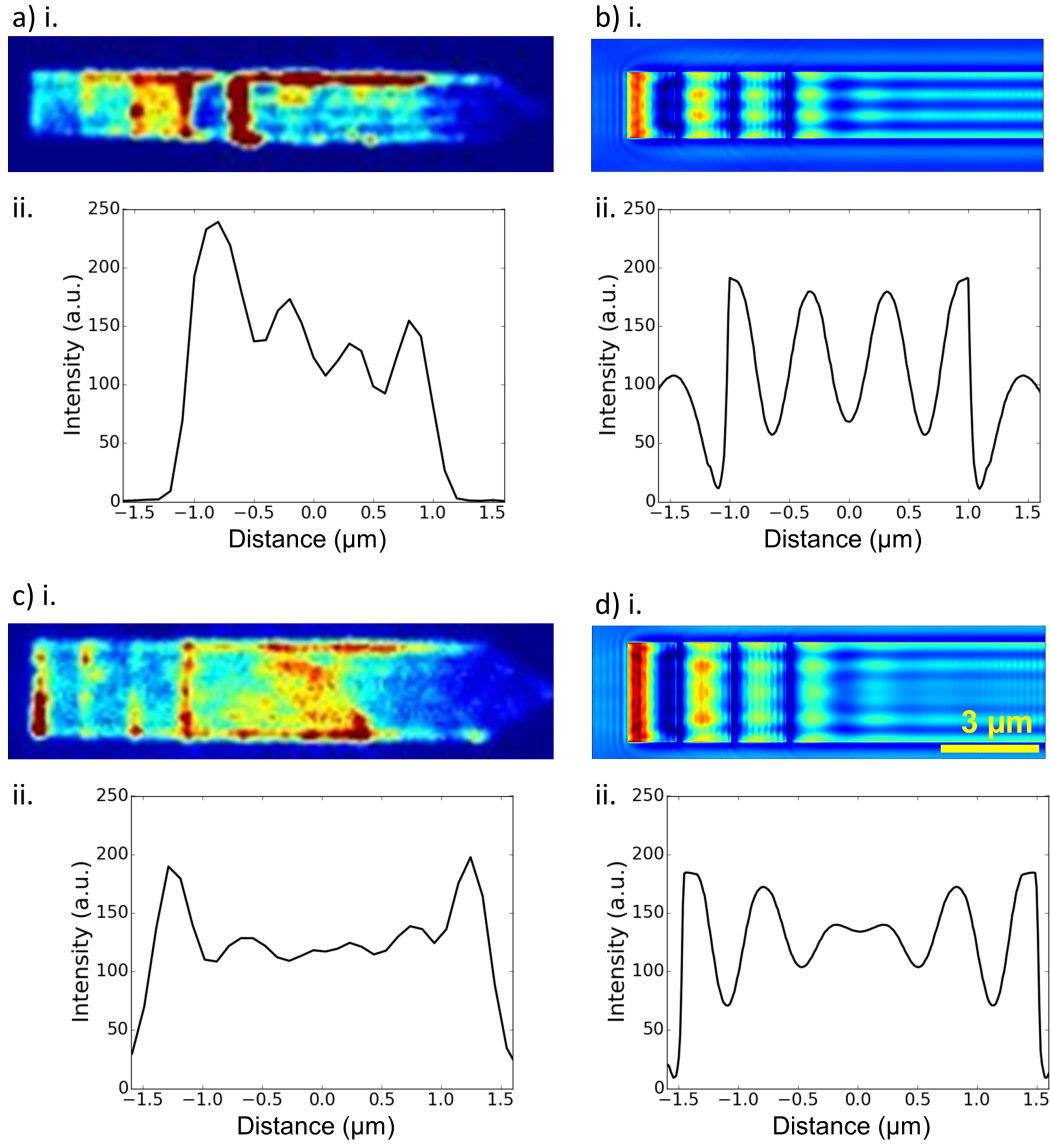
Figure 4.29: a)i. and c)i. pseudocolour 2P-PEEM and b)i. and d)i. simulated images of 2- and 3 μm-wide waveguides under TM polarisation, plus a)-d)ii. intensity profiles across the widths of each waveguide.

bands, but instead show a more randomised spatial distribution of photoemission.

The 1P- and 2P-PEEM images of the waveguides show that there is considerable variation in the surface quality and photoemission intensity between individual waveguides, just as there was between individual nanoantennas in Section 4.1. Even in waveguides that clearly show propagating SPP modes, individual waveguides having the same geometry can display differing, complex combinations of SPPs and LSPs. Any focusing effect that may be present at the taper is challenging to observe, partly due to the hot spots being sources of
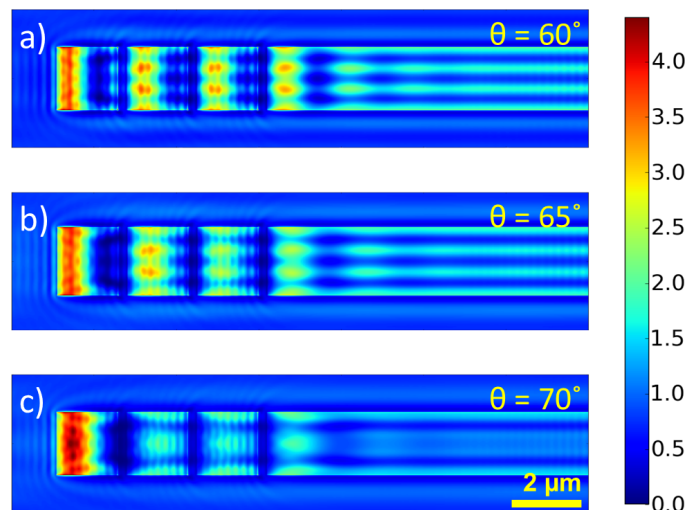
Figure 4.30: Simulated electric field intensities along the surface of the 2 µm-wide waveguide at for incidence angles of a) 60, b) 65, and c) 70°.

radiative loss and thereby reducing propagation length, and partly due to the difficulty in determining whether emission at the tip stems from focused SPPs or localised excitation. The pervasiveness of hot spots on the waveguide surfaces and edges and variability of the surface oxidation over the sample and over time as the sample aged rendered it impossible to reliably correlate plasmonic properties with waveguide geometry. It was therefore decided to monitor the changes in plasmon properties within individual waveguides as the waveguide surface was modified, rather than trying to compare waveguide geometries over the sample.

For in-situ removal of oxide layers from the sample and modification of the waveguide surfaces, the plasma argon ion source (tectra Gen2 Plasma Source) described in Section 3.4.2 was used. By the time the ion source was implemented, the two silver-on-silicon waveguide samples had significantly oxidised. One of the waveguide samples had not previously been imaged in the PEEM, but kept instead in a desiccator under low vacuum for 15 months. This sample was used for the sputtering investigation, as it had been less frequently exposed to air and therefore not as severely oxidised as the other sample. Initial sputtering settings of 300 eV ion energy and an ion dose of $0.4 \times 10^{15}/\text{cm}^2$ were used.

Imaging of this sample after sputtering (Figure 4.32b)) showed an inversion of the relative photoemission intensity from the silver and substrate regions, with the silicon substrate now appearing brighter than the silver waveguides. This can be explained if the sputtering parameters were sufficient to remove the $\approx 1.5\,\text{nm}$ native oxide layer on the substrate, but not on the waveguides. The work functions of silicon, SiO_2, polycrystalline silver, and Ag_2O are 4.6 - 4.85 eV, 5.0 eV, 4.26 eV, and 5.3 eV respectively; the amount that a surface oxide layer increases the work function of a bulk material depends on the layer depth. From the images, it appears that after this initial sputtering dose the work function of the substrate
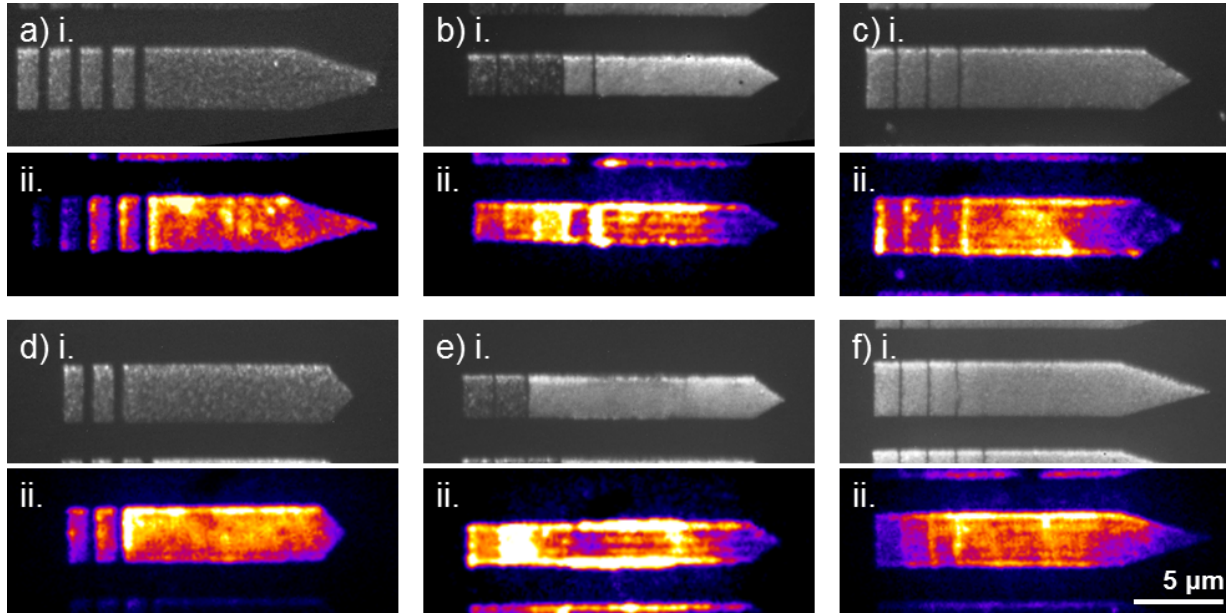
Figure 4.31: i. 1P- and ii. (TM polarised) 2P-PEEM images of waveguides from groups a) 1, b), c) and e) 6, d) 7, and f) 3. The varying silver surface quality can be seen in the 1P-PEEM images — waveguides in a) and d) and parts of the gratings in b) and e) appear dark and uneven, likely indicating some surface oxidation has taken place. Waveguides in b), c), e) and f) which appear to have a more even and unoxidised silver surface display intensity bands across the width of the waveguide, characteristic of higher-order propagating SPP modes. There is strong localised emission from all waveguides, such as that from the roughened edges of the waveguide in e).

became lower relative to that of the surface of the waveguides. A subsequent sputtering dose of $8.0 \times 10^{15}/\mathrm{cm}^2$ at 1000 eV inverted the relative intensities of waveguides and substrate again (Figure 4.32c)), although the surfaces of waveguides now appear uneven, as they did for the previous sample. The process of removing surface layers by sputtering is inherently unstable, as material is removed from concave regions (pits) much more readily than from convex regions. Observed surface irregularities in the sputtered samples are therefore the result of initial surface roughness, which may have worsened over time with oxidation compared to freshly prepared waveguides.

A new sample using the same waveguide design and material on an ITO/glass substrate with a 2 nm chromium adhesion layer was fabricated. The first PEEM images of these waveguides showed little contrast between substrate and waveguide brightness, particularly for 2P-PEEM images. Speckled emission from the substrate was also seen in 2P-PEEM images, as shown in Figure 4.34a). This result is likely a combination of some surface oxidation during sample transfer and residual PMMA on the substrate. In-situ argon ion sputtering at 300 eV ion energy and a dose of $0.3 \times 10^{15}/\mathrm{cm}^2$ improved the waveguide-substrate contrast and removed much of the substrate photoemission. Figures 4.33 and 4.34 compare 1P- and 2P-PEEM images taken a) before and b) after this dose of sputter
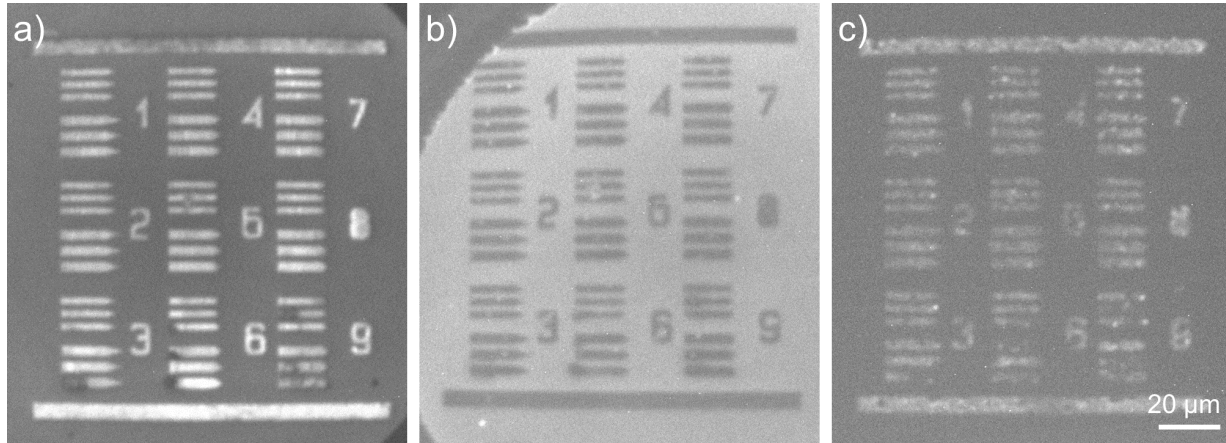
Figure 4.32: 1P-PEEM images of an oxidised waveguide sample on an SiO_2 substrate a) before sputtering, b) after sputtering at an ion energy of 300 eV and dose of $0.4 \times 10^{15}/cm^2$, and c) after sputtering at an ion energy of 1000 eV and dose of $8.0 \times 10^{15}/cm^2$.

cleaning. Waveguides in Figure 4.34b) under TM polarisation appear bright, with visible central intensity bands. In this image, the 3 μm-wide stripes all show two central bands, one less than for the previously imaged sample.
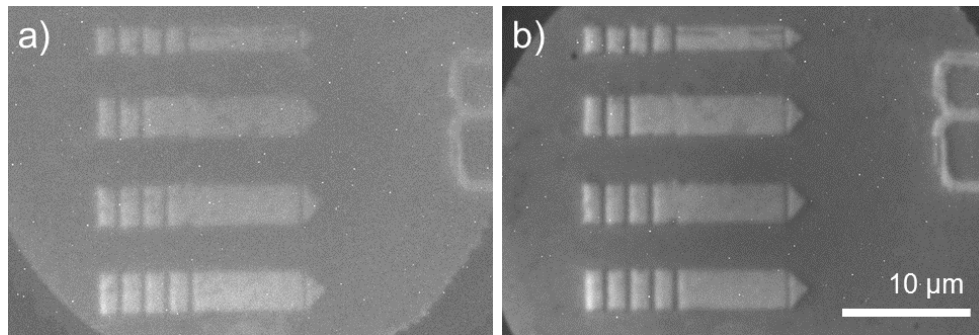
Figure 4.33: 1P-PEEM images of the waveguides in group 8 from the sample on an ITO substrate a) before and b) after sputter cleaning at 300 eV ion energy and a dose of $0.3 \times 10^{15}/cm^2$.

Two-photon PEEM images and intensity profiles taken across the widths of four waveguides — two on silicon and two on ITO — are presented in Figure 4.35. In all cases, the excitation source is TM polarised, and can therefore couple to the grating. For waveguides on the silicon substrate, 3- and 2 μm-wide stripes display three and two central intensity bands respectively. For the waveguides on ITO, the number of central bands drops to two and one in each case.

There are several differences between the two samples which could account for the different number of bands along the stripe. The most apparent difference is the substrate. At an excitation wavelength of 405 nm, the dielectric constants of silicon and ITO are $\varepsilon_{Si} =$
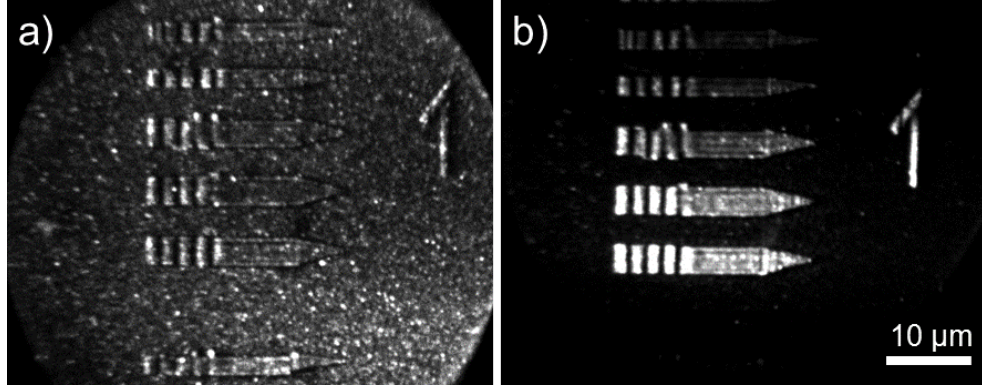
Figure 4.34: 2P-PEEM TM polarised images of the waveguides in group 1 from the sample on an ITO substrate a) before and b) after sputter cleaning at 300 eV ion energy and a dose of $0.3 \times 10^{15}/\text{cm}^2$.
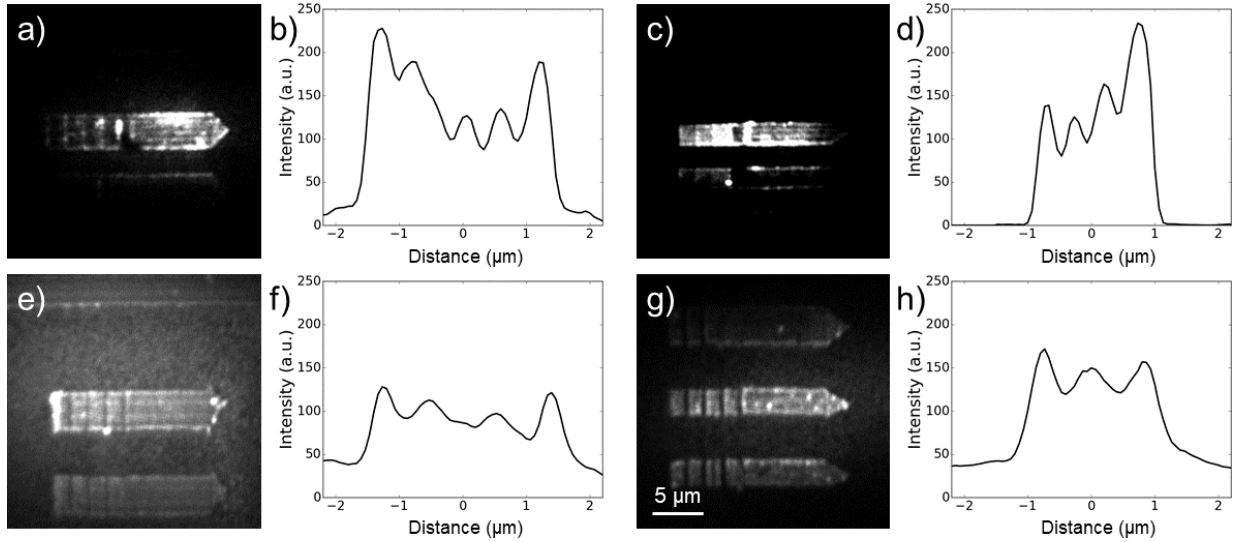
Figure 4.35: (a) and (c) Two photon (3.1 eV) TM polarised PEEM images of two waveguides with different widths (3- and 2 μm) on the silicon substrate; (e) and (g) waveguides with the same geometry on an ITO substrate. The corresponding averaged intensity profiles (b), (d), (f), and (h) through the width of the waveguides are shown to the right of each 2P-PEEM image.

$29.45 + 3.72i$ and $\varepsilon_{ITO} = 4.11 + 0.04i$ [247, 248]. Measured values and calculations of the dielectric constant for silver at this wavelength vary considerably; commonly used values include $\varepsilon_{Ag} = -4.7 + 0.22i$ [69] and $\varepsilon_{Ag} = -4.02 + 0.69i$ [243]. This means that according to Equation 2.26, plasmons cannot exist at the silver/silicon interface, but may do so for the silver/ITO interface. Given the thickness of the silver film, any photoemission from the silver/substrate interface would be suppressed. Therefore it is impossible to know whether propagating modes exist at this interface from these 2P-PEEM images alone.

However, FDTD simulations do not show a change in the number of central bands when

the substrate index is changed. They also do not show fields present at the silver/substrate interface, which remains the case whether the substrate is silicon ($n = 5.45$) or ITO on glass ($n = 1.9$), or if the dielectric constant for silver is set as ($\varepsilon = -4.02 + 0.69i$) or ($\varepsilon = -4.7 + 0.22i$). Figure 4.36 shows the simulated electric field intensity in the y-z plane at $x = 2\,\mu m$ for the $2\,\mu m$-wide waveguide on a substrate with $n = 1.9$ when silver is modelled with a) $\varepsilon_{Ag} = -4.02 + 0.69i$ and b) $\varepsilon_{Ag} = -4.7 + 0.22i$. The shape and relative intensities of fields at the vacuum/silver interface differ for the two dielectric constants, but the number of maxima across the width of the waveguide remains the same.
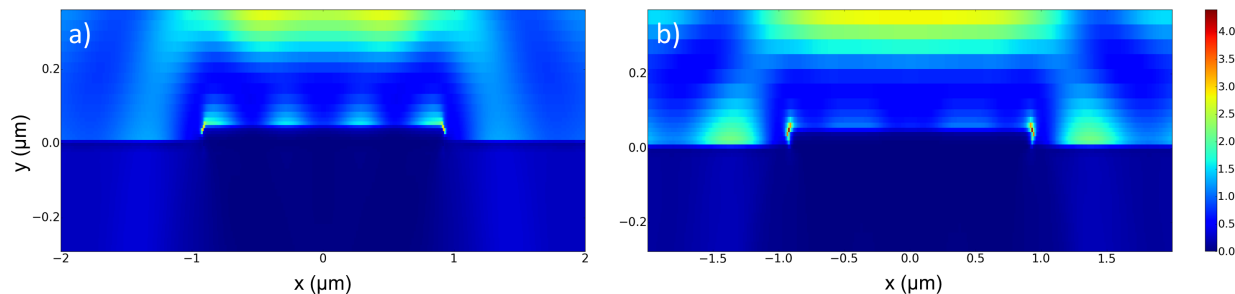
Figure 4.36: Simulated electric field intensities through cross sections of the $2\,\mu m$-wide waveguide on ITO/glass substrates ($n = 1.9$) using a) $\varepsilon_{Ag} = -4.02 + 0.69i$ and b) $\varepsilon_{Ag} = -4.7 + 0.22i$ for the dielectric constants of silver. In both cases, there are two central intensity peaks at the vacuum/silver interface, and none at the silver/ITO interface.

There is also a slight difference in the fabricated widths of the waveguides in the two samples. Waveguides on the silicon substrate were approximately 5% larger than designed, measuring 2.1 and 3.2 µm. No SEM images of the ITO sample were taken after lift-off, but if the fabricated grating period is assumed to be correct, then from PEEM images waveguide widths are approximately 5% smaller than designed, measuring 1.9 and 2.8 µm. Figure 4.37 shows the simulated field intensities along waveguides with widths a) 1.8 µm, b) 1.7 µm, and c) 1.6 µm. As the waveguide is narrowed the two central bands merge into one, with the crossover point occurring somewhere around 1.7 µm. This merge may occur at slightly wider widths in the experiment than what has been simulated, due to assumptions and uncertainties in the dielectric model and illumination geometry. The source in the simulations is approximated by a plane wave, when in experiments it has a 2D Gaussian shape with different beam widths along the x- and y-axes. The incidence angle is also assumed to be exactly 65° from the sample normal and perfectly parallel to the waveguide body, when in reality this has a small dependence on sample mounting in the PEEM and laser alignment. From Equation 4.2 and as seen in Figure 4.30, small changes in the incidence angle can have significant effects on the interactions between incident light and SPPs on the waveguides.

The waveguide sample on ITO was subjected to sputter treatment several more times, with 1P- and 2P-PEEM imaging performed between each run. For subsequent argon ion sputtering, the ion energy was kept at 300 eV and the ion dose increased incrementally by
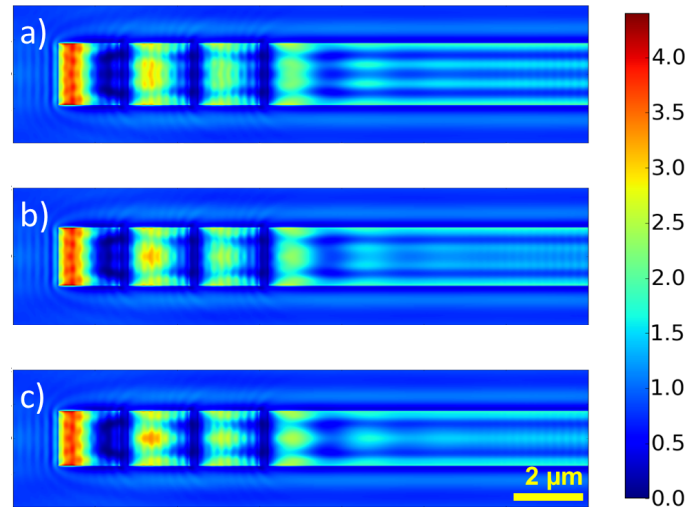
Figure 4.37: Simulated electric field intensities along waveguides with waveguides with widths a) 2.0, b) 1.8, and c) 1.6 µm.

increasing the sputter time. Five sputtering runs were performed on this sample in total; each run up to and including the penultimate run had an observable effect on the intensity of features in the 2P-PEEM images. An overview of all sputtering runs performed on both samples is given in Table 4.1, listed in chronological order. For ion energies of 300 eV the Monte Carlo simulations presented in Chapter 3 calculate a sputter yield of 1.7 Ag atoms/ion. Using this yield and the Ag lattice constant 0.408 nm, the depth of Ag removed per $10^{15}/cm^2$ dose can be estimated at 1.2 nm.

Figure 4.38 shows the effect of sputtering on two of the hot spots on one waveguide. Similar results are seen on other waveguides and on the numerical indicators. The 2P-PEEM images were taken after ion doses of $0.3 \times 10^{15}/cm^2$ and $2.0 \times 10^{15}/cm^2$ respectively. A small area on each was selected and three dimensional surface plots made, normalised to the average background emission from the substrate. Whilst not completely removing the hot spots, the sputtering reduces their two-photon photoemission intensity by a factor of two. Furthermore, the central intensity band becomes more clearly visible. The sputtering also improves the waveguide-substrate contrast from approximately a factor of 2:1 to a factor of 3:1.

In Figure 4.39, 2P-PEEM images of two waveguides after ion doses of $0.3 \times 10^{15}/cm^2$ and $2.0 \times 10^{15}/cm^2$ are shown, along with averaged intensity profiles taken across the width of the stripes. The image brightness has been normalised to the average brightness of the substrate emission. In both cases, the intensities of the central bands have increased with respect to the emission from both the waveguide edges and the substrate. Several hot spots can also be seen on the surface and along the edges of the waveguides which, as in Figure 4.38, are reduced in intensity by a factor of two after sputtering.

Sample (Substrate)	Ion Energy (eV)	Ion Dose ($\times 10^{15}/\mathrm{cm}^2$)	Effect
Silicon (old)	300	0.4	Removal of substrate native oxide layer
Silicon (old)	1000	8.0	Partial removal of silver layer
ITO/glass	300	0.3	Removal of surface oxidation and contamination
ITO/glass	300	0.8	Hot spot and edge intensity reduced
ITO/glass	300	1.2	(As above)
ITO/glass	300	2.0	(As above)
ITO/glass	300	3.8	No measurable change

Table 4.1: Overview of the sputter process performed on silver waveguides on silicon and ITO substrates.

4.3   Conclusion and Outlook

Two different types of plasmonic devices with a range of geometries were fabricated and investigated in the PEEM. For both nanoantennas and stripe waveguides, the surface quality has a significant affect on photoemission from the silver, especially in the case of 2P-PEEM imaging where the photoemission is greatly augmented by the presence of localised and propagating plasmonic fields.

Two-photon photoemission from double bowtie and ellipse nanoantennas was dominated by hot spots from areas of surface roughness, which could be selectively excited by rotating the polarisation of the excitation laser. Due to these hot spots, it was difficult to draw conclusions about the effect of the designed antenna geometry and size on the field enhancement from these images alone.

FDTD simulations showed that, for perfectly smooth nanoantennas, the strongest field enhancement occurs under TM polarisation, and increases with decreasing antenna size. Bowties and ellipses produced similar levels of enhancement. For bowties, the strongest fields occur at the vertices, in particular the vertex that points in the direction of the incident light vector, due to the excitation of SPPs at the left edges of the nanostructures which propagate towards the right. To compare the near fields of these idealised nanoan-
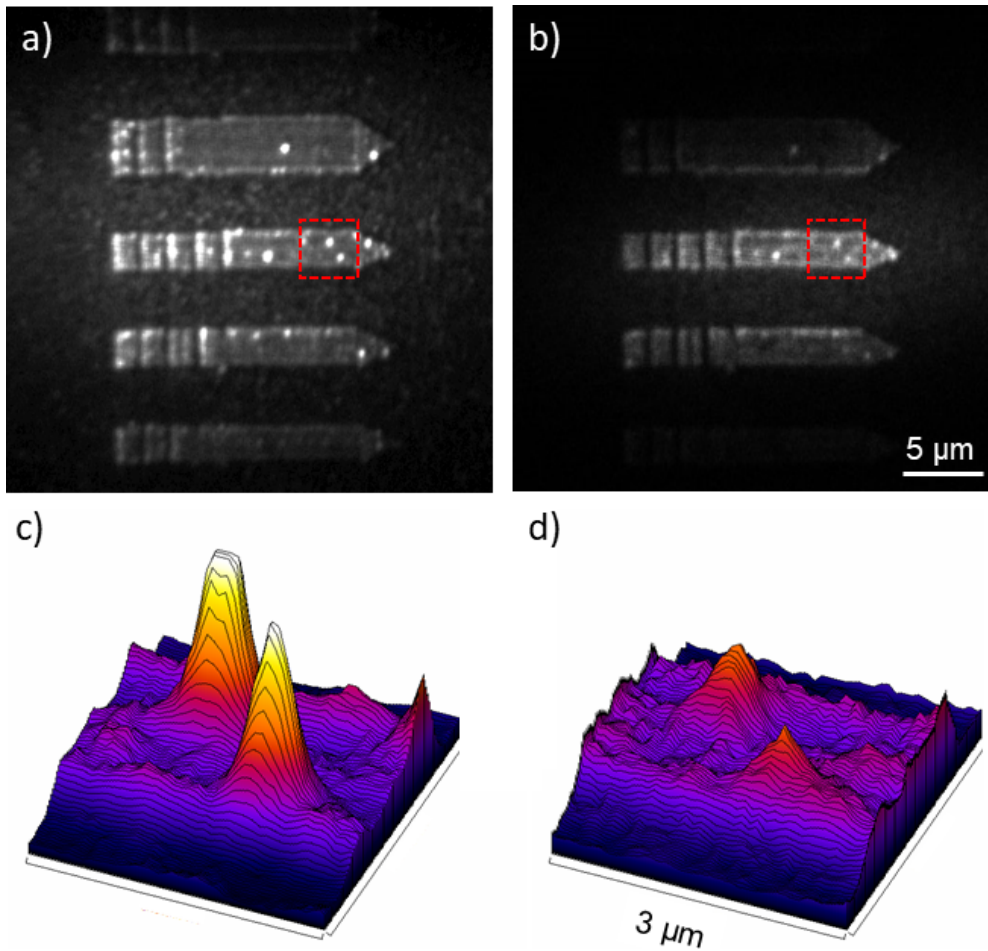
Figure 4.38: (a) and (b) 2P-PEEM images of a silver waveguide on ITO at ion doses of (a) $0.3 \times 10^{15}/\text{cm}^2$ and (b) $2.0 \times 10^{15}/\text{cm}^2$ with ion energies of 300 eV; (c) and (d) surface intensity plots of the photoemission from an area on the sample containing two hot spots, marked by a red box. The intensity has been normalised to that of the substrate.

tennas with the experimentally-fabricated ones, the observable photoemission from surface roughness hot spots was lessened by creating images with the TE polarisation subtracted from the TM polarisation. These images also showed field enhancement at the edges and vertices of the nanoantennas.

Simulations were used to show that the field intensity at the vertices of bowtie nanoantennas depends on the size of the gap between antenna halves and its radius of curvature. A monochromatic light source was used, so shifts in the resonance wavelength with gap size were not considered. For double ellipse nanoantennas, strong enhancement can also occur across small gaps ($\approx 10\,\text{nm}$) between the edges of adjacent ellipses. Simulations with added surface roughness showed that for values equal to or greater than $\approx 3\,\text{nm}$ RMS, the resulting field profile is governed by the surface morphology more than the geometry of the
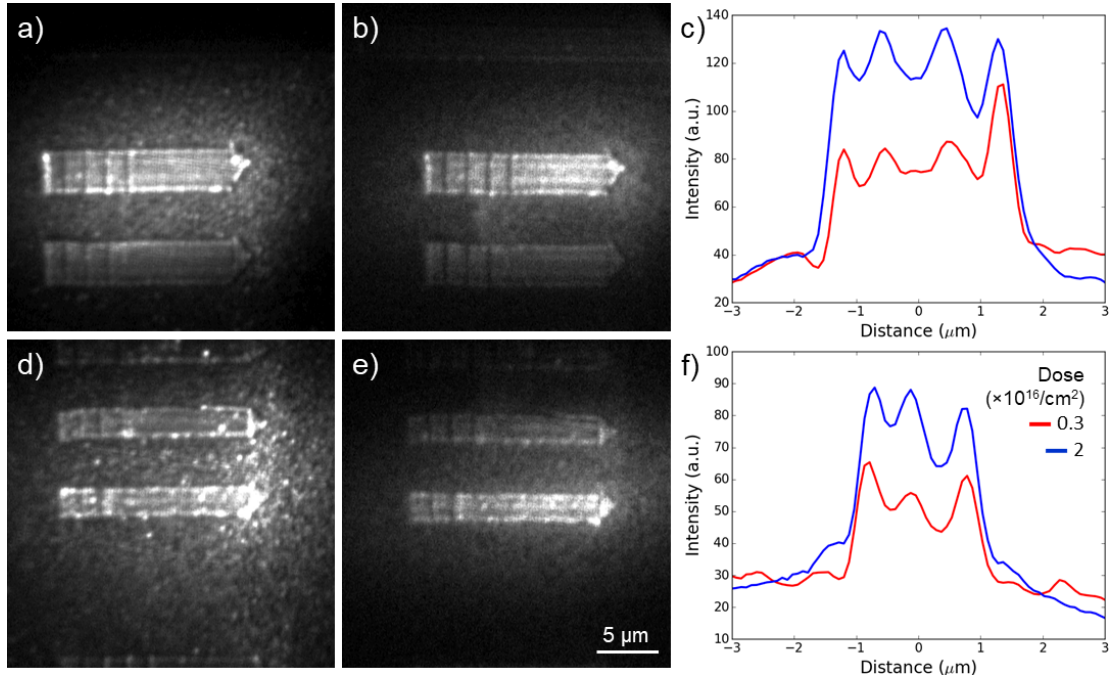
Figure 4.39: 2P-PEEM images of waveguides after (a) and (d) $0.3 \times 10^{15}/cm^2$ and (b) and (e) $2.0 \times 10^{15}/cm^2$ total ion dose at 300 eV; (c) and (f) intensity plots across the width of the waveguide, averaged over the length. The ratio of the intensity of the central peak to both that of the substrate and edge diffraction has increased with increasing dose.

underlying nanoantenna.

Stripe waveguides were shown to support propagating SPP modes when the incoupling grating was illuminated with TM polarised light, as designed. For waveguides where the surface appeared to have an even coverage of silver, bands of high photoemission intensity could be seen along the long axis of the waveguide, resulting from the complex interference between propagating SPPs and the excitation source. These bands were reproduced in FDTD simulations. More randomised photoemission was seen in regions where the waveguide edges were visibly rough, or the surface appeared partially oxidised. Treatment of the sample surface with low-energy argon ion sputtering was shown to reduce the photoemission from hot spots whilst improving the contrast between the intensity bands on the waveguide surface and the substrate. This improvement saturated at ion doses above $2.0 \times 10^{15}/cm^2$. There is a large space for investigation concerning parameters for sputter treatment which was not explored in this thesis, including choice of ion species, use of ion clusters, and combination with annealing.

Chapter 5

Extraordinary Optical Transmission

This chapter describes the simulation and experimental implementation of pump-probe transmission experiments on arrays of nanoholes in gold films, using ultrashort pulses centred in the near infrared for both beams. The aim was to examine the effect of the fields induced by an initial ultrashort pulse on the transmission of a second ultrashort pulse through the array, and gauge whether any resulting effect could be used for ultrafast switching.

To construct arrays which maximise surface fields whilst minimising losses, the array material should have a large real absolute value of the dielectric constant $|Re(\varepsilon)|$ and a small value of the imaginary part $|Im(\varepsilon)|$. This makes silver most suitable for visible wavelengths, and gold most suitable for wavelengths above $\approx 600\,\mathrm{nm}$. Gold also has the advantage of being more oxidation resistant than silver, so it has been used for all the arrays in this thesis, which are studied in air.

Several fabrication methods were available for the experiments — namely FIB, EBL, and photolithography. The focused ion beam lithography process has fewer steps and a higher resolution but is rather slow and less suited to large-scale structures than the latter two [14]. Both FIB and EBL were trialled, but ultimately samples were fabricated using EBL with a negative photoresist to create many arrays on the same film within the available time frame.

5.1   Simulations

5.1.1   Setup

Simulations of the extraordinary transmission through nanohole arrays were performed using a commercial-grade simulator based on the finite-difference time-domain (FDTD) method [241]. Details of this method can be found in the Appendix.

A simple schematic of the simulation layout is shown in Figure 5.1. The simulation region was centred on a unit cell of the two-dimensional hole array in the xy plane, which was arranged as either a square or hexagonal lattice. Unit cells for each of these lattice types are shown in Figure 5.2. Periodic boundaries in the x- and y-directions defined the lattice constant a. The boundaries in the z-direction consisted of perfectly matched layers placed 500 nm from each surface of the film, with the distance, number of layers, and absorption properties chosen following a series of convergence tests, to ensure that boundaries did not introduce significant errors into the simulation. Convergence testing was also used to select the size of the mesh steps throughout the simulation and around the holes. It was found that a mesh accuracy niveau of 4 and a mesh step around the holes of 1.5 nm provided an error of less than 0.002 without compromising simulation time [249]. In the case of parameter scans, this mesh step was increased to 4 nm to reduce the simulation time.

Standard values for the thickness h, the hole diameter d, and the lattice constant a were defined based on typical values used in other EOT experiments, expected fabrication capabilities, and desired wavelengths of the transmission resonances. These parameters could then be varied to investigate their influence on the transmission. A thickness h of 200 nm ensured that the film was perfectly opaque in the absence of holes, but was sufficiently thin to allow EOT. Following successful fabrication of the experimental samples, simulations were also run with film thicknesses of 120 nm with and without a 2 nm titanium seed layer. The film was placed on a semi-infinite silicon nitride (Si_3N_4) substrate to reduce the scattering and reflections that were found to be artificially introduced by a substrate of finite thickness. The dielectric functions of gold and Si_3N_4 were taken from References [69] and [250], respectively.

The focal spot of the oscillator beam in the experimental setup was approximately one to two orders of magnitude larger than the lattice constant of the array, so the source fields could be regarded as uniform. Plane wave sources were therefore used, polarised along the x-axis and propagating in the negative z-direction. The sources had a central wavelength of 760 nm with a bandwidth of 300 nm, and a pulse length of 5 fs. The first pulse was always injected 20 fs after the beginning of the simulation to ensure the entire pulse envelope fit comfortably within the simulation; the second was injected at a variable time delay Δt after the first. The total simulation time was 300 fs.
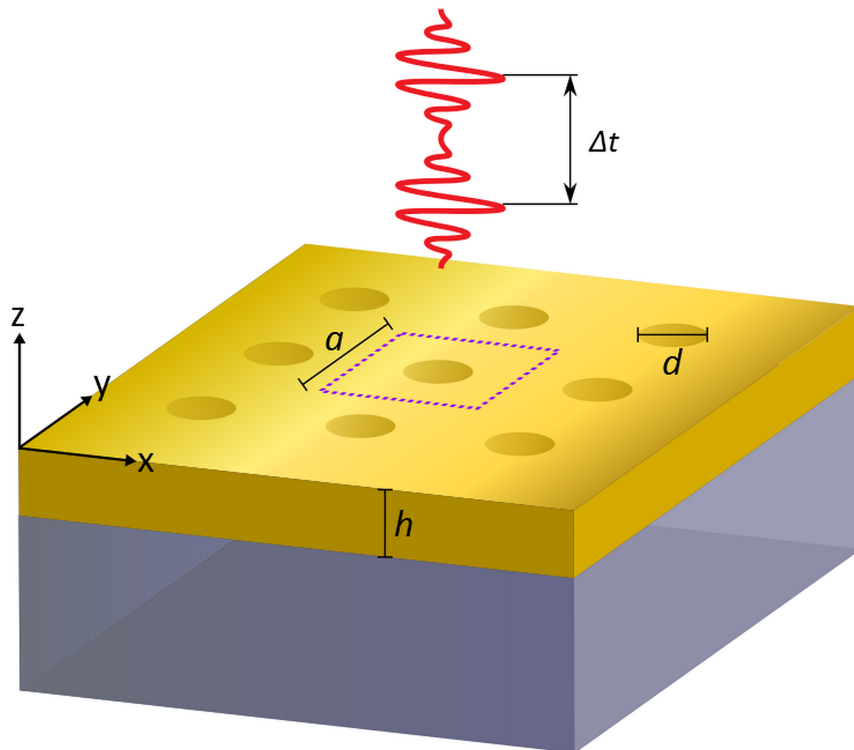
Figure 5.1: Setup of the FDTD simulation for gold nanohole array transmission. The gold film of thickness h is perforated with an array of holes with diameter d arranged in either a square or hexagonal lattice. The simulation region is defined by a unit cell of this array with lattice constant a. Two 5 fs pulses separated in time by a delay Δt are injected at normal incidence to the air/gold interface. The film sits on a semi-infinite Si_3N_4 substrate.

The electric fields and transmitted and reflected spectra were recorded by time- and frequency-domain monitors. Time-domain monitors — placed at a point in the centre of the hole, at mid-points on the metal/substrate interfaces, and as planes on the interfaces — returned the electric fields passing through these points and planes as a function of time. Two planar frequency domain power monitors were placed on either side of the metal film, parallel to and 300 nm from the interfaces. These recorded the electric fields passing through the plane in the time domain and carried out Fourier transforms to return the transmitted and reflected spectra in the frequency domain. These monitors normalised the transmitted power to the power of the source pulse, thereby returning the impulse response of the system.

To observe the influence of the plasmonic fields on the transmission of an individual pulse, the measured pulses must be separable. This is difficult to implement spatially in the simulation given the periodic boundary conditions, so instead the pulses were separated temporally. This was achieved by applying an apodisation window, to ensure only the fields from the second pulse were included in the Fourier transform used to calculate the
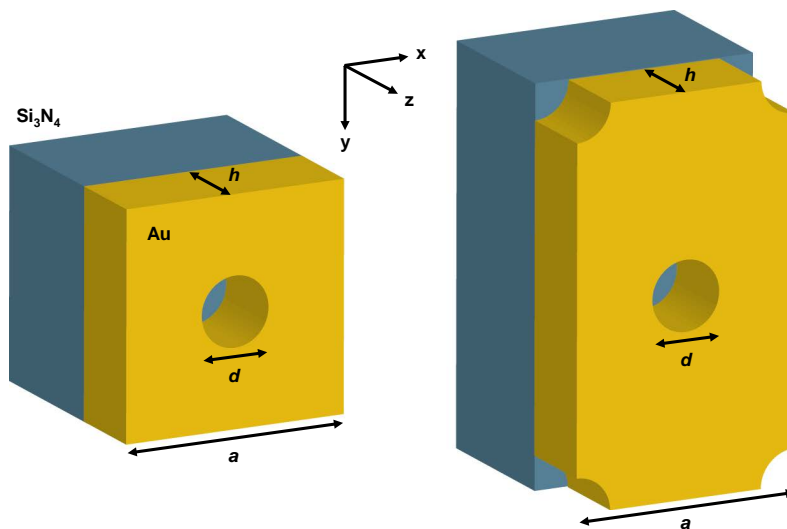
Figure 5.2: Unit cells of the two hole array types, which define the simulation boundaries in the xy plane.

transmitted spectra. These fields acquire the signature of the plasmonic fields induced by the first pulse; the amount of overlap is determined by the time delay.

5.1.2   Single-Pulse Results

Figures 5.3 - 5.5 show the transmission spectra through 200 nm-thick gold hole arrays with square and hexagonal lattices, respectively. The lattice constant in the first two cases is 650 nm; it is 750 nm in the third case. The square lattice displays two resonances within the excitation band at 692 nm and 756 nm, while the hexagonal lattices display three at 629 nm, 685 nm, and 761 nm for $a = 650$ nm and 695 nm, 753 nm, and 849 nm for $a = 750$ nm.

For a given lattice geometry and dielectric environment, Equations 2.49 and 2.50 can be used to estimate the location of the array resonances. From [69] and [250], at a wavelength of 760 nm, $\varepsilon_m = -20.95 + 1.29i$ and $\varepsilon_d = 4$ for the Si_3N_4 substrate, and $\varepsilon_d = 1$ for air. The low-order peaks that lie within the excitation bandwidth for the square array are therefore predicted by Equation 2.49 at $\lambda \approx 670$ nm ($p, q = \pm 1, 0$) for the air/gold interface and $\lambda \approx 740$ nm ($p, q = \pm 2, 0$) for the gold/substrate interface. These wavelengths are within 30 nm of the peaks seen in the spectra, consistent with previous approximations using this method [152]. For the hexagonal array with $a = 650$ nm, Equation 2.50 predicts peaks at $\lambda \approx 580$ nm ($p, q = \pm 1, 0$) for the air/gold interface and $\lambda \approx 645$ nm ($p, q = \pm 2, 0$) and $\lambda \approx 745$ nm ($p, q = \pm 1, 1$) for the gold/substrate interface. For $a = 750$ nm, Equation 2.50 predicts peaks at $\lambda \approx 665$ nm ($p, q = \pm 1, 0$) for the air/gold interface and $\lambda \approx 740$ nm ($p, q = \pm 2, 0$) and $\lambda \approx 855$ nm ($p, q = \pm 1, 1$) for the gold/substrate interface. These results
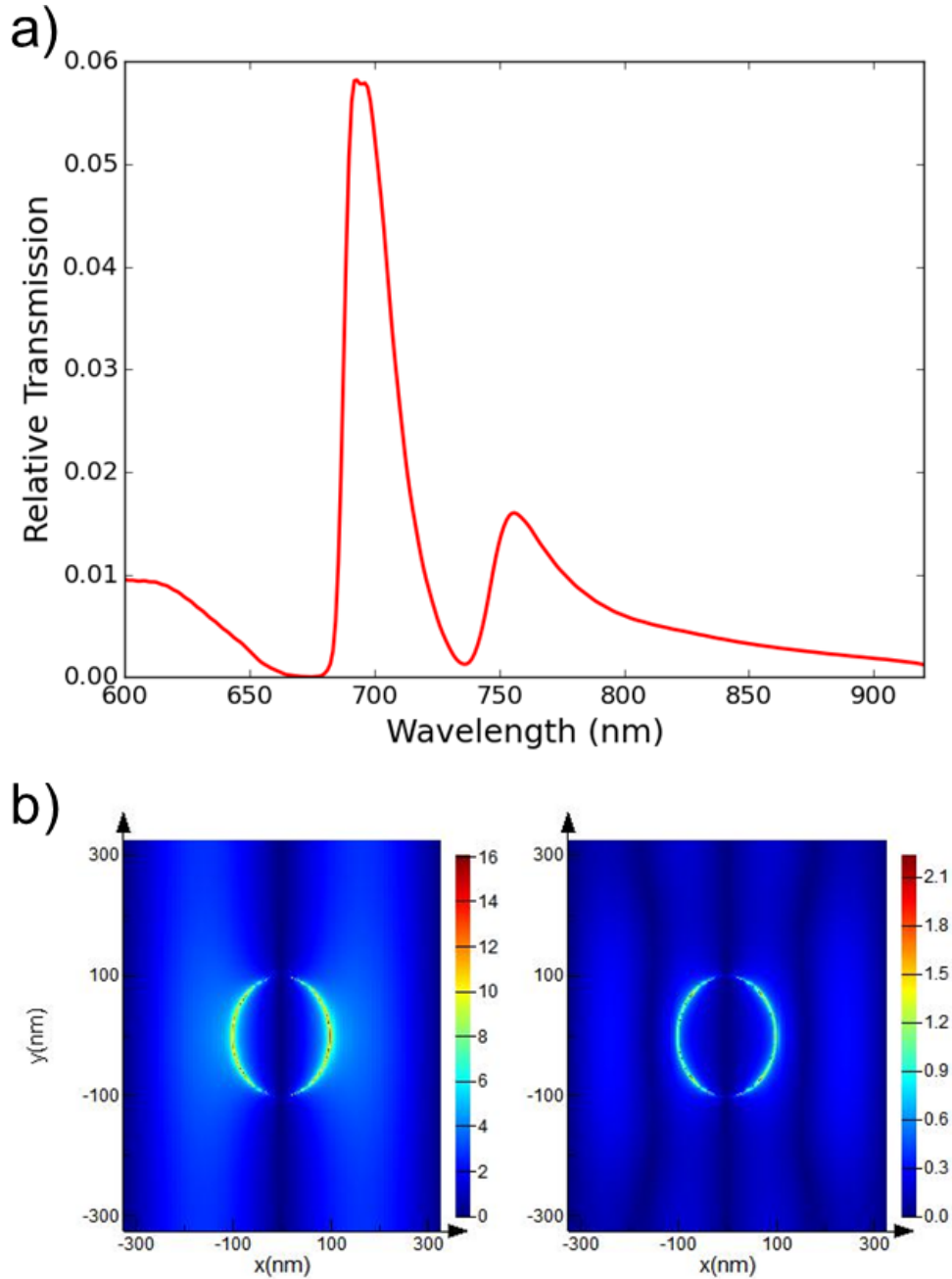
Figure 5.3: a) Transmission spectrum of a square array with $a = 650\,\text{nm}$. The two peaks at $692\,\text{nm}$ and $756\,\text{nm}$ correspond to resonances at the air/gold and gold/substrate interfaces, respectively. b) The absolute values of the time-averaged electric field profiles at the air/gold (left) and gold/substrate (right) interfaces for these peak wavelengths.
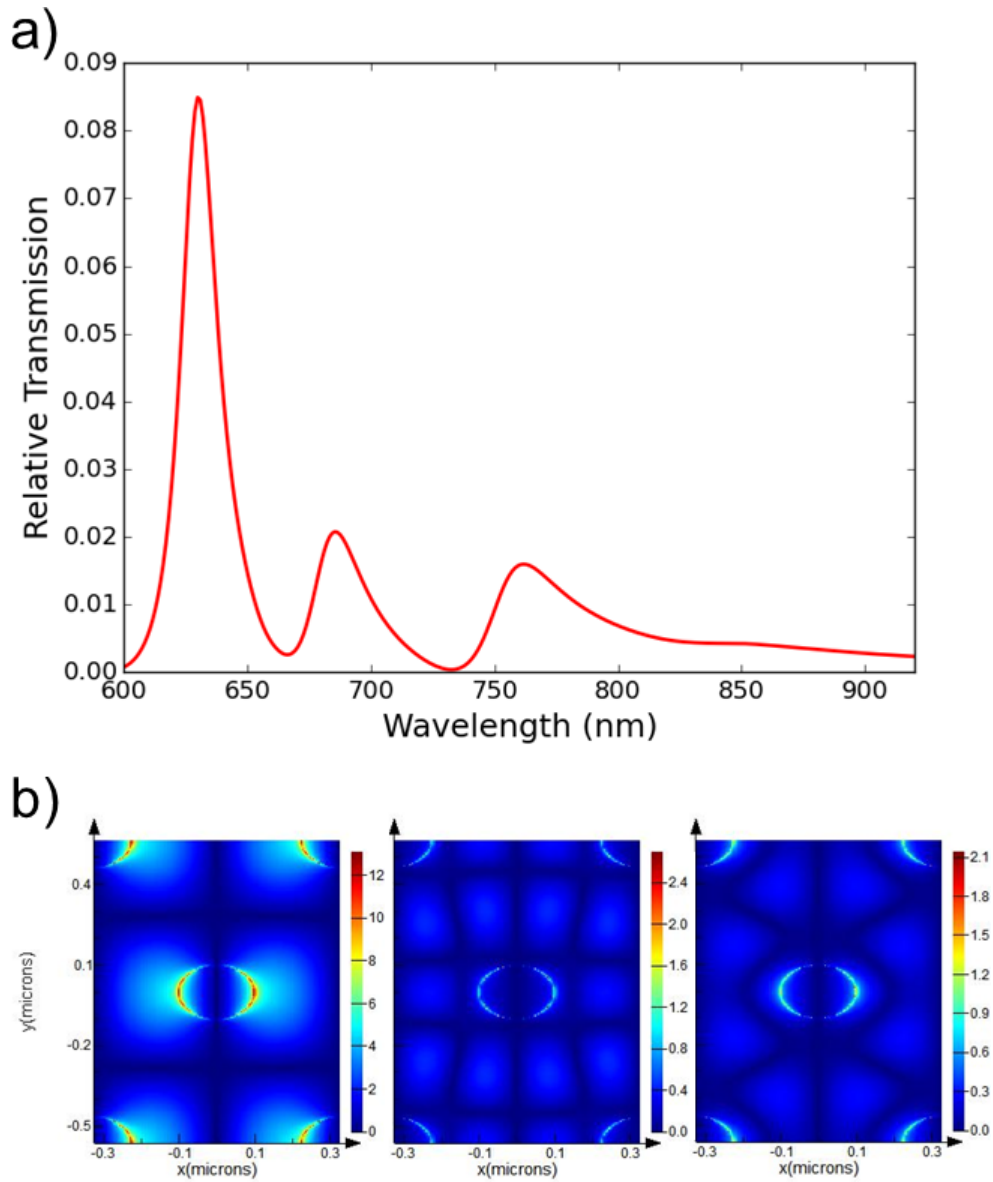
Figure 5.4: a) Transmission spectrum of a hexagonal array with $a = 650\,\text{nm}$. The three peaks at $629\,\text{nm}$, $685\,\text{nm}$, and $761\,\text{nm}$ correspond to a resonance at the air/gold interface and two resonances at the and gold/substrate interface, respectively. b) The absolute values of the time-averaged electric field profiles at the air/gold (left) and gold/substrate (middle, right) interfaces for these peak wavelengths.
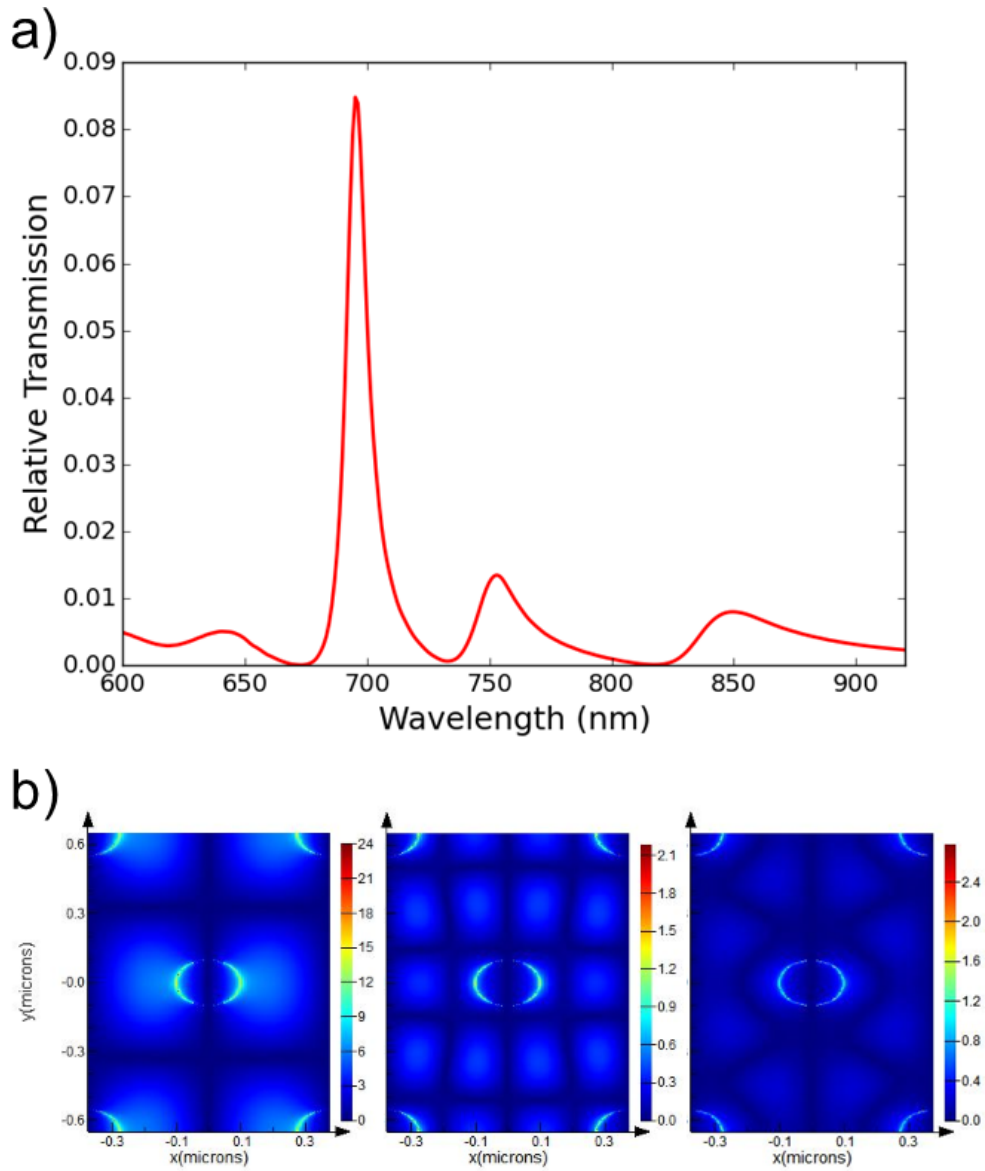
Figure 5.5: a) Transmission spectrum of a hexagonal array with $a = 750\,\text{nm}$. The three peaks at $695\,\text{nm}$, $753\,\text{nm}$, and $849\,\text{nm}$ correspond to a resonance at the air/gold interface and two resonances at the gold/substrate interface, respectively. b) The absolute values of the time-averaged electric field profiles at the air/gold (left) and gold/substrate (middle, right) interfaces for these peak wavelengths.

		Peak (nm)		
		air/Au $(p, q = \pm 1, 0)$	Au/Si_3N_4 $(p, q = \pm 2, 0)$	Au/Si_3N_4 $(p, q = \pm 1, 1)$
$a = 650\,\mathrm{nm}$, square	Eqn 2.49	666	743	-
	FDTD	692	756	-
$a = 650\,\mathrm{nm}$, hexagonal	Eqn 2.50	577	643	743
	FDTD	629	685	761
$a = 750\,\mathrm{nm}$, hexagonal	Eqn 2.50	666	742	857
	FDTD	695	753	849

Table 5.1: Comparison of resonance peak wavelengths predicted by the FDTD simulation and Equations 2.49 and 2.50

are summarised in Table 5.1. It has been shown that, for lattice periods below $700\,\mathrm{nm}$, the predictions of Equation 2.50 diverge faster from FDTD theory than those of Equation 2.49 [173].

The correlation of these peaks with enhanced fields at given interfaces is confirmed via planar frequency-domain field monitors. Profiles of the time-averaged total electric fields at the resonant frequencies are shown below each transmission spectra. In each case, the largest resonance is associated with strong fields around the hole and at the air/gold interface, shown on the left; the other resonances are associated with strong fields at the gold/substrate interface, shown to the right. For the square array, the fields are strongly directional along the polarisation axis and agree with the results of Equation 2.49, namely that the mode excited at the air/gold interface $(p, q = \pm 1, 0)$ is a lower-order mode than that excited at the gold/substrate interface $(p, q = \pm 2, 0)$. The fields for the hexagonal array are more complex, displaying multiple symmetry axes. Given that the excitation source is x-polarised, these off-axis modes are caused by diffraction of the incident light at the nanoholes.

Figures 5.6 to 5.9 show the effects of changing several array parameters on the static transmission spectra. In this case, the standard (basis) array was hexagonal with $a = 672\,\mathrm{nm}$, $h = 120\,\mathrm{nm}$, and $d = 200\,\mathrm{nm}$. As expected, larger hole sizes and thinner films increase the transmission, whilst smaller holes and thicker films decrease it. The first peak displays a prominent redshift with increasing hole size. Changing the film thickness changes the relative heights of the resonant peaks, with the longer-wavelength peaks becoming more prominent with decreasing thickness. Additional results for a square film can be found in Reference [249]. Figure 5.8 shows that adding a thin layer of titanium as a seed layer has

a similar effect to increasing the film thickness — it decreases the total transmission and suppresses the longer-wavelength resonances. One possible effect of having an imperfect film is shown in Figure 5.9. For this simulation, one of the holes in the unit cell was removed, one hole had a larger radius ($d = 250$ nm), and one hole only penetrated 60 nm into the film. The resonant peaks have broadened and become slightly redshifted; increased linewidths correspond to shorter SPP lifetimes. The boundary conditions of the simulation are still periodic so this "flawed" array retains a high degree of symmetry. For a real array containing flaws, the expected broadening would be much higher.

5.1.3 Double-Pulse Results

The evolution of the fields at several points on the arrays is shown in Figures 5.10 and 5.11. The time-domain monitors at (a) record the x-component of the electric field in the centre of the holes for time delays of 0 and 20 fs. At zero delay, the fields of the incident pulse — which remain nearly unperturbed for the square array — are followed by a long, decaying tail. This decay is evident of the plasmonically resonant nature of the cylindrical hole [196]. For a 20 fs pulse delay, the fields of the individual pulses are seen, but the tail retains the same shape. Both arrays display a small degree of ringing, evidence of oscillating energy transfer between the two interfaces. This beating pattern is much stronger for the z-components of the fields midway between the holes on the gold/substrate interface at (b) and (c). Since the incident pulses contain no z-components, these fields are due purely to plasmon interactions at the surface, and the beating therefore originates from the interference of plasmons propagating from different holes. The amplitude and non-stationary frequency of this beating is modified by the introduction of a delay between the pulses.

Spectrograms for various array geometries were obtained by sweeping the delay between the first and second pulses. The effect of the second pulse on the transmission spectra is complex, and encompasses processes which transpire over a range of timescales, so the step between adjacent delays has to be quite small and the final delay rather large. This requires a significant amount of computation time, so the response of the spectrogram to just a few array parameters was investigated. It was seen that in both the square and hexagonal arrays, peaks corresponding to the same mode order behaved comparably with changing parameters. Since the hexagonal arrays display one more peak ($p, q = \pm 1, 1$), only these spectrograms have been analysed in detail. A few examples are shown in Figures 5.12 and 5.13; the remaining spectrograms and those for a square array can be found in the Appendix. Here, the standard array has parameters $a = 650$ nm, $h = 200$ nm, and $d = 200$ nm.

A conspicuous feature in each spectrogram is that the intensity of each transmission peak as a function of delay oscillates between a local maxima and minima within a few femtosec-
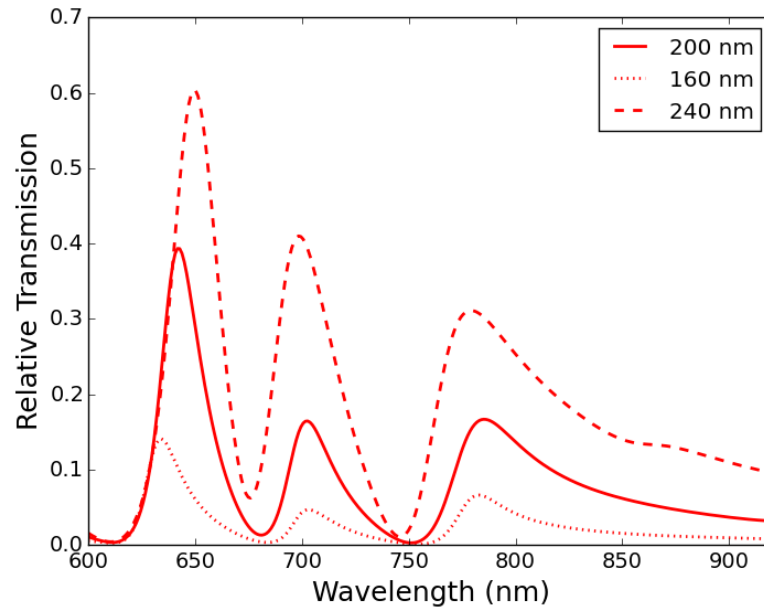
Figure 5.6: The relative transmission spectra for various hole sizes d.
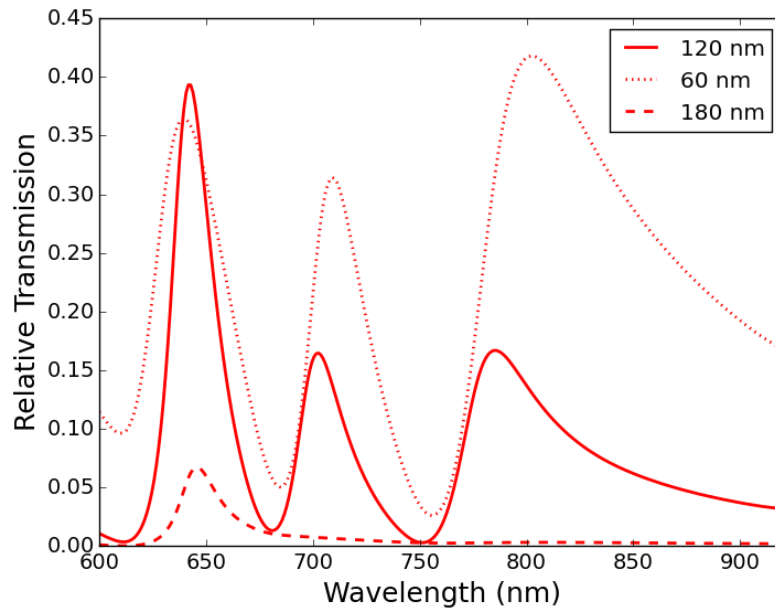
Figure 5.7: The relative transmission spectra for various thicknesses h.
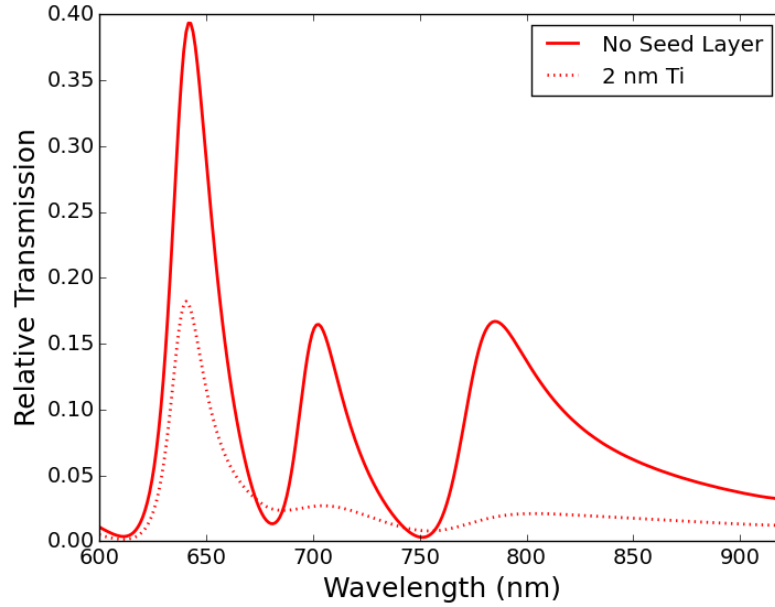
Figure 5.8: The effect of a titanium seed layer between the substrate and the gold on the relative transmission.
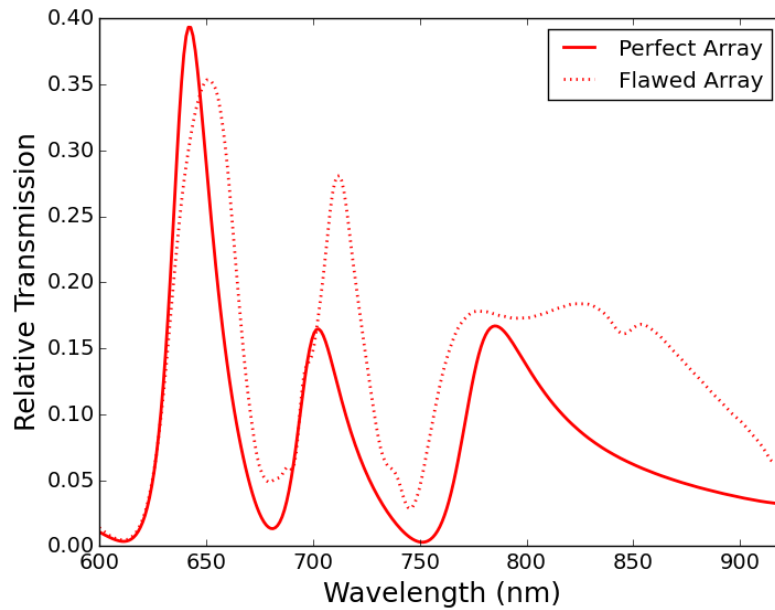
Figure 5.9: The transmission of a perfect array compared to an array containing missing and differently-sized holes. Decreasing uniformity broadens the transmission peaks.
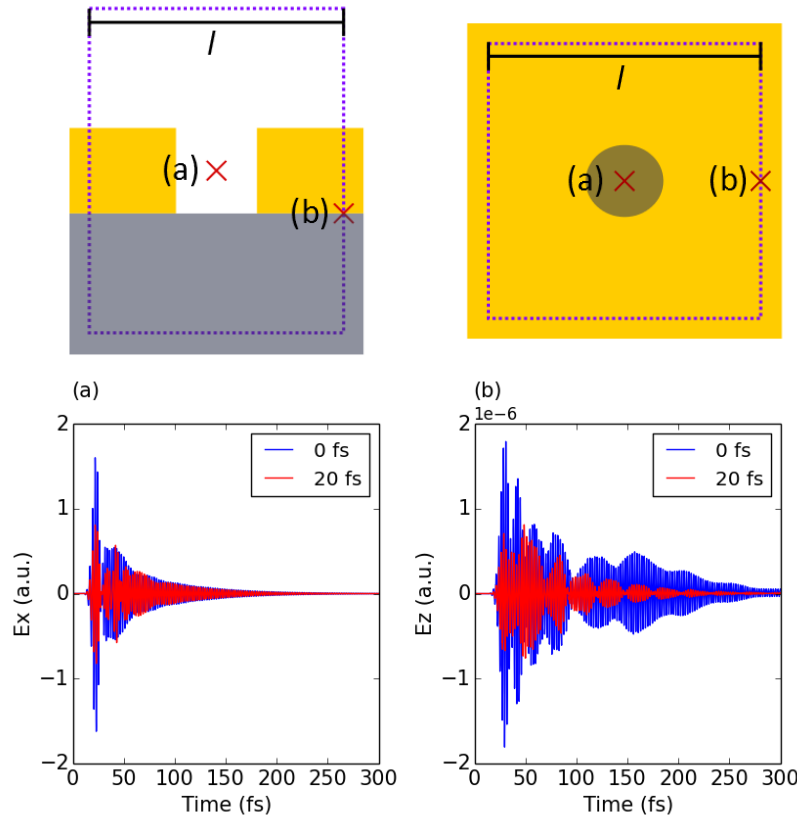
Figure 5.10: Evolution of the electric fields at two points in the simulation for two different time delays between the pulses. a) The x-component of the electric field in the centre of the hole. b) The z-component of the electric field midway between the holes on the gold/substrate interface.

onds. The relationship between the period of this oscillation and the wavelength of the transmission peak is the same as that expected from an autocorrelation between the two incident pulses. Since the apodisation window of excludes the directly-transmitted part of the first pulse from the frequency monitor, this signal must result from the interference between the second pulse and the excited surface plasmons, which retain the frequency of their excitation source. The magnitude of this oscillation decreases with increasing delay as the plasmonic fields induced by the first pulse decay. If no apodisation is applied, as in Figure B.5, the transmission peaks become chirped and all dynamics apart from the autocorrelation signal are lost.

Figure 5.14 shows a plot of the change in intensity with delay of the peak centred at 634 nm in the standard array. The intensity is calculated as the integrated intensity over the FWHW of the peak at zero delay. Cubic spline interpolation is then applied to achieve a smoother curve. From this plot, it is evident that the envelope of the signal contains another contribution aside from the exponential decay related to the plasmon lifetime. Other plasmonic interactions are expected to have effects on the transmission, such as
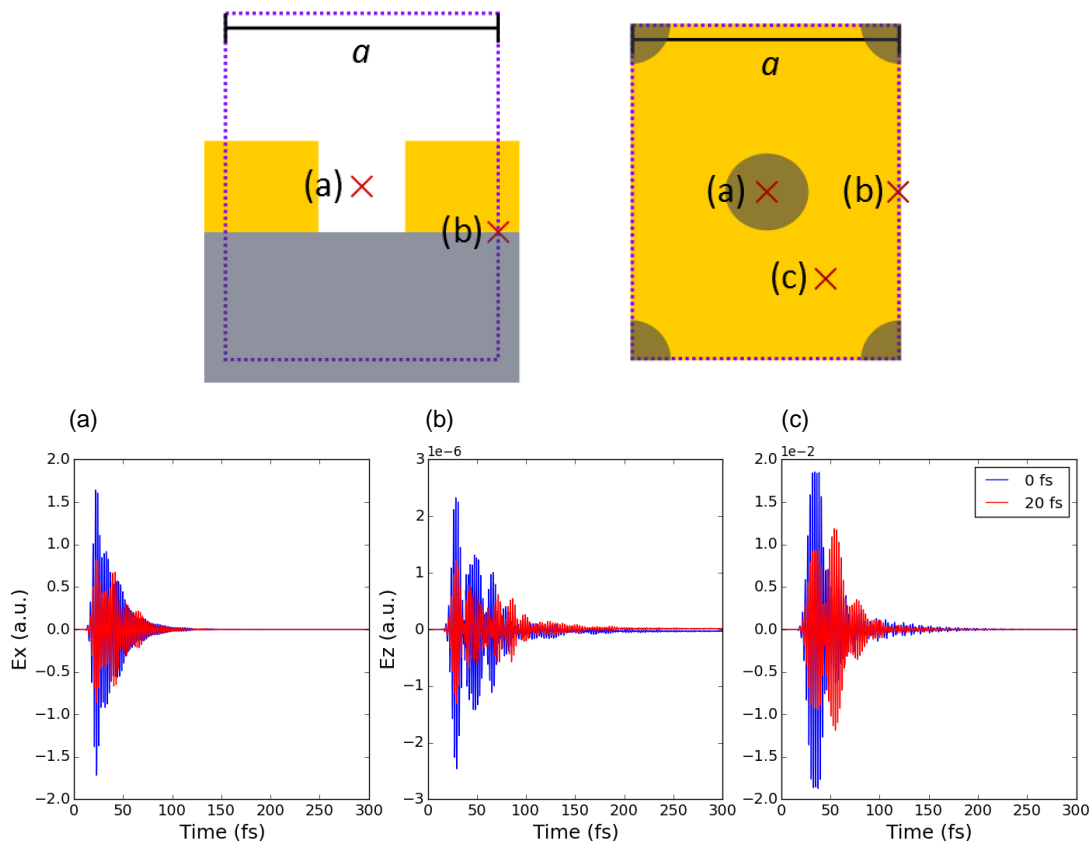
Figure 5.11: Evolution of the electric fields at two points in the simulation for three different time delays between the pulses. a) The x-component of the electric field in the centre of the hole. The z-component of the electric field midway between the holes on the gold/substrate interface for b) $x = a/2, y = 0$ and c) $\sqrt{y^2 + x^2} = a$

the interference between SPPs originating from different holes and coupling between the interfaces. The beating frequencies of the fields seen in the time domain monitors indicate that the timescales of these interactions are in the tens of femtoseconds, so any oscillations in the transmission caused by such processes will only undergo a few cycles before decaying. Moreover, these beating frequencies are non-stationary, making analysis of the signal via Fourier decomposition impractical. Methods of time-frequency analysis that rely on windowing the signal in time are also impractical due to the relatively few periods.

A time series analysis method that is designed to cope with nonlinear and nonstationary data is *empirical mode decomposition* (EMD). The EMD method is an iterative algorithm which decomposes a time series signal into a set of *intrinsic mode functions* (IMF) — narrowband functions representing simple oscillatory modes with an equal number of extrema and zero-crossings (or differing at most by one), and whose envelopes defined by local maxima and minima are symmetric with respect to zero. This decomposition is complete
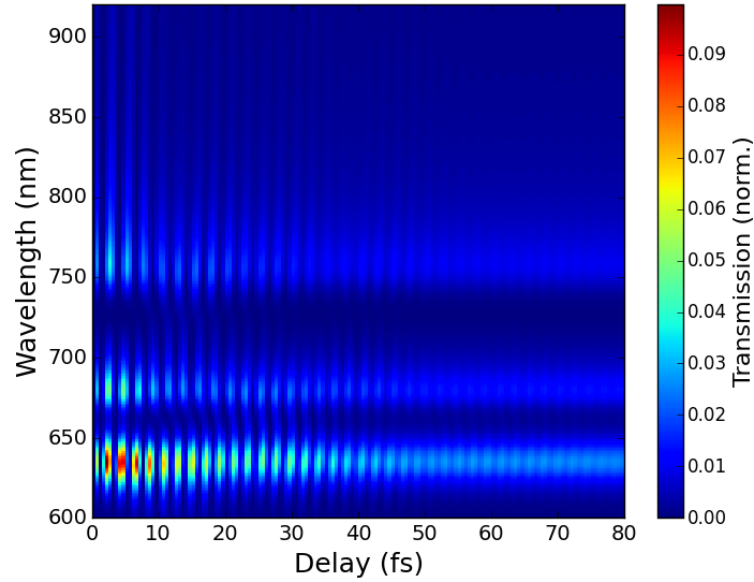
Figure 5.12: Simulated spectrogram of the transmission of a gold nanohole array on a Si_3N_4 substrate with parameters $a = 650\,\text{nm}$, $h = 200\,\text{nm}$, and $d = 200\,\text{nm}$. The x-axis gives the delay between the two incident 5 fs pulses.
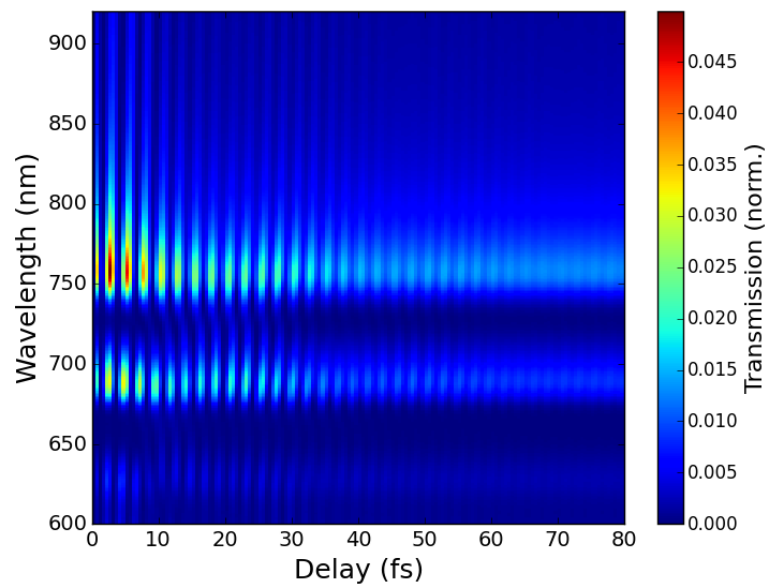
Figure 5.13: As above, but here the background refractive index has been changed from $n = 1.0$ to $n = 1.8$.

and almost orthogonal. The process of EMD is as follows:

1. Locate all local extrema in a signal

2. Construct upper and lower envelopes by joining all local maxima and minima, respectively, with a cubic spline

3. Calculate the mean of the envelopes and subtract it from the original signal

4. Repeat the above steps until the resulting function fulfils the requirements for an IMF

5. Subtract this IMF from the original signal

6. Repeat the above steps until no IMFs remain in the signal. The remaining monotonic function is called a *residue*

The Hilbert transform can be applied to each IMF component to compute the *instantaneous frequency*, which is defined as:

$$\omega(t) = \frac{1}{2\pi}\frac{d}{dt}arctan\left[x_a(t)\right] \tag{5.1}$$

where $x_a(t)$ is the complex-valued, analytic signal.
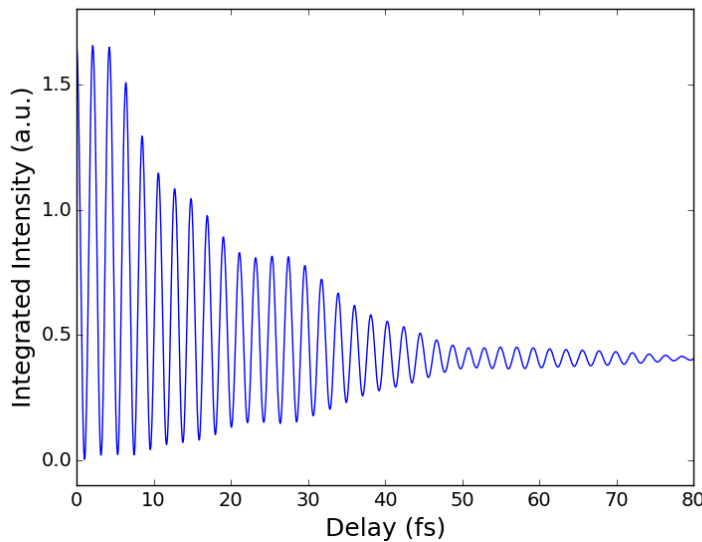
Figure 5.14: An example of the change in intensity of a transmission peak over the FWHM with pulse delay. The rapid autocorrelation signal is clearly visible, as is the plasmon decay, but there is also a slow, complex modulation envelope.

The first two IMFs of each peak for several film thicknesses are shown in Figure 5.16. From Figures 5.7 and 5.12, as well as B.1, it can be seen that decreasing the film thickness increases the height of all transmission peaks, but especially the $(p, q = \pm 1, 1)$ peak relative to the other two. For film thicknesses of $h = 160\,\text{nm}$ and $h = 200\,\text{nm}$ (purple and black curves, respectively), there is a slight increase in the amplitude and frequency of the IMFs for the thinner film; coupling between the interfaces is stronger and the interaction time governed by the length of the nanochannel is shorter. Upon reducing the film thickness to $h = 120\,\text{nm}$, a feature around 17 fs for the $(p, q = \pm 1, 0)$ and $(p, q = \pm 2, 0)$ modes becomes apparent. The $(p, q = \pm 1, 1)$ mode for the thinnest film displays oscillations with a much higher intensity, longer period, and longer lifetime.

When the hole diameter is widened, again the intensity of all transmission peaks increases, but this time the second $(p, q = \pm 2, 0)$ peak becomes prominent relative to the others. A greater proportion of light is able to directly tunnel through the larger holes, decreasing the excitation of the $(p, q = \pm 1, 0)$ mode at the incident surface. This peak undergoes an appreciable redshift, partially merging it with the second for the largest hole diameter $d = 250\,\text{nm}$. The efficiency of the diffraction-excited $(p, q = \pm 1, 1)$ mode at the gold/substrate decreases for larger hole sizes and scattering losses increase, so the relative intensity of the third peak decreases. There is again an inflection point around 17 fs that becomes a local maximum in the $(p, q = \pm 2, 0)$ peak for the largest hole diameter. The emergence of this feature for thin films and large holes suggests that it represents the onset of significant coupling between the two interfaces, or a waveguiding mode in the hole. From Figures 5.10 and 5.11, at 17 fs after the injection of the pulses, the fields from these pulses have decayed and fields from plasmon excitation begin to oscillate. In contrast to the results of Müller et al. [24], the period of the oscillations increases with hole size for the $(p, q = \pm 1, 0)$ and $(p, q = \pm 2, 0)$ peaks. The oscillations of the third peak display a complex dependence on hole size, with several peaks and inflection points appearing for the smaller hole diameters. Note that in Figure 5.18, the IMF amplitudes for the 150 and 250 nm holes have been multiplied by 10 and 0.1 respectively, for clarity.

Increasing the lattice constant a redshifts all the peaks (see Figures 5.12 and B.3, as well as B.7 and B.10) but their mode number remains the same. The $(p, q = \pm 1, 0)$ peak increases in intensity and decreases in linewidth, indicating a more efficient coupling to this mode and a longer plasmon lifetime. This agrees with the results shown in Figure 5.20, where the first peak for the array with $a = 750\,\text{nm}$ shows a much slower decay compared to the array with $a = 650\,\text{nm}$. The second peak for the larger array exhibits distinct IMFs with a slightly longer period and again, a slower decay, whilst the period of the third peak becomes shorter.

The dielectric environment of the array has significant effects on both the relative intensity of the transmission peaks and their dynamics. Making the sub- and superstrates equal by either removing the Si_3N_4 substrate or setting the background refractive index to $n = 2$ ensures strong coupling between the top and bottom interfaces, and so enhances the
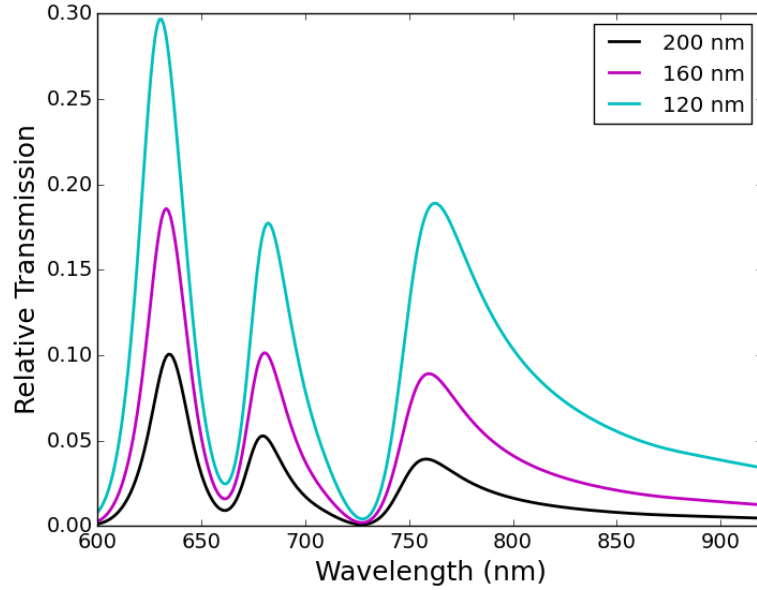
Figure 5.15: Spectra of the hole array at zero delay with varying thickness h
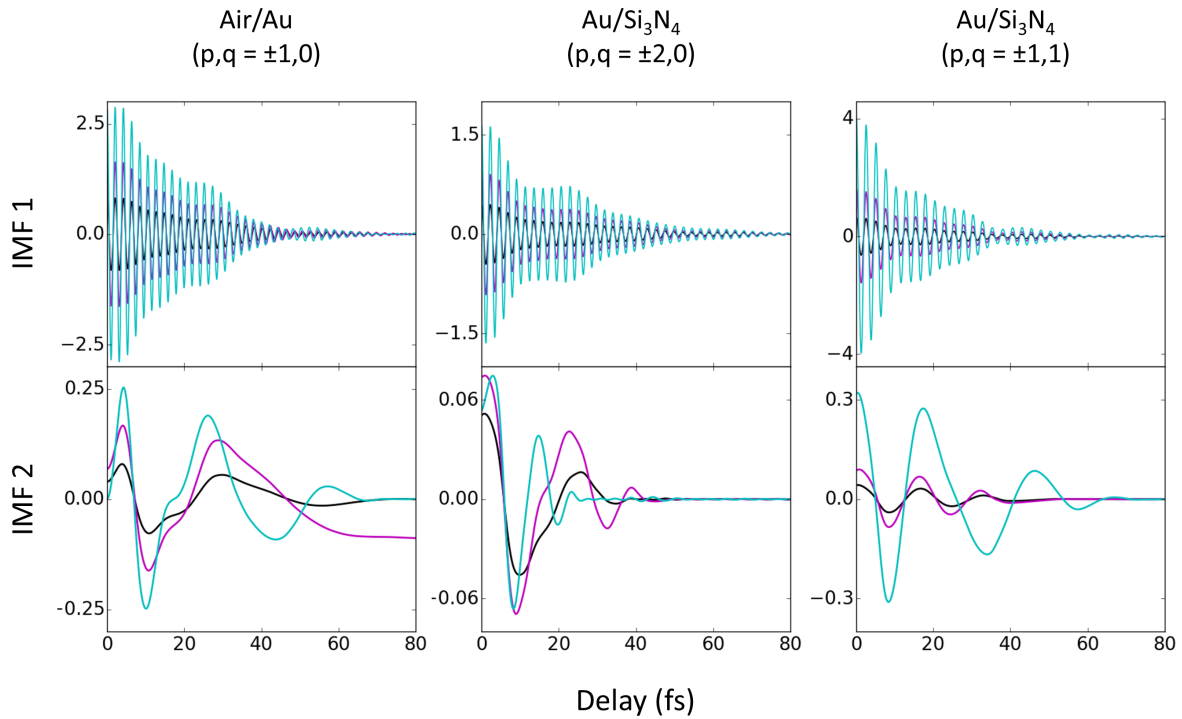
Figure 5.16: The intrinsic mode functions of the intensity change with delay for the transmission peaks and their dependence on film thickness.
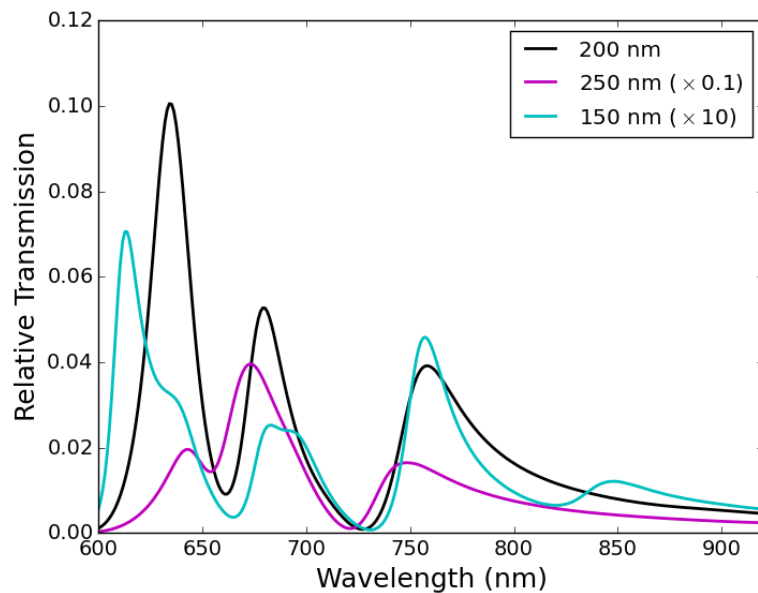
Figure 5.17: Spectra of the hole array at zero delay with varying hole diameter d
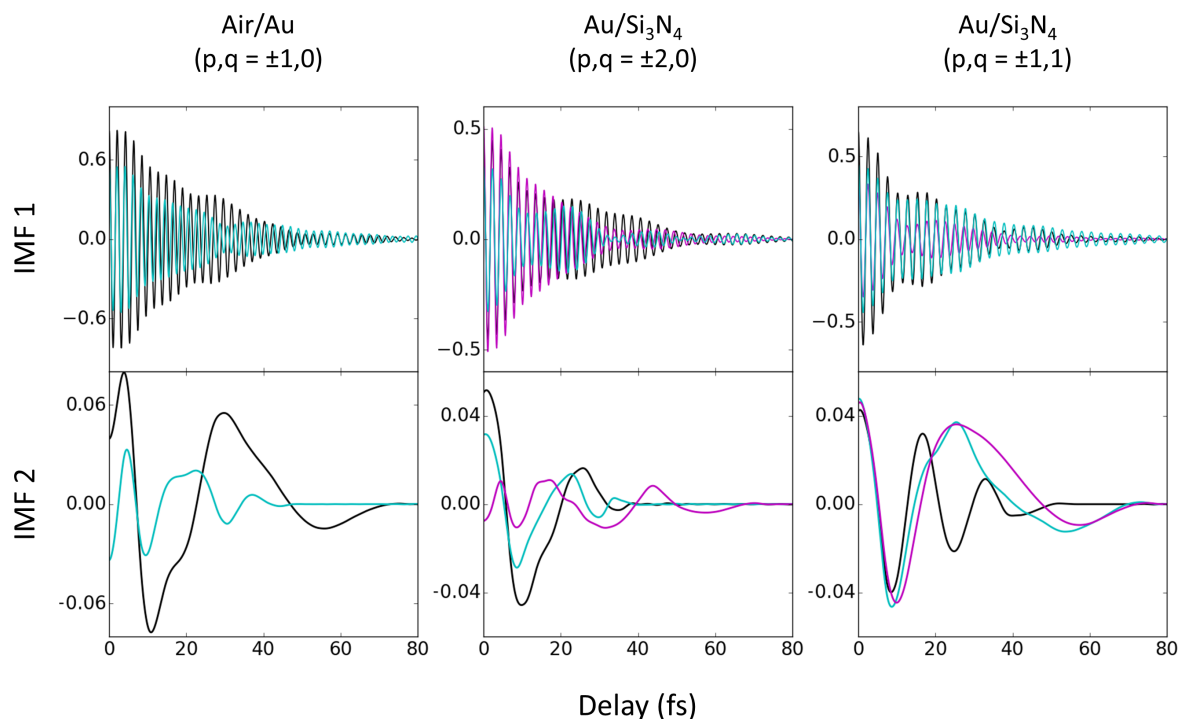
Figure 5.18: The intrinsic mode functions of the intensity change with delay for the transmission peaks and their dependence on hole diameter. Due to the large differences in transmission intensity for these hole sizes, the relative transmission and IMFs of the arrays with $d = 250\,\text{nm}$ and $d = 150\,\text{nm}$ have been multiplied by 0.1 and 10, respectively.
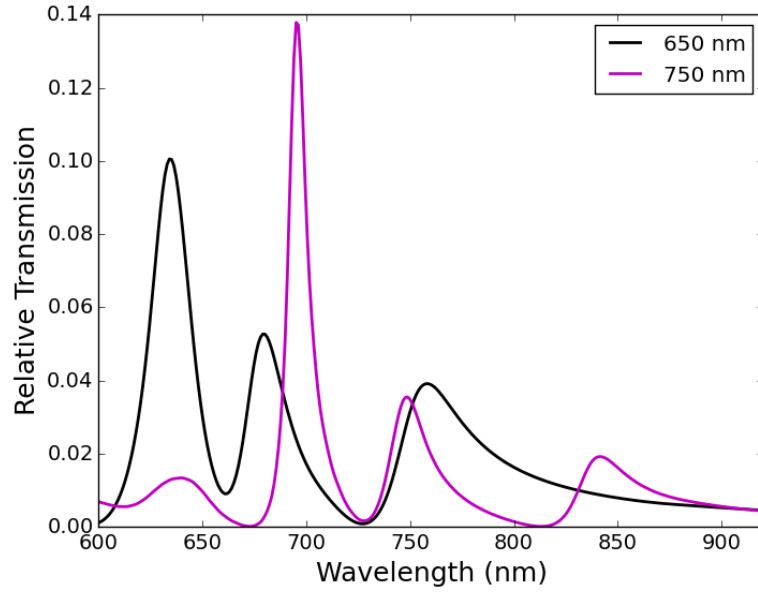
Figure 5.19: Spectra of the hole array at zero delay for two values of the lattice constant a
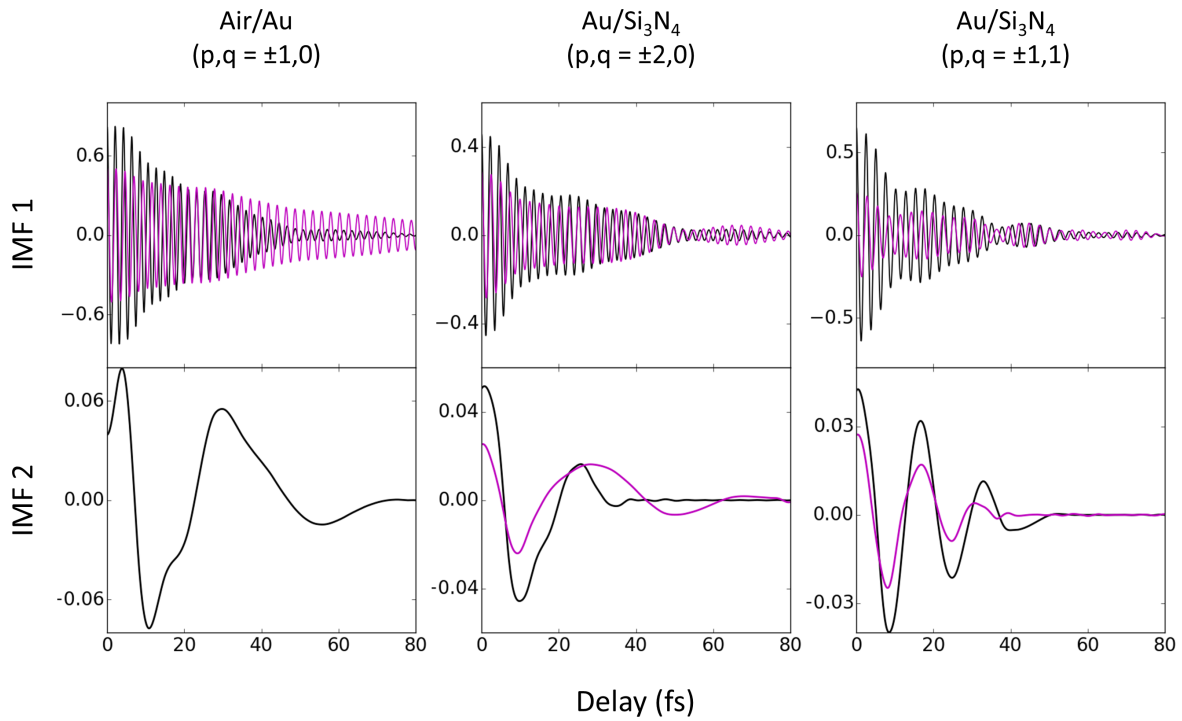
Figure 5.20: The intrinsic mode functions of the intensity change with delay for the transmission peaks and their dependence on lattice constant.

transmission of the corresponding peaks. This can be seen in Figures B.4 and B.11. In Figure 5.22, for the array in a symmetric dielectric environment, the $(p, q = \pm2, 0)$ mode shows clear oscillations with a period around 20 fs, whilst the $(p, q = \pm1, 1)$ mode simply decays exponentially with no strong additional modulations.

Setting the background refractive index to $n = 1.3$ reduces the relative intensity of the transmission peaks around 630 and 680 nm, but gives an enormous and relatively narrow transmission peak at 795 nm, indicating a strong suppression of the damping for this mode. From Equation 2.50, if $\varepsilon_2 = 1.69$, the resonance wavelength of the $(p, q = \pm1, 0)$ peak shifts from 629 to 763 nm, which is very close to the 743 nm peak predicted by the equation for the $(p, q = \pm1, 1)$ mode at the gold/Si_3N_4 interface. In this case diffraction at the hole exit causes an efficient excitation of the $(p, q = \pm1, 1)$ mode on the bottom surface. As shown in Figure 5.23, this peak decays slowly with no apparent additional modulation. This is also the case for the $(p, q = \pm1, 1)$ mode in the case above with $n = 2.0$.

If the background index is set to $n = 1.8$, the predicted resonance wavelength of 636 nm for the $(p, q = \pm1, 1)$ mode at the top interface lies close to the 643 nm predicted for the $(p, q = \pm2, 0)$ mode on the bottom. Yet in this case, there is no strong resonance around this wavelength. This may owe itself to the divergence of Equation 2.50 from the simulated results below 700 nm. Instead there is a decrease in the relative transmission of the $(p, q = \pm2, 0)$ peak and a redshift to around 690 nm, and an increase in the transmission of the $(p, q = \pm1, 1)$ peak around 760 nm. These changes are accompanied by shorter and longer oscillation periods respectively, as seen in Figure 5.24.
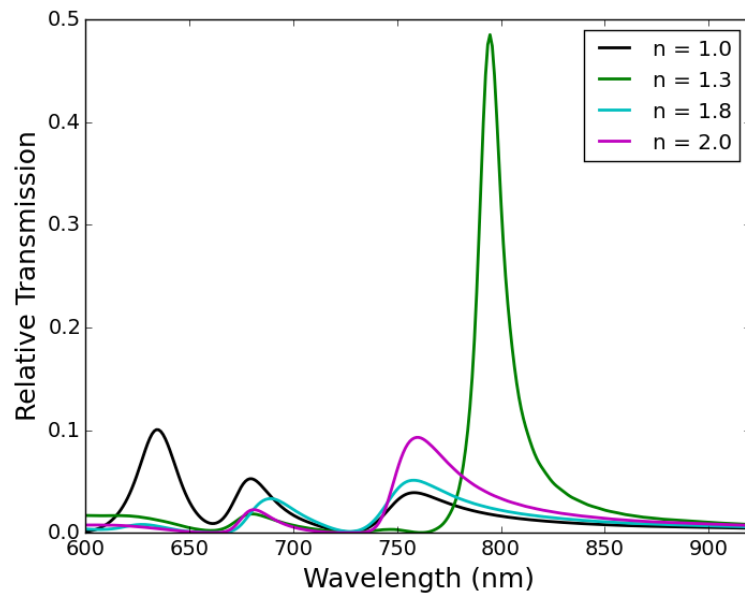
Figure 5.21: Spectra of the hole array at zero delay for various values of the background refractive index.
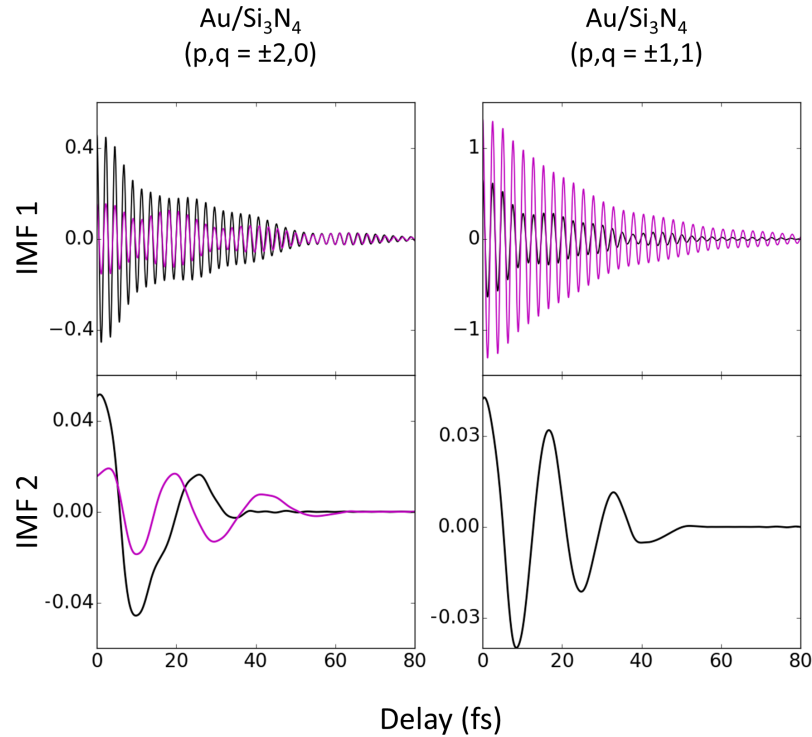
Figure 5.22: The intrinsic mode functions of the intensity change with delay for the transmission peaks with background refractive indices $n = 1.0$ (black) and $n = 2.0$ (magenta). The index $n = 2.0$ matches that of the substrate, putting the latter array in a symmetric dielectric environment.
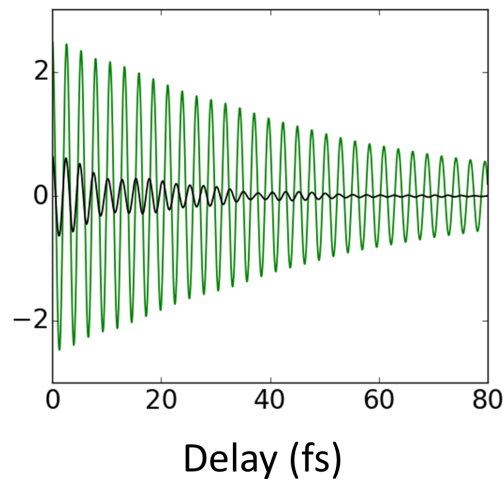
Figure 5.23: The intrinsic mode functions of the intensity change with delay for the transmission peaks around 750 - 800 nm with background refractive indices $n = 1.0$ (black) and $n = 1.3$ (green). For the $n = 1.3$ case, this peak lies close to the $(p, q = \pm 1, 0)$ and $(p, q = \pm 1, 1)$ modes at the top and bottom interfaces, respectively.
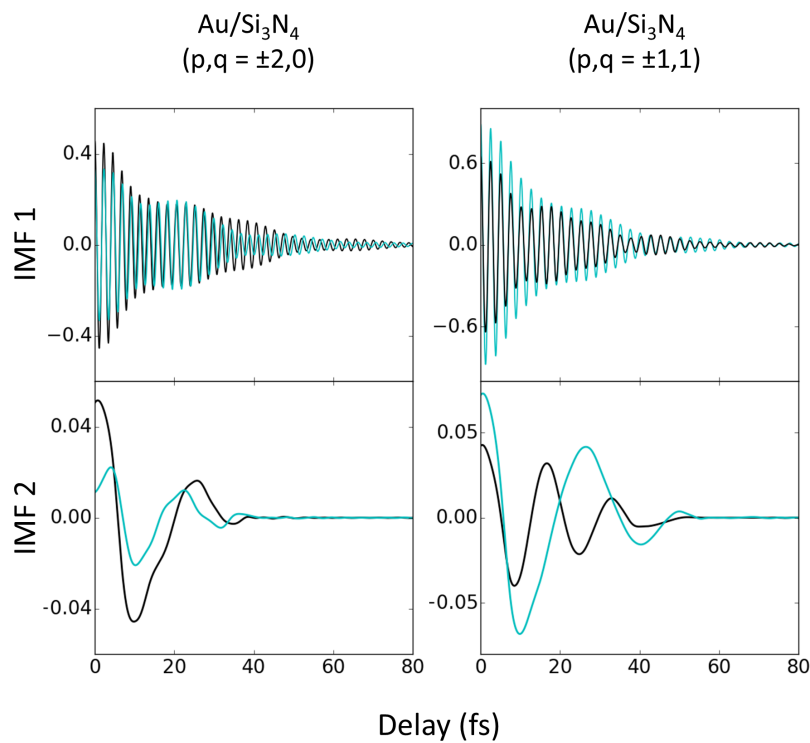
Figure 5.24: The intrinsic mode functions of the intensity change with delay for the transmission peaks with background refractive indices $n = 1.0$ (black) and $n = 1.8$ (cyan).

5.2 Results of Fabrication

For transmission experiments, gold nanoarray samples on ITO substrates were fabricated according to the bilayer EBL method outlined in Section 3.4.1. The resulting arrays were inspected and imaged using light and scanning electron microscopy. Some of these images can be found below; others in References [230] and [232].

Two samples with thicknesses 60 and 120 nm were produced, each containing multiple rows of hexagonal hole arrays arranged in rows with nominal hole diameters 200 nm and lattice constant 650 nm. Individual arrays are parallelogram-shaped, due to the relative ease of designing these structures based on a hexagonal unit cell, and have x- and y-dimensions of $40\,\mu\text{m} \times 40\,\mu\text{m}$. The diameter of the laser focal spot has been measured as $38\,\mu\text{m}$ [230], so it the laser spot should critically fill one array. The EBL area dose was varied between the rows to try to find the ideal dosage.

After lift-off, arrays were inspected via light microscopy and SEM. Overview images of two different arrays from the 120 nm are shown in Figure 5.25. Holes that still contain PMMA appear as light circles. Arrays from rows which received a higher area dose showed lower amounts of residual resist than rows which received a lower dose, as did arrays on the thinner (60 nm) film. Some arrays also contain small regions where the lithography appears to no have worked at all, and no holes are visible. Further details of the fabrication results, including area dosages and light microscope images can be found in Reference [232].

The geometry of the individual holes can be inspected under higher magnification. The measured lattice spacing is within one percent of the designed 650 nm. Images of an array with good lift-off in Figure 5.26 show that there is some asymmetry in the hole diameter; on average holes are a little larger than 200 nm in diameter. There are also some irregularities around the circumference of the holes.

5.3 Transmission Experiments

5.3.1 Single-Pulse Results

Transmission spectra for the arrays were measured in the setup described in Section 3.3.3. Single-pulse (static) spectra were recorded with the piezostage at the position where it does not introduce a delay between the beams, which is also the position that gives a maximum signal for the autocorrelation measurement. When the oscillator beam passes through a nanohole array, spectra measured by the spectrometer will be those from the oscillator, modified by the hole array. In order to obtain the response of the array (the array
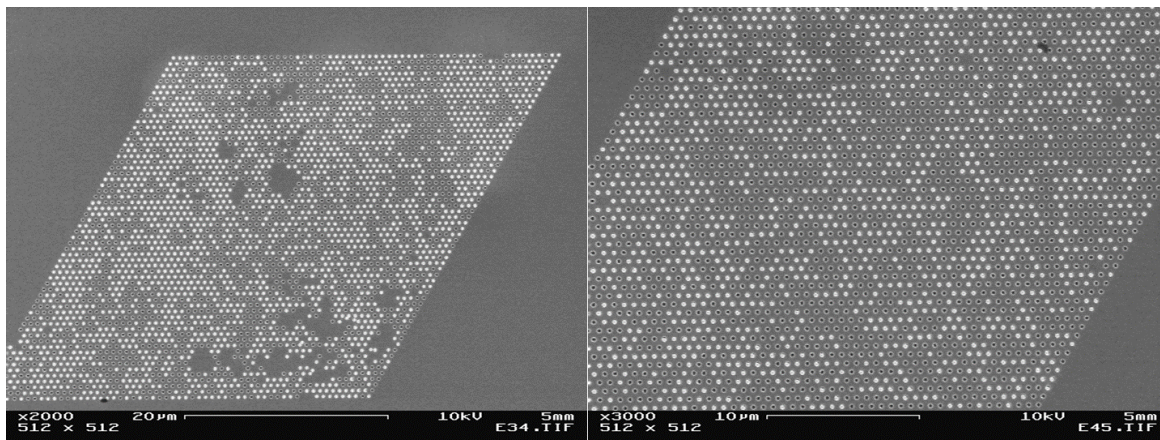
Figure 5.25: SEM images of two of the hole arrays on the 120 nm film that received lower area doses. Residual resist in the nanoholes appears as light circles. The array on the left also contains regions where the lithography was unsuccessful.
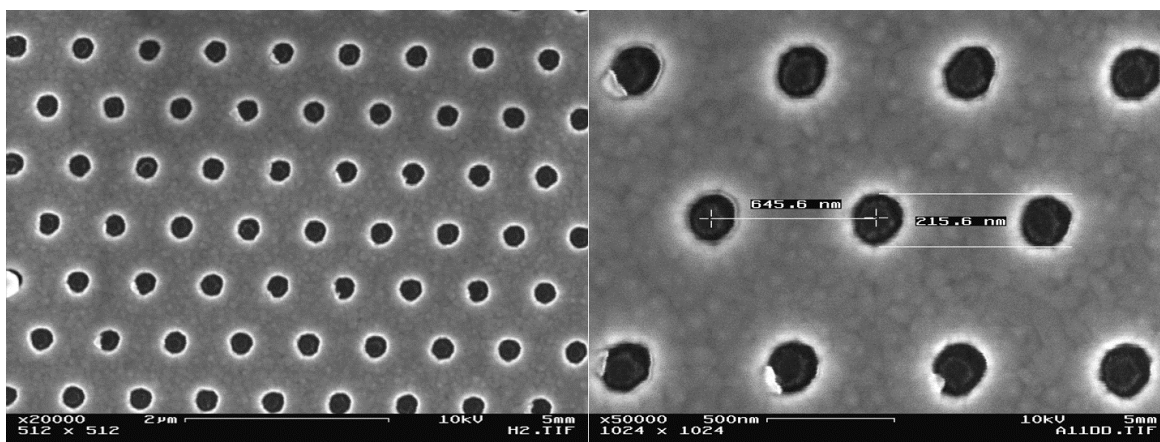
Figure 5.26: SEM images of one of the hole arrays on the 120 nm film that received higher area doses.

spectrum) the result (the raw spectrum) must therefore be normalised to the spectrum recorded without a sample in the beam (the reference spectrum). In the case of the 60 nm-thick arrays the film is partially transparent even in areas without holes, so for these arrays the transmission of the bare film has also been subtracted from the result (film spectrum). Since the integration times used to obtain the reference and raw spectra are usually different, this has to be factored into the calculation. Finally, spectra are smoothed using a 3.5 nm-wide boxcar filter. Figure 5.27 shows examples of raw, film, and reference spectra from the 60 nm-thick sample, and the resulting smoothed array spectrum. Using $S(\lambda)$ and t to represent spectra and integration times, this can be written as

$$S_{array}(\lambda) = \frac{S_{raw}(\lambda) - S_{film}(\lambda)}{S_{reference}(\lambda)} \times \frac{t_{reference}}{t_{raw}} \qquad (5.2)$$
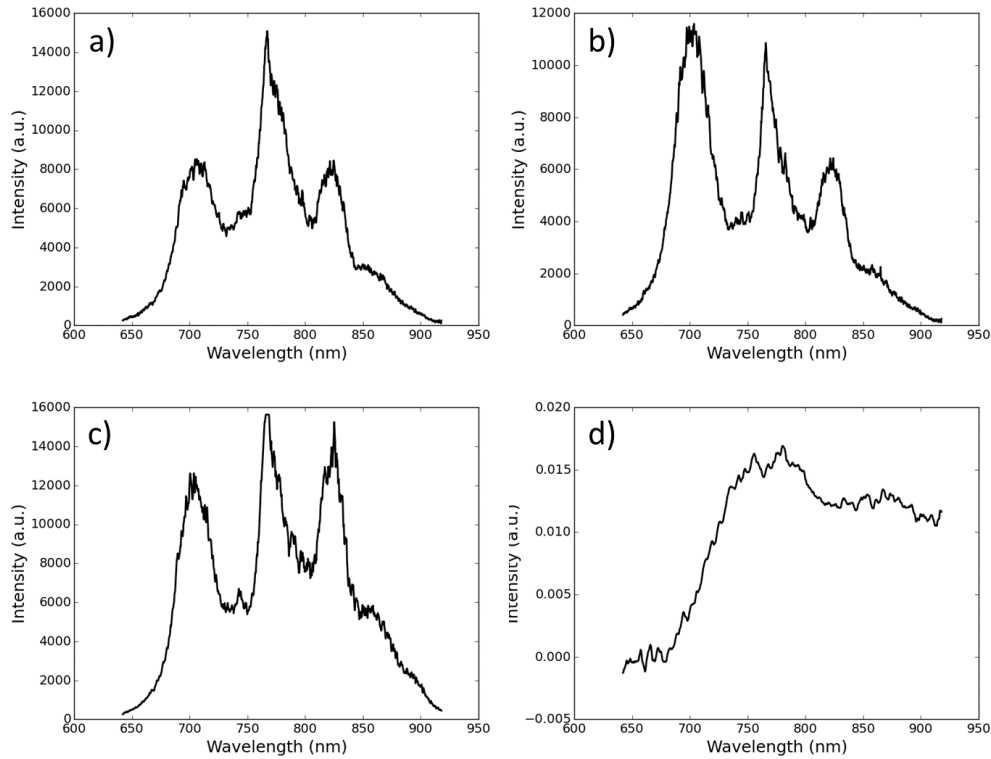
Figure 5.27: Examples taken from measurements of the 60 nm-thick sample of a) a raw transmission spectrum of a nanohole array, b) the transmission spectrum of the bare film, and c) the reference spectrum taken without a sample. To calculate the spectral response of a nanohole array, b) is subtracted from a), the result is then divided by c) and multiplied by a factor to account for the differences in integration times. A 3.5 nm-wide boxcar filter has been applied to the final result shown in d). For 120 nm-thick films the bare film is opaque, so the first step is omitted.

Figure 5.28 shows two spectra from different arrays on the 120 nm-thick sample. The red curve is the transmission through an array that had relatively good lift-off results — a high proportion of the nanoholes were free of resist. In contrast, the blue curve is from an array with a lower fraction of free holes after lift-off. A smaller proportion of free holes significantly reduces the transmission.

Transmission spectra from arrays on the 120 and 60 nm-thick films are shown in Figure 5.29. There is both an increase in intensity and a redshift of the peaks for the thinner film, as predicted by the simulations.

Simulations presented in the previous section were all performed using a Si_3N_4 substrate. It later proved more feasible to fabricate arrays on ITO substrates. The simulated transmission spectrum from a 120 nm-thick film on ITO with lattice spacing 650 nm is shown in Figure 5.30. As for the simulations on the Si_3N_4 substrate, there is a predicted transmission peak just below 650 nm, corresponding to a resonance at the air/gold interface. This peak
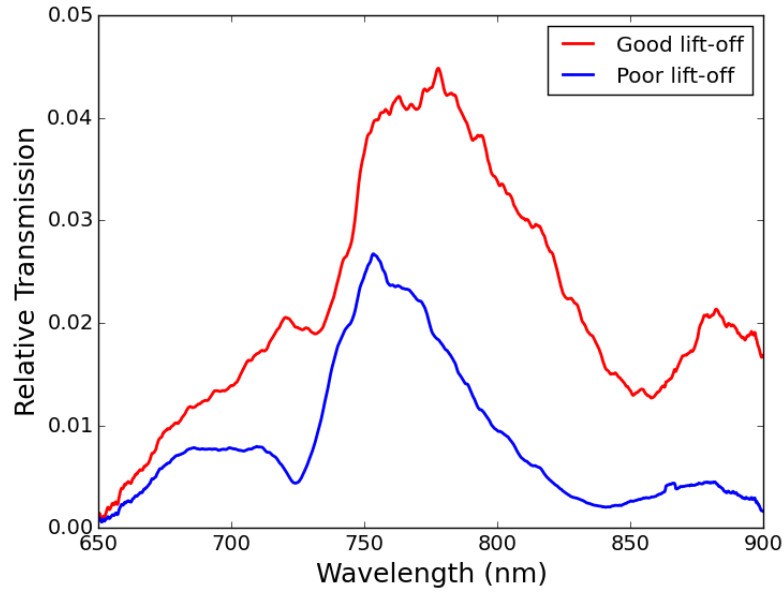
Figure 5.28: Transmission spectra of two arrays from different rows on the same 120 nm-thick film. The array which has a smaller fraction of free nanoholes due to residual PMMA shows a lower relative transmission.
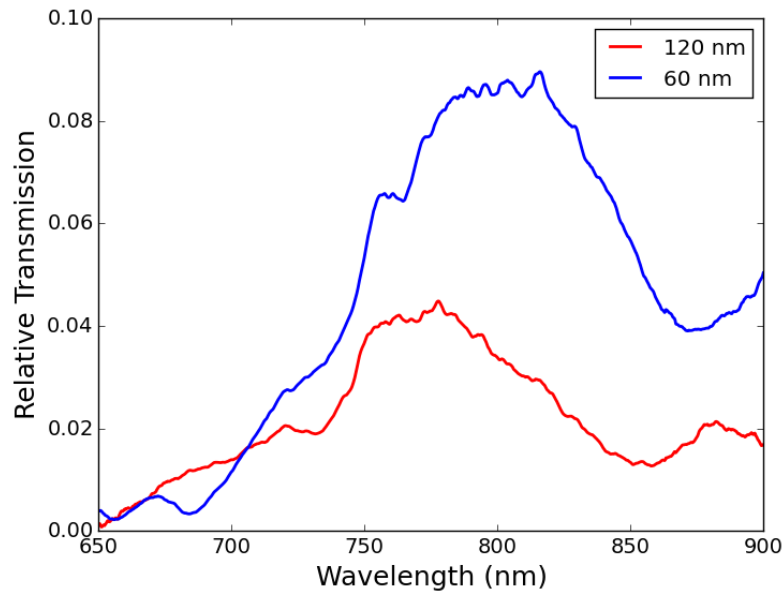
Figure 5.29: Transmission spectra from two arrays on the 120 and 60 nm-thick films. As in the simulations there in a redshift and increase in relative transmission of the peaks for the thinner film.
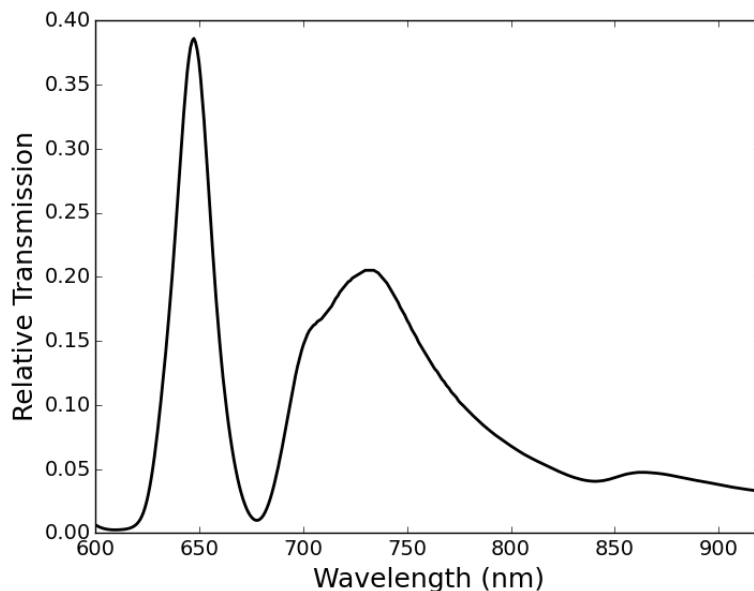
Figure 5.30: Simulated transmission spectrum of a nanohole array used in experiments — a triangular array with lattice spacing 650 nm in a 120 nm-thick film on an ITO substrate.

cannot be easily identified in the experimental results (or at least, is not as prominent). The intensity of the laser at this wavelength is very low (3% of its maximum at 650 nm) and subsequently the signal-to-noise ratios of the measured spectra below ≈ 670 nm are high. It is possible that the peak is lost in the noise and suppressed by the boxcar filtering, or that the peak is either much smaller or lies at a shorter wavelength in reality than in the simulation. In both experiment and simulation there is a broad, complex peak around 740 - 760 nm, and a smaller broad peak around 860 - 870 nm. Both of these peaks are smaller than predicted by the simulations, which could be explained by incomplete lift-off of the holes, or by the laser spot not being perfectly centrally positioned over the array in the experiment.

5.3.2 Double-Pulse Results

The first pump-probe measurements were made with using the PX 38 piezoelectric linear translation stage Piezosystem Jena GmbH to set the delay. Some discontinuities were seen in the resulting spectrograms. As described in Chapter 3 and Reference [230], these were found to be caused by interference between the piezostage and a nearby turbopump, as well as nonlinear movement of the stage near the end of its range. The stage was replaced with another from Piezosystem Jena GmbH (PX 50) which provided finer time resolution and did not suffer interference problems.
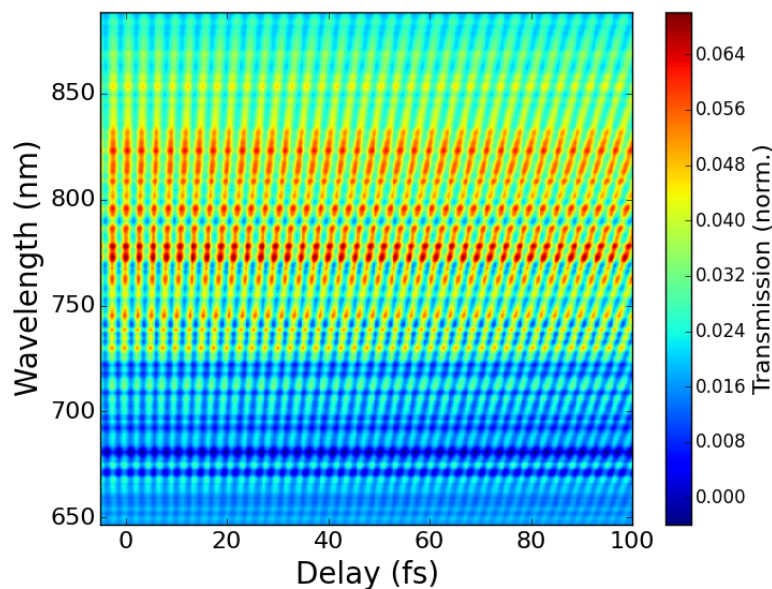
Figure 5.31: Spectrogram of an array on the 60 nm-thick film at normal incidence, measured using the upgraded piezostage. The transmission of the unpatterned film has been subtracted.

Spectrograms taken using this second translation stage for arrays on the 60 nm and 120 nm films are shown in Figures 5.31 and 5.32. A couple of differences are apparent between these measured spectrograms and those taken from simulations, such as those shown in Figures 5.12 and 5.13. The first difference is that the peaks become chirped with increasing delay, and the second is that there is neither decay over the delay range nor discernible modulation aside from the autocorrelation contribution.

This result can be reproduced in the simulations by either removing the apodisation window, as in Figure B.5, or by using a much longer incident pulse, as in Figure B.6. Experimental results on bare film (i.e. with no hole array) showed that for a detector positioned to collect only scattered light between the two transmitted beams there was some residual autocorrelation signal, indicating that there is some spatial overlap of the beams at this point; this is equivalent to incomplete apodisation. Positioning the detector instead in the path of a single transmitted beam eliminated this autocorrelation signal, yet the appearance of array spectrogram did not significantly change. If the appearance of the spectrogram is due to partial spatial overlap of the incident beams caused by scattering, this could be mitigated by appropriate choice of the incident angle.

The apparent overlap of the incident pulses could also be caused by the collection optics. The transmitted pulses are focused by a lens into a multimode optical fibre several tens of centimetres long which is coupled into a spectrometer. The lens, glass fibre, and the spectrometer grating will all introduce chromatic dispersion, stretching the pulse lengths
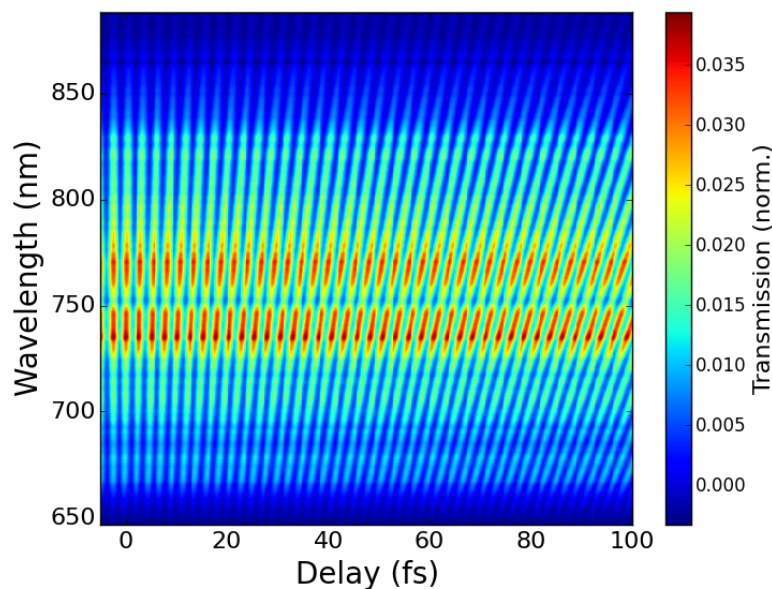
Figure 5.32: Spectrogram of an array on the 120 nm-thick film at normal incidence.

and resulting in temporal overlap. For this reason the collection optics were later replaced by a photodiode, at the cost of a loss of spectral information.

Plots of the measured photodiode voltage as a function of stage delay for several configurations are shown in Figures 5.33 to 5.36. In Figure 5.33, the iris is positioned to collect the signal in the centre of the transmitted pump and probe beams. As in the spectrometer case, with this geometry there is a small background signal present when the sample is absent, which is shown in green. When a sample is introduced and the beams focused on a hole array (labelled A1 for reference), there is a significant change in the signal. At time zero the transmitted signal is at a maximum, which decays rapidly with increasing delay. This decay is modulated by a beating pattern, similar to those seen in simulations in the previous section. Deconvolving the "no sample" signal from the "array" signal produces the signal seen in Figure 5.34.

Transmission through a different hole array (A6) is shown in Figure 5.35. The transmission is lower through this second array, but the beating pattern remains similar.

If the iris is positioned to allow just the transmitted probe beam onto the photodiode, the background signal (without a sample) drops, but so does the intensity of the sample transmission. Figure 5.36 shows the results of measurement of the array A1 with this geometry. The beating pattern is still present, but more difficult to distinguish.
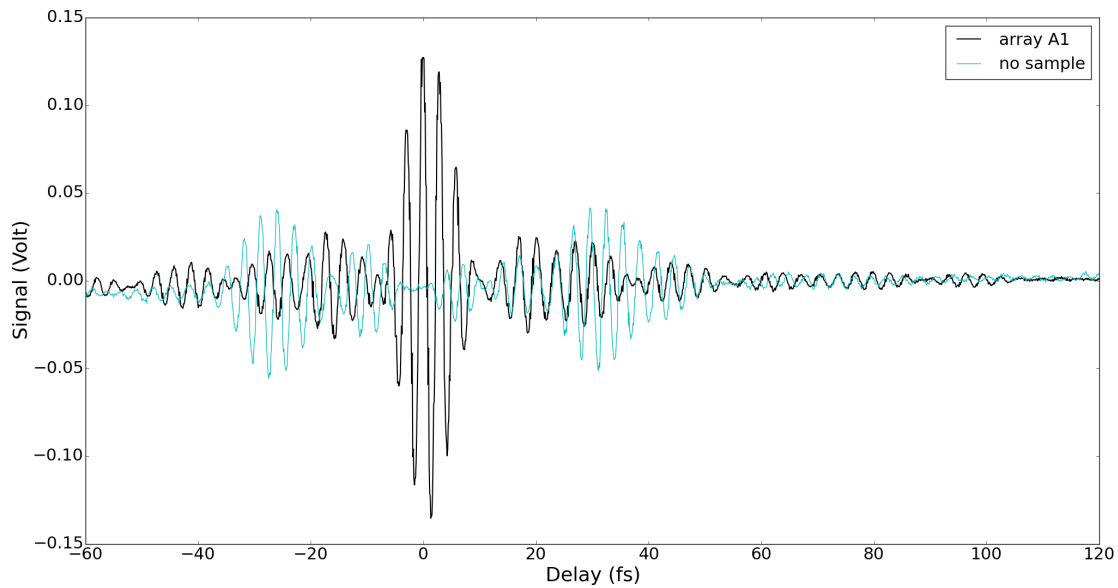
Figure 5.33: Photodiode signal as a function of pulse delay through hole array A1 (black curve) on the 120 nm-thick film, with the iris positioned centrally between transmitted pump and probe beams. The light blue curve shows the signal when no sample is present.
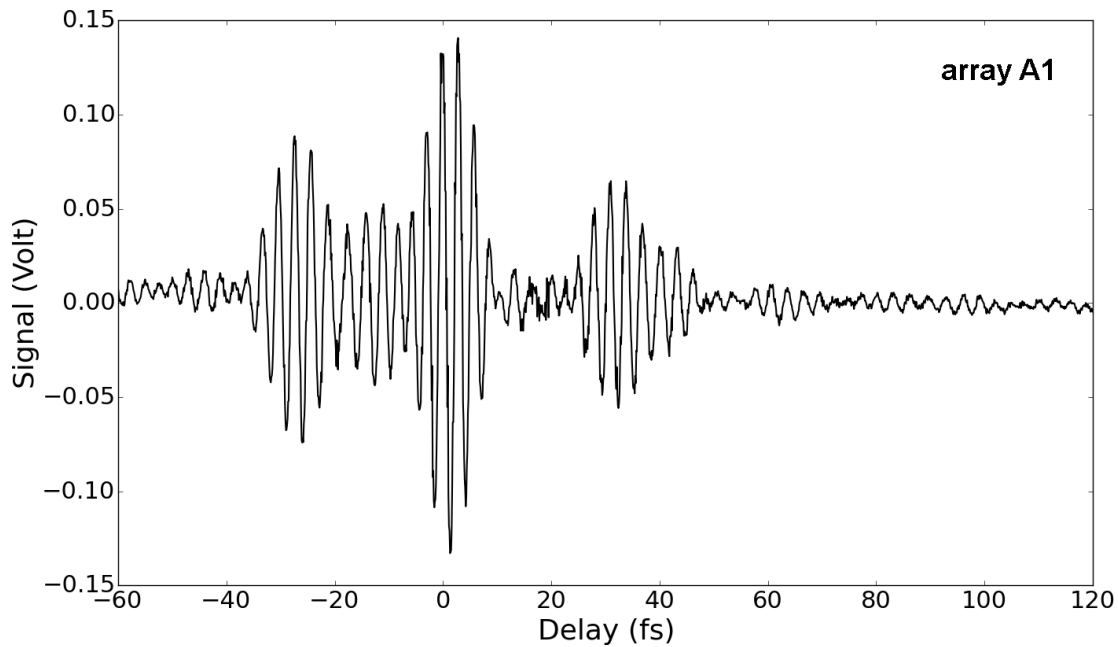
Figure 5.34: Photodiode signal as a function of pulse delay through hole array A1, after deconvolving the background signal.
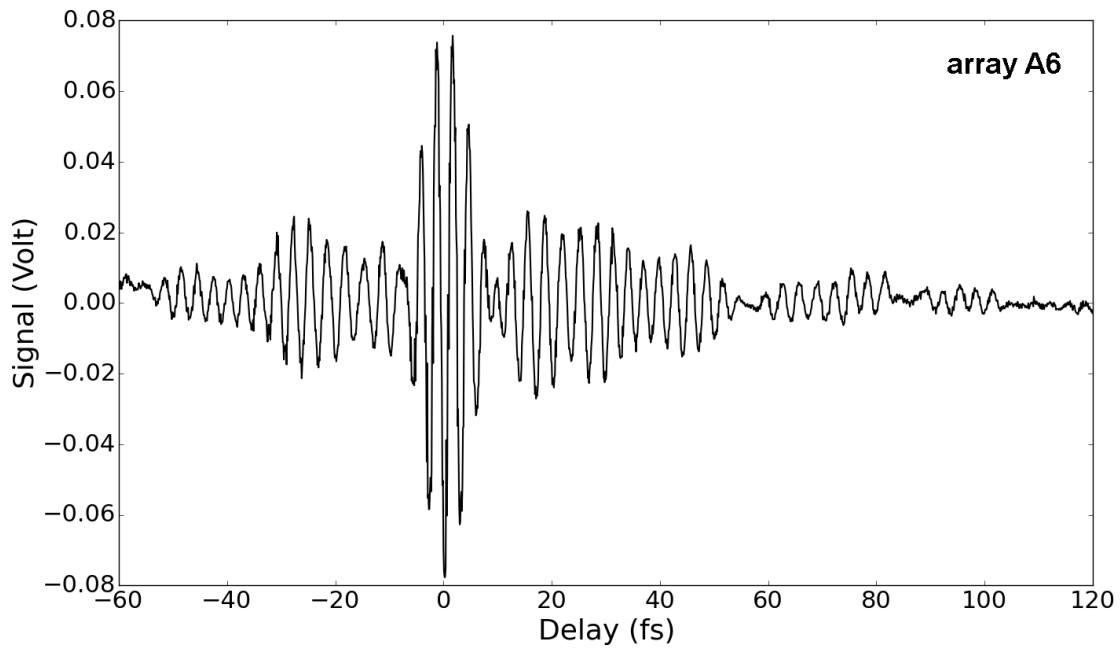
Figure 5.35: Photodiode signal as a function of pulse delay through hole array A6, after deconvolving the background signal.
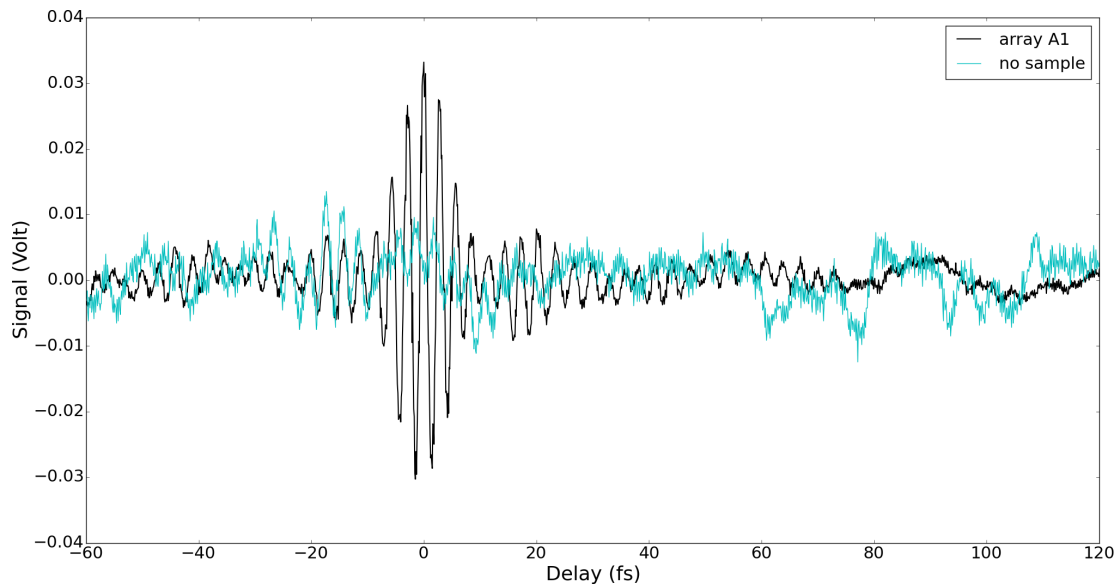
Figure 5.36: Photodiode signal as a function of pulse delay through hole array A1 (black curve) on the 120 nm-thick film, with the iris positioned to collect the transmitted probe beam. The background signal when the sample is absent (light blue) is much smaller, but so is the signal from the array transmission.
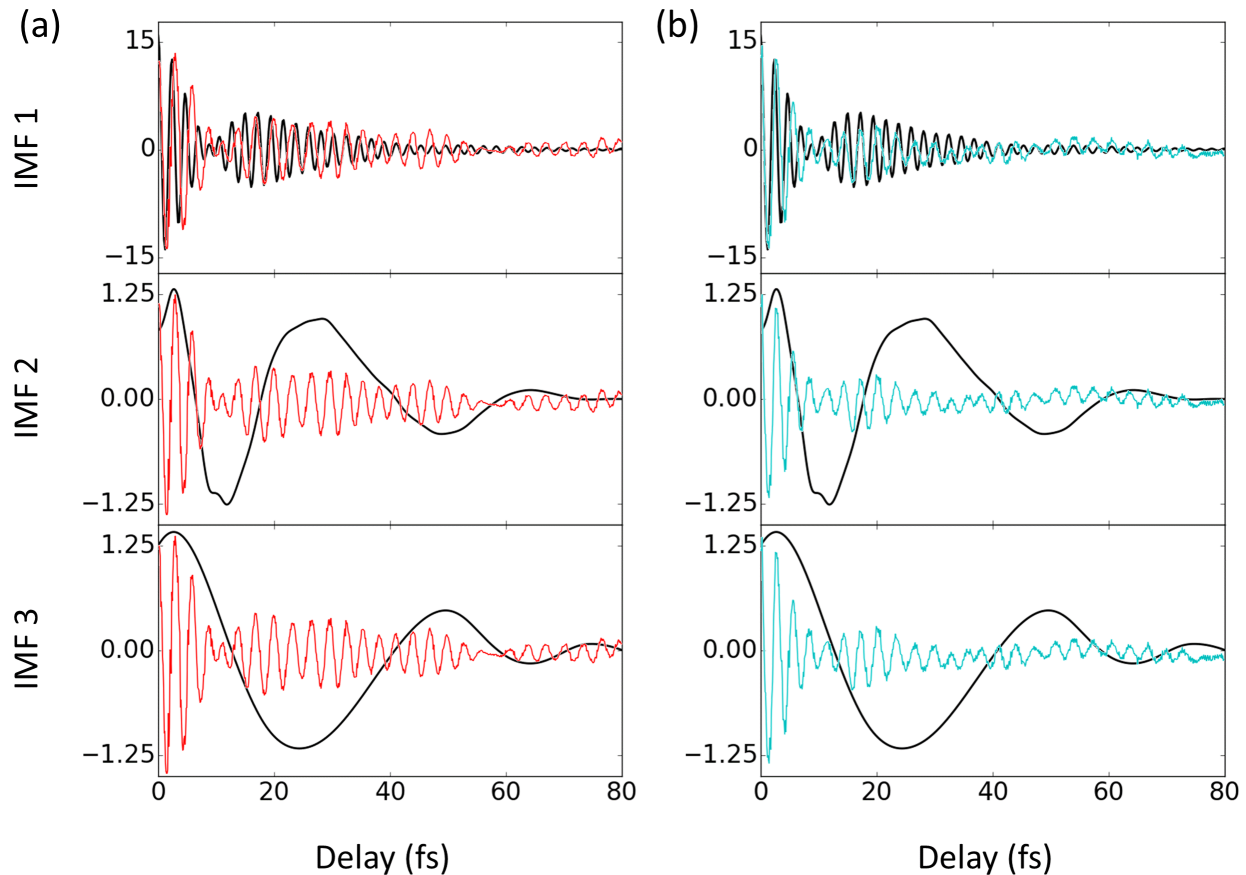
Figure 5.37: The three intrinsic mode functions of the transmitted intensity as a function of time delay for a simulated 120 nm-thick array on ITO (black lines), overlaid with the photodiode signals from hole arrays A6 (left, red lines) and A1 (right, cyan lines).

To compare simulated and experimental results, the total simulated transmission at each time delay must be found by integrating over the whole spectrum. The transmission spectrum for this array was presented in Figure 5.30 in the previous section. The black curves in Figure 5.37 are the three intrinsic mode functions for the transmission of a 10 fs pulse through this array, overlaid with the photodiode signals from hole arrays A6 (left, red) and A1 (right, cyan). In both the experimental and simulated results, the maximum at time zero decays to a node between 10 - 15 fs. The transmission then increases to a secondary maximum at around 18 fs before slowly tapering off over several tens of femtoseconds, interspersed with faint beating. Fitting exponential functions to the signal envelopes provides estimates of the SPP lifetimes of 25, 30, and 19 fs for the arrays A1, A6, and the simulated array.

5.4 Conclusion and Outlook

Simulations demonstrate that the transmission dynamics of plasmonic nanohole arrays is determined by near-field interactions. At the time of writing these are the only known simulations to show the wavelength dependence of the dynamics, and therefore the role of individual modes on the interfaces. From these results it cannot be concluded that coupling strength between the modes on the two interfaces alone determines the frequency or number of oscillations in the transmission, as this is also affected by the nature of the modes and their primary loss mechanism. There are many possible interactions between plasmons propagating along the interfaces, localised around the nanoholes, and tunnelling or guided through the nanochannels, so for a more comprehensive understanding of these interactions many simulations exploring a greater variety of array parameters would be needed.

The intensity of transmission peaks can be tuned by careful selection of the array parameters, which determine the coupling efficiency of different modes and their main damping mechanism. This is especially evident in the results for different refractive indices of the superstrate.

Just as for plasmonic nanoantennas and waveguides, the quality of the film has been shown to be important parameter in the optical properties of the arrays. Optimising the seed layer material and thickness would help to reduce SPP scattering and absorption losses at the interfaces. The uniformity of the hole shapes has a large effect on the near-fields at these points and therefore on the interactions between localised and propagating plasmons. This could feasibly be improved by different EBL dose rates or resist thicknesses, or by switching to FIB lithography. Irregularities on the surface could be reduced by surface treatment such as the Ar^+ sputter cleaning presented in Chapter 4. This would increase the SPP lifetime and ease the requirement for even shorter probe pulses.

The first time-resolved measurements performed using an optical fibre and spectrometer as the collection optics produced chirped spectrograms that were dominated by the autocorrelation signal of the incident pulses, masking any effects caused by plasmonic fields. When the collection optics were switched for a photodiode — thus preventing the introduction of additional dispersion — a time-dependent modulated signal from the nanohole arrays could be seen. The shape of this modulated signal closely resembled that calculated from FDTD simulations.

Coating the films with self-assembled monolayers for time-resolved sensing was briefly trialled [230], but remains to be explored in depth. There is also the possibility combine the films with nonlinear material to exploit the enhanced near-fields for all-optical switching.

A combination of ultrafast time-resolved spectroscopy with back-illuminated or normal-

incidence PEEM on the nanohole arrays would help to relate the measured transmission dynamics to the near-field distributions. The advantages of PEEM over NSOM for mapping fields in nanohole arrays are that PEEM is sensitive to the out-of-plane z-fields, and fields around the holes cannot be smeared out by sample-probe interactions [122].

Chapter 6

Conclusions

This work has presented several methods for characterising plasmonic devices on femtosecond time scales and nanometre spatial scales. In the first part PEEM was used to map localised and propagating plasmonic modes in several types of metal nanostructures including nanoantennas and tapered stripe waveguides fabricated by electron beam lithography. Three sizes of double bowtie and double ellipse nanoantennas were studied, each of which showed areas of highly localised photoemission. These hot spots could be selectively excited by controlling the polarisation of the incident light source. FDTD simulations showed the dependence of the intensity and location of field enhancement on the nanoantenna size and geometry. Further simulations modelled the sensitivity of field enhancement in a bowtie nanoantenna to small changes in gap size, radii of curvature of the corners, and surface roughness. The field profile was shown to be very sensitive to the presence of roughness on the surface, which dominated the signal for values equal or greater to $3\,\mathrm{nm}$ RMS.

Tapered silver stripe waveguides with various widths, lengths, grating profiles, and taper angles were fabricated to try to find an optimal nanofocusing geometry. When illuminated with $405\,\mathrm{nm}$, TM-polarised light incident at $65°$ from the normal, propagating plasmon modes were excited at the silver/vacuum interface. Interference between SPPs reflected from the waveguide edges and the incident light created bands of high field intensity along the propagation axis of the waveguides. Experiments and FDTD simulations showed that the number of ridges depends on both the stripe width and incident angle of the light.

Current challenges for plasmonic device fabrication and implementation include optimising structures for accuracy and reliability and reducing propagation losses from scattering. Both silver nanoantennas and waveguides studied in this thesis showed photoemission hot spots and irregularities from surface roughness, oxidation, and contamination. A simple method for reducing these surface irregularities using in-situ $\mathrm{Ar^+}$ sputtering has been presented. Argon ion sputtering at low energies was shown to reduce hotpot intensity and improve the contrast between the substrate and photoemission from the near fields of

propagating SPPs in PEEM images. The surface roughness may still be further improved by fine-tuning the ion energy or dose, by using an alternative ion type or ion clusters, or by combining this process by thermal annealing.

FDTD simulations have been used to relate near-fields in nanohole arrays on gold films to the extraordinary optical transmission properties. Peaks in the transmission are associated with individual modes on given interfaces, which are determined by the dielectric environment, hole shape and size, film thickness, and lattice constant of the hole array. These parameters also influence the interactions between different localised and propagating surface modes. Imperfect arrays with missing or irregular nanoholes display broadened transmission peaks and as such shorter plasmon lifetimes.

When two identical ultrashort pulses are incident on a nanohole array but separated by a time delay the overall transmission is modified by the presence of the second pulse. Plots of the change in transmission spectra with delay (spectrograms) show that there is an autocorrelation component to this variable transmission, the period of which is governed by the frequency of the incident pulses, but also a modulation envelope which is unique to each transmission peak. The time structure of this envelope can be deconstructed by empirical mode decomposition. The structure is complex, being shaped by the many possible interactions between propagating and localised modes on different interfaces, and damping from scattering and radiative losses. Some of these interactions have been correlated with features of the peak modulation envelopes; a greater number of simulations using a wider number of array parameters would be needed to fully untangle the relationships. High and narrow transmission peaks can be achieved by coupling between different interface modes.

Nanohole arrays in gold films were fabricated using a combination of thermal evaporation and electron beam lithography. Fabricated arrays display some irregularities around the holes and some degree of incomplete lift-off, giving broad linewidths and low relative transmission, consistent with simulations of flawed arrays. When dispersive detection optics are used to collect the transmitted signal, the autocorrelation signal present in the simulation becomes dominant, masking any modulation envelope. When a photodiode was used to collect the transmitted signal, the modulation of this signal by the hole array could be clearly observed. The shape of the transmitted signal matched well between experiment and simulation.

For future experiments, to link the transmission dynamics with near-field interactions plasmonic near-fields on the film could be imaged with back-illuminated or normal-incidence PEEM. The prospect of dynamic molecular sensing could be realised by combining the nanohole arrays with molecular layers or nanofluidics.

Appendix A

FDTD theory and convergence testing results

The finite-difference time-domain method numerically solves Maxwell's equations by using finite differences to approximate the spatial and temporal derivatives. The simulation region consists of a computation space which is divided into a grid of small cells. Material properties are specified at points within each cell to represent physical objects. At an initial time an incident field is injected and the FDTD algorithm computes the electric and magnetic fields resulting between the interaction of the object and the incident field after a very short time interval. The process is repeated over successive time intervals with the aim of eventually achieving a steady-state result. Frequency-domain results can be obtained from the Fourier transform of the time-domain results.

Making the finite computation space appear infinite to the incident fields requires careful selection of the boundary conditions. Layers of lossy cells known as perfectly matched layers (PMLs) around the outside of the simulation region are commonly used to suppress reflections from the boundaries. Alternatively, periodic or Bloch boundaries can be used when the physical object and the fields along those axes are uniform or periodic.

Simulation parameters such as the cell size and boundary conditions can have important implications on the validity of results. Generally, having smaller cells and a greater number of PMLs reduces the errors inherent in the numerical simulation, but at the cost of increased computation time. Testing the convergence of simulation results with respect to these parameters ensures that parameters can be chosen which give minimal errors without requiring overlong, impractical simulations.

For the EOT simulations performed in this thesis, transmission was chosen as the result to test convergence. If a parameter is varied by N steps, the rolling error between each

successive step i via can be estimated from the difference in total transmission via

$$\Delta\sigma(i) = \sqrt{\frac{\int_{\lambda_1}^{\lambda_L}(\sigma_i - \sigma_{i-1})^2 d\lambda}{\int_{\lambda_1}^{\lambda_N}(\sigma_i)^2 d\lambda}} \tag{A.1}$$

and the absolute error from the difference between the current step i and final step N

$$\Delta\sigma_N(i) = \sqrt{\frac{\int_{\lambda_1}^{\lambda_L}(\sigma_i - \sigma_N)^2 d\lambda}{\int_{\lambda_1}^{\lambda_L}(\sigma_i)^2 d\lambda}} \tag{A.2}$$

Summaries of the convergence testing for the simulation span along the z-axis and the reflectivity of the PMLs can be found in Reference [249]. Converge test results for the mesh size in the mesh override region (around the nanoholes), the mesh accuracy niveau, and the number of PML layers are presented in Figures A.1 to A.3. Values for Equation A.1 and A.2 are shown in blue and green, respectively.
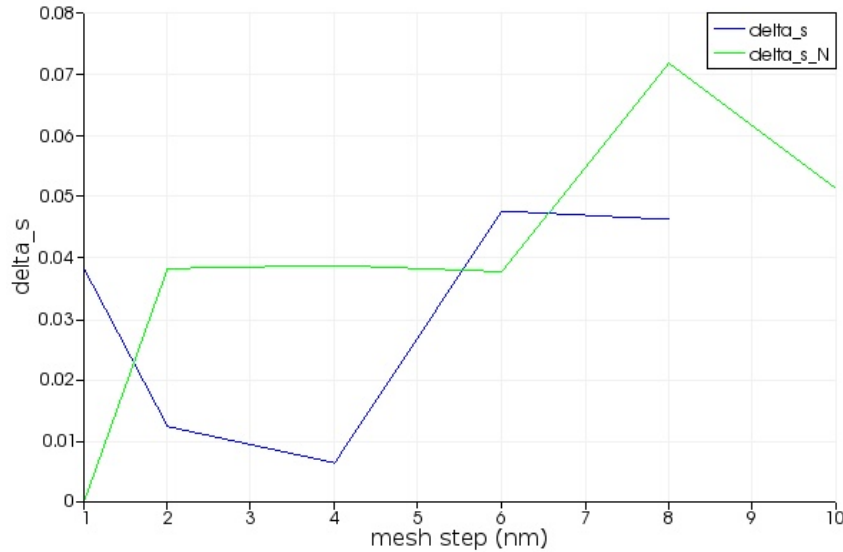
Figure A.1: The results of convergence testing for a range of different overall mesh steps in the override region. Enabling a mesh override region establishes a simulation subvolume in which there is a fixed, given mesh step size. As is generally the case, smaller step sizes produce smaller errors with increased computation time. For stand-alone simulations mesh steps of 1.5 nm were used; for scans of the transmission versus pulse delay and 4 nm were used, respectively.
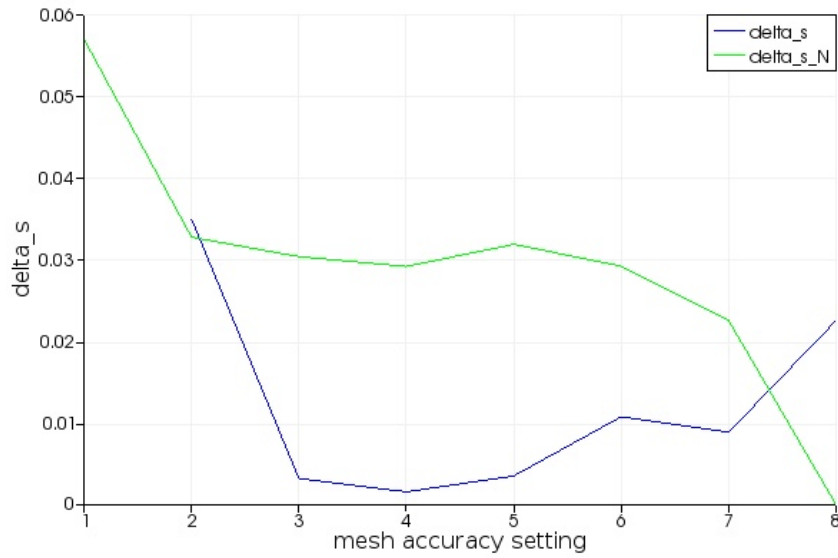
Figure A.2: The results of convergence testing for a range of different overall mesh accuracy niveaus. This parameter sets the number of mesh points per wavelength, varying from 6 per wavelength for a niveau of 1 to 34 per wavelength for a niveau of 8. Increasing from a niveau of 4 to 7 delivers no great reduction in error, and at a niveau of 8 the simulation time becomes extensive.
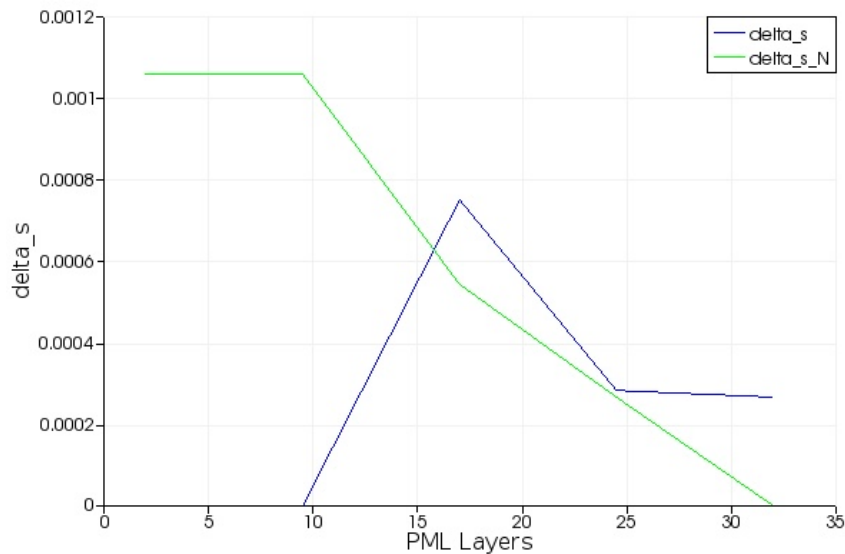
Figure A.3: The results of convergence testing for various numbers of PMLs in the z-direction. The level of error introduced for any number of layers in very small in this case, so the default value of 12 layers was used.

Appendix B

Spectrograms for Various Array Parameters

Simulated spectrograms of the transmission of 5 fs pulses for various nanohole arrays which were not presented in the previous chapters are shown below. Figures B.1 to B.6 are spectrograms for a hexagonal array with 'standard' or base parameters $a = 650\,\text{nm}$, $h = 200\,\text{nm}$, and $d = 200\,\text{nm}$, and a silicon nitride substrate and air superstrate/background (refer to Figure 5.2).
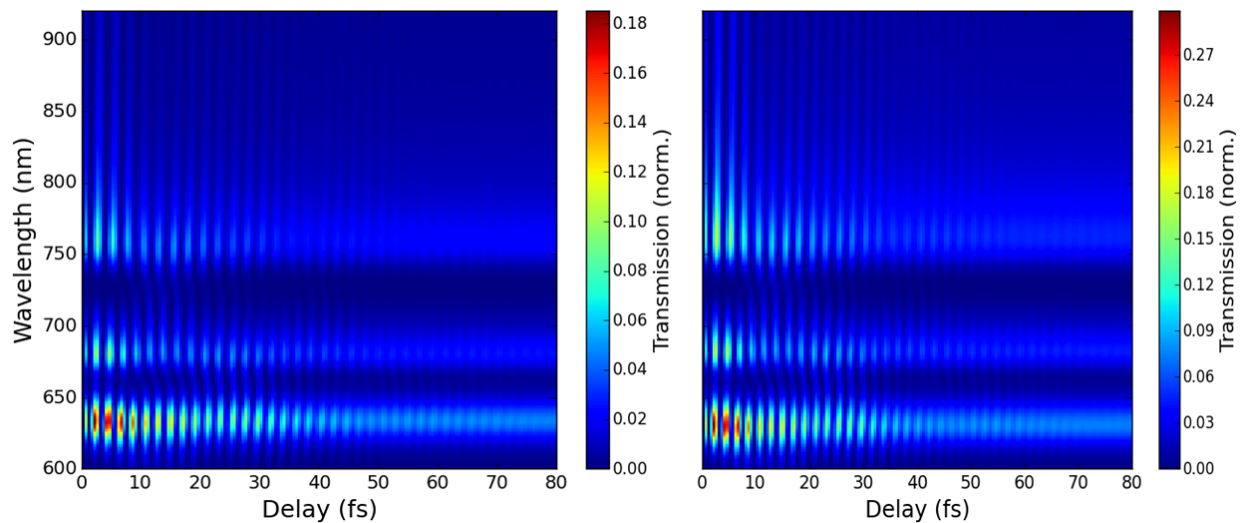
Figure B.1: Simulated spectrograms of the transmission of hexagonal gold nanohole arrays with $h = 160\,\text{nm}$ (left) and $h = 120\,\text{nm}$ (right), 40 nm and 80 nm thinner, respectively, than the standard array.

Figures B.7 to B.11 are spectrograms for a square nanohole array with $a = 650\,\text{nm}$, $h = 200\,\text{nm}$, and $d = 200\,\text{nm}$.
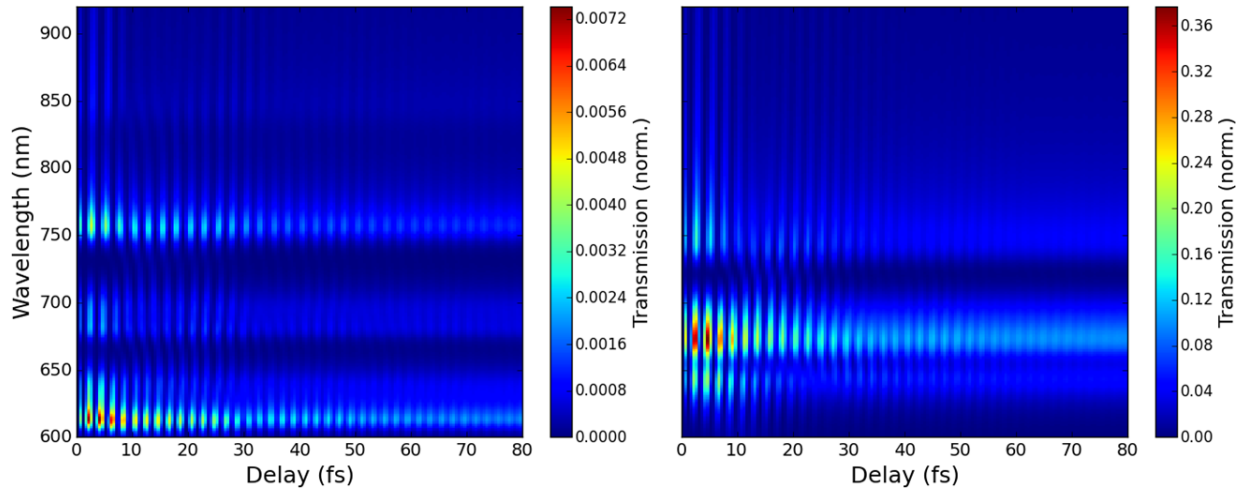
Figure B.2: Simulated spectrogram of the transmission of hexagonal gold nanohole arrays with a smaller hole size $d = 150\,\text{nm}$ (left) and larger hole size $d = 250\,\text{nm}$ (right) than the standard array.
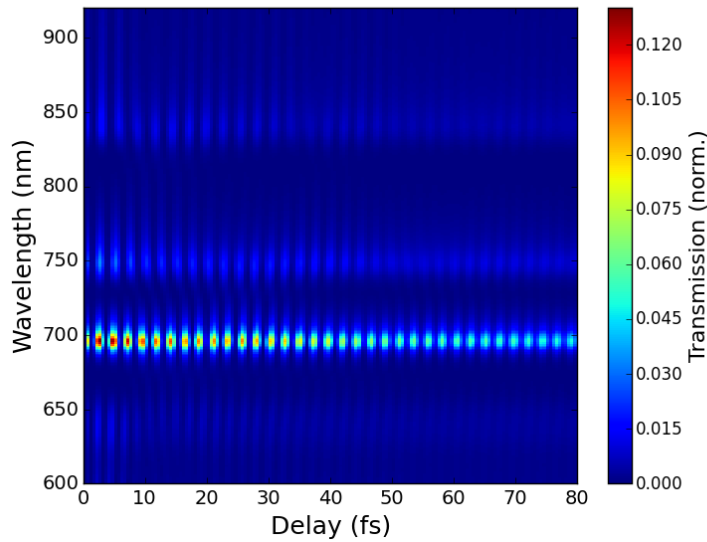
Figure B.3: Simulated spectrogram of the transmission of a hexagonal gold nanohole array with a larger lattice spacing $a = 750\,\text{nm}$ than the standard array.
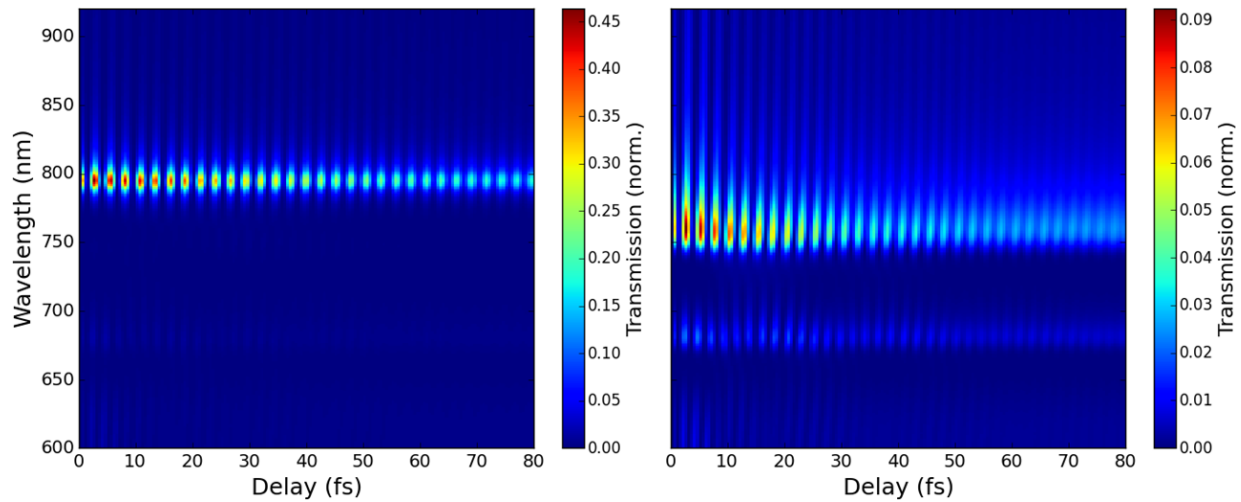
Figure B.4: Simulated spectrogram of the transmission of hexagonal gold nanohole arrays with background indices $n = 1.3$ (left) and $n = 2.0$ (right)
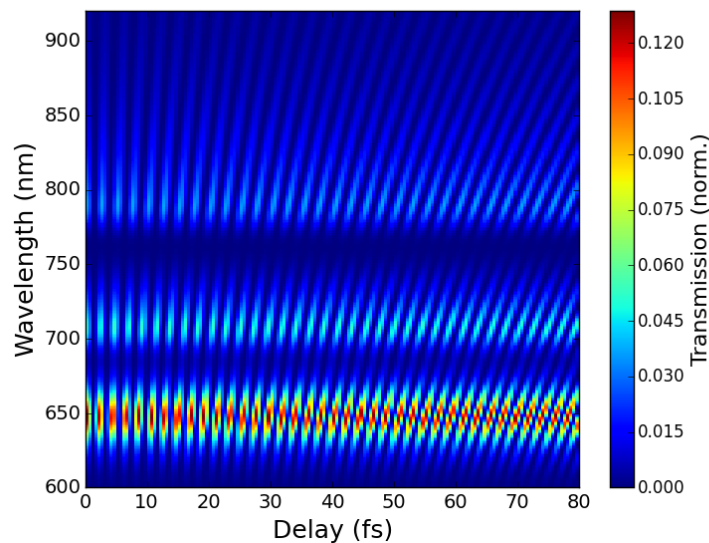
Figure B.5: Simulated spectrogram of the transmission of a hexagonal gold nanohole array with the apodisation window removed.
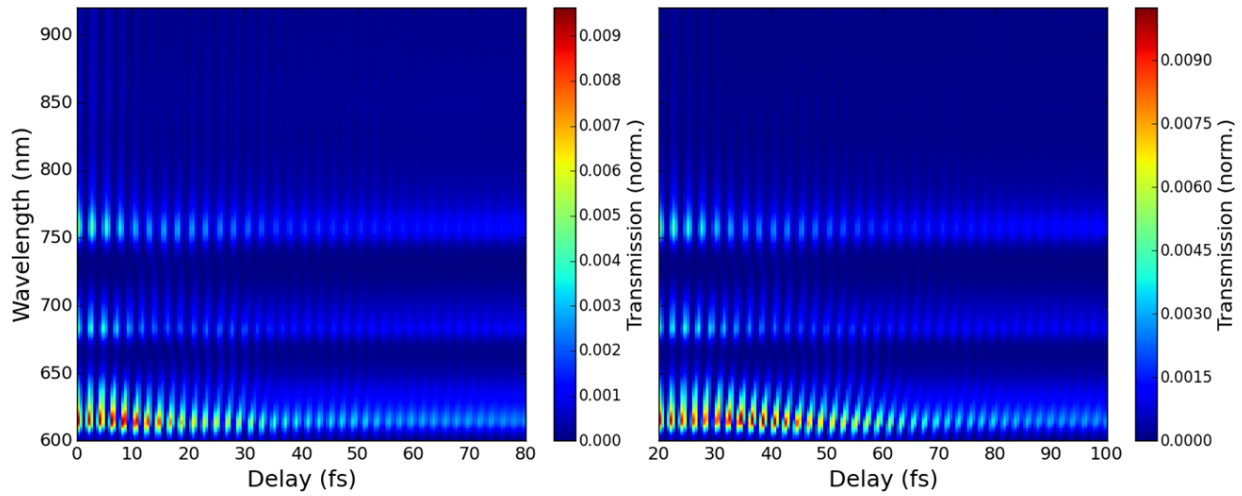
Figure B.6: Simulated spectrogram of the transmission of hexagonal gold nanohole arrays with 10 fs (left) and 20 fs (right) incident pulses.
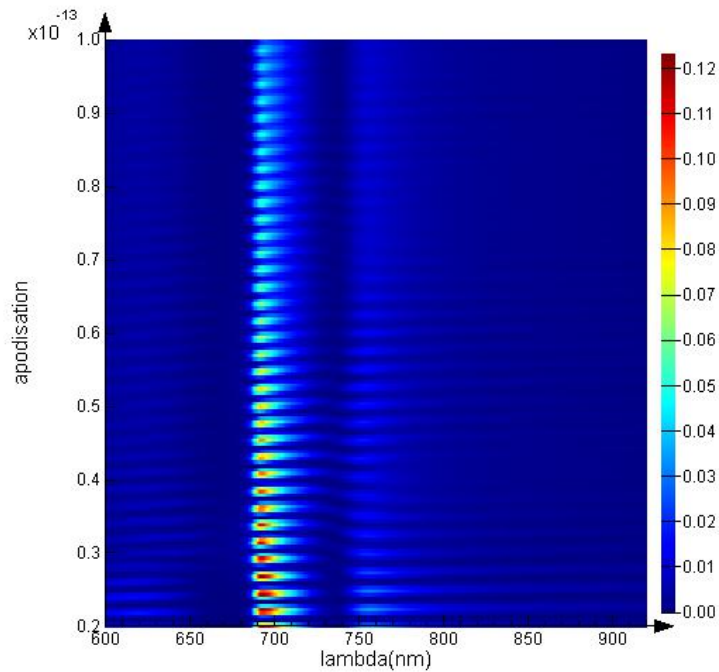
Figure B.7: Simulated spectrogram of the transmission of a square gold nanohole array on a silicon nitride substrate with standard parameters $a = 650\,\text{nm}$, $h = 200\,\text{nm}$, and $d = 200\,\text{nm}$.
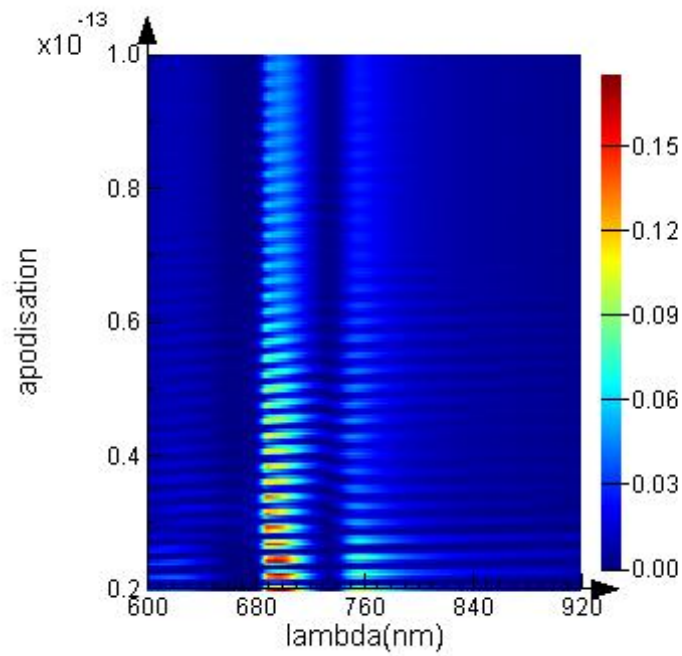
Figure B.8: Simulated spectrogram of the transmission of a square gold nanohole array with $h = 150\,\mathrm{nm}$, $50\,\mathrm{nm}$ thinner than the standard array.
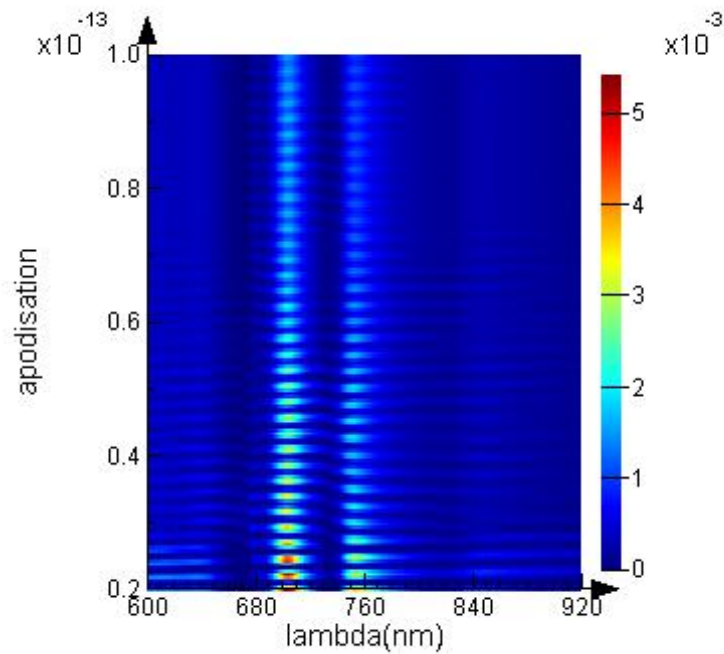
Figure B.9: Simulated spectrogram of the transmission of a square gold nanohole array with a smaller hole size $d = 150\,\mathrm{nm}$ than the standard array
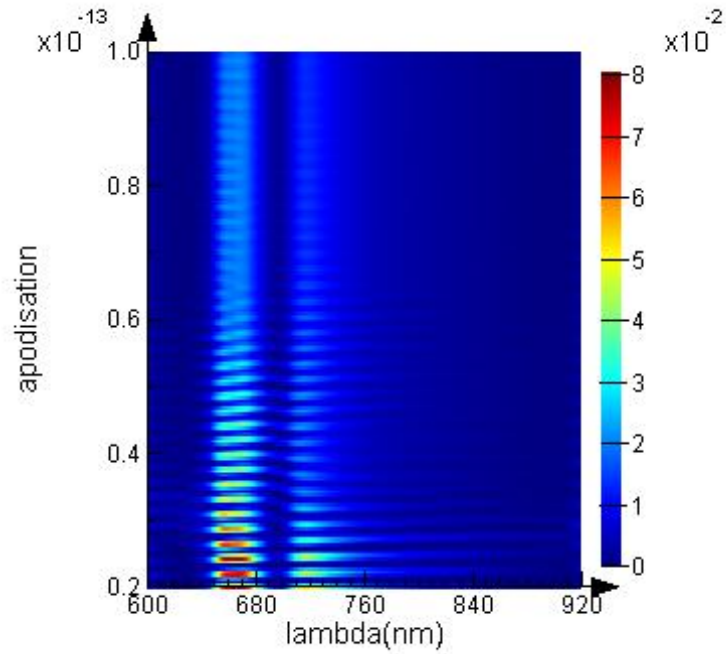
Figure B.10: Simulated spectrogram of the transmission of a square gold nanohole array with a smaller lattice spacing $a = 600\,\mathrm{nm}$ than the standard array
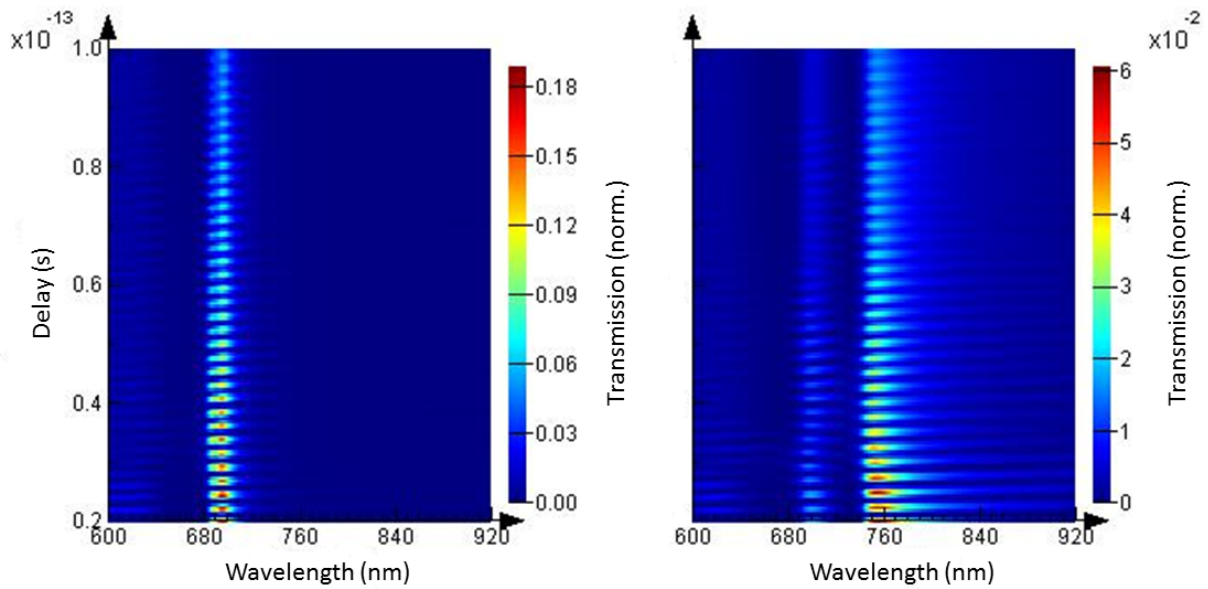
Figure B.11: Simulated spectrograms of the transmission of square gold nanohole arrays in symmetric dielectric environments, with background indices $n = 1.0$ (left) and $n = 2.0$ (right)

Bibliography

[1] M. Bai, C. Guerrero, S. Ioanid, E. Paz, M. Sanz, and N. Garc'ıa. Measuring the speed of a surface plasmon. *Phys. Rev. B*, 69:115416, 2004.

[2] Y. Gong, A. G. Joly, D. Hu, P. Z. El-Khoury, and W. P. Hess. Ultrafast imaging of surface plasmons propagating on a gold surface. *Nano Lett.*, 15:3472–3478, 2015.

[3] T. W. Ebbesen, C. Genet, and S. I. Bozhevolnyi. Surface-plasmon circuitry. *Phys. Today*, 61:44–50, 2008.

[4] D. Gramotnev, M. W. Vogel, and M. I. Stockman. Optimized nonadiabatic nanofocusing of plasmons by tapered metal rods. *J. Appl. Phys.*, 104:034311, 2008.

[5] K. C. Vernon, D. Gramotnev, and D. K. Pile. Adiabatic nanofocusing of plasmons by a sharp metal wedge on a dielectric substrate. *J. Appl. Phys.*, 101:104312, 2007.

[6] D. Gramotnev and S. I. Bozhevolnyi. Nanofocusing of electromagnetic radiation. *Nat. Photon.*, 8:13–22, 2013.

[7] N. Lindquist, P. Nagpal, K. M. McPeak, D. J. Norris, and S-H. Oh. Engineering metallic nanostructures for plasmonics and nanophotonics. *Rep. Prog. Phys.*, 75:036501, 2012.

[8] E. J. Teo, N. Toyoda, C. Yang, A. A. Bettiol, and J. H. Teng. Nanoscale smoothing of plasmonic films and structures using cluster ion beam irradiation. *Appl. Phys. A*, 117:719–723, 2014.

[9] H. M. Wassel, J. K. Valamehr, and Chong F. T. Opportunities and challenges of using plasmonic components in nanophotonic architectures. *IEEE Trans. Emerg. Sel. Topics Circuits Syst.*, 2:154–168, 2012.

[10] K. Y. Kim. *Plasmonics - Principles and Applications*. InTech, 2012.

[11] Vincenzo Giannini, Antonio I. Fernández-Domínguez, Susannah C. Heck, and Stefan A. Maier. Plasmonic nanoantennas: Fundamentals and their use in controlling the radiative properties of nanoemitters. *Chemical Reviews*, 111(6):3888–3912, 2011.

[12] B. Lamprecht, J. R. Krenn, G. Schider, H. Ditlbacher, M. Salerno, N. Felidj, A. Leitner, F. R. Aussenegg, and J-C. Weeber. Surface plasmon propagation in microscale metal stripes. *App. Phys. Lett.*, 79(1):51–53, 2001.

[13] J-C. Weeber, J. R. Krenn, A. Dereux, B. Lamprecht, Y. Lacroute, and J. P. Goudonnet. Near-field observation of surface plasmon polariton propagation on thin metal stripes. *Phys. Rev. B*, 64:045411, 2001.

[14] C. Genet and T. W. Ebbesen. Light in tiny holes. *Nature*, 445:39 – 46, 2007.

[15] H. S. Lee, Y. T. Yoon, S. S. Lee, S. H. Kin, and K. D. Lee. Color filter based on a subwavelength patterned metal grating. *Opt. Exp.*, 15:15457–15463, 2007.

[16] T. Onishi, T. Tanigawa, T. Ueda, and D. Ueda. Polarization control of vertical-cavity surface-emitting lasers by utilizing surface plasmon resonance. *IEEE J. Quantum Electron.*, 43:1123, 2007.

[17] F. J. García-Vidal, L. Martín-Moreno, T. W. Ebbesen, and L. Kuipers. Light passing through subwavelength apertures. *Rev. Mod. Phys.*, 82:729–787, 2010.

[18] C. Ropers, T. Elsaesser, G. Cerullo, M. Zavelani-Rossi, and C. Lienau. Ultrafast optical excitations of metallic nanostructures: from light confinement to a novel electron source. *New J. Phys.*, 9:397, 2007.

[19] M. Cooper. Optical biosensors in drug discovery. *Nat. Rev. Drug Discovery*, 1:515–528, 2002.

[20] A. G. Brolo, R. Gordon, B. Leathem, and K. L. Kavanagh. Surface plasmon sensor based on the enhanced light transmission through arrays of nanoholes in gold films. *Laser & Photon. Rev.*, 20:4813, 2004.

[21] T. Rindzevicius, Y. Alaverdyan, A. Dahlin, F. Höök, D. S. Sutherland, and M. Käll. Plasmonic sensing characteristics of single nanometric holes. *Nano Lett.*, 5:2335–2339, 2005.

[22] F. Eftekhari, C. Escobedo, J. Ferreira, X. Duan, E. M. Girotto, A. G. Brolo, R. Gordon, and D. Sinton. Nanoholes as nanochannels: Flow-through plasmonic sensing. *Analytical Chemistry*, 81:4308–4311, 2009.

[23] S. Maier. *Plasmonics: Fundamentals and Applications*. Springer, 2007.

[24] R. Müller, V. Malyarchuk, and C. Lienau. Three-dimensional theory on light-induced near-field dynamics in a metal film with a periodic array of nanoholes. *Phys. Rev. B*, 68:205415, 2003.

[25] J. Dintinger, I. Robel, P. V. Kamat, C. Genet, and T. W. Ebbesen. Terahertz all-optical molecule- plasmon modulation. *Advanced Materials*, 18:1645–1648, 2006.

[26] V. Halté, A. Benabbas, L. Guidoni, and J.-Y. Bigot. Femtosecond dynamics of the transmission of gold arrays of sub-wavelength holes. *Phys. Stat. Sol.*, 242:1872–1876, 2005.

[27] E. Hendry, M. J. Lockyear, J. Gómez Rivas, L. Kuipers, and M. Bonn. Ultrafast optical switching of the thz transmission through metallic subwavelength hole arrays. *Phys. Rev. B*, 75:235305, 2007.

[28] A. Sommerfeld. Über die Fortpflanzung elektrodynamischer Wellen an längs eines Drahts. *Ann. Phys. und Chemie*, 67:233–290, 1899.

[29] J. Zenneck. Über die Fortpflanzung ebener elektromagnetischer Wellen längs einer ebenen Leiterfläche und ihre Beziehung zur drahtlosen Telegraphie. *Ann. Phys.*, 328:846–866, 1907.

[30] R. W. Wood. On a remarkable case of uneven distribution of light in a diffraction grating spectrum. *Proc. Phys. Soc. London*, 18:269, 1902.

[31] U. Fano. The theory of anomalous diffraction gratings and of quasi-stationary waves on metallic surfaces (Sommerfeld waves). *J. Opt. Soc. Am.*, 31:213–222, 1941.

[32] A. Goswami. *Thin Film Fundamentals*. New Age International, 1996.

[33] L. Eckertová. *Physics of Thin Films*. Plenum Press, 1977.

[34] G. Ruthemann. Elektronenbremsung an Röntgenniveaus. *Ann. Phys.*, 437:135–146, 1948.

[35] W. Lang. Geschwidigkeitsverluste mittelschneller Elektronen beim Durchgang durch dunne Metallfolien. *Optik*, 3:233–246, 1948.

[36] D. Pines and D. Bohm. A collective description of electron interactions: Ii. collective vs individual particle aspects of the interactions. *Phys. Rev.*, 85:338–353, 1952.

[37] L. Tonks and I. Langmuir. Oscillations in ionized gases. *Phys. Rev.*, 33:195–211, 1929.

[38] R. H. Ritchie. Plasma losses by fast electrons in thin films. *Phys. Rev.*, 106:874–881, 1957.

[39] C. J. Powell and J. B. Swan. Origin of the characteristic electron energy losses in aluminum. *Phys. Rev.*, 115:869–875, 1959.

[40] E. A. Stern and R. A. Ferrell. Surface plasma oscillations of a degenerate electron gas. *Phys. Rev.*, 120:130–136, 1960.

[41] R. H. Ritchie, E. T. Arakawa, J. J. Cowan, and R. N. Hamm. Surface-plasmon resonance effect in grating diffraction. *Phys. Rev. Lett.*, 21:1530–1533, 1968.

[42] I. Freestone, N. Meeks, M. Sax, and C. Higgitt. The Lycurgus cup — a Roman nanotechnology. *Gold Bulletin*, 40:270–277, 2007.

[43] A. Myers. Plasmons resonate in atomic-scale metal particles, March 2012.

[44] A. Otto. Excitation of nonradiative surface plasma waves in silver by the method of frustrated total reflection. *Z. Physik*, 216:398–410, 1968.

[45] E. Kretschmann. Die Bestimmung optischer Konstanten von Metallen durch Anregung von Oberflächenplasmaschwingungen. *Z. Physik*, 241:313–324, 1971.

[46] M. Fleischmann, P. J. Hendra, and A. J. McQuillan. Raman spectra of pyridine adsorbed at a silver electrode. *Chem. Phys. Lett.*, 26:163 – 166, 1974.

[47] S. Nie and S. R. Emory. Probing single molecules and single nanoparticles by surface-enhanced raman scattering. *Science*, 275:1102–1106, 1997.

[48] E. J. Blackie, E. C. Le Ru, and P. G. Etchegoin. Single-molecule surface-enhanced raman spectroscopy of nonresonant molecules. *J. of the Am. Chem. Soc.*, 131:14466–14472, 2009.

[49] J. Homola. Surface plasmon resonance sensors for detection of chemical and biological species. *Chem. Rev.*, 108:462–493, 2008.

[50] B. Sepúlveda, P. C. Angelomé, L. M. Lechuga, and L. M. Liz-Marzán. Lspr-based nanobiosensors. *Nano Today*, 4:244 – 251, 2009.

[51] K. Saha, S. S. Agasti, C. Kim, X. Li, and V. M. Rotello. Gold nanoparticles in chemical and biological sensing. *Chem. Rev.*, 112:2739–2779, 2012.

[52] X. Huang, I. H. El-Sayed, W. Qian, and M. A. El-Sayed. Cancer cell imaging and photothermal therapy in the near-infrared region by using gold nanorods. *J. of the Am. Chem. Soc.*, 128:2115–2120, 2006.

[53] P. K. Jain, I. H. El-Sayed, and M. A. El-Sayed. Au nanoparticles target cancer. *Nano Today*, 2:18 – 29, 2007.

[54] E. Boisselier and D. Astruc. Gold nanoparticles in nanomedicine: preparations, imaging, diagnostics, therapies and toxicity. *Chem. Soc. Rev.*, 6:1759–1782, 2009.

[55] O. Sqalli, I. Utke, P. Hoffmann, and F. Marquis-Weible. Gold elliptical nanoantennas as probes for near field optical microscopy. *J. of App. Phys.*, 92:1078–1083, 2002.

[56] N. Fang, H. Lee, C. Sun, and X. Zhang. Sub-diffraction-limited optical imaging with a silver superlens. *Science*, 308:534–537, 2005.

[57] W. Srituravanich, N. Fang, C. Sun, Q. Luo, and X. Zhang. Plasmonic nanolithography. *Nano Lett.*, 4:1085–1088, 2004.

[58] L. Pan, Y. Park, Y. Xiong, E. Ulin-Avila, Y. Wang, L. Zeng, S. Xiong, J. Rho, C. Sun, D. B. Bogy, and X. Zhang. Maskless plasmonic lithography at 22 nm resolution. *Sci. Rep.*, 1, 2011.

[59] H. A. Atwater and A. Polman. Plasmonics for improved photovoltaic devices. *Nat. Mater.*, 9:205–213, 2010.

[60] V. E. Ferry, M. A. Verschuuren, H. B. T. Li, E. Verhagen, R. J. Walters, R. E. I. Schropp, H. A. Atwater, and A. Polman. Light trapping in ultrathin plasmonic solar cells. *Opt. Express*, 18:A237–A245, 2010.

[61] X. Li, W. C. H. Choy, L. Huo, F. Xie, W. E. I. Sha, B. Ding, X. Guo, Y. Li, J. Hou, J.i You, and Y. Yang. Dual Plasmonic Nanostructures for High Performance Inverted Organic Solar Cells. *Adv. Mater.*, 24(22):3046–3052, 2012.

[62] J-S. Huang, V. Callegari, P. Geisler, C. Bruening, J. Kern, J. C. Prangsma, X. Wu, T. Feichtner, J. Ziegler, P. Weinmann, M. Kamp, A. Forchel, P. Biagioni, U. Sennhauser, and B. Hecht. Atomically flat single-crystalline gold nanostructures for plasmonic nanocircuitry. *Nat. Comm.*, 1, 2010.

[63] J. A. Schuller, E. S. Barnard, W. Cai, Y. C. Jun, J. S. White, and M. L. Brongersma. Plasmonics for extreme light concentration and manipulation. *Nat. Mater.*, 9:193–204, 2010.

[64] P. Zijlstra, J. W. M. Chon, and M. Gu. Five-dimensional optical recording mediated by surface plasmons in gold nanorods. *Nature*, 459(7245):410–413, 2009.

[65] W. A. Challener, C. Peng, A. V. Itagi, D. Karns, W. Peng, Y. Peng, X. Yang, X. Zhu, N. J. Gokemeijer, Y-T. Hsia, G. Ju, R. E. Rottmayer, M. A. Seigler, and E. C. Gage. Heat-assisted magnetic recording by a near-field transducer with efficient optical energy transfer. *Nat. Photon.*, 3:220–224, 2009.

[66] B. Liedberg, C. Nylander, and I. Lunström. Surface plasmon resonance for gas detection and biosensing. *Sens. Actuators*, 4:299 – 304, 1983.

[67] D. Sarid and W. Challener. *Modern Introduction to Surface Plasmons*. Cambridge, 2010.

[68] W. Cai and V. Shalaev. *Optical Metamaterials: Fundamentals and Applications*. Springer, 2009.

[69] P. B. Johnson and R. W. Christy. Optical constants of the noble metals. *Phys. Rev. B*, 6:4370–4379, 1972.

[70] Babak Dastmalchi, Philippe Tassin, Thomas Koschny, and Costas M. Soukoulis. A new perspective on plasmonics: Confinement and propagation length of surface plasmons for different materials and geometries. *Adv. Opt. Mater.*, 4(1):177–184, 2016.

[71] Naik G. V., Shalaev M., and Boltasseva A. Optical constants of the noble metals. *Adv. Mat.*, 25:3264–3294, 2013.

[72] L. Novotny and B. Hecht. *Principles of Nano-Optics*. Cambridge University Press, 2012.

[73] H. Ditlbacher, J. R. Krenn, G. Schider, A. Leitner, and F. R. Aussenegg. Two-dimensional optics with surface plasmon polaritons. *Appl. Phys. Lett.*, 81:1762–1764, 2002b.

[74] G. Lévêque and O. J. F. Martin. Optimization of finite diffraction gratings for the excitation of surface plasmons. *J. of App. Phys.*, 100, 2006.

[75] H. W. Kihm, K. G. Lee, D. S. Kim, J. H. Kang, and Q-Han Park. Control of surface plasmon generation efficiency by slit-width tuning. *Appl. Phys. Lett.*, 92:051115, 2008.

[76] A. P. Hibbins. *Grating Coupling of Surface Plasmon Polaritons*. PhD thesis, University of Exeter, 1999.

[77] A. Giannattasio, I. R. Hooper, and W. L. Barnes. Dependence on surface profile in grating-assisted coupling of light to surface plasmon-polaritons. *Opt. Commun.*, 261:291 – 295, 2006.

[78] I. S. Spevak, M. A. Timchenko, and A. V. Kats. Design of specific gratings operating under surface plasmon-polariton resonance. *Opt. Lett.*, 36:1419–1421, 2011.

[79] I. R. Hooper and J. R. Sambles. Dispersion of surface plasmon polaritons on short-pitch metal gratings. *Phys. Rev. B*, 65:165432, 2002.

[80] W. L. Barnes, A. Dereaux, and T. W. Ebbesen. Surface plasmon subwavelength optics. *Nature*, 424:824–830, 2003.

[81] Philip Kahl, Simone Wall, Christian Witt, Christian Schneider, Daniela Bayer, Alexander Fischer, Pascal Melchior, Michael Horn-von Hoegen, Martin Aeschlimann, and Frank-J. Meyer zu Heringdorf. Normal-incidence photoemission electron microscopy (NI-PEEM) for imaging surface plasmon polaritons. *Plasmonics*, 9:1401–1407, 2014.

[82] A. Bouhelier and G. P. Wiederrecht. Surface plasmon rainbow jets. *Opt. Lett.*, 30:884–886, 2005.

[83] L. Novotny and B. Hecht. *Principles of Nano-Optics*. Cambridge University Press, 2006.

[84] B. Hecht, H. Bielefeld, L. Novotny, Y. Inouye, and D. W. Pohl. Local excitation, scattering, and interference of surface plasmons. *Phys. Rev. Lett.*, 77:1889–1892, 2006.

[85] M. V. Bashevoy, F. Jonsson, A. V. Krasavin, N. I. Zheludev, Y. Chen, and M. I. Stockman. Generation of traveling surface plasmon waves by free-electron impact. *Nano Lett.*, 6:1113–1115, 2006.

[86] W. Cai, R. Sainidou, J. Xu, A. Polman, and F. Javier Garcia de Abajo. Efficient generation of propagating plasmons by electron beams. *Nano Lett.*, 9:1176–1181, 2009.

[87] G. I. Stegeman, R. F. Wallis, and A. A. Maradudin. Excitation of surface polaritons by end-fire coupling. *Opt. Lett.*, 8:386–388, 1983.

[88] S. Maier, P. E. Barclay, T. J. Johnson, M. D. Friedman, and O. Painter. Low-loss fiber accessible plasmon waveguides for planar energy guiding and sensing. *Appl. Phys. Lett.*, 84:3990–3992, 2004.

[89] S. Maier, M. D. Friedman, P. E. Barclay, and O. Painter. Experimental demonstration of fiber-accessible metal nanoparticle plasmon waveguides for planar energy guiding and sensing. *Appl. Phys. Lett.*, 86:071103, 2005.

[90] K. L. Kelly, E. C. Coronado, L. L. Zhao, and G. C. Schatz. The optical properties of metal nanoparticles: The influence of size, shape, and dielectric environment. *J. Phys. Chem. B*, 107:668–677, 2002.

[91] S. Maier and H. Atwater. Plasmonics: Localization and guiding of electromagnetic energy in metal/dielectric structures. *J. Appl. Phys.*, 98:011101, 2005.

[92] X. Younan and N. J. Halas. Shape-controlled synthesis and surface plasmonic properties of metallic nanostructures. *MRS Bulletin*, 30:338–348, 2005.

[93] K. A. Willets and R. P. Van Duyne. Localized surface plasmon resonance spectroscopy and sensing. *Annu. Rev. Phys. Chem.*, 58:267–297, 2007.

[94] G. Mie. Beiträge zur optik trüber medien, speziell kolloidaler metallösungen. *Ann. Phys.*, 25:377, 1908.

[95] O Demichel, M Petit, Gérard Colas des Francs, A Bouhelier, E Hertz, F Billard, F Fornel, and Benoit Cluzel. Selective excitation of bright and dark plasmonic resonances of single gold nanorods. *Opt. Express*, 22:15088–15096, 2014.

[96] A. Sundaramurthy, K. B. Crozier, and G. Kino. Field enhancement and gap dependent resonance in a system of two opposing tip-to-tip au nanotriangles. *Phys. Rev. B*, 72:165409, 2005.

[97] D. P. Fromm, A. Sundaramurthy, P. J. Schuck, G. Kino, and W. E. Moerner. Gap-dependent optical coupling of single "bowtie" nanoantennas resonant in the visible. *Nano Lett.*, 4:957–961, 2004.

[98] S. Dodson, M. Haggui, R. Bachelot, J. Plain, S. Li, and Q. Xiong. Optimizing electromagnetic hotspots in plasmonic bowtie nanoantennae. *J. Phys. Chem. Lett.*, 4:496–501, 2013.

[99] M. Kauranen. Nonlinear plasmonics. *Nat. Photon.*, 6:737–748, 2012.

[100] W. Fan, S. Zhang, N.-C. Panoiu, A. Abdenour, S. Krishna, R. M. Osgood, Jr., K. J. Malloy, and S. R. J. Brueck. Second harmonic generation from a nanopatterned isotropic nonlinear material. *Nano Lett.*, 6:1027–1030, 2006.

[101] M. Celebrano, X. Wu, M. Baselli, S. Grossmann, P. Biagioni, A. Locatelli, C. De Angelis, G. Cerullo, R. Osellame, B. Hecht, F. Ciccacci, and M. Finazzi. Mode matching in multiresonant plasmonic nanoantennas for enhanced second harmonic generation. *Nat. Nanotechnol.*, 10:412, 2015.

[102] N. C. Panoiu, W. E. I. Sha, D. Y. Lei, and G-C. Li. Nonlinear optics in plasmonic nanostructures. *J. Opt.*, 20:083001, 2018.

[103] C. Argyropoulos, P.-Y. Chen, G. D'Aguanno, and A. Alù. Temporal soliton excitation in an ϵ-near-zero plasmonic metamaterial. *Opt. Lett.*, 39:5566–5569, 2014.

[104] T. B. Hoang, G.M. Akselrod, C. Argyropoulos, J. Huang, D. R. Smith, and M. H. Mikkelsen. Ultrafast spontaneous emission source using plasmonic nanoantennas. *Nat. Commun.*, 6:7788, 2015.

[105] C. Ciracì, A. Rose, C. Argyropoulos, and D. R. Smith. Numerical studies of the modification of photodynamic processes by film-coupled plasmonic nanoparticles,. *J. Opt. Soc. Am. B*, 31:2601–2607, 2014.

[106] P. Berini. Plasmon-polariton modes guided by metal film of finite width. *Opt. Lett.*, 24:1011–1013, 1999.

[107] P. Berini. Long-range surface plasmon polaritons. *Adv. Opt. Photonics*, 1:484–588, 2009.

[108] Z. Han and S. I Bozhevolnyi. Radiation guiding with surface plasmon polaritons. *Rep. Prog. Phys.*, 76:016402, 2013.

[109] T. Nikolajsen, K. Leosson, I. Salakhutdinov, and S. I. Bozhevolnyi. Polymer-based surface-plasmon-polariton stripe waveguides at telecommunication wavelengths. *App. Phys. Lett.*, 82:668–670, 2003.

[110] S. Park, J. J. Ju, J. T. Kim, M-S. Kim, S. K. Park, J-M. Lee, W-J. Lee, and M-H. Lee. Sub-dB/cm propagation loss in silver stripe waveguides. *Opt. Express*, 17:697–702, 2009.

[111] P. Berini. Plasmon-polariton waves guided by thin lossy metal films of finite width: Bound modes of asymmetric structures. *Phys. Rev. B*, 63:125417, 2001.

[112] V. A. Zenin, R. Malureanu, I. P. Radko, A. V. Lavrinenko, and S. I. Bozhevolnyi. Near-field characterization of bound plasmonic modes in metal strip waveguides. *Opt. Express*, 24(5):4582–4590, 2016.

[113] J. Berthelot, F. Tantussi, R. Padmnabh, G. Colas des Francs, J-C. Weeber, A. Dereux, F. Fuso, M. Allegrini, and A. Bouhelier. Determinant role of the edges in defining surface plasmon propagation in stripe waveguides and tapered concentrators. *J. Opt. Soc. Am. B*, 29:226–231, 2012.

[114] R. Zia, M. D. Selker, and M. L. Brongersma. Leaky and bound modes of surface plasmon waveguides. *Phys. Rev. B*, 71:165431, 2005.

[115] J-C. Weeber, Y. Lacroute, and A. Dereux. Optical near-field distributions of surface plasmon waveguide modes. *Phys. Rev. B*, 68:115401, 2003.

[116] R. Zia, A. Chandran, and M. L. Brongersma. Dielectric waveguide model for guided surface polaritons. *Opt. Lett.*, 30:1473–1475, 2005.

[117] R. Fujimoto, A. Kaneta, K. Okamoto, M. Funato, and Y. Kawakami. Interference of the surface plasmon polaritons with an ag waveguide probed by dual-probe scanning near-field microscopy. *App. Surf. Sci.*, 258:7372–7376, 2012.

[118] V. A. Zenin, A. Andryieuski, R. Malureanu, I. P. Radko, V. S. Volkov, D. Gramotnev, A. V. Lavrinenko, and S. Bozhevolnyi. Boosting local field enhancement by on-chip nanofocusing and impedance-matched plasmonic nanoantennas. *Nano Lett.*, 15:8148–8154, 2015.

[119] D. Gramotnev and S. I. Bozhevolnyi. Plasmonics beyond the diffraction limit. *Nat. Photon.*, 4:83–91, 2010.

[120] K. V. Nerkararyan. Superfocusing of a surface polariton in a wedge-like structure. *Phys. Lett. A*, 237:103–105, 1997.

[121] M. I. Stockman. Nanofocusing of optical energy in tapered plasmonic waveguides. *Phys. Rev. Let.*, 93:137404, 2004.

[122] C. Ropers, C. C. Neacsu, T. Elsaesser, M. Albrecht, M. B. Raschke, and C. Lienau. Grating-coupling of surface plasmons on to metallic tips: a nanoconfined light source. *Nano Lett.*, 7:2784–2788, 2007.

[123] D. Gramotnev and K. C. Vernon. Adiabatic nano-focusing of plasmons by sharp metallic wedges. *Appl. Phys. B*, 86:7–17, 2007.

[124] D. F. P. Pile and D. Gramotnev. Adiabatic and nonadiabatic nanofocusing of plasmons by tapered gap plasmon waveguides. *Appl. Phys. Lett.*, 89:041111, 2006.

[125] D. Gramotnev. Adiabatic nanofocusing of plasmons by sharp metallic grooves: geometrical optics approach. *J. Appl. Phys.*, 98:104302, 2005.

[126] H. Choo, M-K. Kim, M. Staffaroni, T. J. Seok, J. Bokor, S. Cabrini, P. J. Schuck, M. C. Wu, and E. Yablonovitch. Nanofocusing in a metal-insulator-metal gap plasmon waveguide with a three-dimensional linear taper. *Nat. Photon.*, 6:838–844, 2012.

[127] E. Verhagen, A. Polman, and L. K. Kuipers. Nanofocusing in laterally tapered plasmonic waveguides. *Opt. Express*, 16:45–57, 2008.

[128] M. W. Vogel and D. Gramotnev. Optimization of plasmon nano-focusing in tapered metal rods. *J. Nanophoton.*, 2:021852, 2008.

[129] M. Quinten, A. Leitner, J. R. Krenn, and F. R. Aussenegg. Electromagnetic energy transport via linear chains of silver nanoparticles. *Opt. Lett.*, 23:1331–1333, 1998.

[130] S. Maier, P. Kik, H. Atwater, S. Meltzer, E. Harel, B. E. Koel, and A. A. G. Requicha. Local detection of electromagnetic energy transport below the diffraction limit in metal nanoparticle plasmon waveguides. *Nat. Mat.*, 2:229–232, 2003b.

[131] S. Maier, P. Kik, and H. Atwater. Optical pulse propagation in metal nanoparticle chain waveguides. *Phys. Rev. B.*, 67:205402, 2003a.

[132] R. M. Dickson and A. L. Lyon. Unidirectional plasmon propagation in metallic nanowires. *J. Phys. Chem. B*, 104:6095–6098, 2000.

[133] J. R. Krenn, B. Lamprecht, H. Ditlbacher, G. Schider, M. Salerno, A. Leitner, and F. R. Aussenegg. Non-diffraction-limited light transport by gold nanowires. *Europhys. Lett.*, 60:663–669, 2002.

[134] Y. Fang, Y. Li, Z. Huang, P. Zhang, S. Nordlander, and Halas N. J. Branched silver nanowires as controllable plasmon routers. *Nano Lett.*, 10:1950–1954, 2010.

[135] W. Wang, Q. Yang, F. Fan, H. Xu, and Z. L. Wang. Light propagation in curved silver nanowire plasmonic waveguides. *Nano Lett.*, 11:1603–1608, 2011.

[136] K. Tanaka and M. Tanaka. Simulations of nanometric optical circuits based on surface plasmon polariton gap waveguide. *Appl. Phys. Lett.*, 82:1158–1560, 2003.

[137] S. Bozhevolnyi, V. Volkov, S. Valentyn, E. Devaux, and T. W. Ebbesen. Channel plasmon-polariton guiding by subwavelength metal grooves. *Phys. Rev. Lett.*, 95:046802, 2005.

[138] S. Bozhevolnyi, V. Volkov, E. Devaux, J-Y. Laluet, and T. W. Ebbesen. Channel plasmon subwavelength waveguide components including interferometers and ring resonators. *Nature*, 440:508–511, 2006.

[139] D. F. P. Pile, T. Ogawa, D. Gramotnev, M. Okamoto, T. amd Haraguchi, M. Fukui, and S. Matsuo. Theoretical and experimental investigation of strongly localized plasmons on triangular metal wedges for subwavelength waveguiding. *Appl. Phys. Lett.*, 87:061106, 2005.

[140] E. Moreno, S. Rodrigo, S. Bozhevolnyi, L. Martín-Moreno, and F. J. García-Vidal. Guiding and focusing of electromagnetic fields with wedge plasmon polaritons. *Phys. Rev. Lett.*, 100:023901, 2008.

[141] A. Boltasseva, V. S. Volkov, R. B. Nielsen, E. Moreno, S. Rodrigo, and S. Bozhevolnyi. Triangular metal wedges for subwavelength plasmon-polariton guiding at telecom wavelengths. *Phys. Rev. Lett.*, 100:023901, 2008.

[142] R. F. Oulton, V. J. Sorger, D. A. Genov, D. F. P. Pile, and X. Zhang. A hybrid plasmonic waveguide for subwavelength confinement and long-range propagation. *Nat. Photon.*, 2:496–500, 2008.

[143] M. Wu, Z. Han, and V. Van. Conductor-gap-silicon plasmonic waveguides and passive components at subwavelength scale. *Opt. Express*, 18:11728–11736, 2010.

[144] M. Brongersma, J. W. Hartman, and H. Atwater. Electromagnetic energy transfer and switching in nanoparticle chain arrays below the diffraction limit. *Phys. Rev. B*, 62:R16356–R–16359, 2000.

[145] I. Rasskazov, S. Karpov, and V. Markel. Nandecaying surface plasmon polaritons in linear chains of silver nanospheroids. *Opt. Lett.*, 38:4743–4746, 2013.

[146] H. Ditlbacher, A. Hohenau, D. Wagner, U. Kreibig, M. Rogers, F. Hofer, F. R. Aussenegg, and J. R. Krenn. Silver nanowires as surface plasmon resonators. *Phys. Rev. B*, 95:257403, 2005.

[147] H. A. Bethe. Theory of diffraction by small holes. *Phys. Rev.*, 66:163–182, 1944.

[148] C. J. Bouwkamp. On Bethe's theory of diffraction by small holes. *Philips Res. Rep.*, 5:321–332, 1950.

[149] S. B. Cohn. Microwave coupling by large apertures. *Proc. IRE*, 40:696–699, 1952.

[150] A. Roberts. Electromagnetic theory of diffraction by a circular aperture in a thick, perfectly conducting screen. *J. Opt. Soc. Am. A*, 4:1970–1983, 1987.

[151] T. W. Ebbesen, H. J. Lezec, H. F. Ghaemi, T. Thio, and P. A. Wolff. Surface plasmons enhance optical transmission through subwavelength holes. *Nature*, 391:667–669, 1998.

[152] H. F. Ghaemi, T. Thio, D. E. Grupp, T. W. Ebbesen, and H. J. Lezec. Surface plasmons enhance optical transmission through subwavelength holes. *Phys. Rev. B*, 58:6779–6782, 1998.

[153] S. G. Rodrigo, F. J. García-Vidal, and L. Martín-Moreno. Influence of material properties on extraordinary optical transmission through hole arrays. *Phys. Rev. B*, 77:075401, 2008.

[154] W. L. Barnes, W. A. Murray, J. Dintinger, E. Devaux, and T. W. Ebbesen. Surface plasmon polaritons and their role in the enhanced transmission of light through periodic arrays of subwavelength holes in a metal film. *Phys. Rev. Lett.*, 92:107401, 2004.

[155] F. Miyamaru, M. Tanaka, and M. Hangyo. Effect of hole diameter on terahertz surface-wave excitation in metal-hole arrays. *Phys. Rev. B*, 74:153416, 2006.

[156] A. Naweed, F. Baumann, Jr. W. A. Bailey, A. S. Karakashian, and W. D. Goodhue. Evidence for radiative damping in surface-plasmon-mediated light transmission through perforated conducting films. *J. Opt. Soc. Am. B*, 20:2534–2538, 2003.

[157] K. L. van der Molen, F. B. Segerink, N. F. van Hulst, and L. Kuipers. Influence of hole size on the extraordinary transmission through subwavelength hole arrays. *Appl. Phys. Lett.*, 85:4316–4318, 2004.

[158] D. S. Kim, S. C. Hohng, V. Malyarchuk, Y. C. Yoon, Y. H. Ahn, K. J. Yee, J. W. Park, J. Kim, Q. H. Park, and C. Lienau. Microscopic origin of surface-plasmon radiation in plasmonic band-gap nanostructures. *Phys. Rev. Lett.*, 91:143901, 2003.

[159] E. Popov, M. Nevière, S. Enoch, and R. Reinisch. Theory of light transmission through subwavelength hole arrays. *Phys. Rev. B*, 62:16100, 2000.

[160] F. J. García-Vidal, E. Moreno, J. A. Porto, and L. Martín-Moreno. Transmission of light through a single rectangular hole. *Phys. Rev. Lett.*, 95:103901, 2005.

[161] R. Gordon, L.K. Kiran Swaroop, D. Lepage, and A.G. Brolo. Resonant light transmission through a nanohole in a metal film. In *Nanotechnology, 2005. 5th IEEE Conference on*, pages 378–381 vol. 1, 2005.

[162] J. Gomez Rivas, C. Schotsch, P. Haring Bolivar, and H. Kurz. Enhanced transmission of thz radiation through subwavelength holes. *Phys. Rev. B*, 68:201306, 2003.

[163] M. J. Lockyear, A. P. Hibbins, and J. R. Sambles. Surface-topography-induced enhanced transmission and directivity of microwave radiation through a subwavelength circular metal aperture. *Appl. Phys. Lett.*, 84:2040–2042, 2004.

[164] L. Martín-Moreno, F. J. García-Vidal, H. J. Lezec, K. M. Pellerin, T. Thio, J. B. Pendry, and T. W. Ebbesen. Theory of extraordinary optical transmission through subwavelength hole arrays. *Phys. Rev. Lett.*, 86:1114–1117, 2001.

[165] H. J. Lezec and T. Thio. Diffracted evanescent wave model for enhanced and suppressed optical transmission through subwavelength hole arrays. *Opt. Express*, 12:3629–3651, 2004.

[166] G. Gay, O. Alloschery, B. Viaris de Lesegno, C. O'Dwyer, J. Weiner, and H. J. Lezec. The optical response of nanostructured surfaces and the composite diffracted evanescent wave model. *Nat. Phys.*, 2:262–267, 2006.

[167] B. A. Munk. *Frequency Selective Surfaces: Theory and Design.* Wiley Interscience, 2000.

[168] J. B. Pendry, L. Martín-Moreno, and F. J. García-Vidal. Mimicking surface plasmons with structured surfaces. *Science*, 305:847–848, 2004.

[169] P. Lalanne and J. P. Hugonin. Interaction between optical nano-objects at metallo-dielectric interfaces. *Nat. Phys.*, 2:551–556, 2006.

[170] T. D. Visser. Surface plasmons at work? *Nat. Phys.*, 2:509–510, 2006.

[171] L. Haitao and P. Lalanne. Microscopic theory of the extraordinary optical transmission. *Nature*, 452:728–731, 2008.

[172] F. van Beijnum, C. Rétif, C.B. Smiet, L. Haitao, P. Lalanne, and M.P. van Exter. Quasi-cylindrical wave contribution in experiments on extraordinary optical transmission. *Nature*, 492:411–414, 2012.

[173] Y. Ekşioğlu, A. E. Cetin, and J. Petráček. Optical response of plamonic nanohole arrays: comparison of square and hexagonal lattices. *Plasmonics*, 11:851–856, 2015.

[174] T. Thio, K. M. Pellerin, R. A. Linke, H. J. Lezec, and T. W. Ebbesen. Enhanced light transmission through a single subwavelength aperture. *Opt. Lett.*, 26:1972–1974, 2001.

[175] H. J. Lezec, A. Degiron, E. Devaux, R. A. Linke, L. Martín-Moreno, F. J. García-Vidal, and T. W. Ebbesen. Beaming light from a subwavelength aperture. *Science*, 297:820–822, 2002.

[176] L. Martín-Moreno, F. J. García-Vidal, H. J. Lezec, , A. Degiron, and T. W. Ebbesen. Theory of highly directional emission from a single subwavelength aperture surrounded by surface corrugations. *Phys. Rev. Lett.*, 90:167401, 2003.

[177] P. Lalanne, J. P. Hugonin, and J. C. Rodier. Theory of surface plasmon generation at nanoslit apertures. *Phys. Rev. Lett.*, 95:263902, 2005.

[178] T. Søndergaard and S. I. Bozhevolnyi. Surface plasmon polariton scattering by a small particle placed near a metal surface: An analytical study. *Phys. Rev. B*, 69:045422, 2004.

[179] F. López-Tejeira, F. J. García-Vidal, and L. Martín-Moreno. Scattering of surface plasmons by one-dimensional periodic nanoindented surfaces. *Phys. Rev. B*, 72:161405, 2005.

[180] S. C. Hohng, Y. C. Yoon, D. S. Kim, V. Malyarchuk, R. Müller, Ch. Lienau, J. W. Park, K. H. Yoo, J. Kim, H. Y. Ryu, and Q. H. Park. Light emission from the shadows: Surface plasmon nano-optics at near and far fields. *App. Phys. Lett.*, 81:3239–3241, 2002.

[181] E-S. Kwak, J. Henzie, S-H. Chang, S. K. Gray, G. C. Schatz, and T. W. Odom. Surface plasmon standing waves in large-area subwavelength hole arrays. *Nano Lett.*, 5:1963–1967, 2005.

[182] H. Gao, J. Henzie, and T. W. Odom. Direct evidence for surface plasmon-mediated enhanced light transmission through metallic nanohole arrays. *Nano Lett.*, 6:2104–2108, 2006.

[183] M. H. Chowdhury, J. M. Catchmark, and J. R. Lakowicz. Imaging three-dimensional light propagation through periodic nanohole arrays using scanning aperture microscopy. *Appl. Phys. Lett.*, 91, 2007.

[184] M. Mrejen, A. Israel, H. Taha, M. Palchan, and A. Lewis. Near-field characterization of extraordinary optical transmission in sub-wavelength aperture arrays. *Opt. Express*, 15:9129, 2007.

[185] F. Przybilla, A. Degiron, J.-Y. Laluet, C. Genet, and T. W. Ebbesen. Optical transmission in perforated noble and transition metal films. *J. Opt. A: Pure Appl. Opt.*, 8:458–463, 2006.

[186] A. Krishnan, T. Thio, T. J. Kim, H.J. Lezec, T. W. Ebbesen, P. A. Wolff, J. Pendry, L. Martín-Moreno, and F. J. García-Vidal. Evanescently coupled resonance in surface plasmon enhanced transmission. *Opt. Commun.*, 200:1 – 7, 2001.

[187] Xiang S., Amit A., and Ajay N. Role of metal film thickness on the enhanced transmission properties of a periodic array of subwavelength apertures. *Opt. Express*, 13(24):9834–9840, 2005.

[188] A. Degiron, H. J. Lezec, W. L. Barnes, and T. W. Ebbesen. Effects of hole depth on enhanced light transmission through subwavelength hole arrays. *Appl. Phys. Lett.*, 81:4327–4329, 2002.

[189] K. J. Klein Koerkamp, S. Enoch, F. B. Segerink, N. F. van Hulst, and L. Kuipers. Strong influence of hole shape on extraordinary transmission through periodic arrays of subwavelength holes. *Phys. Rev. Lett.*, 92:183901, 2004.

[190] A. Degiron and T. W. Ebbesen. The role of localized surface plasmon modes in the enhanced transmission of periodic subwavelength apertures. *J. Opt. A: Pure Appl. Opt.*, 7:S90, 2005.

[191] K. L. van der Molen, K. J. Klein Koerkamp, S. Enoch, F. B. Segerink, N. F. van Hulst, and L. Kuipers. Role of shape and localized resonances in extraordinary transmission through periodic arrays of subwavelength holes: Experiment and theory. *Phys. Rev. B*, 72:045421, 2005.

[192] J-Y. Chu, T-J. Wang, J-T. Yeh, M-W. Lin, Y-C. Chang, and J-K. Wang. Near-field observation of plasmon excitation and propagation on ordered elliptical hole arrays. *Appl. Phys. A*, 89:387–390, 2007.

[193] A. Dogariu, T. Thio, L. J. Wang, T. W. Ebbesen, and H. J. Lezec. Delay in light transmission through small apertures. *Opt. Lett.*, 26:450–452, 2001.

[194] C. Genet, M. P. van Exter, and J. P. Woerdman. Fano-type interpretation of red shifts and red tails in hole array transmission spectra. *Opt. Commun.*, 225:331–336, 2003.

[195] C. Ropers, D. J. Park, G. Stibenz, G. Steinmeyer, D. S. Kim, and C. Lienau. Femtosecond light transmission and subradiant damping in plasmonic crystals. *Phys. Rev. Lett.*, 94:113901, 2005.

[196] C. Ropers, G. Stibenz, G. Steinmeyer, R. Müller, D. J. Park, K. G. Lee, J. Kim, Q. H. Park, D. S. Kim, and C. Lienau. Ultrafast dynamics of surface plasmon polaritons in plasmonic metamaterials. *Appl. Phys. B: Lasers Opt.*, 84:183, 2006.

[197] B. Luk'yanchuk, N. Zheludev, S. Maier, N. J. Halas, P. Nordlander, H. Giessen, and C. T. Chong. The fano resonance in plasmonic nanostructures and metamaterials. *Nat. Mat.*, 9:707–715, 2010.

[198] E. Altewischer, X. Ma, M. P. van Exter, and J. P. Woerdman. Fano-type interference in the point-spread function of nanohole arrays. *Opt. Lett.*, 30:2436, 2005.

[199] R. Müller, C. Ropers, and C. Lienau. Femtosecond light pulse propagation through metallic nanohole arrays: The role of the dielectric substrate. *Opt. Express*, 12:5067–5081, 2004.

[200] N. P. Kobayashi, M. S. Islam, W. Wu, P. Chaturvedi, N. X. Fang, S. Y. Wang, and R. S. Williams. Microscopic origin of surface-plasmon radiation in plasmonic band-gap nanostructures. *Nano Lett.*, 9:178–182, 2009.

[201] W. Chen, K. P. Chen, M. D. Thoreson, A. V. Kildishev, and V. M. Shalaev. Ultrathin, ultrasmooth, and low-loss silver films via wetting and annealing. *Appl. Phys. Lett.*, 97:211107, 2010.

[202] Tomasz Stefaniuk, Piotr Wróbel, Paweł Trautman, and Tomasz Szoplik. Ultrasmooth metal nanolayers for plasmonic applications: surface roughness and specific resistivity. *Appl. Opt.*, 53(10):B237–B241, 2014.

[203] L. Douillard. and F. Charra. Photoemission electron microscopy, a tool for plasmonics. *J. Electron. Spectrosc. Relat. Phenom.*, 189S:24–29, 2013.

[204] R. Möller, U. Albrecht, J. Boneberg, B. Koslowski, P. Leiderer, and K. Dransfeld. Detection of surface plasmons by scanning tunneling microscopy. *J. Vac. Sci. Technol., B*, 9:506–509, 1991.

[205] L. Douillard. and F. Charra. High-resolution mapping of plasmonic modes: photoemission and scanning tunnelling luminescence microscopies. *J. Phys. D: Appl. Phys.*, 44:464002, 2011.

[206] R. Vogelgesang and A. Dmitriev. Real-space imaging of nanoplasmonic resonances. *Analyst*, 135:1175–1181, 2010.

[207] E. Brüche. Elektronenmikroskopische Abbildung mit lichtelektrischen Elektronen. *Z. Physik*, 86:448–450, 1933.

[208] R. M. Tromp, J. B. Hannon, A. W. Ellis, W. Wan, A. Berghaus, and O. Schaff. A new aberration-corrected, energy-filtered LEEM/PEEM instrument. i. principles and design. *Ultramicroscopy*, 110:852 – 861, 2010.

[209] Focus PEEM, Limburger Str, 75 D-65232 Taunusstein, Germany. *Instruction Manual Focus PEEM*, April 2007.

[210] O. Schmidt, M. Bauer, C. Wiemann, R. Porath, M. Scharte, O. Andreyev, G. Schönhense, and M. Aeschlimann. Time-resolved two photon photoemission electron microscopy. *App. Phys. B*, 74:223–227, 2002.

[211] W. E. Spicer. Photoemissive, photoconductive, and optical absorption studies of alkali-antimony compounds. *Phys. Rev.*, 112:114, 1958.

[212] F. Evers, C. Rakete, K. Watanabe, D. Menzel, and H-J. Freund. Two-photon photoemission from silver nanoparticles on thin alumina films: Role of plasmon excitation. *Surf. Sci.*, 593:43–48, 2005.

[213] G. P. Banfi, G. Ferrini, M. Peloi, and F. Parmigiani. Anomalous photoemission from Ag(100) in the femtosecond regime. *Phys. Rev. B*, 67:035428, 2003.

[214] A. Gloskovskii, D. A. Valdaitsev, M. Cinchetti, S. A. Nepijko, J. Lange, M. Aeschlimann, M. Bauer, M. Klimenkov, L. V. Viduta, P. M. Tomchuk, and G. Schönhense. Electron emission from films of Ag and Au nanoparticles excites by a femtosecond pump-probe laser. *Phys. Rev. B*, 77:195427, 2008.

[215] M. Aeschlimann, C. A. Schmuttenmaer, H. E. Elsayed-Ali, , and R. J. D. Miller. Observation of surface enhanced multiphoton photoemission from metal surfaces in the short pulse limit. *J. Chem. Phys.*, 102:8606, 1995.

[216] G. Ferrini, F. Banfi, C. Giannetti, and F. Parmigiani. Non-linear electron photoemission from metals with ultrashort pulses. *Nucl. Instr. Meth. Phys. Res.*, 601:123–131, 1995.

[217] J. Lin, N. Weber, M. Escher, J. Maul, H-S. Han, M. Merkel, S. Wurm, G. Schönhense, and U. Kleineberg. Three-dimensional characterization of extreme ultraviolet mask blank defects of interference contrast photoemission electron microscopy. *Opt. Express*, 16:15343, 2008.

[218] M. Cinchetti, A. Gloskovskii, S. A. Nepjiko, G. Schönhense, H. Rochholz, and M. Kreiter. Photoemission electron microscopy as a tool for the investigation of optical near fields. *Phys. Rev. Lett.*, 95:047601, 2005.

[219] A. Kubo, K. Onda, H. Petek, Z. Sun, Y. S. Jung, and H. K. Kim. Femtosecond imaging of surface plasmon dynamics in a nanostructured silver film. *Nano Lett.*, 5:1123–1127, 2005.

[220] P. Melchior and M. Aeschlimann. Probing and imaging of optical antennas with PEEM. *AIP Conf. Proc.*, 1398:9–13, 2011.

[221] C. Hrelescu, T. K. Sau, A. L. Rogach, F. Jäckel, G. Laurent, L. Douillard, and F. Charra. Selective excitation of individual plasmonic hotspots at the tips of single gold nanostars. *Nano Lett.*, 11:402–407, 2011.

[222] M. Aeschlimann, M. Bauer, D. Bayer, T. Brixner, F. J. Garcia de Abajo, W. Pfeiffer, M. Rohmer, C. Spindler, and F. Steeb. Adaptive subwavelength control of nano-optical fields. *Nature*, 446:301–304, 2007.

[223] D. Bayer, C. Wiemann, O. Gaier, M. Bauer, and M. Aeschlimann. Time-resolved 2PPE and time-resolved PEEM as a probe of LSP's in silver nanoparticles. *J. of Nanomater.*, 2008:249514, 2008.

[224] M. Rohmer, M. Bauer, T. Leissner, C. Schneider, A. Fischer, G. Niedner-Schatteburg, B. v. Issendorff, and M. Aeschlimann. Time-resolved photoelectron nano-spectroscopy of individual silver particles: Perspectives and limitations. *Phys. Status Solidi B*, 247:1132–1138, 2010.

[225] L. I. Chelaru and F-J. Meyer zu Heringdorf. In situ monitoring of surface plasmons in single-crystalline Ag-nanowires. *Surf. Sci.*, 601:4541 – 4545, 2007.

[226] C. Lemke, C. Schneider, T. Leißner, D. Bayer, J. W. Radke, A. Fischer, P. Melchior, A. B. Evlyukhin, B. N. Chichkov, C. Reinhardt, M. Bauer, and M. Aeschlimann. Spatiotemporal characterization of SPP pulse propagation in two-dimensional plasmonic focusing devices. *Nano Lett.*, 13:1053–1058, 2013.

[227] C. Lemke, T. Leißner, A. Evlyukhin, J. W. Radke, A. Klick, J. Fiutowski, J. Kjelstrup-Hansen, H-G. Rubahn, B. N. Chichkov, C. Reinhardt, and M. Bauer. The interplay between localized and propagating plasmonic excitations tracked in space and time. *Nano Lett.*, 14:2431–2435, 2014.

[228] J. Lin, N. Weber, A. Wirth, S. H. Chew, M. Escher, M. Merkel, M. F. Kling, M. I. Stockman, F. Krausz, and U. Kleineberg. Time of flight-photoemission electron microscope for ultrahigh spatiotemporal probing of nanoplasmonic optical fields. *Rev. Sci. Instrum.*, 75:2323, 2004.

[229] I. Z. Kozma, P. Baum, U. Schmidhammer, S. Lochbrunner, and E. Riedle. Compact autocorrelator for the online measurement of tunable 10 femtosecond pulses. *J. Phys.: Condens. Matter*, 21:314005, 2009.

[230] M. Kestler. *Optical fs-Pump-Probe Spectroscopy on hexagonal Nanohole Gratings.* PhD thesis, Ludwig-Maximilians-Universität München, 2017.

[231] M. Rycenga, C. M. Cobley, J. Zeng, W. Li, C. H. Moran, Q. Zhang, D. Qin, and Y. Xia. Controlling the synthesis and assembly of silver nanostructures for plasmonic applications. *Chem. Rev.*, 111:3669–3712, 2011.

[232] B. Duscner. *The Development, Fabrication and Characterization of Gold Nanohole Arrays for Ultrafast EOT Experiments.* PhD thesis, Ludwig-Maximilians-Universität München, 2016.

[233] E. Taglauer. Surface cleaning using sputtering. *Applied Physics A*, 51:238–251, 1990.

[234] J. C. Kim, J.-Y. Ji, J. S. Kline, J. R. Tucker, and Shen T.-C. Preparation of atomically clean and flat si(100) surfaces by low-energy ion sputtering and low-temperature annealing. *Appl. Surf. Sci.*, 220:293, 2003.

[235] David M. Fryauf, Juan J. Diaz Leon, Andrew C. Phillips, and Nobuhiko P. Kobayashi. Silver film surface modification by ion bombardment decreases surface plasmon resonance absorption. *ACS Applied Materials & Interfaces*, 9(18):15841–15847, 2017.

[236] Farid F. Umarov and Abdiravuf A. Dzhurakhalov. Ion bombardment-induced surface effects in materials. In Waldemar A. Monteiro, editor, *Radiation Effects in Materials*, chapter 14, pages 359–391. IntechOpen, Rijeka, 2016.

[237] L. Hanley and S. B. Sinnott. The growth and modification of materials via ion-surface processing. *Surf. Sci.*, 500:500–522, 2002.

[238] M. A. Makeev, R. Cuerno, and Barabási. Morphology of ion-sputtered surfaces. *Nucl. Instr. Meth. Phys. Res. B*, 197:187–227, 2002.

[239] J. F. Ziegler, M. D. Ziegler, and J. P. Biersack. SRIM - The stopping and range of ions in matter (2010). *Nucl. Instr. Meth. Phys. Res. B*, 268:1818–1823, 2010.

[240] F. Schuknecht. *Characterisation of Surface Plasmon Polaritons on Ion Beam Polished Waveguides via Photoemission Electron Microscopy.* PhD thesis, Ludwig-Maximilians-Universität München, 2016.

[241] Lumerical FDTD Solutions 8.15.

[242] A. Schriffin, T. Paasch-Colberg, N. Karpowicz, V. Apalkov, D. Gerster, S. Mühlbrandt, M. Korbman, J. Reichert, M. Schultze, S. Holzner, J. V. Barth, R. Kienberger, R. Ernstorfer, V. S. Yakovlev, M. I. Stockman, and F. Krausz. Optical-field-induced current in dielectrics. *Nature*, 493:7430, 2013.

[243] E. D. Palik. *Handbook of Optical Constants of Solids*. Academic Press, 1985.

[244] Mohamed Akbi and André Lefort. Work function measurements of contact materials for industrial use. *Journal of Physics D: Applied Physics*, 31:1301, 1999.

[245] F-J. Meyer zu Heringdorf, L. I. Chelaru, S. Möllenbeck, D. Thien, and M. Horn von Hoegen. Femtosecond photoemission microscopy. *Surf. Sci.*, 601:4700–4705, 2007.

[246] N.M. Buckanie, P. Kirschbaum, S. Sindermann, and F-J. Meyer zu Heringdorf. Interaction of light and surface plasmon polaritons in Ag islands studied by nonlinear photoemission microscopy. *Ultramicroscopy*, 130:49–53, 2013.

[247] D. E. Aspnes and A. A. Studna. Dielectric functions and optical parameters of si, ge, gap, gaas, gasb, inp, inas, and insb from 1.5 to 6.0 ev. *Phys. Rev. B*, 27:985–1009, 1983.

[248] Tobias A. F. König, Petr A. Ledin, Justin Kerszulis, Mahmoud. A. Mahmoud, Mostafa A. El-Sayed, John R. Reynolds, and Vladimir V. Tsukruk. Electrically tunable plasmonic behavior of nanocube–polymer nanomaterials induced by a redox-active electrochromic polymer. *ACS Nano*, 8:6182–6192, 2014.

[249] R. Dehde. *FDTD Simulation of a Rectangular Subwavelength Nanohole Array*. PhD thesis, Ludwig-Maximilians-Universität München, 2014.

[250] H. R. Philipp. Optical properties of silicon nitride. *J. Electrochem. Soc.*, 120:295–300, 1973.

Danksagung

I would first of all like to thank my supervisor Prof. Dr. Ulf Kleineberg for giving me the opportunity to work in his group. He was always ready to contribute new ideas, enthusiasm, and resources towards the project. I would also like to thank him for encouraging me to travel to a number of conferences and workshops, where I gained valuable skills and knowledge.

Secondly, I would like to thank my colleagues for all their support. I benefited greatly from the range of expertise within our group. Casey Chew was an invaluable help in teaching me the ways of the PEEM (having learnt the hard way herself), so I thank her for her time and patience. Jürgen Schmidt as the "laser whisperer" was often responsible for ensuring a key piece of the group's infrastructure was doing its job, which was far from an easy task, a task which Stefan Heinrich later took on. Christian Späth, Alexander Guggenmos, Benjamin Duschner, and Anika Spreen committed a lot of time and effort to fabricating various samples, without which I would not have had any experiments. The "hard yakka" of the diploma and bachelors students I supervised also played a key role in achieving the simulated and experimental results.

I am grateful to Peter Weiser of the Walter Schottky Institut, and Mahmoud Hezam, Hassan Ouacha, and Abdallah Azzeer of the King Abdullah Institute for Nanotechnology for their help with focused ion beam lithography. I would also like to thank Christina Graf and Valerie Mondes from the Freie Universität Berlin for supplying me with nanoparticle samples and helpful discussions.

I owe thanks to the many members of the Kraus group who assisted in various ways, whether by loaning hardware, sharing ideas, helping me find my way around the place, or simply offering distractions when necessary.

A big thank you to my family for supporting me, even if you had no idea what I was doing. And last but not least, thanks to my friends back home and new ones I made during my time in Germany. You made it worth the trip.